Characteristics and causes of Irminger Water variability in the subpolar North Atlantic between 1993 and 2022

Kevin Niklas Wiegand

University of Bremen, 2023

Characteristics and causes of Irminger Water variability in the subpolar North Atlantic between 1993 and 2022

Fachbereich für Physik und Elektrotechnik
der Universität Bremen
zur Erlangung des akademischen Grades
Doktor der Naturwissenschaften (Dr. rer. nat.)

von
Kevin Niklas Wiegand
aus Braunschweig

1. Gutachterin: Dr. Dagmar Kieke
2. Gutachter: Prof. Dr. Paul G. Myers
3. Gutachter: Dr. Gunnar Spreen

Eingereicht am: 24.08.2023
Tag des Promotionskolloquiums: 13.12.2023

Abstract

Irminger Water (IW) originates in the subtropical North Atlantic and is transported northeastward with the North Atlantic Current. It is located in the Irminger Sea and the boundary current system (BCS) off Greenland and Labrador. As the warmest and most saline water mass in this region, it impacts glacial melt and convection in the Irminger and Labrador Seas. This thesis focuses on analyzing temporal and spatial variability of IW using the ARMOR3D data set from 1993 to 2022. It adds to analyzing IW in an ocean reanalysis and different model simulations. Utilizing data from ship surveys to the west of Greenland (at eastern AR7W), a local validation of ARMOR3D is performed. Eastern AR7W exhibits IW hydrography and volume transport variability. Seasonal variability results from colder and fresher waters formed during winter convection in the Irminger and Labrador Seas. On multi-year time scales, subpolar gyre changes tied to the North Atlantic Oscillation lead IW volume transports at eastern AR7W by up to three years.

The commonly used static IW definitions generate a physically unrealistic boundary between IW and colder, fresher ambient waters. This thesis introduces a new method using non-static thresholds considering large-scale changes in the subpolar North Atlantic. This method infers hydrographic variability in an Irminger Sea subregion into the BCS. Results indicate that the static method overestimates IW volume transports by 1.3 Sv in saline years and underestimates it 0.9 Sv in fresh years. Another method, based on local water column hydrography, examines warm, saline water variability in regions where IW is mixed with ambient waters.

On average, reanalysis and model data exhibit a bias toward higher temperatures and salinities compared to ARMOR3D. The first new method corrects these biases when examining IW variability. However, aside from these biases, reanalysis and models show different vertical water column structures at eastern AR7W. The two new methods to identify IW partially adjust these differences but cannot fully compensate for them. This thesis provides a new understanding of the characteristics and causes behind IW's spatial and temporal variability. The newly developed methods offer IW variability using a more physical and process-oriented approach of temporally varying hydrographic thresholds.

Zusammenfassung

Irmingerwasser (IW) stammt aus dem subtropischen Nordatlantik und wird mit dem Nordatlantikstrom nach Nordosten transportiert. Es befindet sich in der Irmingersee und im Randstromsystem vor Grönland und Labrador. Als wärmste und salzhaltigste Wassermasse in dieser Region hat es Auswirkungen auf die Gletscherschmelze und die Konvektion in der Irminger- und Labradorsee. Diese Dissertation konzentriert sich auf die Analyse der zeitlichen und räumlichen Variabilität von IW mit dem ARMOR3D Datensatz von 1993 bis 2022. Darüber hinaus wird IW in einer Ozean-Reanalyse und verschiedenen Modellsimulationen analysiert. Unter Verwendung von Daten aus Schiffsmessungen westlich von Grönland (Östlich-AR7W) wird eine lokale Validierung von ARMOR3D durchgeführt. Östlich-AR7W weist eine Variabilität der IW-Hydrographie und des Volumentransports auf. Die saisonale Variabilität resultiert aus kälterem und salzärmerem Wasser, das sich während der Winterkonvektion in der Irminger- und Labradorsee bildet. Auf mehrjährigen Zeitskalen gehen Änderungen des subpolaren Wirbels, die mit der Nordatlantischen Oszillation verbunden sind, dem IW-Volumentransport bei Östlich-AR7W um bis zu drei Jahre voraus.

Die üblicherweise verwendeten statischen IW-Definitionen erzeugen eine physikalisch unrealistische Grenze zwischen IW und kälterem, salzärmerem Umgebungswasser. In dieser Dissertation wird eine neue Methode vorgestellt, die nicht-statische Schwellenwerte verwendet und großräumige Veränderungen im subpolaren Nordatlantik berücksichtigt. Mit dieser Methode wird die hydrographische Variabilität in einer Teilregion der Irmingersee auf das Randstromsystem übertragen. Die Ergebnisse zeigen, dass die statische Methode den IW-Volumentransport in salzhaltigen Jahren um 1,3 Sv überschätzt und in frischen Jahren um 0,9 Sv unterschätzt. Eine weitere Methode, die auf der lokalen Hydrographie der Wassersäule basiert, untersucht die Variabilität des warmen, salzhaltigen Wassers in Regionen, in denen IW mit dem Umgebungswasser vermischt ist.

Im Durchschnitt weisen Reanalyse- und Modelldaten im Vergleich zu ARMOR3D eine Verschiebung in Richtung höherer Temperaturen und Salzgehalte auf. Die erste neue Methode korrigiert diese Verschiebungen bei der Untersuchung der IW-Variabilität. Abgesehen von diesen Verschiebungen zeigen Reanalyse und Modelle jedoch unter-

schiedliche vertikale Strukturen der Wassersäule bei Östlich-AR7W. Die beiden neuen Methoden zur Identifizierung von IW gleichen diese Unterschiede teilweise aus, können sie aber nicht vollständig kompensieren. Diese Arbeit liefert ein neues Verständnis der Eigenschaften und Ursachen hinter der räumlichen und zeitlichen Variabilität von IW. Die neu entwickelten Methoden präsentieren IW-Variabilität mit einem mehr physikalischen und prozessorientierten Ansatz von zeitlich variierenden hydrographischen Schwellenwerten.

Contents

”The Road goes ever on and on, down from the door where it began. Now far ahead the Road has gone, and I must follow, if I can.”

Bilbo Baggins - Adventurer and explorer; from ”The Hobbit” by J.R.R. Tolkien

"We, the inhabitants of planet Earth, are performing a gigantic climate experiment."

Wallace Smith Broecker - Newberry Professor of Earth and Environmental Sciences at Lamont-Doherty Earth Observatory, 1987 (Broecker, 1987)

Chapter 1

Introduction

This thesis focuses on analyzing Irminger Water (IW). IW is a warm and saline water mass of subtropical origin, transported northward within the North Atlantic Current (NAC) into the subpolar North Atlantic (SPNA). IW has a large impact on various aspects of the climate system. For example, it serves as a major contributor of heat to Greenland's marine-terminating glaciers (Holland et al., 2008; Rignot et al., 2012; Straneo & Cenedese, 2015), which contribute to global sea level rise (e.g., The IMBIE Team, 2020; Goelzer et al., 2020). Consequently, understanding IW's variability and long-term changes is crucial for addressing critical societal challenges associated with global warming and rising sea levels. Moreover, IW influences stratification in the Irminger and Labrador Seas (e.g., Cuny et al., 2002; Myers et al., 2007; Rykova et al., 2009), playing a vital role in convective mixing and the formation of deeper waters. To gain a more comprehensive understanding of these impacts driven by IW, I present an overarching perspective of the ocean's importance within the climate system.

1.1 The global ocean and its role in the climate system

The Earth receives energy in the form of short-wave solar radiation. Due to the spherical shape of the Earth, low latitudes receive more short-wave radiation than high latitudes (Figure 1.1). Simultaneously, the Earth emits long-wave radiation into space. Similar to incoming short-wave radiation, outgoing long-wave radiation is higher at low latitudes and lower at high latitudes. However, the latitudinal gradient of the outgoing long-wave radiation is smaller than that of the incoming solar radiation. Thus, the net radiation indicates an energy gain at low latitudes and an energy loss at high latitudes, known as meridional imbalance (Figure 1.1). Among other processes, the meridional imbalance drives atmospheric and oceanic currents that advect the surplus of heat from low latitudes to high latitudes (e.g., Wunsch, 2005), and thus play a crucial role in the climate system (e.g., Guo et al., 2012; D. Hu et al., 2015; Palter, 2015). The ocean currents (Figure 1.2) advect heat, salt, and nutrients, distributing them globally (e.g., Nitani, 1972; Qiu & Lukas, 1996; Imawaki et al., 2013). One of these ocean currents, in particular, is the Gulf Stream, a strong wind-driven western boundary current (Stommel, 1948), transporting water northward along the western boundary of the North Atlantic. The Gulf Stream and its extension eventually merge into the NAC. Consequently, the Gulf Stream transports the warm and saline subtropical waters that constitute IW upon reaching the Irminger Sea.

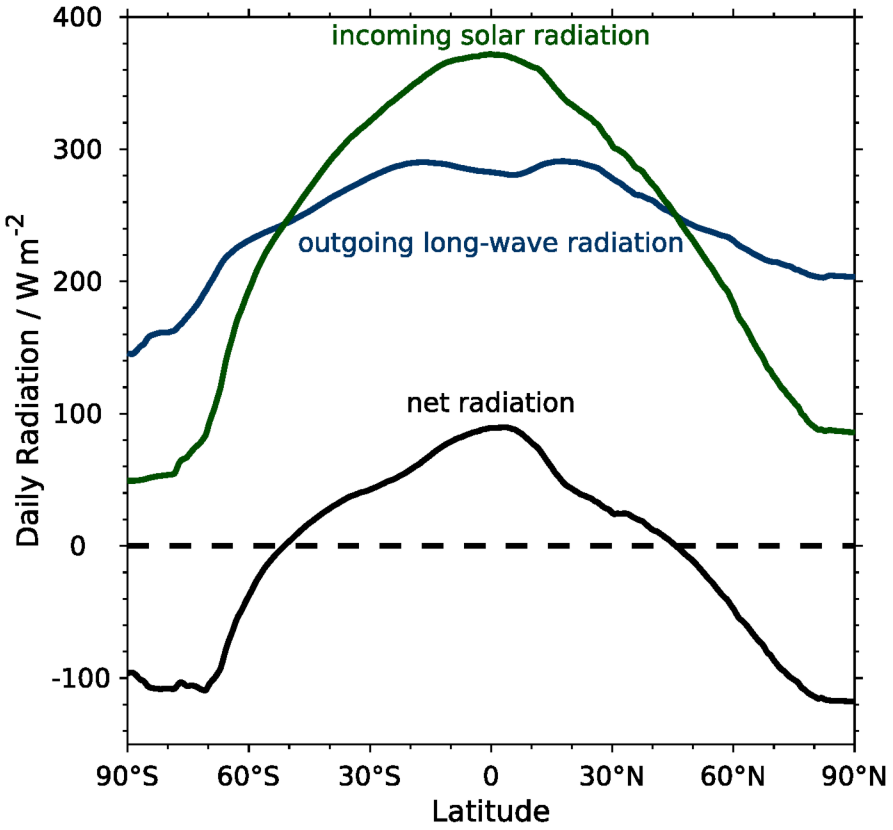

Figure 1.1: Meridional radiation imbalance averaged from 1959 - 2022 from the European Centre for Medium-Range Weather Forecasts Re-Analysis 5 (Hersbach et al., 2019). The black line indicates net radiation for individual latitudes. Blue and green lines indicate net outgoing longwave and incoming solar radiation. Data are averaged over all longitudes.

Broecker (1987) first introduced a largely simplified description of global ocean currents known as the "oceanic conveyor belt". This representation was subsequently refined (e.g., Schmitz, 1996; Rahmstorf, 2002; Kieke, 2005) by adding more details. Kuhlbrodt et al. (2007) later published another modified version of the previously described conveyor belt, referred to as the "global overturning circulation system". Generally, warm and saline waters are transported northwards in the upper ocean toward the poles. In higher latitudes, the ocean releases heat to the atmosphere due to the elevated temperature differences between the ocean and atmosphere, along with additional cold winds. The cooling, along with sea ice formation and the accompanied brine rejection, increases the density of the water, reduces its buoyancy, and therefore decreases the stratification in the water column until the water overturns. At depth, the water is transported back southward along the western boundaries toward the equator. At the ocean-atmosphere interface, the ocean exchanges gases with the atmosphere, among

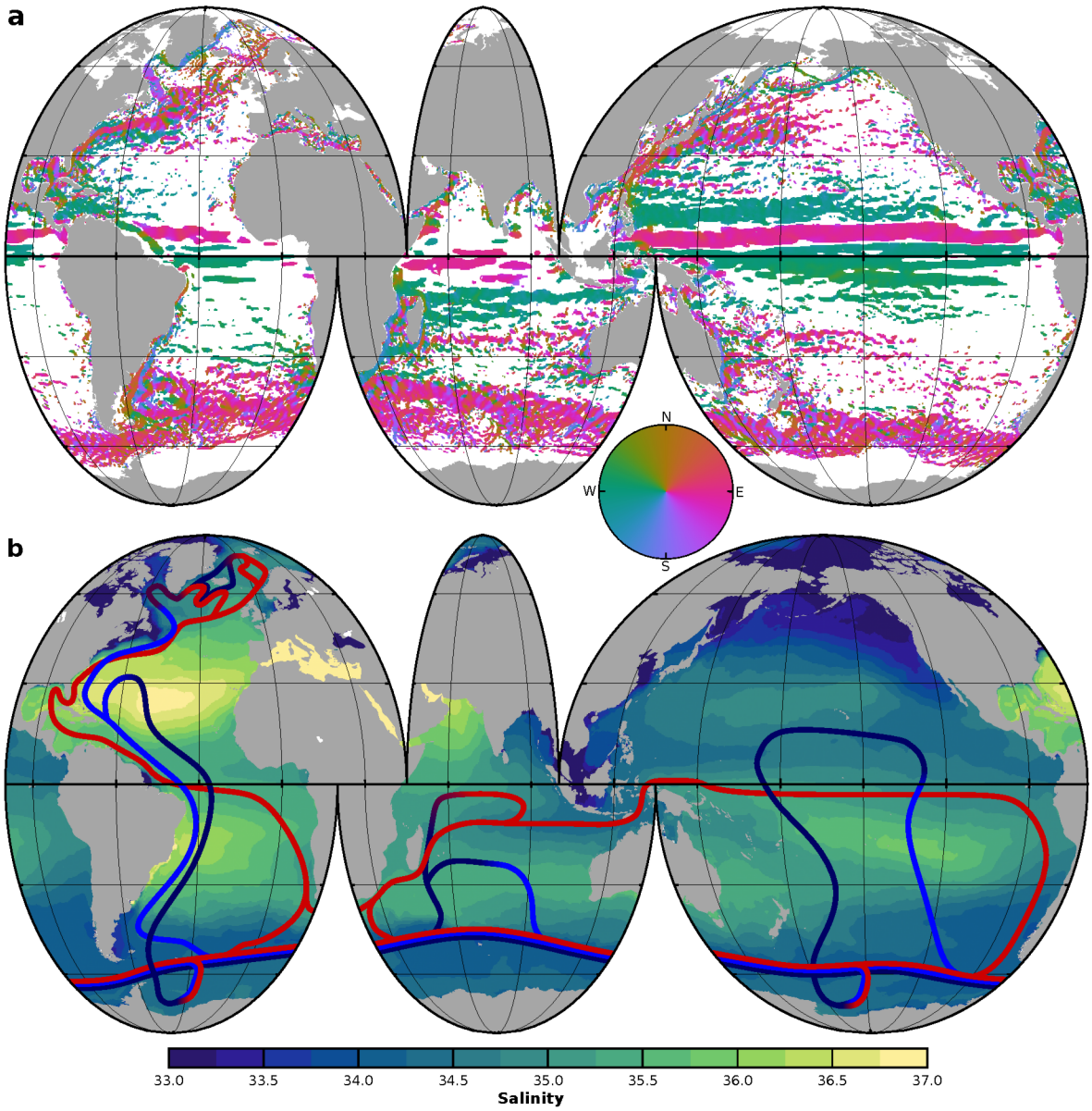

Figure 1.2: (a) Global ocean geostrophic velocity direction for velocities $>5\,\mathrm{cm\,s^{-1}}$ in the upper ocean (0 - 1,000 m) from ARMOR3D (see Chapter 2.1) averaged from 1993 - 2022. (b) Simplified sketch of ocean currents contributing to the global overturning circulation system modified after Schmitz (1996), Rahmstorf (2002), Kieke (2005), and Kuhlbrodt et al. (2007) superimposed on mean upper ocean salinity (0 - 1,000 m) from ARMOR3D averaged from 1993 - 2022. Red colors denote warm and saline waters, blue colors denote cold and fresh waters.

those oxygen, to achieve equilibrium. Once the water is isolated from the surface, gas exchange with the atmosphere ceases. Therefore, convection plays a vital role in ventilating the water column. Additionally, also carbon and nutrients are transported from the surface into deeper ocean layers (e.g., Frajka-Williams et al., 2019).

When the stratification is weak, and the buoyancy loss is strong, convection reaches greater depths (e.g., Yashayaev, 2007a). This process is known as deep convection, during which deep waters are formed. In the Northern Hemisphere, the regions of deep water formation are located in the Nordic Seas (e.g., Malmberg & Jónsson, 1997), the Irminger Sea (e.g., Pickart et al., 2003b), and the Labrador Sea (e.g., Lazier, 1973). In the Southern Hemisphere, these regions are located in the Weddell and Ross Seas (both, e.g., Killworth, 1983), as well as generally at the Antarctic ice shelves (e.g. Orsi, 2010) and, occasionally, in open-ocean polynyas (e.g. Killworth, 1983; Gülk et al., 2023). The newly formed deep waters are transported toward the equator in the deeper ocean (Figure 1.2 b). The global overturning circulation is a meridional measure of the zonally and vertically integrated flow (e.g., Frajka-Williams et al., 2019). As a result, the global overturning circulation is often referred to as the Meridional Overturning Circulation. The strength of the Meridional Overturning Circulation can be quantified as the maximum of the vertically and cummulatively integrated overturning streamfunction, expressed as volume transport (e.g., Frajka-Williams et al., 2019; Lozier, 2023). Processes of upwelling in the subtropical gyres (e.g., Kuhlbrodt et al., 2007), at the equator (e.g., Cromwell, 1953), along coasts (e.g., Huyer, 1983), around Antarctica (e.g., Kuhlbrodt et al., 2007), as well as mixing (e.g., Kuhlbrodt et al., 2007) contribute to closing the circulation.

The Intergovernmental Panel on Climate Change (IPCC, 2021) asserts that "it is unequivocal that human influence has warmed the atmosphere, ocean, and land." Water has a higher heat capacity than air and land (e.g., Stewart, 2008). As a result, the ocean's warming accounts for 91 % of the heating of the entire climate system (IPCC, 2021). Relative to the average from 1971 to 2000, the global surface (land and ocean) temperature increased by 0.7 °C between 2018 and 2022 (Figure 1.3), according to global surface temperature data from the National Oceanic and Atmospheric Administration (NOAA, 2023a). Compared to the average from 1880 to 1900, the global mean temperature has increased by 1.2 °C. However, these values represent a global average. The highest warming rates are observed at high latitudes (Figure 1.3), where the subarctic regions and the Arctic, in particular, have experienced the highest temperature increase of 2.3 °C since the average from 1971 to 2000 and 3.8 °C since 1880 to 1900. Different factors lead to an anomalously strong warming of the Arctic, a phenomenon called Arctic Amplification (Wendisch et al., 2023). One of these factors is

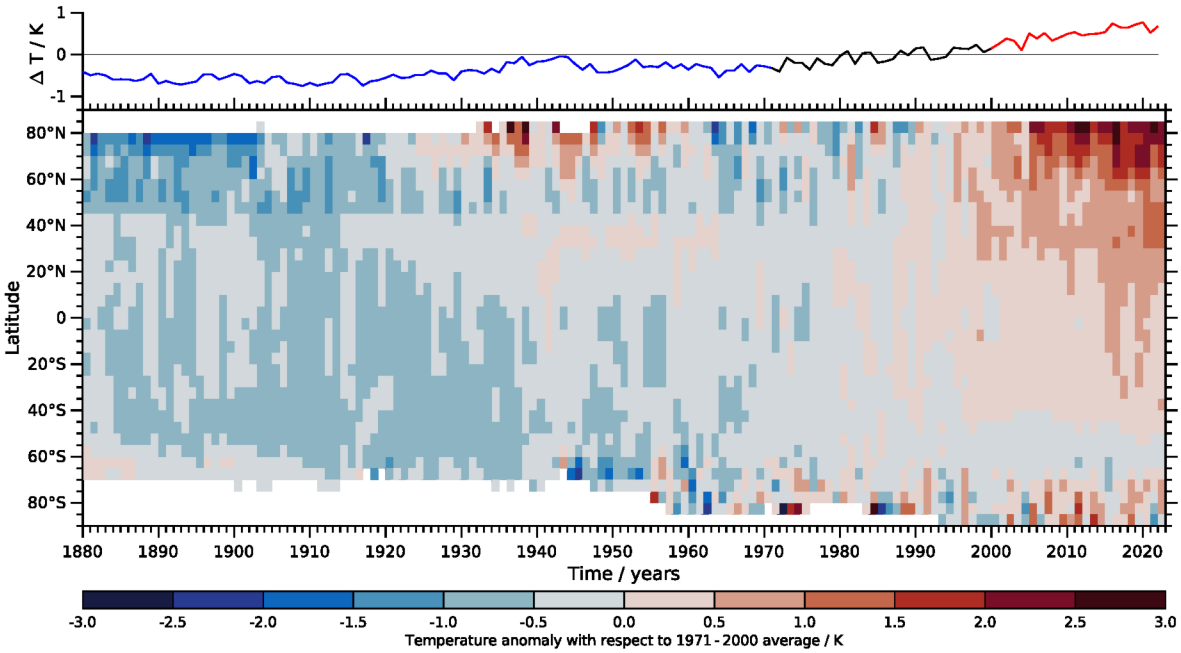

Figure 1.3: Global temperature anomalies from NOAA (2023a) with respect to the 1971 - 2000 average. (a) Globally averaged annual surface (land and ocean) temperature anomalies (1880 - 1970 in blue, 1971 - 2000 in black, and 2001 - 2022 in red) with respect to the 1971 - 2000 average. (b) annual global surface (land and ocean) temperature anomalies between 1880 and 2022 with respect to the 1971 - 2000 average for averaged bins of 5° in latitude. Red colors indicate positive anomalies. Blue colors indicate negative anomalies.

the ice-albedo-feedback (e.g., Siedler et al., 2013; Wendisch et al., 2023). The present sea ice reflects solar radiation due to its high albedo. With less sea ice and exposing the darker ocean, more solar radiation is absorbed due to the lower ocean's albedo. Changing albedo also occurs as melting glaciers expose dark bedrock. This process describes a positive feedback loop, as ice retreat leads to greater heat uptake, resulting in higher temperatures and, in turn, even more extensive ice retreat.

1.2 A detailed look into the North Atlantic Ocean

One of the dominant oceanic features in the North Atlantic Ocean is the NAC (Figure 1.4). The NAC is the continuation of the Gulf Stream and its extension (e.g., Krauss, 1986). Directed northeastward, the NAC transports warm and saline waters across the North Atlantic (e.g., Rossby, 1996; Hátún et al., 2005; Yashayaev & Seidov, 2015a). While different branches leave the NAC toward the southeast as recirculation of the subtropical gyre, the branches relevant for this thesis propagate eastward (e.g.,

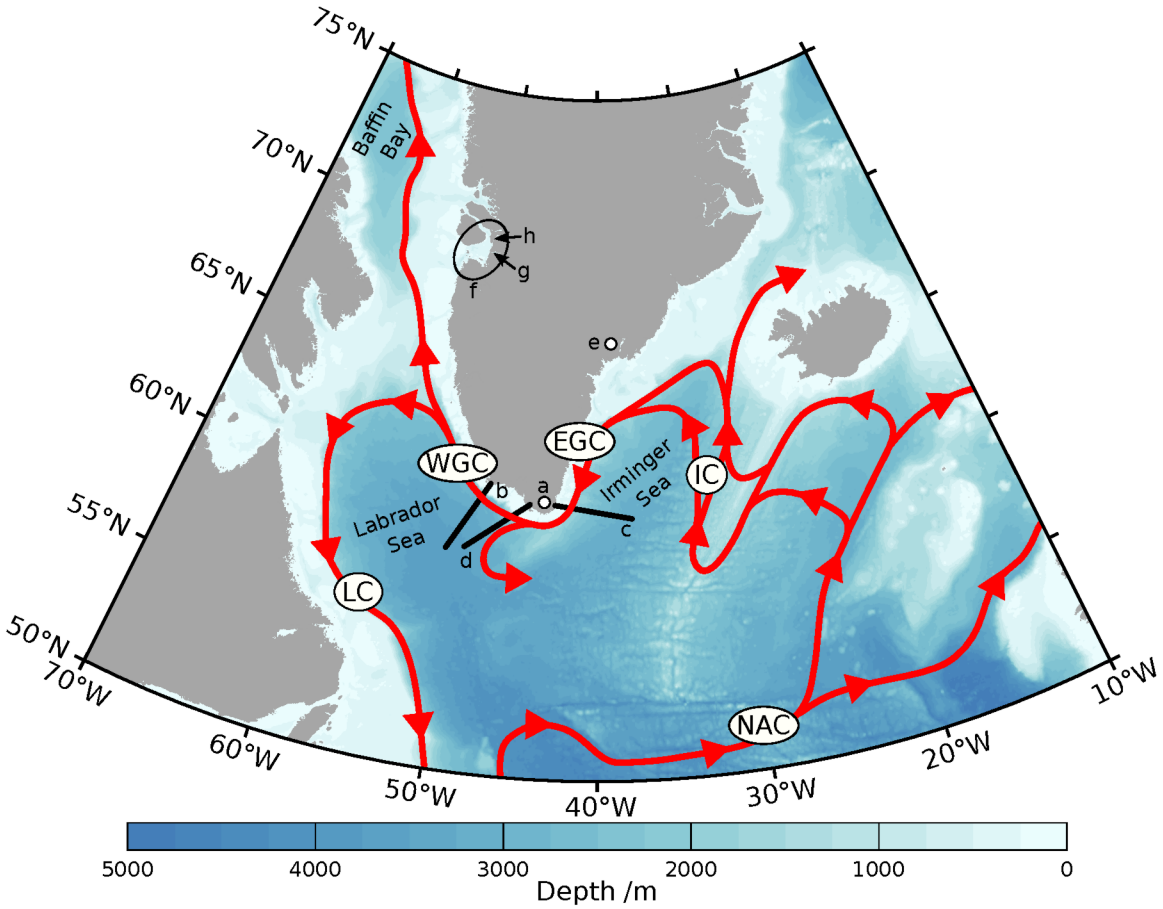

Figure 1.4: Map of the subpolar North Atlantic, including the Irminger and Labrador Seas, and parts of Baffin Bay. Colors denote bathymetry. Red lines demonstrate idealized schematic warm and saline water pathways that represent parts of major ocean currents. Locations mentioned in Chapter 1: a - Cape Farewell, b - Eastern AR7W, c - OSNAP East, d - OSNAP West, e - Sermilik Fjord, f - Disko Bay, g - Jakobshavn Isbræ, h - Atâ Sound. Abbreviations: NAC - North Atlantic Current, IC - Irminger Current, EGC - East Greenland Current, WGC - West Greenland Current, LC - Labrador Current.

Stendardo et al., 2020). Depending on the North Atlantic Oscillation (NAO), which describes anomalies of meridional atmospheric pressure differences in the North Atlantic, the NAC favors a more northern branch or a more southern branch (Holliday et al., 2020; Biló et al., 2022) when crossing the Mid-Atlantic Ridge eastward.

During periods of a positive NAO phase, when positive anomalies of westerly winds prevail across the North Atlantic, the NAC is shifted to the location of the southern branch (Buch et al., 2004; Holliday et al., 2020), resulting in a widening and strengthening of the subpolar gyre (SPG). This location of the NAC prevents larger amounts of Atlantic-origin waters from entering the Irminger Sea (e.g., Holliday et al., 2020;

Chafik et al., 2022). Instead, these waters are transported into the Nordic Seas (e.g., Holliday et al., 2008) and further into the Arctic Ocean (e.g., Muilwijk et al., 2018), where the warm waters release heat to the atmosphere. Subsequently, this heat is carried westwards toward Europe by the westerly winds, leading to anomalously warm temperatures compared to similar latitudes on the American continent (e.g., Maury & Leighly, 1855; Latif et al., 2000). Thus, the NAC plays a crucial role in shaping the climate on the European continent. The warm and saline waters transported into the Arctic Ocean have reached higher latitudes in recent years. As a result, temperature and salinity in the subsurface Arctic Ocean have increased, a phenomenon referred to as Arctic Atlantification (Polyakov et al., 2017; Smedsrud et al., 2021; Wendisch et al., 2023). Polyakov et al. (2017) argued that substantial changes would impact the Arctic Ocean system, bringing "dramatic influences on other geophysical and biogeochemical components" of the system. Interactions between the ocean and atmosphere are expected to increase as the insulating sea ice retreats, potentially affecting weather patterns in the mid-latitudes (Cohen et al., 2014; Vihma et al., 2019). Other changes involve freshwater storage and its export (Carmack et al., 2016) and an intensified exchange between the shelf and the basin interior (Williams & Carmack, 2015). Changes involving the northward shift of the sea ice edge and increased vertical mixing have already been observed in the Barents Sea (Polyakov et al., 2017), with consequences for local primary production (Reigstad et al., 2002; Wassmann et al., 2004).

During periods of a negative NAO phase, when negative anomalies of westerly winds prevail across the North Atlantic, the NAC propagates at the location of the northern branch (Buch et al., 2004; Holliday et al., 2020), resulting in a contraction and weakening of the SPG. This location of the NAC allows larger amounts of Atlantic-origin waters to recirculate in the Iceland and Irminger Basins (e.g., Holliday et al., 2020; Chafik et al., 2022). Once reaching the Irminger Sea, this branch is known as Irminger Current (IC, e.g., Straneo & Heimbach, 2013). The IC carries the warm and saline Atlantic-origin waters (here IW, e.g., Cuny et al., 2002; Pacini et al., 2020). In the western Irminger Sea, the IC propagates along the East Greenland Current (EGC) near the continental slope (e.g., Daniault et al., 2011a, 2011b). Major parts of the IC round Cape Farewell, the southern tip of Greenland (Figure 1.4), and, together with the EGC, become the West Greenland Current (WGC, e.g., Cuny et al., 2002; Holliday et al., 2009; de Jong et al., 2014) in the eastern Labrador Sea. Remnants of IW recir-

culate eastward into the Irminger Sea (Holliday et al., 2007), along with waters from the Labrador Sea's interior (Lavender et al., 2000). In this thesis, the entire system of boundary currents along the Greenland (EGC, WGC) and Labrador continental slopes (Labrador Current) is referred to as the boundary current system (BCS).

The warm and saline waters that are transported into the Nordic Seas and the Arctic Ocean or into the Iceland Basin and Irminger Sea impact regions where deep convection occurs. Following deep convection, the newly formed dense water masses propagate further within the Deep Western Boundary Current toward the equator (Pickart, 1992). Both the NAC and the Deep Western Boundary Current play a dominant role in the Atlantic Meridional Overturning Circulation (AMOC, Brambilla et al., 2008b; Desbruyères et al., 2019). Analyzing mooring observations in the Irminger Sea between 2014 and 2020, Sanchez-Franks et al. (2023) showed that the Irminger Sea accounts for 55 % of the AMOC's lower limb variability on monthly time scales. Thus, the Irminger Sea represents the region of greatest importance for subpolar AMOC variability in this period (Megann et al., 2021; Chafik et al., 2022). However, on multi-decadal time scales, the Labrador Sea's role in contributing to the formation of dense Labrador Sea Water (LSW) is essential for shaping AMOC variability (e.g., Yeager et al., 2021; Yashayaev et al., 2022; Böning et al., 2023). In the 21st century, the projected decrease in the meridional imbalance and the associated Arctic Amplification (Wendisch et al., 2023), is projected to weaken the AMOC very likely (IPCC, 2021), which would have large impacts on the climate system. Jackson et al. (2015) argued that the North Atlantic and the general Northern Hemisphere, would cool as less warm water would be transported northward from the subtropics. This cooling would be accompanied by reduced precipitation in the mid-latitudes due to less evaporation in the SPNA and changes in tropical precipitation patterns (Jackson et al., 2015).

1.3 Introducing Irminger Water

1.3.1 Irminger Water and where to find it

The IC transports IW counter-clockwise in the Irminger Sea, following the bathymetry. Eventually, IW ends up within the WGC, for example, at the eastern end of the Atlantic Repeat Hydrography 7 West (AR7W) section (see Figure 1.4). In the following, I refer to the eastern end of the AR7W section as eastern AR7W. Here, IW covers depths between 200 and 600 m (Figure 1.5). This range represents the mean state between 1993 and 2022 in the ARMOR3D data set (see Chapter 2.1). At eastern AR7W, IW represents water with the highest salinities accompanied by the highest temperatures in the upper 1,500 m (Figure 1.5). Horizontally, IW extends from the continental slope approximately 60 km into the Labrador Sea (Figure 1.5). These observations are consistent with other studies that have analyzed IW for almost 100 years, starting in the 1930s. These studies found IW at depths ranging from around 100 to over 500 m (e.g., Myers et al., 2007). From the total WGC volume transport of 30 - 54 Sv (e.g., Clarke, 1984; Reynaud et al., 1995; Holliday et al., 2009; Pacini et al., 2020), where $1\,\mathrm{Sv} = 1\,\mathrm{Sverdrup} \mathrel{\widehat{=}} 10^6\,\mathrm{m^3\,s^{-1}}$, the IW volume transport contributes about 3.2 - 11.0 Sv (Clarke, 1984; Myers et al., 2007; Pacini et al., 2020). IW is also advected from the BCS into the interior Labrador Sea (e.g., Lilly et al., 2003; Gelderloos et al., 2011; Palter et al., 2016), partially via eddies that detach from the WGC (e.g., Kawasaki & Hasumi, 2014; Pennelly et al., 2019) and also modulates local convection (Tagklis et al., 2020).

1.3.2 Irminger Water and its variability in the boundary current system

Previous studies have analyzed IW in the EGC (e.g., Johannessen et al., 2011), but primarily focused on the WGC in the eastern Labrador Sea (e.g., Cuny et al., 2002; Myers et al., 2007; Rykova et al., 2015). Using in-situ ship-based data, Myers et al. (2007) analyzed three WGC locations, two north of eastern AR7W and one at Cape Farewell. They found quasi-decadal variability in the layer-averaged IW temperature and salinity from 1950 to 2005. In the 1990s and early 2000s, they noted increased geostrophic IW volume transport that coincided with increased IW salinity upstream in the interior Irminger Sea (Bersch, 2002). Both increases in IW volume transport and salinity were accompanied by increased IW temperature and salinity at eastern

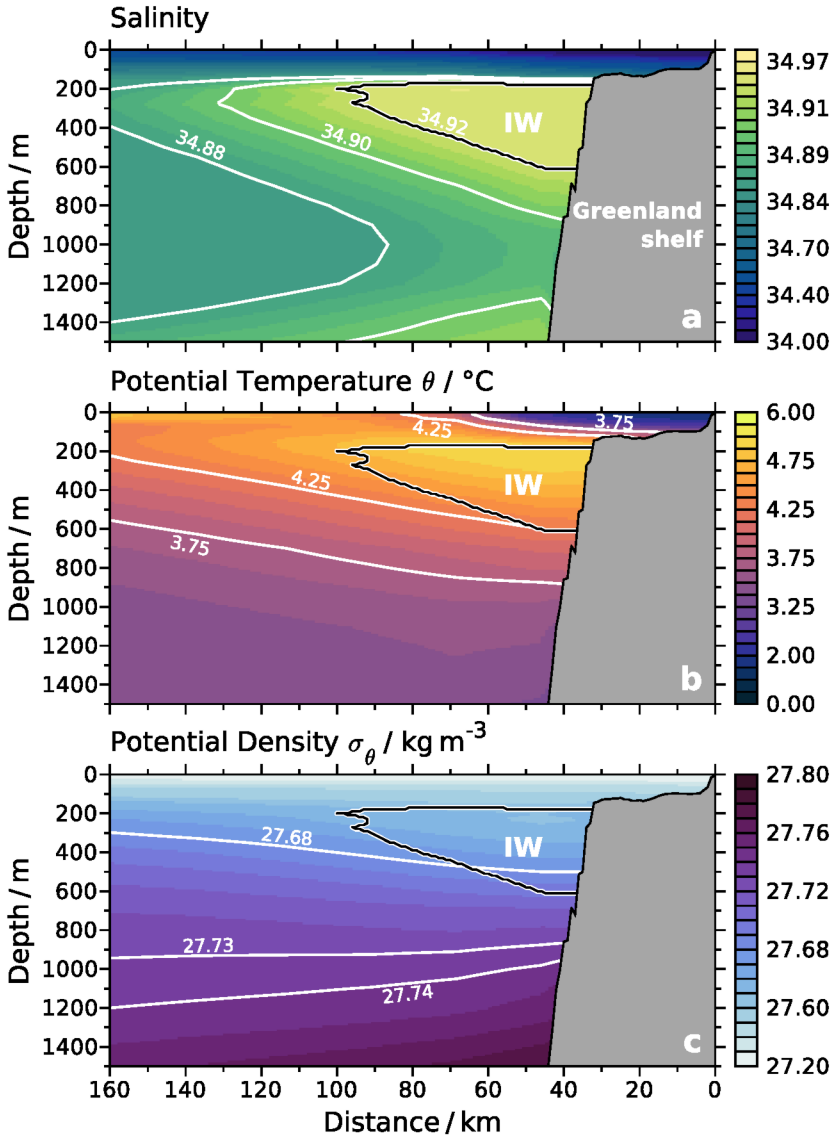

Figure 1.5: Eastern AR7W across the West Greenland Current, as represented in ARMOR3D (see Chapter 2.1), from the Greenland shelf (right) into the Labrador Sea (left). Data are averaged over the period 1993 - 2022 for (a) salinity, (b) potential temperature θ, and (c) potential density σ_θ. White lines represent selected isolines. Black lines encompass Irminger Water as defined in Chapter 3.2.

AR7W (Rykova et al., 2015). A follow-up study by Myers et al. (2009) found notable interannual variability of the IW volume transport at six repeat sections crossing the WGC. Using updated data from the same and additional sections, Ribergaard (2014) analyzed 1993 to 2013 and detected the largest IW thickness at Cape Farewell in 2010, rapidly decreasing until 2013. Similar IW variability was noted downstream along the WGC, with generally smaller IW volume as it was constantly mixed with colder and fresher ambient waters.

All the studies mentioned previously primarily relied on ship-based data from late spring to summer, limiting their use for investigating seasonal variability in the IW layer. However, seasonal variability within the IW layer is substantial. Kenchington et al. (2017) used ship-based data and observations from profiling floats at the south-western Greenland shelf break and observed seasonal temperature variability in the upper 500 m of the water column caused by local cooling and winter convective mixing in the Irminger Sea. Grist et al. (2014) addressed year-round subsurface (below 200 m) temperature records from the World Ocean Database and Argo floats combined with marine-mammal borne temperature sensors. They found a spatial variability of the subsurface temperature maximum determined by the advection time from the Irminger Sea downstream in the BCS.

Pacini et al. (2020) recently analyzed seasonal IW variability by examining data from mooring observations. These moorings have been deployed along two lines in the SPNA as part of the 'Overturning in the Subpolar North Atlantic Program' (OSNAP, Lozier et al., 2017). They cross the Labrador Sea from the Labrador shelf to the western Greenland shelf and the eastern SPNA from the eastern Greenland shelf across the Mid-Atlantic Ridge to the Irish shelf. The arrays crossing the EGC and the WGC are referred to as OSNAP East and OSNAP West, respectively. Both have been maintained since 2014. In this thesis, the focus is on the moorings within the EGC and the WGC. The OSNAP moorings deployed in the WGC (OSNAP West, located approximately 150 km upstream of eastern AR7W and 125 km downstream of Cape Farewell, Figure 1.4) revealed pronounced seasonal IW variability between 2014 and 2018 (Pacini et al., 2020). IW volume transport was weakest in spring and strongest in fall. Pacini et al. (2020) analyzed four different mooring arrays upstream of OSNAP East in the Irminger Sea (Figure 1.4) and observed IW being modified to a colder and fresher state caused by winter air-sea interactions causing oceanic heat and buoyancy loss. Furthermore, Pacini et al. (2020) identified the modification of IW through winter air-sea interaction as the primary cause for seasonal variability of hydrographic IW properties and volume transport. Using mooring data from the Irminger Sea, including OSNAP East, Le Bras et al. (2020) found that local wintertime convection modified warm and saline Atlantic-origin waters (here IW) to colder and fresher Irminger Sea Intermediate Water (ISIW) in 2014 to 2016. In Chapter 3, I present the variability of IW and their causes at eastern AR7W in ARMOR3D. ARMOR3D comprises thirty years of

weekly observation-based data between 1993 and 2022 at a horizontal resolution of 1/4°. Therefore, it offers the advantage of studying seasonal and multi-year variability within one data set. Thus, I do not rely solely on ship-based measurements from late spring and summer for multi-year analyses of IW or on temporally limited mooring observations for seasonal analyses of IW.

An observation-based data set often used in oceanographic studies is EN4 (Good et al., 2013). For example, Desbruyères et al. (2019) and Biló et al. (2022) utilized EN4 to describe large-scale processes in the entire SPNA. Such large-scale analyses seem to deliver robust results comprising the 1° horizontal resolution of EN4. However, especially for analyses within the BCS, a horizontal resolution of 1° is insufficient to resolve the areas along the continental slopes or horizontal fronts of the boundary currents. Additionally, its monthly temporal resolution is suitable for multi-year analyses. However, it lacks the required resolution when analyzing features occurring on smaller time scales.

IW has been analyzed in various model studies. Garcia-Quintana et al. (2019) and Pennelly and Myers (2020) investigated IW transported within Irminger Rings from the WGC into the interior Labrador Sea. While Garcia-Quintana et al. (2019) utilized model simulations comprising different horizontal resolutions of 1/4° (ANHA4, see Chapter 2.3) and 1/12° (ANHA12, see Chapter 2.3), Pennelly and Myers (2020) utilized a model simulation comprising a horizontal resolution of 1/60° (LAB60, see Chapter 2.3). Myers et al. (2021) did not focus their analysis on IW but utilized the same 1/12° model simulation as Garcia-Quintana et al. (2019) to analyze the variability of heat transport at Davis Strait, among other parameters. As IW is the warmest water mass in this region, it greatly contributes to the total heat transport. Additionally, two studies using the 1/60° model simulation similar to Pennelly and Myers (2020) investigated the temporal variability of, among other parameters, heat transport in the WGC. Gou et al. (2021) analyzed the heat transport in the WGC for seasonal variability. At the same time, (Gou et al., 2022) analyzed the heat transport in the WGC for multi-year variability. Another recent study utilizing LAB60, (Gou et al., 2023) analyzed the variability of eddy formation in the WGC. Among other water masses, they also quantified IW at different cross-slope sections, including eastern AR7W. They found that at Cape Desolation, IW describes a layer of warm and saline waters throughout the year rather than a distinct water mass. However, none of these mentioned model stud-

ies validated the representation of IW within the individual model simulations against observations. Therefore, this thesis provides a detailed comparison of the mentioned model simulations (ANHA4, ANHA12, and LAB60, see Chapter 2.3) and an oceanic reanalysis (GLORYS, see Chapter 2.2) with ARMOR3D in Chapter 5.

1.3.3 Irminger Water and how it is defined

Studies that previously analyzed IW used different salinity, temperature, and density definitions to identify IW in the water column and to distinguish it from ambient waters. These thresholds represented either a range or a lower limit of the respective hydrographic property characterizing IW. Individual studies differentiated between IW and Irminger Mode Water (Buch, 2000; Buch et al., 2004) or between "pure" and "modified" IW (Myers et al., 2009; Ribergaard, 2014). I stick to the description of pure and modified IW when referring to these studies. The authors described modified IW as being formed by mixing pure IW with colder and fresher ambient waters on its pathway in the BCS. They found that pure or modified IW dominated the water column at individual cross-slope sections along the WGC on decadal time scales. Therefore, IW tended to be either warmer and more saline or colder and less saline, respectively. Buch et al. (2004) found that before 1970 pure IW dominated the water column over modified IW at Cape Farewell. Between 1970 and 1995, modified IW became dominant, and after 1995 pure IW dominated again. Buch et al. (2004) suggested that the dominant modified IW was likely caused by an increased inflow of polar waters from the Arctic linked to the Great Salinity Anomaly (Dickson et al., 1988). Another reason for the dominance of the modified IW between 1970 and 1995 is the positive NAO phase, which led to less inflow of warm and saline Atlantic-origin waters into the BCS (Buch et al., 2004; Holliday et al., 2020; Chafik et al., 2022).

IW is subject to property changes due to mixing along the IW pathway and large-scale variability. These effects can occur on both seasonal and decadal time scales. Studies have suggested temporally changing core water mass properties for other water masses to account for these changes. Pickart et al. (2003b) and Yashayaev and Loder (2017) did so for LSW and Le Bras et al. (2022) suggested such an analysis for ISIW. In Chapter 4, I present methods that use temporally changing core water mass properties to identify IW in the BCS. Based on the changing core water mass properties, it is expected that the fixed property-range method tends to either overestimate (when the

water column is anomalously saline) or underestimate the IW volume transport (when the water column is anomalously fresh). With the new method, I analyze the extent of over- and underestimations of IW properties and its volume transport in the BCS and compare the results to the previous estimates based on the assumption of static water mass properties.

Le Bras et al. (2020) found that IW is modified to colder and fresher ISIW due to wintertime convection in the Irminger Sea. They differentiated between an upper ISIW (uISIW) and deep ISIW, which exceeds a depth of 1,500 m. In contrast to Le Bras et al. (2020), other studies considered ISIW as a type of LSW that recirculates from the Irminger Sea (e.g., Pickart et al., 2003b; Våge et al., 2011; Pacini et al., 2020). de Jong and de Steur (2016) referred to this water as iLSW to indicate the Irminger Sea as its origin. Further studies even directly addressed the convectively formed water from the Irminger Sea as LSW (e.g., van Aken et al., 2011; de Jong et al., 2012). However, the defined density range of LSW ($27.68\,\mathrm{kg\,m^{-3}} < \sigma_\theta < 27.80\,\mathrm{kg\,m^{-3}}$, e.g., Kieke & Yashayaev, 2015) is higher compared to ISIW ($27.65\,\mathrm{kg\,m^{-3}} < \sigma_\theta < 27.77\,\mathrm{kg\,m^{-3}}$, Le Bras et al., 2020). Consequently, existing studies do not always separate between convectively formed waters in the Irminger and Labrador Seas.

Instead, I interpret ISIW as a layer that is colder and fresher than IW, filled with waters of different origins and modified by wintertime convective mixing in the Irminger Sea. It denotes a mix of waters formed in the SPNA due to mixing outside the Labrador Sea convection zone. The sources of ISIW may include the Irminger Sea, the Iceland Basin, the Reykjanes Ridge, and slope regions. Additionally, it might be fed by recirculating LSW (e.g., Yashayaev, 2007a; van Aken et al., 2011; Böning et al., 2023) from the Labrador Sea. Throughout this thesis, I refer to the convectively formed water from the Irminger Sea as ISIW, following Le Bras et al. (2020). In contrast, I refer to the convectively formed water from the Labrador Sea as LSW.

1.3.4 Irminger Water and its impact in the subpolar North Atlantic

In the BCS, IW mixes with colder and fresher ambient waters through horizontal exchange, contributing to regional heat and salt budgets (Cuny et al., 2002; Straneo, 2006). In the Irminger and Labrador Seas, IW increases the stratification in the water column (e.g., Cuny et al., 2002; Myers et al., 2007; Rykova et al., 2009). Consequently, it reduces the vertical mixing depth and the intensity of winter convection (e.g., Cuny

et al., 2002). However, heat and salt oppose each other in their respective contributions to the IW density and, thus, the stratification. In turn, oceanic convection intensity shapes the properties and volume of newly formed LSW, an essential ingredient of the deep and cold limb of the AMOC (e.g., Yashayaev & Loder, 2016, 2017). Thus, IW is a major heat and salt supplier to the northwestern SPNA (e.g., Reynaud et al., 1995; Cuny et al., 2002) in the upper 1,000 m. Therefore, processes causing IW variability, require attention and a better understanding.

As stated before, IW is the warmest water mass southeast and west of Greenland. Thus, it plays a dominant role in the heat supply at the melting sites of individual marine-terminating glaciers (Holland et al., 2008; Rignot et al., 2012; Straneo & Cenedese, 2015) and the associated contribution to global sea level rise (The IMBIE Team, 2020; Goelzer et al., 2020). For example, IW is known to penetrate the Sermilik Fjord (eastern Greenland, Figure 1.4, e.g., Johannessen et al., 2011) and into the coastal Disko Bay area (western Greenland, e.g., Holland et al., 2008; Mortensen et al., 2014, 2018; Rysgaard et al., 2020). Due to the more extensive heat content of IW compared to the ambient waters, it thus contributes to the reduction of the stability of marine-terminating glaciers in these regions (Porter et al., 2018). Marine-terminating glaciers alone contribute 50 ± 20 % to Greenland's total mass loss through ice discharge due to increasing ocean temperatures (Choi et al., 2021).

One marine-terminating glacier is the Jakobshavn Isbræ, located within Disko Bay on the western coast of Greenland (Holland et al., 2008). It is connected to the surrounding open ocean via deep troughs. These troughs reach depths of 400 m, approximately the depth at which warm subsurface IW has been detected in previous studies (e.g., Holland et al., 2008; Rykova et al., 2015; Pacini et al., 2020). Holland et al. (2008) and Myers and Ribergaard (2013) showed that IW reaches the glacier's tongue through those deep troughs, thus enhancing subsurface melting. In the 2000s, Jakobshavn Isbræ experienced the largest discharge anomaly from the entire Greenland Ice Sheet (Enderlin et al., 2014). Since 2014, the glacier has instead been thickening again (Khazendar et al., 2019). On the contrary, other glaciers within Disko Bay are shielded by an underwater ridge in the Atâ Sound (Beaird et al., 2015). As a result, IW cannot penetrate beyond that ridge, and thus it does not reach glaciers downstream.

Similar to Greenland's western coast, its southeastern coast is affected by glacial melting induced by the entrainment of IW. Seale et al. (2011) found that an increase in

glacier mass loss is linked to large amounts of subtropical water in the Irminger Sea. Beaird et al. (2018) analyzed the melting of the Sermilik glacier on the eastern coast of Greenland (Figure 1.4) and found that IW plays a major role in its melting process. The resulting amounts of meltwater are highest at the surface. However, they are also present at 250 m depth, indicating subglacial melt. Additionally, Porter et al. (2018) found significant co-variability between ice-sheet thinning and ocean heat content near the glacier's grounding line. This co-variability is most pronounced to the east and southeast of Greenland but is less evident in western Greenland. Straneo and Heimbach (2013) suggested that the increase in glacial melting in the 1990s is, to some extent, likely due to an increasing presence of warm IW in the fjord systems. Wood et al. (2021) argues that a warming of subsurface ocean waters by approximately 1.9 °C between the averaged periods from 1992 to 1997 and 1998 to 2007 caused glacial melt at the grounding line in 62 % of the investigated glaciers. Smedsrud et al. (2021) showed that subsurface temperatures in northeast Greenland strongly increased between 2000 and 2017, accompanied by rapid simulated melting of marine-terminating glaciers. The authors further stated that marine-terminating glaciers have a long response time. Hence, even if a further increase of subsurface temperatures does not occur or the temperatures are to return to a previous level, the marine-terminating glaciers will likely retreat further (Smedsrud et al., 2021). Melting of the Greenland Ice Sheet already contributed to a global sea level rise of more than 10 mm since 1992 (The IMBIE Team, 2020). Projections suggest that Greenland's glaciers will contribute between 32 ± 17 mm and 90 ± 50 mm to the global sea level rise by 2100, depending on the evolution of greenhouse gases in the atmosphere (Goelzer et al., 2020). Consequently, understanding IW's variability and possible multi-year trends is critical to further examining Greenland's melting of marine-terminating glaciers and the associated sea level rise.

1.4 Thesis objectives

This thesis aims to contribute to a better understanding of various physical processes related to IW, such as its contribution of heat toward Greenland's marine-terminating glaciers or its increase in stratification in the convection region in the Irminger and Labrador Seas. Within this thesis, I contribute to increasing the knowledge of IW based on three overarching research questions:

1. **What processes shape the variability of Irminger Water at eastern AR7W on seasonal and multi-year time scales?**

2. **How can large-scale changes in the subpolar North Atlantic be incorporated into the process of identifying IW, and what are the resulting consequences for Irminger Water variability?**

3. **How do different model simulations represent Irminger Water, and how does its observed variability compare to these simulations?**

This thesis is structured as follows: In Chapter 2, I present the data used throughout the entire thesis. These include the primary data sets utilized to analyze IW variability and secondary data sets used for comparison. Chapter 3, Chapter 4, and Chapter 5 comprise the main analyses in this thesis. Each of the three chapters follows a specific color scheme (Chapter 3: yellow; Chapter 4: green; Chapter 5: blue) and starts with an individual introduction, where I introduce more specific research questions. Following the main analyses, each of the three chapters closes with a conclusion in which I address the specific research questions.

In Chapter 3, I focus on analyzing IW at eastern AR7W. I compare existing analyses of seasonal and multi-year variability utilized within different in-situ measurements with the multi-source observation-based data set ARMOR3D that allows for analyzing both seasonal and multi-year variability. From 1993 to 2022, I compare the data set against in-situ measurements to test its performance in the region southwest of Greenland at eastern AR7W. I analyze seasonal and multi-year variability and discuss the physical mechanisms driving the variability.

In Chapter 4, I extend the previous analysis to three other regions within the BCS: the Irminger Sea, Baffin Bay, and the western Labrador Sea. By developing new methods to identify IW, I consider large-scale changes in the water column in the analysis of IW. Additionally, the second developed method allows for analyzing variability of IW remnants in regions where IW itself is mixed to such a degree that it is not identifiable with the commonly used method. These newly developed methods contribute to the understanding of local IW variability along its pathway in the BCS.

In Chapter 5, I include an ocean reanalysis and different simulations of an ocean model with varying horizontal resolutions in the analysis of IW variability. Comparing the pre-

vious analyses with the reanalysis and model simulations contributes to understanding IW variability. It highlights possible aspects requiring consideration in future model simulations. Additionally, I extend the analysis of spatial IW variability to encompass the entire BCS, spanning from the Irminger Sea into Baffin Bay and the western Labrador Sea. In this extension, I analyze 25 cross-slope sections and two sections that follow the 1,500 m isobath from the Irminger Sea along the two pathways of IW in the BCS - into Baffin Bay and the western Labrador Sea. This analysis enables the continuous tracking of IW along its pathway in the BCS. It provides detailed insights into its spatial changes as it becomes progressively mixed with colder and fresher ambient waters.

Chapter 6 of this thesis comprises an overarching summary and conclusion. In Chapter 7, I close the thesis by providing an outlook on possible future research that builds upon the primary conclusions. An Appendix includes supplementary figures I chose to relocate from the main body.

"Data is a tool that helps you tell a story.
It's not the story itself."

Kim Goodwin - Author and user experience (UX) designer

Chapter 2

Data

In this chapter, I introduce the data used in this thesis. I start with the multi-source observation-based ARMOR3D data set (Chapter 2.1), which serves as the main data set in Chapter 3 and Chapter 4. Following that, the Global Ocean Physics Reanalysis (GLORYS, Chapter 2.2) and different regional configurations of the Nucleus for European Modelling of the Ocean (NEMO) model (Chapter 2.3) are introduced. Reanalysis and model results are analyzed in Chapter 5. Subsequently, the different horizontal and vertical resolutions of the previously introduced data sets are discussed (Chapter 2.4). Finally, I present data used to validate and compare the main data sets against and that serve as important pillars to underline and draw the main conclusions from the gridded data sets (Chapter 2.5). Additionally, I give an overview of all used data at the end of this thesis in the 'Funding and Data Acknowledgements'. In this overview, I present links to guide the reader to additional information on the individual data, including websites, user manuals, and download sites.

2.1 Observation-based data - ARMOR3D

ARMOR3D (Guinehut et al., 2012; Mulet et al., 2012), produced by the Copernicus Marine Environmental Monitoring Service, provides the hydrographic and geostrophic velocity data that form the core data set of this thesis. ARMOR3D has a horizontal resolution of 1/4° and covers 50 depth levels with increasing distance from the surface to a depth of 5,500 m. Its temporal resolution used in this thesis covers weekly data between 1993 and 2022. Years until 2021 comprise reprocessed delayed-time data, while 2022 is near-real-time data. Differences between the reprocessed and near-real-time data were not statistically significant for testing data from 2018 in the near-real-time configuration (Greiner et al., 2020). I tested ARMOR3D for differences between the reprocessed and near-real-time data in 2021 at eastern AR7W. Notable differences are limited to the upper 200 m where the reprocessed data is colder and more saline than the near-real-time data by approximately 0.1 °C and 0.1, respectively. Below 200 m, these differences fall below 0.01 °C and 0.01, respectively. Hence, impacts on IW using the near-real-time data instead of the reprocessed data in 2022 are expected to be negligible. Therefore, I implement the full-year period in the analysis and do not assume a significant break in the time series between 2021 and 2022. Unlike data sets like EN4 that build entirely on available oceanic in-situ information regarding temperature and salinity (Good et al., 2013), ARMOR3D takes advantage of satellite data. These data

have been temporally well-resolved since their introduction in the early 1990s and are combined with in-situ observations from the deeper ocean. The parameters provided by ARMOR3D used in this thesis are ocean temperature, converted to potential temperature θ, salinity, zonal and meridional geostrophic velocities, and the geopotential height at the ocean surface.

To my knowledge, ARMOR3D has not been used so far for a detailed water mass analysis in the region of interest. I summarize the three main steps that have resulted in constructing the ARMOR3D temperature, salinity, and velocity fields. For detailed information on the methods, I further refer to Greiner et al. (2020) and Guinehut (2020).

1) The product considers satellite data comprising sea level anomalies from CNES-CLS18 (Mulet et al., 2021), sea surface temperature from the 'Operational Sea Surface Temperature and Sea Ice Analysis' (OSTIA, Stark et al., 2007), and sea surface salinity from the Copernicus Marine Environmental Monitoring Service. Sea surface salinity builds on 'Soil Moisture and Ocean Salinity' (SMOS) data and in-situ measurements (Droghei et al., 2018). Hence, the surface geostrophy matches the altimetry-based anomalies. These satellite data are projected into the vertical via a multiple linear regression approach (Mulet et al., 2012). The approach derives temperature and salinity by combining sea level anomalies with sea surface temperature and sea surface salinity anomalies together with monthly temperature and salinity fields, respectively (Guinehut et al., 2012; Greiner et al., 2020). Each given parameter, such as sea level anomaly, sea surface temperature, and sea surface salinity, is provided with a regression coefficient expressed as covariances that vary in all four dimensions. The covariances are calculated using all available observations in a given radius of influence (Guinehut et al., 2012). Guinehut et al. (2012) provide a detailed expression on calculating the respective regression coefficients. These steps result in synthetic 3D fields of temperature and salinity profiles for the upper 1,500 m range of the water column. To obtain hydrographic anomalies, the World Ocean Atlas 2018 monthly climatology (Boyer et al., 2018) from 2005 to 2017 is subtracted from the synthetic fields.

2) An optimum interpolation method (Bretherton et al., 1976) is considered to combine available in-situ profiles for temperature and salinity from various sources (ship-based conductivity-temperature-depth (CTD), Argo floats, expendable bathythermograph, mammal-borne sensors, and moorings) with the synthetic fields. With these in-situ

temperature and salinity profiles, the large-scale part of the synthetic fields obtained from step 1) is corrected. The applied optimum interpolation method incorporates a statistical description of the data's errors. As a result, ARMOR3D benefits from both data sets. This second processing step leads to the construction of the ARMOR3D combined fields for the upper 1,500 m of the water column and incorporates anomalies from the synthetic fields into the data set.

3) The 3D fields are extended to the water column below 1,500 m by incorporating the seasonal World Ocean Atlas 2018 climatology. Furthermore, the thermal wind equation with a reference level at the sea surface is exploited to combine satellite altimetry-derived geostrophic surface currents with the ARMOR3D temperature and salinity fields. Additionally, the 3D fields of the geostrophic currents and geopotential heights are inferred (Mulet et al., 2012).

Greiner et al. (2020) analyzed differences between ARMOR3D and independent in-situ measurements (ARMOR3D minus observations) for the global ARMOR3D fields. Root mean square differences for temperature were about 0.8 °C at 100 m, and 0.2 °C at 1,000 m depth (Greiner et al., 2020). For salinity, the root mean square difference was 0.1 at 100 m and 0.05 at 1,000 m depth. Greiner et al. (2020) stated that ARMOR3D is slightly too barotropic, as expected, due to the data set being constrained to altimetry. The resulting bias in the geostrophic currents was in the order of $\mathcal{O}(0.01\,\mathrm{cm\,s^{-1}})$ (Greiner et al., 2020), root mean square differences are $6.4\,\mathrm{cm\,s^{-1}}$ and $5.2\,\mathrm{cm\,s^{-1}}$ for the zonal and meridional components, respectively. These differences can be enhanced in the regions of western boundary currents (Greiner et al., 2020). When calculating volume transports, these differences in the geostrophic currents might introduce a bias toward higher volume transports.

In this thesis, I focus on depths between 200 to 1,000 m where the vertical resolution of ARMOR3D ranges from 25 m to 100 m intervals, respectively. As the water masses of interest in this thesis are all found within the upper part of the water column, I only include the upper 1,500 m range in the analysis. ARMOR3D represents only the climatological state at depths beyond 1,500 m and thus lacks variability in the deeper water column. While ARMOR3D is available with a horizontal resolution of 1/4°, I am aware that the resulting data are subject to a certain degree of interpolation based on the available sources data. These data are, in turn, limited in space and time. Additionally, the seasonal cycle, upper ocean processes, and clouds strongly affect

input data like sea surface temperature. ARMOR3D has a resolution sufficient for resolving the local barotropic Rossby radius of deformation (estimated $R \approx 500\,km$ at the shelf break at 250 m depth). It thus can represent the horizontal structures in the boundary current discussed in this thesis. However, ARMOR3D does not resolve the baroclinic Rossby radius of deformation in the Labrador Sea ($R < 10\,km$, e.g., Chelton et al., 1998) and thus cannot represent small-scale features like eddies.

2.2 Ocean reanalysis data - GLORYS

In an ocean reanalysis, observations and outputs from a numerical ocean general circulation model are combined by data assimilation. The result is a synthesized estimate of the ocean state and its temporal changes. In this thesis, I compare ARMOR3D with an ocean reanalysis. The goal is to identify differences and similarities between an observation-based data set and a reanalysis that includes observations but is assimilated with an ocean model. For this purpose, this thesis analyzes the Global Ocean Physics Reanalysis (GLORYS) in its configuration GLORYS12V1 (Drévillon et al., 2022a, 2022b), referred to as GLORYS. It is available between 1993 and 2020 with monthly and daily temporal resolutions. This thesis considers the latter. GLORYS has a horizontal resolution of 1/12° and covers 50 depth levels with increasing cell distance from the surface to a depth of ∼5,700 m. The output of GLORYS is regularly situated on a 3D Arakawa C-grid (Mesinger & Arakawa, 1976). In a C-grid configuration, the individual variables are 'centered' in each grid cell, either directly in the middle, at the upper/lower faces, or the left/right faces of the grid cell. In GLORYS, the scalar variables of the T-grid cells, like temperature and salinity, are centered in the 3D model cell. The zonal (u) and meridional (v) velocity vectors are located at the centers of the left/right faces of the model cell. In contrast, the vertical (w) velocity vector is located at the center of the upper/lower faces. However, the version of GLORYS used in this thesis has been interpolated to a regular horizontal and vertical grid (Drévillon et al., 2022a), expressed by similar longitude, latitude, and depth distances.

The numerical ocean general circulation model NEMO (see Chapter 2.3) forms the foundation for GLORYS. NEMO is driven at the surface by the European Centre for Medium-Range Weather Forecasts Re-Analysis Interim data between 1993 and 2018, followed by the European Centre for Medium-Range Weather Forecasts Re-Analysis 5 reanalysis for subsequent years (Drévillon et al., 2022b). A reduced-order Kalman filter

is used to jointly assimilate observations of vertical in-situ temperature and salinity profiles, sea level anomaly, sea surface temperature, and sea ice concentration (Drévillon et al., 2022b). For further detailed information, I refer to Drévillon et al. (2022b).

2.3 Model data - ANHA NEMO Simulations

In addition to comparing the observation-based data set ARMOR3D and the ocean reanalysis GLORYS, I compare the data with output from different regional configurations of the Nucleus for European Modelling of the Ocean (NEMO). In total, this thesis covers three major data sets that contain only observations (ARMOR3D), observations and model physics (GLORYS), and a pure physical model (NEMO) model. Another goal of this thesis is to find differences within individual model simulations regarding horizontal resolution. Therefore, three different configurations of NEMO are analyzed using the Arctic Northern Hemisphere Atlantic (ANHA) simulations, covering a horizontal resolution of 1/4° (ANHA4), 1/12° (ANHA12), and 1/60° (restricted to the Labrador - LAB - Sea with an outer nest in the subpolar gyre - SPG, ANHA4-SPG12-LAB60, referred to as LAB60). For ANHA4 and ANHA12, the numerical framework 3.4 is used. For LAB60, it is the numerical framework 3.6 (Madec et al., 1998, 2023). The initial conditions for the model simulations are 3D temperature, salinity, horizontal velocities, and 2D sea surface height (SSH), and sea ice fields provided by GLORYS (see Chapter 2.2). Similarly, the boundary conditions for the 3D ocean fields are also from GLORYS. Hence, the depth levels are also on a grid similar to GLORYS: 50 levels with increasing distance from the surface to a depth of $\sim$5,700 m for ANHA4 and ANHA12. LAB60 comprises in total 75 depth levels between the surface and $\sim$5,900 m.

NEMO comprises multiple ocean-related components that can be individually coupled for different model runs. These NEMO components used to model the fields analyzed in this thesis include ocean dynamics and thermodynamics from the Ocean Engine (OCE, Madec et al., 2023) and sea ice dynamics and thermodynamics using the Louvain-La-Neuve sea ice model (LIM, Fichefet & Maqueda, 1997; Bouillon et al., 2009). Furthermore, it includes on- and offline oceanic tracers transport using the Tracers in the Ocean Paradigm (TOP Aumont et al., 2019), and biogeochemical processes using Biogeochemistry with Light Iron and Nutrient limitation and Gases (BLING, Galbraith et al., 2009; Castro de la Guardia et al., 2019). In this thesis, I focus on examining the ocean component only. The relevant output discussed is similar

to the previously described data sets: temperature, salinity, and ocean current velocities. These individual output variables are distributed on a 3D Arakawa C-grid (see Chapter 2.2, Mesinger & Arakawa, 1976).

To simplify the model, the following approximations are implemented (Madec et al., 2023):

Spherical Earth approximation	Geopotential surfaces are considered spheres. Gravity is vertical and independent of latitude.
Thin-shell approximation	The ocean depth is significantly smaller than Earth's radius. Additional effects of ocean depth on gravity are neglected.
Turbulent closure hypothesis	Turbulent fluxes are parameterized in large-scale features.
Boussinesq hypothesis	$\rho = \rho(T, S, p)$, only density variations contributing to buoyancy are considered.
Hydrostatic hypothesis	$\frac{\partial p}{\partial z} = -\rho g$, vertical momentum is expressed with the balance between vertical pressure gradient and gravitational force.
Incompressibility hypothesis	$\nabla \cdot U = 0$, water is assumed to be incompressible.
Neglect additional Coriolis terms	The part of Coriolis terms that include $cos(\phi)$ is neglected.

Including these approximations with the Navier-Stokes equations (Equation 1, following, e.g., Olbers et al., 2012) and a nonlinear equation of state to couple temperature and salinity as active tracers, the ocean state in NEMO is described with seven primitive equations (Pennelly, 2021; Madec et al., 2023). These are the horizontal momentum equations (Equation 2), the equations for the conservation of heat (Equation 3) and salt (Equation 4), the hydrostatic equilibrium (Equation 5), the incompressibility equation (Equation 6), and the equation of state (Equation 7).

$$\underbrace{\rho\frac{D\boldsymbol{u}}{Dt}}_{\text{momentum}} = \underbrace{-\nabla p}_{\substack{\text{pressure}\\ \text{gradient}}} + \underbrace{\nu\nabla^2\boldsymbol{u}}_{\text{diffusion}} + \underbrace{\frac{\nu}{3}\nabla(\nabla\cdot\boldsymbol{u})}_{\substack{\text{viscous}\\ \text{stress term}}} + \underbrace{\boldsymbol{f}^v}_{\substack{\text{volume}\\ \text{force}}} \tag{1}$$

$$\frac{\partial U_h}{\partial t} = -[(\nabla\times U)\times U + \frac{1}{2}\nabla(U^2)]_h - fk\times U_h - \frac{1}{\rho_0}\nabla_h p + D^U + F^U \tag{2}$$

$$\frac{\partial T}{\partial t} = -\nabla\cdot(TU) + D^T + F^T \tag{3}$$

$$\frac{\partial S}{\partial t} = -\nabla\cdot(SU) + D^S + F^S \tag{4}$$

$$\frac{\partial p}{\partial z} = -\rho g \tag{5}$$

$$\nabla\cdot U = 0 \tag{6}$$

$$\rho = \rho(S,T,p) \tag{7}$$

The individual terms include the 3D velocity vector U, h indicating the horizontal components, the Coriolis parameter f, k indicating the vertical component, the in-situ density ρ, the pressure p, the potential temperature T, the salinity S, the acceleration of gravity g, D describes the small-scale parameterization, and F the forcing terms at the surface.

The three model simulations analyzed in this thesis are based all on the ANHA configuration but with different horizontal resolutions. All configurations are calculated on a tripolar mesh. This tripolar mesh allows for the shifting of the North Poles onto land to avoid a singularity in the ocean. Additionally, it further increases the horizontal resolution in the region of interest. Thus, the North Poles are located near the Canadian archipelago and Siberia, while the South Pole remains in Antarctica.

ANHA4 The 1/4° horizontal resolution of the Atlantic Ocean represents a subdomain of the global ORCA025 mesh (Bernard et al., 2006). The temporal resolution of the ANHA4 output used in this thesis is five days. The analyzed model simulation was set up by Tahya Weiss-Gibbons, University of Alberta, following Weiss-Gibbons (2022).

ANHA12 The 1/12° horizontal resolution of the Atlantic Ocean represents a subdomain of the global ORCA12 mesh. The temporal resolution of the ANHA12 output used in this thesis is five days. The analyzed model simulation was set up by Xianmin Hu, University of Alberta, following X. Hu et al. (2018).

LAB60 The 1/60° horizontal resolution of the Labrador Sea represents a subdomain of the ANHA4 simulation. It contains a 1/12° nesting in the subpolar gyre and a second nest with a 1/60° resolution in the Labrador Sea. The temporal resolution of the LAB60 output used in this thesis is one day. The analyzed model simulation was set up by Clark Pennelly, University of Alberta, following Pennelly and Myers (2020).

2.4 Differences between the individual data sets

The introduced data sets used in this thesis differ in their individual horizontal (Figure 2.1) and vertical resolutions (Figure 2.2). ARMOR3D and GLORYS are projected onto a regular horizontal grid, a Cartesian grid with constant latitude and longitude ranges between the individual grid points. In contrast, the output variables of the three ANHA simulations used in this thesis are distributed on a 3D Arakawa C-grid (see Chapter 2.3). Among the different ANHA simulations, the horizontal resolution varies from the coarsest resolution in ANHA4 and the finest resolution in LAB60. However, the notations 1/4°, 1/12°, and 1/60° for the respective horizontal resolutions of ANHA4, ANHA12, and LAB60 refer to the tripolar NEMO grid. Thus, the net distances between two grid points in the SPNA strongly depend on the exact location. In the region of interest, the horizontal resolution is approximately 20 km for ARMOR3D, 7 km for GLORYS, 15 km for ANHA4, and 5 km for ANHA12 (Figure 2.1). As this thesis uses the LAB60 simulation only to analyze local processes at eastern AR7W, an analysis of the horizontal resolution was omitted.

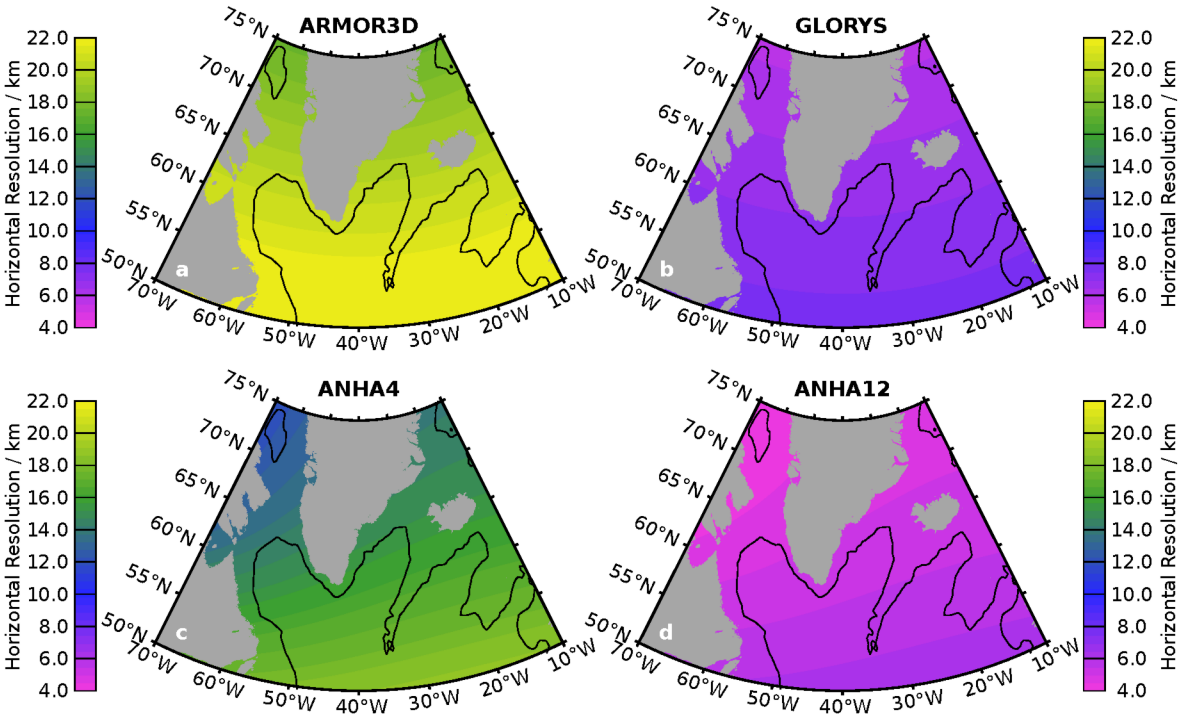

Figure 2.1: Different horizontal resolutions of the individual gridded data sets used in this thesis. Data sets are ARMOR3D (a), GLORYS (b), ANHA4 (c), ANHA12 (d). Horizontal grids of ARMOR3D and GLORYS are equidistant for different longitudes, while grid size varies within longitudes for ANHA4 and ANHA12. The black line in all subfigures represents smoothed 2,000 m isobath from the ETOPO1 1 Arc-Minute Global Relief Model (NOAA, 2009; Amante & Eakins, 2009).

The data sets used in this thesis also differ regarding their vertical resolutions. GLORYS and all ANHA simulations are arranged on the same vertical grid. However, ARMOR3D has different vertical spacing between depth levels. In ARMOR3D, the cell distances are constant within certain depth ranges (Figure 2.2 a). Within the depth range where IW is typically identified, the cell distance varies from 25 m at 200 m depth to 100 m at 1,000 m depth covering 15 depth levels. In GLORYS and the ANHA simulations, the distance between the individual grid points, the cell distance, continuously increases with depth (Figure 2.2 b). As the individual cells do not cover the same depths as ARMOR3D, directly comparing the individual depth levels is impossible. Within the typical IW depths, the cell distances for ANHA4 and ANHA12 vary from 36 m at $\sim$200 m depth to $\sim$160 m at 1,000 m depth covering in total 9 levels (LAB60 comprises 16 depth levels in the typical IW depths). Therefore, within the typical IW depth range between 200 and 1,000 m, ARMOR3D delivers a higher vertical resolution than GLORYS and the ANHA simulations. When analyzing sections within this the-

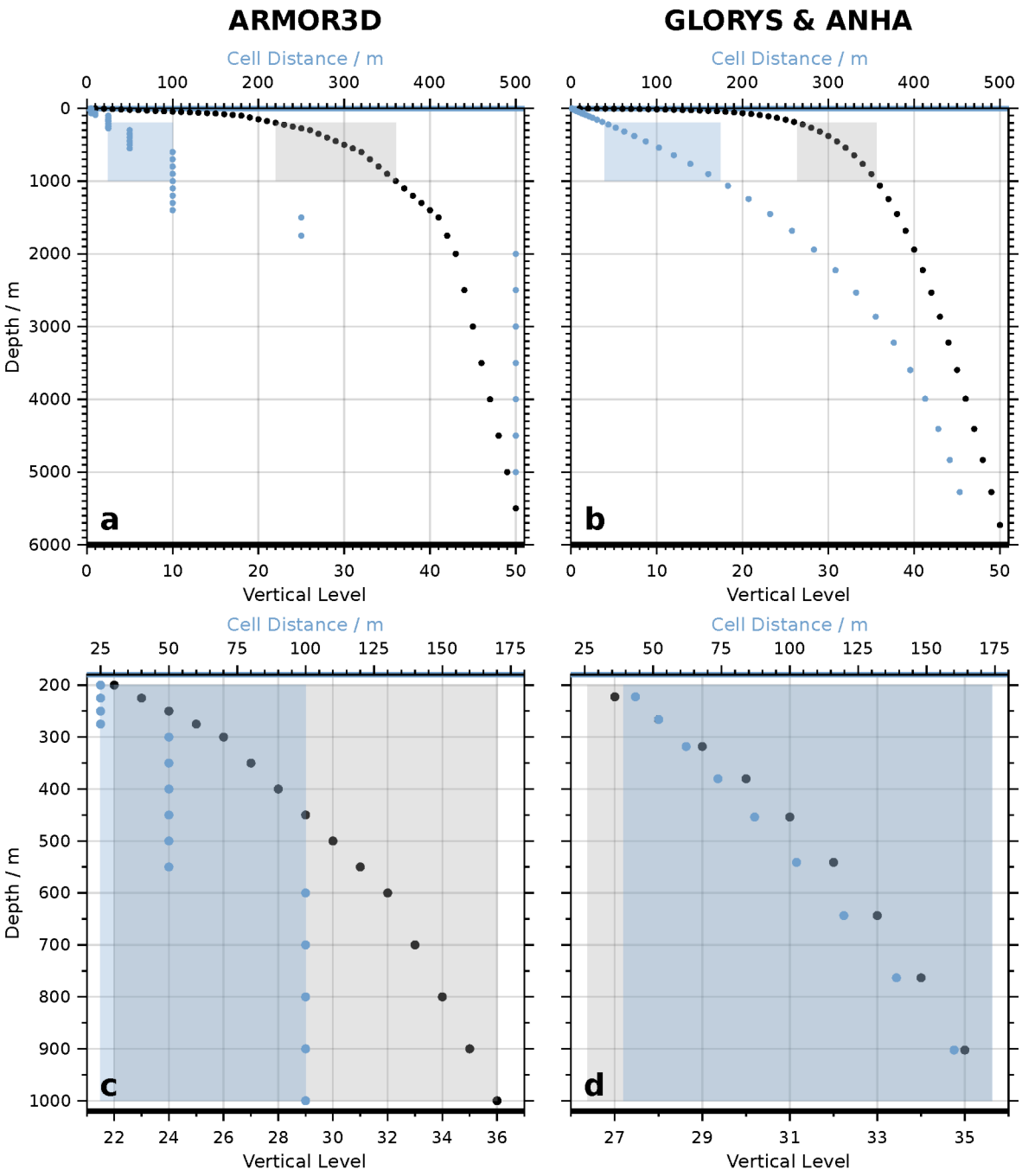

Figure 2.2: Vertical resolutions of the individual gridded data sets for ARMOR3D (a) and GLORYS, ANHA4, and ANHA12, which are each built on the same vertical grid (b). Vertical level (black) on the lower x-axis, cell distance (blue) on the upper x-axis. Blue and gray shades highlight the number of the vertical level and the cell distance within the typical depth range of Irminger Water in the Irminger Sea. (c) and (d) present a zoom into the Irminger Water layer depths for ARMOR3D and the other data sets, respectively.

sis, I treated each data set equally by interpolating all sections to the same grid with a spatial resolution of $\Delta x = 1\,km$, and $\Delta z = 10\,m$. This approach adds influence from interpolation but ensures the best comparability within each other.

2.5 Secondary data sets for comparison

2.5.1 Ship-based hydrographic data

Comparing ARMOR3D with different observational in-situ data sets is an important step to validate and interpret the water mass variability in ARMOR3D. I use CTD data from 29 research cruises conducted along eastern AR7W between 1993 and 2018. The entire AR7W section crosses the central Labrador Sea from the Canadian to its Greenland side (e.g., Lazier et al., 2002; Yashayaev, 2007a; Kieke & Yashayaev, 2015; Yashayaev et al., 2015b). AR7W originated from the World Ocean Circulation Experiment (WOCE) of the early to late 1990s. It was initially sampled by Canadian teams from the Bedford Institute of Oceanography of the Department of Fisheries and Oceans (e.g., Lazier et al., 2002). After WOCE was finished, AR7W was surveyed within the programs 'Climate and Ocean - Variability, Predictability, and Change' (CLIVAR), the Canadian 'Atlantic Zone Off-Shelf Monitoring Program' (AZOMP), as well as within parts of individual national programs. Hence, the entire line from the Labrador to the Greenland shelf was regularly surveyed in the framework of various national and international programs for more than three decades since 1990 (e.g., Lazier et al., 2002; Yashayaev, 2007a; Kieke & Yashayaev, 2015; Yashayaev et al., 2015b).

I limit eastern AR7W (Figure 1.4 b) at 60°42'N/48°04'W ($\sim 10\,m$ water depth), which serves as a reference location on the Greenland shelf. From there, the section extends 300 km southwestwards into the Labrador Sea to 58°17'N/50°30'W ($\sim 3{,}570\,m$ water depth). Rykova et al. (2015) analyzed IW at eastern AR7W between 1993 and 2006. To increase the robustness of the results, I added additional cruises in this period not available to Rykova et al. (2015) and extended this data set until 2018. A list of all research cruises considered in this thesis and their respective details are given in Table 2.1. The timing of the individual cruises is highlighted in Figure 2.3 and will be discussed in detail in Chapter 3. The vertical resolution of the available CTD profiles varies between 1 and 2 dbar. However, the number of available profiles providing the horizontal resolution of the section changes for each cruise. To exclude the influence of

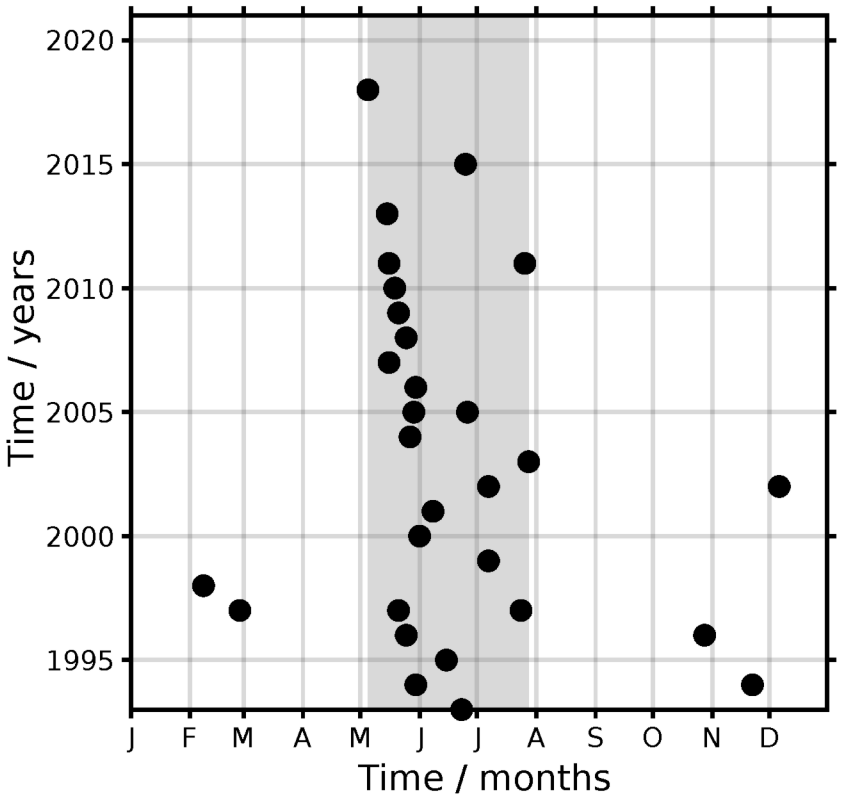

Figure 2.3: Temporal distribution of ship-based data (circles) at eastern AR7W used in this thesis. Gray shaded area represents the late spring and summer period where most ship-based data analyzed in this thesis have been taken.

small-scale features, I have smoothed the ship-based data by averaging CTD profiles within a distance of $\Delta x < 5\,km$. This smoothing allows for a better comparison of the ship-based data to ARMOR3D.

CTD-derived in-situ temperature (International Temperature Scale of 1990 - ITS-90) and practical salinity (Practical Salinity Scale 1978 - PSS-78, addressed as salinity, Fofonoff & Millard, 1983) are used. I calculate potential temperature and potential density anomalies σ_θ from these parameters relative to the surface pressure, referred to as temperature and density in the following. The precision and quality of the CTD system for all cruises follow WOCE standards (Gordon et al., 1994). I calculate geostrophic velocities from temperature and salinity and compare them to geostrophic surface velocities from ARMOR3D (see Chapter 2.1, Greiner et al., 2020), referred to as velocities. I focus on the cross-section component of the velocity at eastern AR7W and define the velocity as positive in the downstream direction of the WGC. Positive cross-section velocities point downstream in the BCS, for example, to the northwest at eastern AR7W.

Table 2.1: List of research cruises included in this thesis. The columns 'Start' and 'End' provide information on the first and last date of the respective eastern AR7W survey. '#' is the number of CTD profiles within 160 km from the chosen reference point closest to the Greenland coast. 'A3D' shows whether the relevant profiles of the specific cruise are included within ARMOR3D.

Year	**Start**	**End**	**Cruise ID.**	**#**	**A3D**	**Data reference**
1993	Jun 23	Jun 23	18HU93019_1	5	Yes	Lazier (1993)
1994	May 30	May 31	18HU94008_1	8	Yes	Lazier (1994)
1994	Nov 21	Nov 24	M30/3	6	Yes	WOCE (2002)
1995	Jun 15	Jun 16	18HU95011_1	7	Yes	Lazier (1995)
1996	May 23	May 25	18HU96006_1	8	Yes	Lazier (1996)
1996	Oct 27	Oct 28	18HU96026_1	8	-	Clarke (1996)
1997	May 21	May 22	18HU97009_1	7	Yes	Clarke (1997)
1997	Feb 26	Feb 28	KN147	18	-	Pickart (1997)
1997	Jul 24	Jul 24	M39/4	4	Yes	Schott (1997)
1998	Feb 8	Feb 8	KN156	6	Yes	d'Asaro (1998)
1999	Jul 7	Jul 8	18HU19990627	8	-	Clarke (1999)
2000	May 31	Jun 1	18HU2000009_1	5	-	Harrison (2000)
2001	Jun 8	Jun 9	18HU2001022_1	10	Yes	Clarke (2001)
2002	Jul 7	Jul 8	18HU20021129	10	Yes	Head (2002)
2002	Dec 6	Dec 7	18HU20020623	4	Yes	Clarke (2002)
2003	Jul 28	Jul 29	18HU200307_1	10	Yes	Clarke (2003)
2004	May 25	May 27	18HU20040515	8	Yes	Harrison (2004)
2005	May 29	May 30	18HU20050526	10	Yes	Harrison (2005)
2005	Jun 26	Jun 27	SUBPOLAR	6	Yes	Rhein et al. (2015)
2006	May 30	May 30	18HU20060524	5	Yes	Hendry (2006)
2007	May 16	May 17	18HU20070510	6	Yes	Hendry (2007)
2008	May 23	May 25	18HU20080520	6	Yes	Harrison (2008)
2009	May 20	May 22	18HU20090517	10	Yes	Hendry (2009)
2010	May 18	May 20	18HU20100513	10	Yes	Harrison (2010)
2011	May 16	May 17	18HU20110506	11	Yes	Yashayaev (2011)
2011	Jul 26	Jul 27	M85/1	3	Yes	Stendardo et al. (2015)
2013	May 15	May 15	MSM28	4	Yes	Schneider et al. (2015)
2015	Jun 25	Jun 25	MSM43	7	-	Steinfeldt et al. (2019a)
2018	May 5	May 5	MSM73	13	-	Steinfeldt et al. (2019b)

Within the individual cruises, the position of the most inshore CTD profile varied. I extrapolated each section from its profile closest to the coast toward the previously defined reference location. Data gaps between the two profiles may arise at the bottom due to the steep topography at the continental slope. These gaps were filled using a 2D extrapolation method considering the respective parameter's vertical and horizontal gradients. I ensured that values did not exceed the measured minimum and maximum values, preventing over-extrapolation of the data. To ensure consistency, I interpolated all sections to the same grid with a spatial resolution of $\Delta x = 1\,km$, and $\Delta z = 10\,m$. Consequently, I obtained a uniform grid for each realization of the eastern AR7W ship sections, derived from a varying number of CTD profiles for each survey.

Similar to studies by Rykova et al. (2015) and Myers et al. (2007, 2009), which investigated either eastern AR7W or conducted surveys at nearby locations, I utilize data from ship surveys primarily carried out in late spring and summer. In total, 83 % of the eastern AR7W surveys were conducted from May to July (Figure 2.3). Therefore, long-term IW variability obtained from these data represents early summer conditions. In contrast, the data do not provide sufficient coverage for a comprehensive seasonal variability analysis.

I compare ARMOR3D to the pure ship-based data that are either included or not included in ARMOR3D. Hence, the data sets are only partially independent of each other. Information on which ship-based data is included in ARMOR3D is provided in Table 2.1.

2.5.2 The DOORS data set

Furthermore, I compare ARMOR3D with the Deep-Ocean Observation and Research Synthesis (DOORS) data set (Yashayaev et al., 2022), referred to as DOORS. Temperature and salinity observations in the Labrador Sea have been collected as part of international efforts initiated by WOCE. Since 2000, observations also include data from the Argo program, which provides year-round measurements of seawater properties transmitted by profiling floats (Argo, 2000). For the present thesis, all available profiles from vessel surveys and Argo floats operating in the Labrador Sea from 1993 to 2021 have been quality controlled through semi-automated and visual inspections, calibrated, and validated. In the case of Argo floats, ship-platform and inter-platform optimizing calibration procedures were developed and used. The individual steps of

subsequent vertical interpolation and data processing are discussed by Yashayaev et al. (2022). The described work on the DOORS data was all performed by I. Yashayaev (Bedford Institute of Oceanography), who also provided me with the data.

The collection and analysis of oceanographic observations (ship and profiling float data from pre-Argo and Argo eras) in the Labrador Sea were conducted as part of DOORS (Yashayaev et al., 2022). I use DOORS, focusing on eastern AR7W, to compare with the core data set ARMOR3D from Chapter 2.1. Individual profiles within DOORS were selected in the boundary region of the Labrador Sea along Greenland's continental slope, centered at eastern AR7W (Figure 1.4), and confined to the upper 1,500 m. Following, these profiles were projected onto eastern AR7W following isobaths and have calculated IW hydrography for seasonal and long-term variability. Like the pure ship-based data (Chapter 2.5.1), the DOORS data is also partially included in ARMOR3D. Eventually, ARMOR3D, the ship-based data, and DOORS have been interpolated onto the same grid to reconstruct eastern AR7W with a constant spatial resolution. I filled bottom triangles at the seafloor near steep topography through vertical and horizontal extrapolation. Similar to the ship-based data, any over-extrapolation for ARMOR3D and DOORS was avoided.

2.5.3 The OSNAP mooring observations

I also consider observations and results from the OSNAP mooring array (Lozier et al., 2017), focusing exclusively on the locations upstream of eastern AR7W (refer to Figure 1.4). The OSNAP West moorings have sensors recording point measurements for ocean velocity and hydrographic parameters (Pacini et al., 2020). The instruments were installed at vertical intervals of 250 to 500 m. I compare time series of IW hydrography and volume transport from the period 2014 to 2018 as analyzed in Pacini et al. (2020) against those inferred from ARMOR3D. A. Pacini (University of Washington) and R. S. Pickart (Woods Hole Oceanographic Institution) provided me with the IW time series. Presently, ARMOR3D does not include these data. Furthermore, I reference the analysis of seasonal variability in uISIW by Le Bras et al. (2020), which was derived from the OSNAP East mooring array located at the southeastern Greenland shelf break (refer to Figure 1.4), as well as moorings from the Ocean Observatories Initiative in the central Irminger Sea, both for years between 2014 and 2016.

"An investment in knowledge pays the best interest."

Benjamin Franklin - American writer, scientist, statesman;
the first to map the Gulf Stream together
with his cousin Timothy Folger (Figure 3.1)

Chapter 3

Irminger Water - Variability and its causes

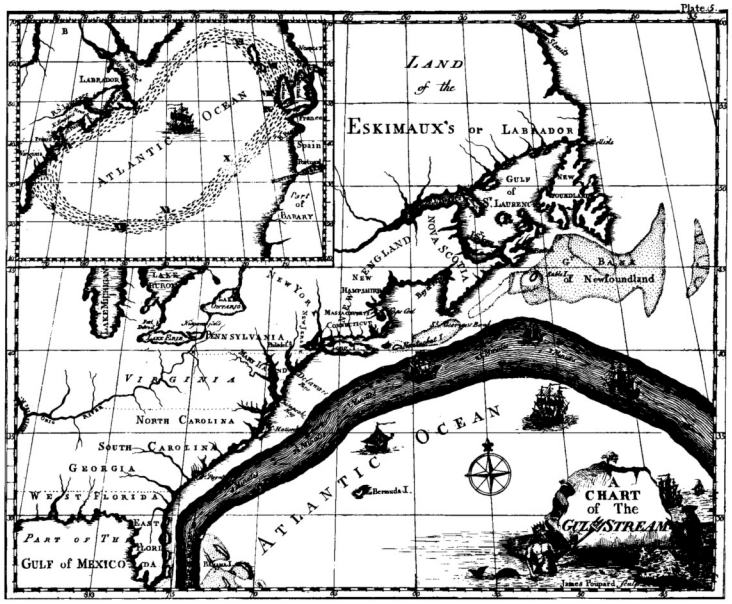

Figure 3.1: Franklin-Folger map of the Gulf Stream from 1786. Picture taken from Stewart (2008).

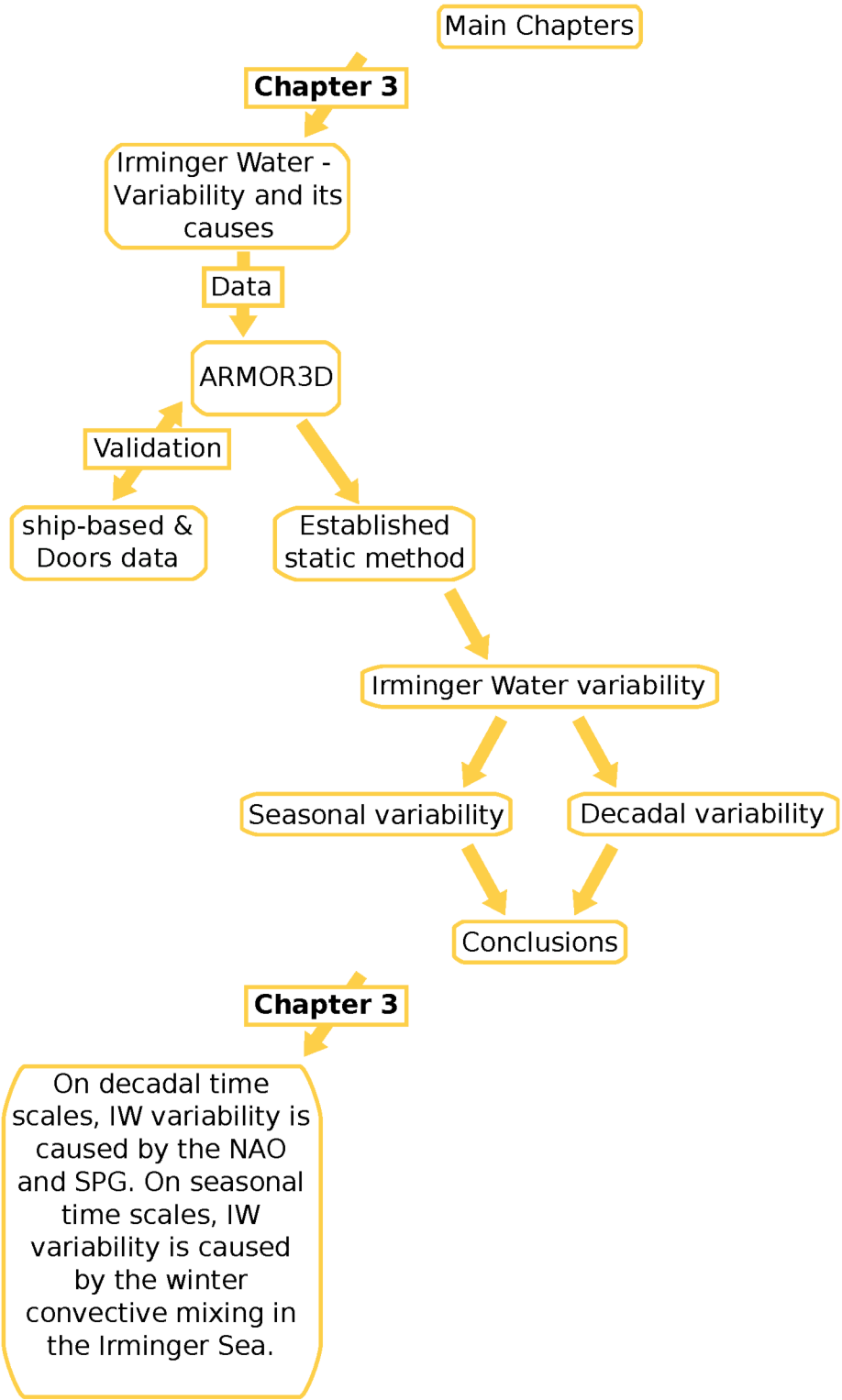

Figure 3.2: Graphical outline of Chapter 3. I add more details to the outline in Chapter 4 and Chapter 5. Eventually, it shows the connection within the main chapters.

This chapter is currently under review (as of August 24, 2023) for publication in the Journal of Geophysical Research: Oceans. The text has been partially adapted to fit the context of this thesis. I was responsible for the calculation, analyses, visualization and writing of the manuscript. Dagmar Kieke, Paul G. Myers, and Igor Yashayaev are co-authors and provided scientific input and helped to revise the text for publication.

3.1 Setting the scene - ARMOR3D at eastern AR7W

In this chapter, I aim to address the challenge posed by the limited duration of existing mooring-derived IW time series and the absence of year-round coverage of ship sections. These limitations hinder the examination of IW variability and its underlying causes on different time scales. To overcome these limitations, I utilize the multi-source observation-based data set ARMOR3D (see Chapter 2.1, Guinehut et al., 2012; Mulet et al., 2012) spanning the years 1993 to 2022.

Previous studies showed that ARMOR3D delivers physically meaningful results in the North Atlantic. In particular, Iakovleva and Bashmachnikov (2021) utilized ARMOR3D to analyze the interannual variability of the upper ocean heat content in the SPNA, which is linked to the NAO. Their study revealed that ARMOR3D captures interannual variability in upper ocean heat content similar to the established oceanic reanalysis data sets Ocean Reanalysis System 5 (ORAS5) and Simple Ocean Data Assimilation 3 (SODA3). Additionally, Desbruyères et al. (2019) considered ARMOR3D along with other data sets (e.g., EN4) to analyze low-frequency AMOC variability. They successfully validated model-based AMOC reconstructions at 45°N. In another study, Wett et al. (2023) utilized ARMOR3D to extent an array of in-situ measurements along 47°N onto the shelf regions at the eastern and western boundaries to allow a basin-wide AMOC calculation in the North Atlantic.

I analyze water mass variability concerning IW on seasonal to decadal time scales and focus on the west Greenland shelf break region, particularly on eastern AR7W. In order to evaluate the representation of IW in ARMOR3D, I compare the results obtained from ARMOR3D with three additional in-situ observational data sets: 1) a collection of ship surveys; 2) the DOORS data set (Yashayaev et al., 2022), which combines data from ship surveys and other platforms, and 3) time series from the mooring arrays at the two OSNAP lines southwest and southeast of Greenland (Pacini et al., 2020;

Le Bras et al., 2020). This comparison of the mentioned data serves to investigate advantages and potential weaknesses when using ARMOR3D for water mass analyses in this region.

In particular, I address the following objectives:

1. **How do Irminger Water hydrographic properties and volume transports based on ARMOR3D compare with in-situ observations at eastern AR7W?**
2. **What is the seasonal and long-term variability of Irminger Water at eastern AR7W between 1993 and 2022?**
3. **What causes Irminger Water temporal variability on different time scales at eastern AR7W?**

Chapter 3 is structured as follows: In Chapter 3.2, I begin by discussing the hydrographic structure of the upper water column in the WGC at eastern AR7W, as previously introduced in Figure 1.5. In Chapter 3.3, I provide an overview of the results related to seasonal and longer-term variability of IW and uISIW at eastern AR7W and their likely causes. Following, I summarize the findings and conclusions in Chapter 3.4.

3.2 Hydrography at eastern AR7W

In the following, I investigate the hydrography and velocity structure of the WGC at eastern AR7W and focus on IW and uISIW. Both cover the upper 1,000 m of the water column and are expected to interact strongly regarding their depth ranges and spatial extension. I analyze IW and uISIW using static definitions that do not change over time by following the definitions given in Pacini et al. (2020) for IW and Le Bras et al. (2020) for uISIW, as shown in Table 3.1. Pacini et al. (2020) and Le Bras et al. (2020) analyzed IW and uISIW for the first time throughout the year using mooring observations. In addition to the given static water mass definitions from Pacini et al. (2020) and Le Bras et al. (2020), I associate IW and uISIW with positive geostrophic velocities in the boundary current: the flow direction is downstream (Table 3.1). I do not consider any isolated IW and uISIW patches detached from the main region if these occur further offshore than 100 km from the coast. Other studies have used different, but also static,

definitions (e.g., Kiilerich, 1943; Lee, 1968; Buch, 2000; Myers et al., 2007, 2009). When analyzing volume transports of the two water masses later in Chapter 3.3, these results are sensitive to the choice of the respective definitions. However, in this chapter, I focus on the performance of ARMOR3D regarding the general state and temporal variability of IW while providing new estimates that are compatible and methodically comparable with the published ones. Implementing time-dependent definitions, for example, based on the local hydrography, is analyzed in Chapter 4. However, the sensitivity of the results from these static definitions affects the interpretation of the amount of the respective water mass present at eastern AR7W. Thus, when the IW is anomalously fresh, its salinity may fall below the given threshold and is therefore not identified any longer as IW.

Within the years 1993 to 2022, the mean water mass structure in the WGC at eastern AR7W as seen in ARMOR3D appears as follows (Figure 3.3). IW's warm and saline core covers depths between 200 and 600 m. It is thicker and reaches greater depths directly at the continental slope. Further offshore, it thins and becomes shallower. On top of IW lies the cold and fresh Upper Polar Water transported in the East/West Greenland Coastal Current. Upper Polar Water is limited to the upper 200 m. It covers the entire Greenland shelf and extends until 60 km offshore (Pacini et al., 2020), but is not of further interest to this thesis. uISIW is found beneath IW until a depth of about 1,000 m with an offshore extent of 120 to 130 km (Figure 3.3). Deep ISIW is located even deeper but is not addressed further due to the mentioned limitations of ARMOR3D at depths exceeding 1,500 m. The geostrophic velocity at eastern AR7W indicates a strong WGC flowing in the northwestern direction on the shelf, at the shelf break, and along the continental slope (Figure 3.3 d). However, it weakens further offshore (Figure 3.3 d). At about 120 km offshore, the velocities point to the southeast,

Table 3.1: Water mass criteria for Irminger Water (IW) and upper Irminger Sea Intermediate Water (uISIW). Shown are the salinity and potential density criteria for Irminger Water, the two potential density criteria for upper Irminger Sea Intermediate Water, and the additional geostrophic cross-section velocity criterion for both.

	Salinity	**Min. Density / kg m^{-3}**	**Max. Density / kg m^{-3}**	**Downstream Velocity / m s^{-1}**
IW	> 34.92		< 27.74	> 0
uISIW	< 34.92	> 27.65	< 27.73	> 0

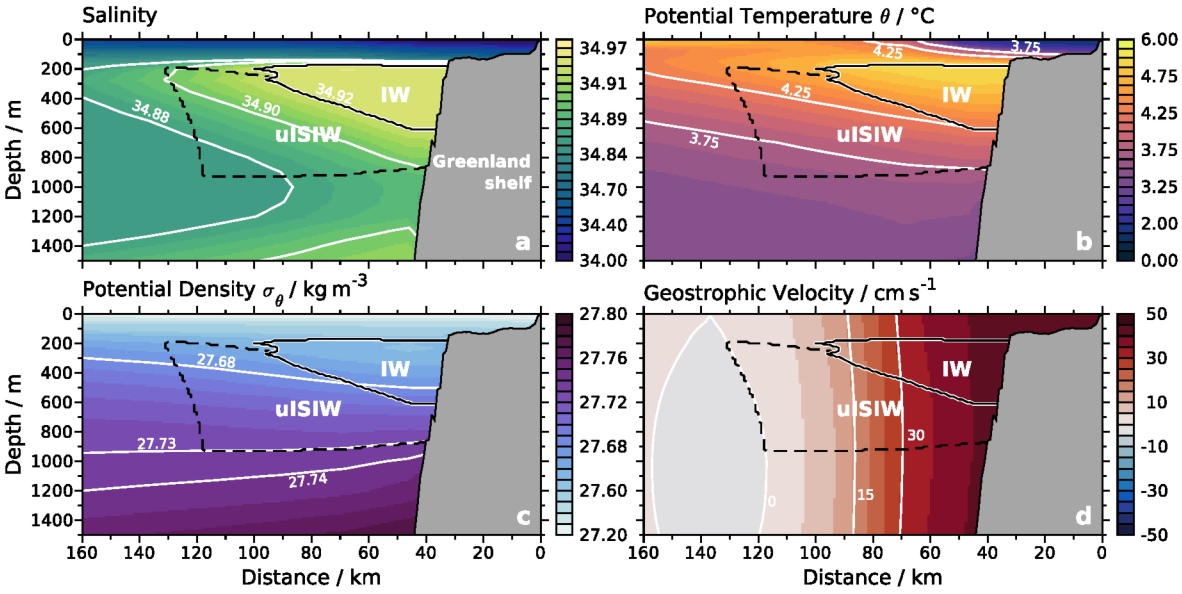

Figure 3.3: Eastern AR7W across the West Greenland Current in ARMOR3D, from the Greenland shelf (right side) into the Labrador Sea (left side) averaged from 1993 - 2022. Properties are salinity (a), potential temperature θ (b), potential density σ_θ (c), geostrophic velocity (d). Thick and solid white lines overlayed with thin and solid black lines encompass Irminger Water. Black, dashed lines encompass upper Irminger Sea Intermediate Water. White lines represent selected isolines.

indicating the presence of a counter-current that may be a part of the basin-wide recirculation (Lavender et al., 2000; Käse et al., 2001).

The frequencies of IW, the rate of identified IW at a given location within eastern AR7W in the ship-based data and ARMOR3D agree well (Figure 3.4). Please note that an IW frequency of 100 % indicates that IW is identified at this location at all available time steps. For better comparability, I binned both data sets horizontally using a bin length of 10 km and calculated a horizontal running average over three such bins. Both data sets suggest that IW mainly covers the area close to the continental slope and up to approximately 70 km offshore. As shown previously in Figure 3.3, the closer to the continental slope, the deeper the IW extends. Further offshore, the IW becomes shallower. The pure ship-based data (Figure 3.4 a) indicate generally lower IW frequencies and a less confined IW frequency distribution compared to ARMOR3D (Figure 3.4 c). In ARMOR3D, the maximum frequencies are located at the continental slope, similar to the maximum frequencies in the ship-based data, which show a preference for greater depths at the slope. I also calculated the IW frequencies within ARMOR3D only for times with available ship-based data (Figure 3.4 b). For these times, the ARMOR3D IW frequency pattern better matches the ship-based IW fre-

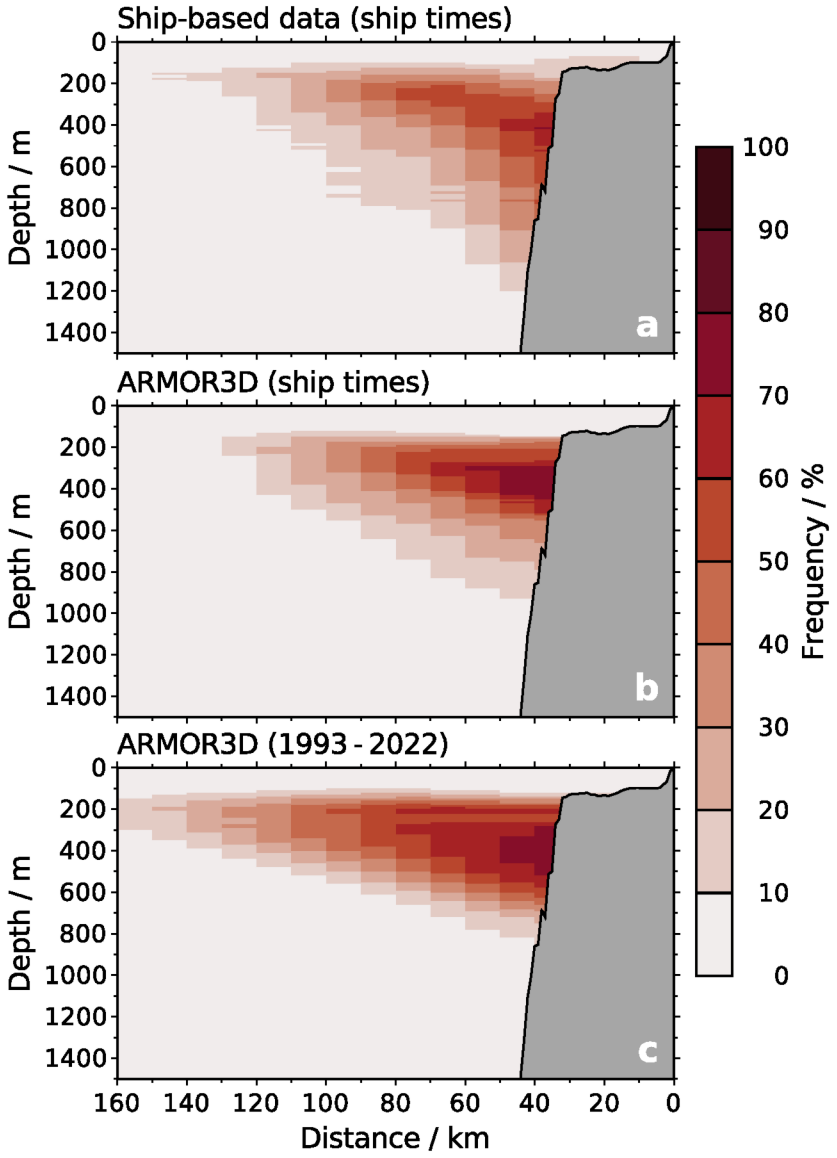

Figure 3.4: Total Irminger Water frequency (%) at eastern AR7W for (a) the pure ship-based data from Chapter 2.5.1 (Table 2.1), (b) ARMOR3D only for times with available ship-based data (Table 2.1), (c) ARMOR3D for all available time steps (1993 - 2022).

quency pattern. It is horizontally more confined toward the continental slope, where it also reaches greater depths, though not as frequently and not as deeply compared to the ship-based data. The ARMOR3D IW frequency patterns reveal notable differences between the two times (Figure 3.4 b, c). IW covers a limited area in times of the available ship-based data in spring and summer (Figure 2.3) compared to the entire period, including all seasons. These seasonal differences are further discussed in Chapter 3.3.1.

Additionally, I calculate the IW frequency pattern with DOORS. Compared to the ship-based data and ARMOR3D, the IW frequencies in DOORS tend to be similar

(Figure A.1 f). A minor difference is that IW in DOORS is more frequent in intermediate layers further offshore. Restricting DOORS to the times of available ship-based measurements does not show noticeable differences. However, a sharp break to a zero frequency occurs only further offshore due to a lack of measured profiles in this area (Figure A.1 e).

In the following, I compare individual ship-based sections at eastern AR7W with the section from ARMOR3D. I analyze individual comparisons between ARMOR3D and ship surveys for particular times when the abundance of IW is low (e.g., summer 1995, Figure 3.5) or high (e.g., summer 2011, Figure 3.6). These comparisons are made when the entire water column in the WGC region exhibits distinct hydrographic states.

The two ship-based sections in 1995 and 2011 differ in spatial resolution, leading to a varying level of data interpolation. In 1995, seven CTD profiles covered eastern AR7W, while only three CTD profiles were available in 2011. The ship section from the summer of 1995 reveals a colder and fresher IW with a minimum area embedded in a generally cold and fresh water column. In contrast, the summer section 2011 shows a warmer and more saline IW, with an enlarged area embedded within a warmer and more saline water column. Both sections indicate high velocities at the continental slope, decreasing further offshore. These features are also represented in ARMOR3D.

The velocity distributions of both data sets are notably better aligned in 2011 than in 1995. The analysis highlights that the influence of a single vertical profile in the ship-based data can substantially shape the velocity structure of the entire section, as observed in the summer of 1995. Specifically, one profile in the ship-based data from 1995, featuring negative velocities, contributes to the velocity structure along the continental slope. Outside this area, the highest velocities in the ship-based data are located 80 km offshore. In contrast, in ARMOR3D, the highest velocities are directly situated at the continental slope. It is important to note that the calculation of the ARMOR3D fields incorporates the ship-based data for both years; thus, the data sets are not entirely independent.

To demonstrate that ARMOR3D also yields comparable results to ship-based data not included in the calculation of ARMOR3D, I compare the data set with ship-based data from early May 2018 (Figure 3.7). Both data sets are independent and yet exhibit similar water mass structures. When there is no water with salinities of $S > 34.92$, IW

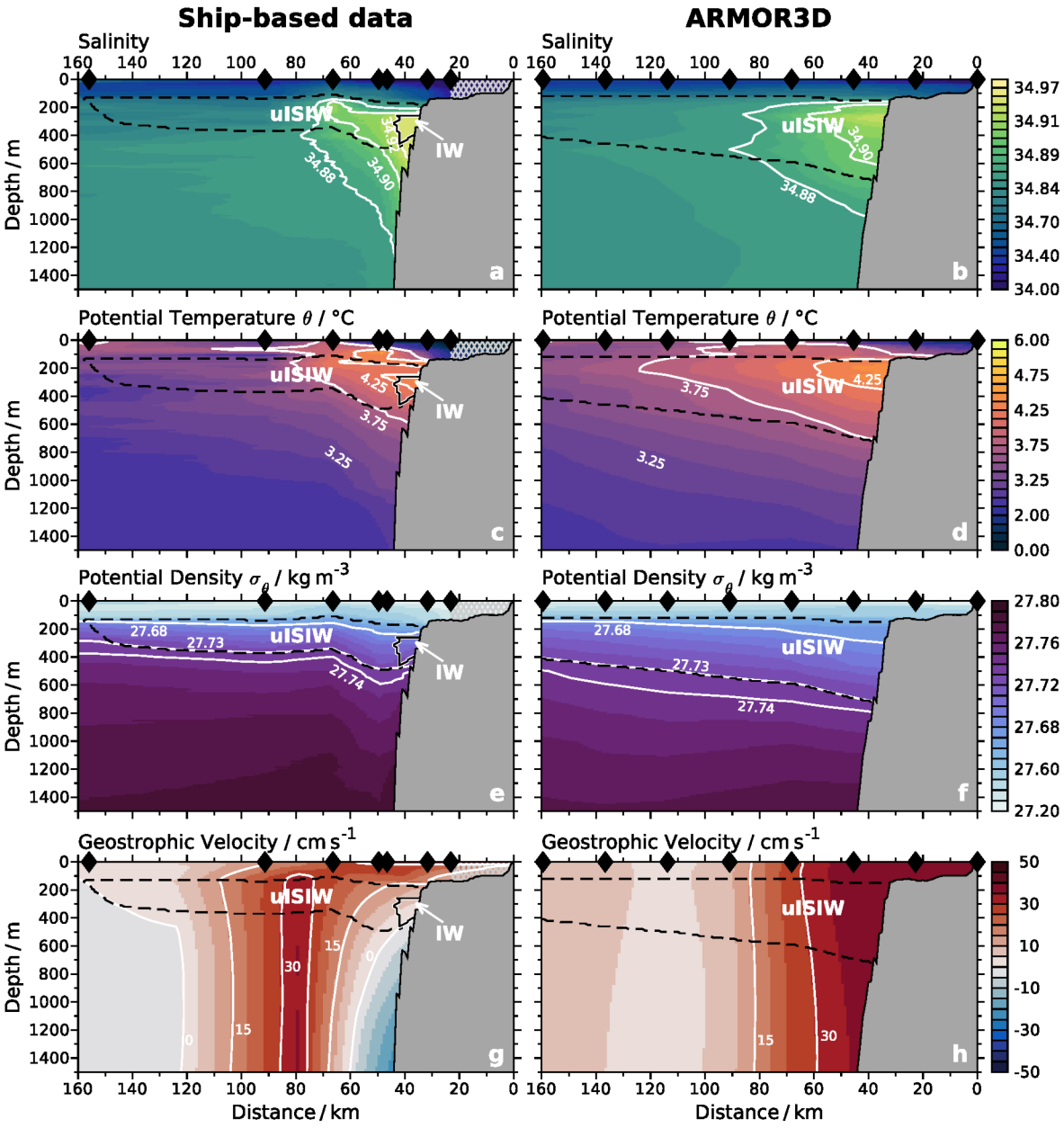

Figure 3.5: Comparison between ship-based data from cruise 18HU95011_1 (left column) and ARMOR3D (right column) for a reduced Irminger Water area at eastern AR7W in mid-June 1995. Properties from top to bottom: salinity (a, b), potential temperature θ (c, d), potential density σ_θ (e, f), geostrophic velocity (g, h). A thick and solid white line overlayed with a thin and solid black line encompasses Irminger Water. The dashed, black line encompasses upper Irminger Sea Intermediate Water. White lines represent individual isolines. Diamonds denote the position of individual hydrographic profiles for ship-based data and represent horizontal resolution for ARMOR3D. Shading in the ship-based data highlights the area based on extrapolating the section toward the Greenland coast.

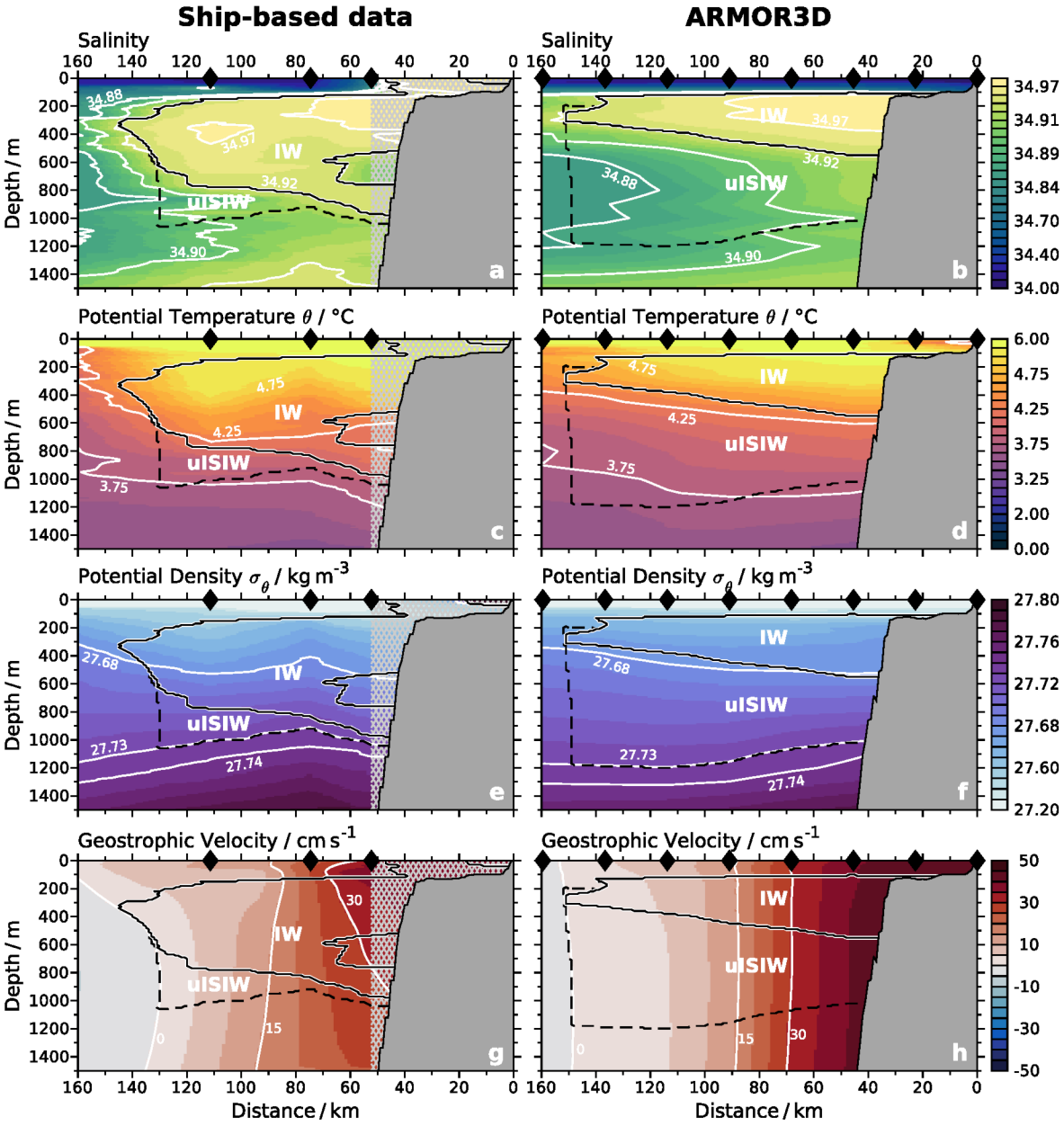

Figure 3.6: Similar to Figure 3.5 but for late July 2011.
Comparison between ship-based data from cruise M85/1 (left column) and ARMOR3D (right column) for an enlarged Irminger Water area at eastern AR7W in late July 2011. Properties from top to bottom: salinity (a, b), potential temperature θ (c, d), potential density σ_θ (e, f), geostrophic velocity (g, h). A thick and solid white line overlayed with a thin and solid black line encompasses Irminger Water. The dashed, black line encompasses upper Irminger Sea Intermediate Water. White lines represent individual isolines. Diamonds denote the position of individual hydrographic profiles for ship-based data and represent horizontal resolution for ARMOR3D. Shading in the ship-based data highlights the area based on extrapolating the section toward the Greenland coast.

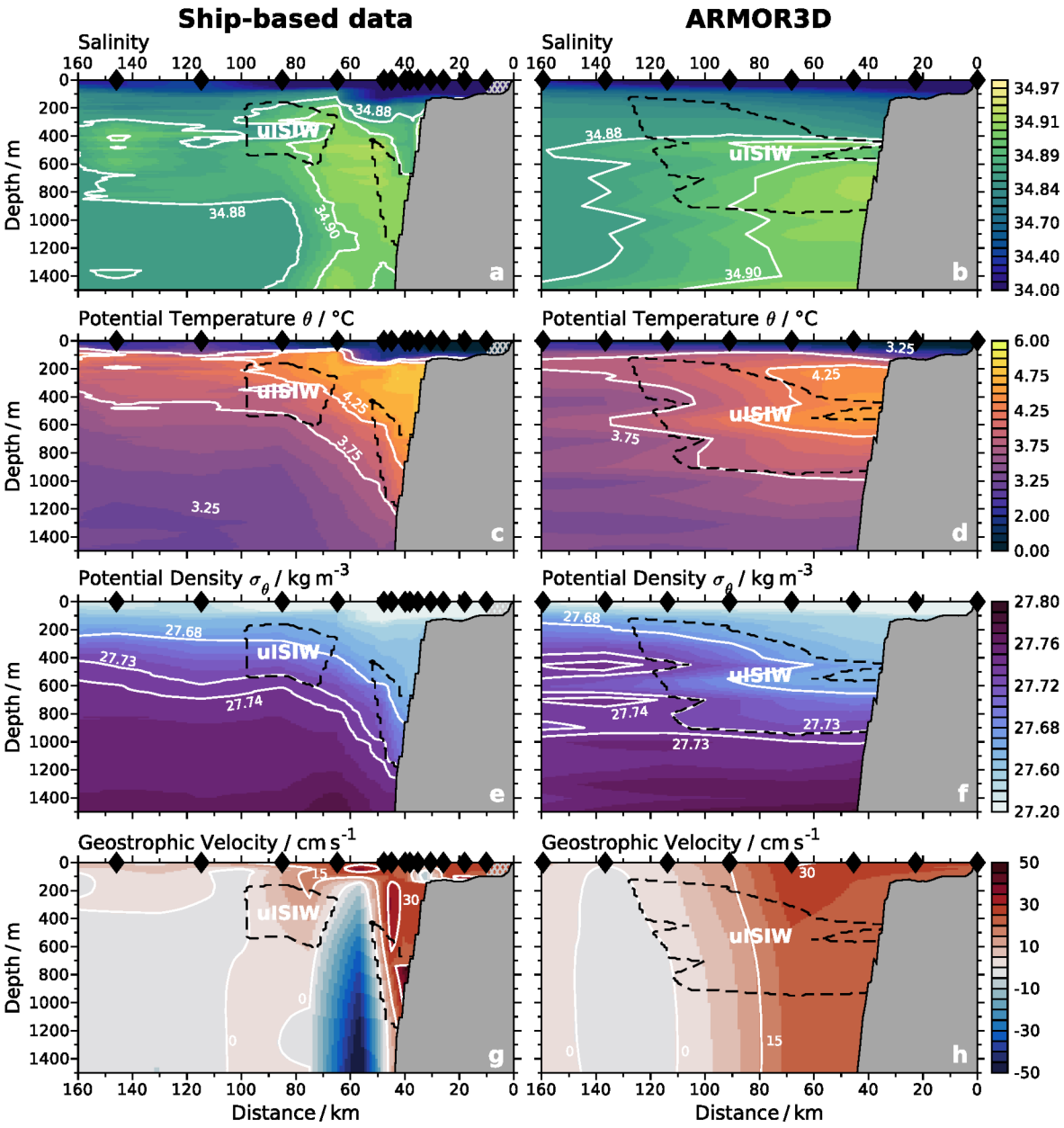

Figure 3.7: Similar to Figure 3.5 but for May 2018.
Comparison between ship-based data from cruise MSM73 (left column) and ARMOR3D (right column) for an enlarged Irminger Water area at eastern AR7W in late July 2011. Properties from top to bottom: salinity (a, b), potential temperature θ (c, d), potential density σ_θ (e, f), geostrophic velocity (g, h). A thick and solid white line overlayed with a thin and solid black line encompasses Irminger Water. The dashed, black line encompasses upper Irminger Sea Intermediate Water. White lines represent individual isolines. Diamonds denote the position of individual hydrographic profiles for ship-based data and represent horizontal resolution for ARMOR3D. Shading in the ship-based data highlights the area based on extrapolating the section toward the Greenland coast.

is mixed to salinities below the defined salinity threshold and is no longer detectable using this definition. I identify an intermediate layer of uISIW located at greater depths along the continental slope and lifting further offshore. The differences are akin to those observed in 1995 (Figure 3.5) and 2011 (Figure 3.6), where the area covered by uISIW is generally larger in ARMOR3D. The most important similarity between ARMOR3D and the ship-based data is the apparent absence of IW in both data sets. This finding is noteworthy, especially since the continental slope region was surveyed with short distances between individual vertical profiles in 2018.

As stated by Greiner et al. (2020), velocities in ARMOR3D appear to be more barotropic. At the same time, the density gradients suggest a higher baroclinic velocity component in the ship-based data. Such overestimation of the barotropic boundary current based on high-latitude altimetry data was previously described by Brachet and Traon (2004) due to a lower sampling rate compared to lower latitudes. Nevertheless, the similarities between the individual ship sections and ARMOR3D prevail, except for the mentioned velocities.

Despite the mentioned limitations, ARMOR3D is a generally suitable data set to analyze hydrographic variability in the upper 1,500 m of the water column at eastern AR7W. On average, I observe all major water masses at the expected depths and within the expected temperature and salinity range. Different times when the water column is in different states, with enlarged or reduced IW areas, are primarily represented in ARMOR3D and agree with the available ship-based measurements and DOORS. This agreement also applies to years before the start of the Argo program in 2000. Therefore, I use ARMOR3D for further detailed analyses of seasonal to long-term variability of IW.

3.3 Variability of IW and uISIW

Applying the water mass definitions from Chapter 3.2 (Table 3.1), I calculate ARMOR3D time series of IW and uISIW layer-averaged salinity, temperature, and velocity, along with their respective volume transports between 1993 and 2022. Subsequently, I construct annual climatologies with a weekly resolution over the entire period. Similarly, I calculate weekly climatologies for available IW and uISIW properties from DOORS (Chapter 2.5.2) and for properties from the OSNAP West IW time series (see

Chapter 2.5.3). Statistical coherence between different time series is calculated using correlation analyses in this thesis. For this purpose, all time series are detrended. Unless stated otherwise, all calculated correlations are tested to be significantly different from zero. To determine significance, bootstrapping analyses are realized (e.g., Wilks, 2011) with 1,000 bootstraps to test the significance for the one-sided 1% confidence interval (0.5% on both sides). I report the correlation coefficient and the lower and upper bounds of significant correlation values in brackets.

3.3.1 Seasonal variability of Irminger Water

The respective IW time series (Figure 3.8, left column) reveal pronounced seasonal variability for all investigated parameters. The ARMOR3D-based IW salinity (Figure 3.8 a) exhibits periods of low salinity between April and July when IW mixes with colder and fresher ambient waters close to the chosen salinity threshold of $S = 34.92$. A sharp salinity increase up to $S = 34.96$ follows this period within the four following weeks. The DOORS and OSNAP West mooring data reveal a similar evolution but do not imply such a salinity jump. I repeated the analysis of IW salinity further up- and downstream of eastern AR7W at the location of the OSNAP West moorings and Cape Desolation (not shown). The results indicate that the jump toward higher salinities only occurs at eastern AR7W and further downstream in the WGC. The jump does not occur upstream of eastern AR7W at the OSNAP West location (see Figure B.1). At first glance, this jump appears to be an inherent signal in ARMOR3D. However, individual ship sections (see Figure B.2) reveal elevated salinities at this time of the year that are higher than those in DOORS and the OSNAP West data. Additionally, I examined individual CTD sections from the WOCE-AR7E-line, which runs from the Greenland shelf break southeast across the Irminger Sea (e.g., Kieke & Yashayaev, 2015). A few surveys from the early and later 1990s conducted in August and September also revealed IW salinities well exceeding 34.95 (not shown), and this signal is expected to propagate further into the WGC.

I can only speculate here that ARMOR3D thus performs correctly at eastern AR7W, and the noted salinity jump is indeed a valid signal. The reason why ARMOR3D shows lower salinities in the upstream region and the salinity jump is not present may relate to the fact that high-resolution CTD sections capturing these high salinities close to the shelf break are often missing, either for the specific time or in general. Frequent CTD

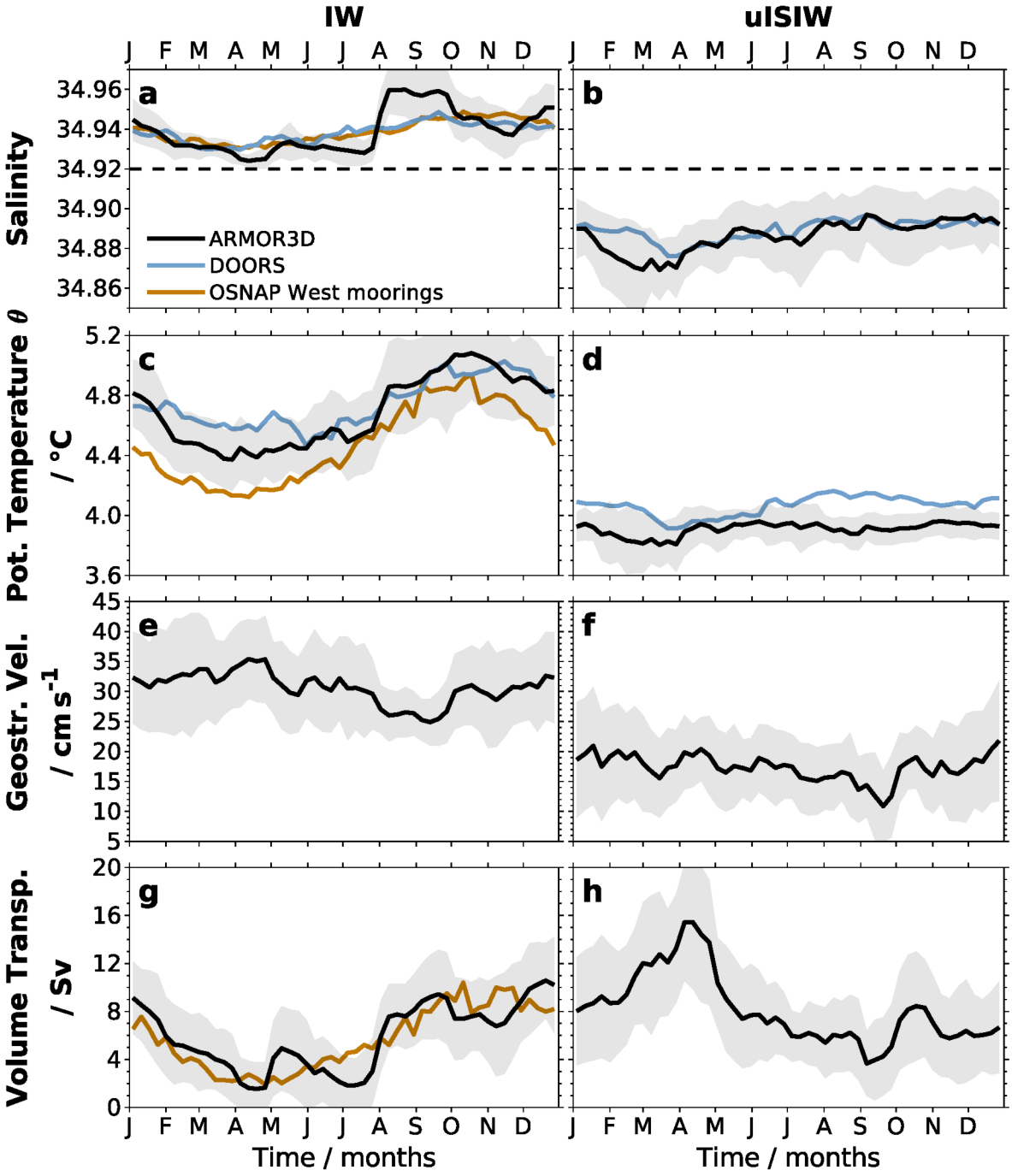

Figure 3.8: Annual climatology of mean Irminger Water (left column) and upper Irminger Sea Intermediate Water (right column) properties at eastern AR7W from 1993 - 2022. Properties are salinity (a, b), potential temperature θ (c, d), geostrophic velocity (e, f), volume transport (g, h). Bold, black lines indicate ARMOR3D with shaded standard deviation. Blue lines represent DOORS from 1993 - 2021; orange lines represent OSNAP West mooring observations from 2014 - 2018, OSNAP West data from Pacini et al. (2020).

sections from the OSNAP sections starting in 2014 generally capture a relatively cold and fresh state of the entire water column. Argo floats may not necessarily drift within the IW core since the water column is shallow near the shelf break. Thus, ARMOR3D may underrepresent the salinity in these regions. The same may be true for DOORS, which projects all kinds of observations onto eastern AR7W. A higher proportion of potentially fresher profiles, for example, from the later Argo period or different seasons, may erode the high salinities at eastern AR7W. The OSNAP West moorings, on the other hand, consist of single point measurements with vertical distances of about 250 m (Pacini et al., 2020). They may miss the peak salinity in the IW layer and generally cover a period characterized by a colder and fresher state of the entire SPNA.

The temperature exhibits a similar seasonal cycle in all three data sets (Figure 3.8 c), where ARMOR3D is, on average, approximately 0.25 °C warmer in comparison to the record from OSNAP West, but is very similar to DOORS. In spring, DOORS even reveals slightly higher temperatures. Depending on the actual location of the individual mooring instruments, the OSNAP West mooring data may undersample the sharp gradient of the warm layer. Another reason for the differences between the OSNAP West data and the two other data sets might be that the mooring-based record covers only 2014 to 2018. When limiting the climatology of IW temperatures from ARMOR3D and DOORS to the mooring period between 2014 and 2018, all data sets are in the same order of magnitude (not shown). The IW properties in ARMOR3D and DOORS are closer to those obtained from the OSNAP West moorings, although the rapid increase of ARMOR3D salinity is persistent.

The seasonal cycle with the highest temperatures in fall agrees with findings based on in-situ data from Grist et al. (2014, their Figure 3). Similarly, Curry et al. (2014) found a seasonal cycle for temperature by analyzing six years of mooring data across Davis Strait. Likewise, Myers et al. (2021) considered a model-based time series of heat transport across Davis Strait and exhibited a seasonal maximum in late fall. In contrast to the temperature and salinity, the climatological velocities (Figure 3.8 e) indicate maximum values from February to April and a decrease until September. A recent study analyzing the velocity of the WGC at Cape Desolation in a high-resolution model also found the highest seasonal buoyancy-driven velocities in spring and the lowest in fall (Gou et al., 2022).

Low values characterize the climatological volume transport in ARMOR3D down to 2 Sv in April and July, followed by a rapid increase up to 8 Sv in August and a subsequent slower increase up to 10 Sv until September (Figure 3.8 g). While the ARMOR3D IW volume transport at eastern AR7W is significantly correlated with its salinity (r = 0.79 [0.68, 0.90]) and temperature (r = 0.76 [0.52, 0.89]), it is significantly anti-correlated with its velocity (r = -0.34 [-0.59, -0.02]). Therefore, the results indicate that the IW volume transport at eastern AR7W is dominated by the varying area of the cross-slope section covered by IW, not by its velocity. This result agrees with observations from the OSNAP West moorings (Pacini et al., 2020).

The OSNAP West IW volume transport based on the mooring record indicates a minimum plateau between March and May with 2 Sv, followed by a constant increase up to 10 Sv in fall (Figure 3.8 g). However, the mean transport (and standard deviation) of ARMOR3D and the OSNAP West moorings are very similar, with 5.9 Sv (2.7 Sv) for ARMOR3D at eastern AR7W and 5.7 Sv (2.6 Sv) for the OSNAP West mooring observations. When comparing ARMOR3D to the mooring-derived time series directly at the OSNAP West site, ARMOR3D reveals an IW volume transport that is higher compared to the mooring record by approximately 3.5 Sv (Figure B.1, left column). This difference slightly decreases to 3 Sv when considering ARMOR3D for the OSNAP West mooring record period (Figure B.1, right column). When considering only the period from 2014 to 2018 at eastern AR7W, both IW volume transports are similar (not shown).

For the uISIW salinity (Figure 3.8 b), ARMOR3D reveals an amplitude ranging between 34.87 and 34.90 at eastern AR7W. The lowest salinities occur in February and March, while the highest salinities are found between September and December. Similarly, the uISIW temperature ranges between 3.80 °C and 3.96 °C. In contrast to IW, the velocity of uISIW in ARMOR3D is significantly correlated with its volume transport (r = 0.42 [0.14, 0.63], Figure 3.8 f, h). The highest volume transport occurs in April, and the lowest is observed in September. Unlike IW, hydrographic parameters of uISIW are anti-correlated (though not significantly for temperature) with its volume transport (salinity: r = -0.56 [-0.77, -0.35], temperature: r = -0.24 [-0.61, 0.11]).

To compare the area covered with IW in different seasons, I calculate the IW and uISIW frequency following the methodology outlined in Chapter 3.2 for two specific weeks indicating the seasonal minimum of IW volume transport in spring (uISIW

dominates, 09 Apr - 15 Apr) and the seasonal maximum of IW volume transport in fall (IW dominates, 03 Sep - 09 Sep). During periods when uISIW dominates at eastern AR7W (Figure 3.9, left column), nearly the entire water column exhibits lower salinity compared to the periods when IW dominates (Figure 3.9, right column). When uISIW dominates, it covers the entire area between approximately 100 to 1,200 m. Notable is a core with its center at a depth of 600 m and located 120 km offshore, where uISIW is consistently identified in all years. Furthermore, uISIW extends to greater depths, reaching ∼1,100 m at about 50 % of the time (Figure 3.9 e). Conversely, when IW dominates at eastern AR7W (Figure 3.9, right column), IW covers a depth range from ∼150 m at the shelf break until ∼800 m (Figure 3.9 d). Moving further offshore, the lower boundary of IW rises until only a thin layer remains, spanning roughly 200 to 300 m. Below this, uISIW covers the area from the lower boundary of IW down to a depth of ∼1,000 m (Figure 3.9 f).

3.3.2 Seasonal variability in the core of the boundary current system

Rykova et al. (2015) observed an IW core region with the highest salinity at the continental slope in a depth range between 300 and 700 m and distances of 65 to 85 km offshore. Building upon the findings of Rykova et al. (2015) and considering the results obtained at eastern AR7W from the ship-based data, DOORS, and ARMOR3D, I define an IW core that extends 40 km offshore from the 300 m isobath. As a result, the defined IW core area encompasses both the continental slope and the region where the maximum salinity was detected by Rykova et al. (2015) and Pacini et al. (2020). I calculate a specific annual climatology for IW salinity, temperature, velocity, and volume transport, exclusively for the area of the defined IW core (Figure 3.10). The salinity, temperature, and volume transport results do not differ notably from the analysis within the entire section. de Jong et al. (2014) similarly analyzed seasonal differences by comparing temperatures at eastern AR7W in May and August 2008 and found similar results to those obtained in ARMOR3D. Within this IW core region (Figure 3.10 a - d), IW velocity demonstrates a significantly positive correlation with the IW volume transport ($r = 0.62$ [0.35, 0.81]). In contrast, for the entire IW area (Figure 3.8), the correlation between velocity and volume transport is significantly anti-correlated ($r = -0.34$ [-0.59, -0.02]). The highest velocities within the IW core region are observed in December. In contrast, the lowest occur between May and July

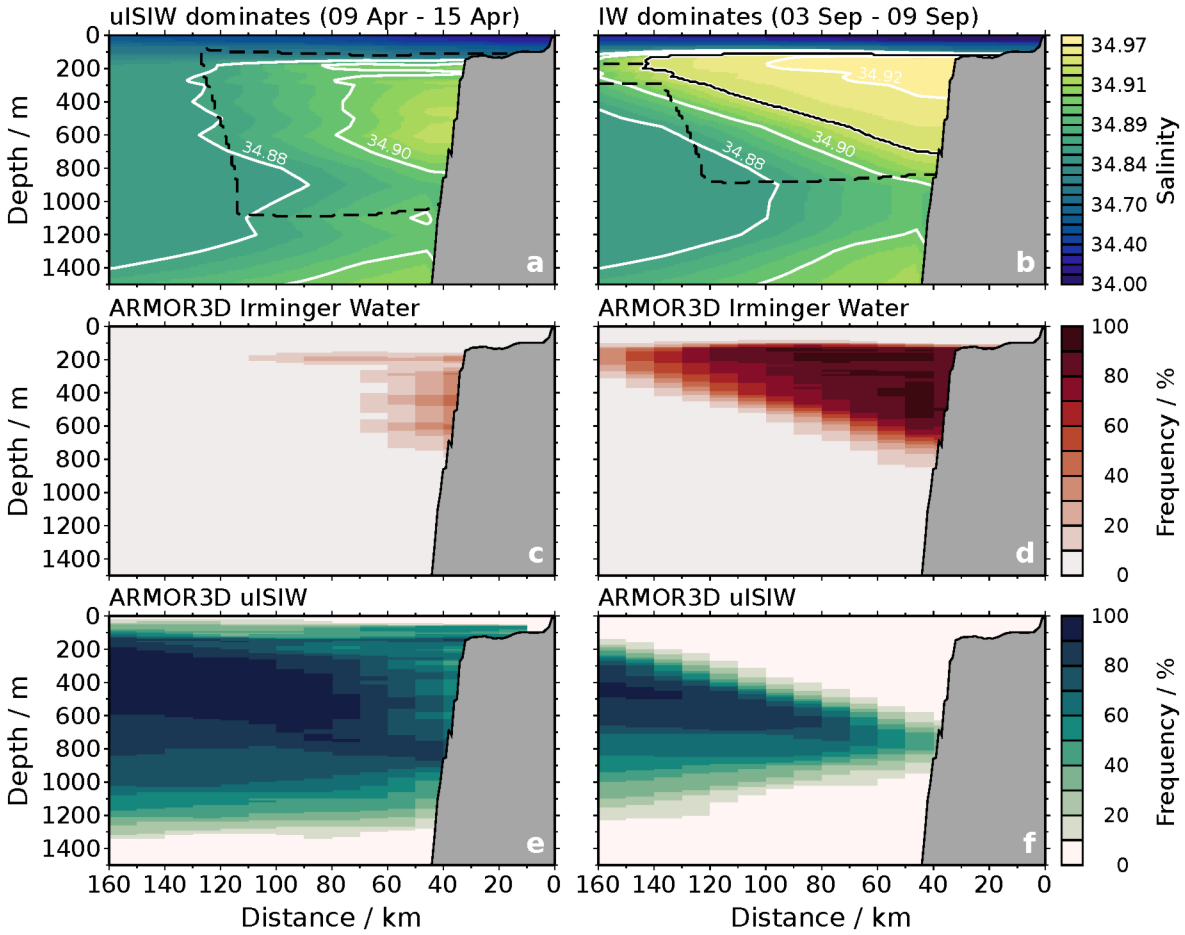

Figure 3.9: (a) ARMOR3D annual climatology of salinity at eastern AR7W in the week from 09 Apr - 15 Apr when upper Irminger Sea Intermediate Water dominates at eastern AR7W. (b) The same for the week from 03 Sep - 09 Sep when Irminger Water dominates at eastern AR7W. Thick and solid white lines overlaid with thin and solid black lines encompass Irminger Water. Dashed, black lines encompass upper Irminger Sea Intermediate Water. White lines represent selected isohalines. (c) and (d) illustrate the frequency of Irminger Water occurrence at eastern AR7W from 1993 - 2022 for the respective weeks. (e) and (f) show the same for upper Irminger Sea Intermediate Water.

(Figure 3.10 e). Consequently, the seasonal variability of IW velocity at the entire section (Figure 3.8 e) is predominantly influenced by low velocities farther offshore when the IW covers a larger area beyond the IW core region. When the IW area contracts, it encompasses a region with higher velocities, increasing the inferred mean IW velocity. Notably, velocities within the IW core region are at their lowest during late spring and summer, reaching their peak during fall and winter. This pattern suggests a potential connection to the seasonal variability of the NAO, which exhibits its strongest influence in fall and winter while showing weaker effects in late spring and summer (e.g., Portis et al., 2001).

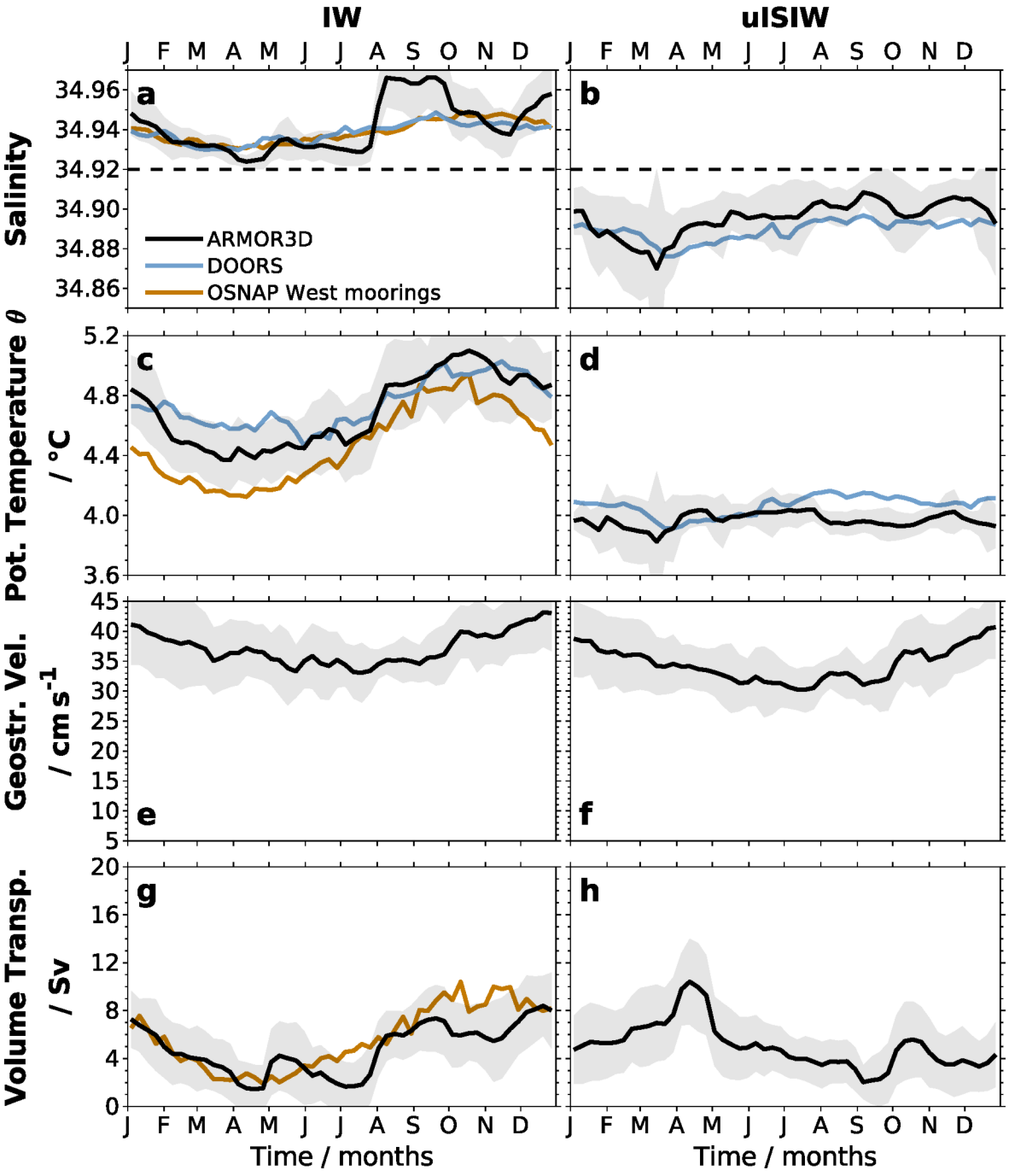

Figure 3.10: Similar to Figure 3.8 but in the IW core region.
Annual climatology of mean Irminger Water (left column, IW) and upper Irminger Sea Intermediate Water (right column, uISIW) properties at eastern AR7W within the IW core region 40 km offshore from the 300 m isobath from 1993 - 2022. Properties are salinity (a, b), potential temperature θ (c, d), geostrophic velocity (e, f), volume transport (g, h). Bold, black lines indicate ARMOR3D with shaded standard deviation. Blue lines represent DOORS from 1993 - 2021; orange lines represent OSNAP West mooring observations from 2014 - 2018, OSNAP West data from Pacini et al. (2020).

Using data from the upper 1,500 m, I construct Hovmöller diagrams depicting the hydrographic parameters and the current velocity by calculating spatial averages for all parameters within the IW core region (Figure 3.11). The presence of IW is observed between ∼150 and 600 m depth from August to March. However, IW experiences strong mixing below the salinity threshold between April and July (Figure 3.11). The relationship between velocity and IW presence in the water column (Figure 3.10) is again highlighted in the Hovmöller diagram (Figure 3.11). No present IW accompanies the lowest velocities in July, while the highest velocities in December are accompanied by a large thickness of IW.

Consequently, the horizontal and vertical structure of IW undergo substantial seasonal changes. Notably, the spacing between instruments in the OSNAP West moorings (250 m in the vertical IW range; Pacini et al., 2020) may introduce a bias to the vertical IW structure due to a coarser resolution in representing the water column. A similar bias might also be present in ARMOR3D, albeit to a lesser degree. In ARMOR3D, the vertical distance between grid points in the IW depth ranges between 25 and 100 m.

3.3.3 Causes for seasonal Irminger Water variability

According to Le Bras et al. (2020), uISIW predominantly forms in the Irminger Sea during winter convection. It is subsequently subducted into the EGC over the following three months, potentially through an eddy transport mechanism. Additionally, a substantial portion of the convection occurs slantwise, as denser waters are horizontally pushed toward lighter waters (Le Bras et al., 2022). This slantwise convection is especially prominent in the Irminger Sea's western boundary current region, where northerly winds induce an Ekman transport that advects the Atlantic-origin waters (here IW) toward the continental shelf (Le Bras et al., 2022). Other local wind patterns like the Greenland tip jet strongly influence vertical convection. The frequency of wind events associated with the tip jet depends positively on the state of the winter NAO (e.g., Pickart et al., 2003a; Våge et al., 2008a, 2009; Josey et al., 2019). In a model study covering 2003 to 2010, Paquin et al. (2016) demonstrated that only these Greenland tip jets result in sufficient ocean heat loss to induce vertical ocean convection in the Irminger Sea. Another model study by Garcia-Quintana et al. (2019) indicated that high-frequency winds had a major impact on the formation of LSW between 2004 and 2016. By excluding these winds, the March mixed layer depth (MLD) did not ex-

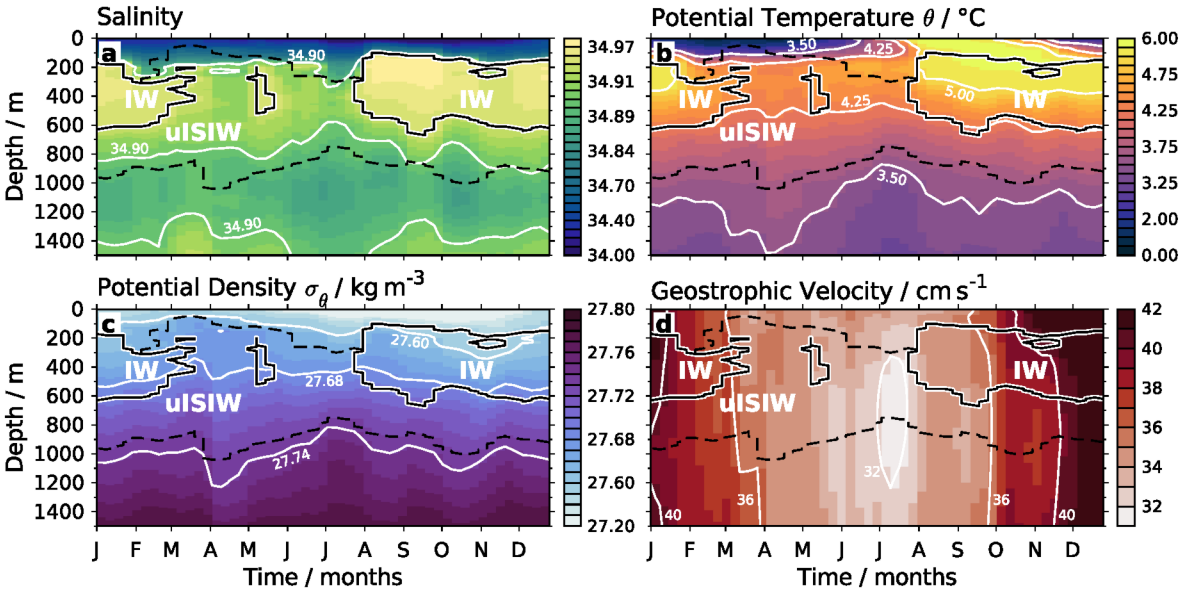

Figure 3.11: ARMOR3D-derived Hovmöller diagrams within the IW core region 40 km offshore from the 300 m at eastern AR7W as annual climatologies from 1993 - 2022. Properties are salinity (a), potential temperature θ (b), potential density σ_θ (c), and geostrophic velocity (d). Thick and solid white lines overlaid with thin and solid black lines encompass Irminger Water. Dashed, black lines encompass upper Irminger Sea Intermediate Water. White lines in (a) and (b) represent selected isolines.

ceed 400 m. This depth is 1,300 m shallower compared to the model run that included variable winds. During these tip jet events that only occur in winter months (Duyck et al., 2022), freshwater is exported eastward from the southeast Greenland shelf in the vicinity of Cape Farewell into the Irminger Sea (Duyck & de Jong, 2023). Notably, Le Bras et al. (2020) observed that the winter convection in the Irminger Sea substantially dilutes the characteristic strong salinity maximum of Atlantic-origin waters. Despite this, uISIW still exhibits a local salinity maximum following convection, albeit weaker than the maximum salinity of the Atlantic-origin waters before the convection phase (Le Bras et al., 2020).

By analyzing the velocity distribution of the EGC/WGC in ARMOR3D, I have determined that uISIW exhibits an advection time of approximately six weeks from OSNAP East to eastern AR7W. As a result, I propose that the expanding uISIW area contributes to reducing the IW area at eastern AR7W during late spring and summer, consequently leading to a decrease in IW volume transport. Exploring the upper 700 m of the water column, Kenchington et al. (2017) explained the seasonal cooling through local winter mixing along the southwest Greenland continental slope, followed by the advection of mixed water from the Irminger Sea. Moreover, I conclude that the on-

set of high IW volume transport at eastern AR7W, coupled with the subsequent rise in temperature and salinity in late July, aligns with the stop of upstream convection approximately 4.5 months earlier (three months from the Irminger Sea convection site into the EGC at OSNAP East as provided by Le Bras et al. (2020) and additional six weeks for the advection toward eastern AR7W). This alignment suggests that the strong modification of IW at eastern AR7W in late spring and summer can likely be attributed to winter convective mixing in the Irminger Sea. However, LSW formed during convection in the Labrador Sea is regularly transported into the Irminger Sea (e.g., Straneo et al., 2003; Yashayaev et al., 2007b, 2007c) leading to a preconditioning of the water column in the Irminger Sea to favor local convection (e.g., Falina et al., 2007). Yeager et al. (2021) illustrated how areas of convection in the Labrador Sea extend into the western Irminger Sea. Thus, I suggest that the attribution of seasonal IW variability at eastern AR7W solely to the Irminger Sea might only hold for individual years when the influence of Irminger Sea convection exceeds the one from Labrador Sea convection. Consequently, I consider the modification of IW in late spring and summer as a result of winter convective mixing in the Irminger and Labrador Seas.

The peak of maximum uISIW volume transport at eastern AR7W in spring (Figure 3.8 h) is accompanied by minima of temperature and salinity. This relationship was expected since the maximum uISIW volume transport aligns with the peak convection in the Irminger Sea, leading to enhanced cooling and freshening of the Atlantic-origin waters (Le Bras et al., 2020). The temporal range between February and April corresponds well with the 4.5 months that uISIW requires to be advected from its formation region to eastern AR7W. Furthermore, the timing of the significant increase in IW volume transport by the end of July and its peak in September coincides with the period when uISIW exhibits its weakest volume transport (Figure 3.8 h).

The modification of IW is only moderate during periods of reduced convection in the Irminger Sea due to diminished buoyancy loss, allowing warm and saline IW to be transported with the EGC/WGC (Figure 3.12 a, b). However, focusing on the hydrographic properties of the water column, it cannot be ruled out that the local mixing of IW with surrounding waters and the incorporation of older ISIW fed back into the boundary current play a role. Consequently, the IW propagating around southern Greenland experiences only minor decreases in temperature and salinity. In the climatological analysis, I identify that during times of minimal IW volume transport

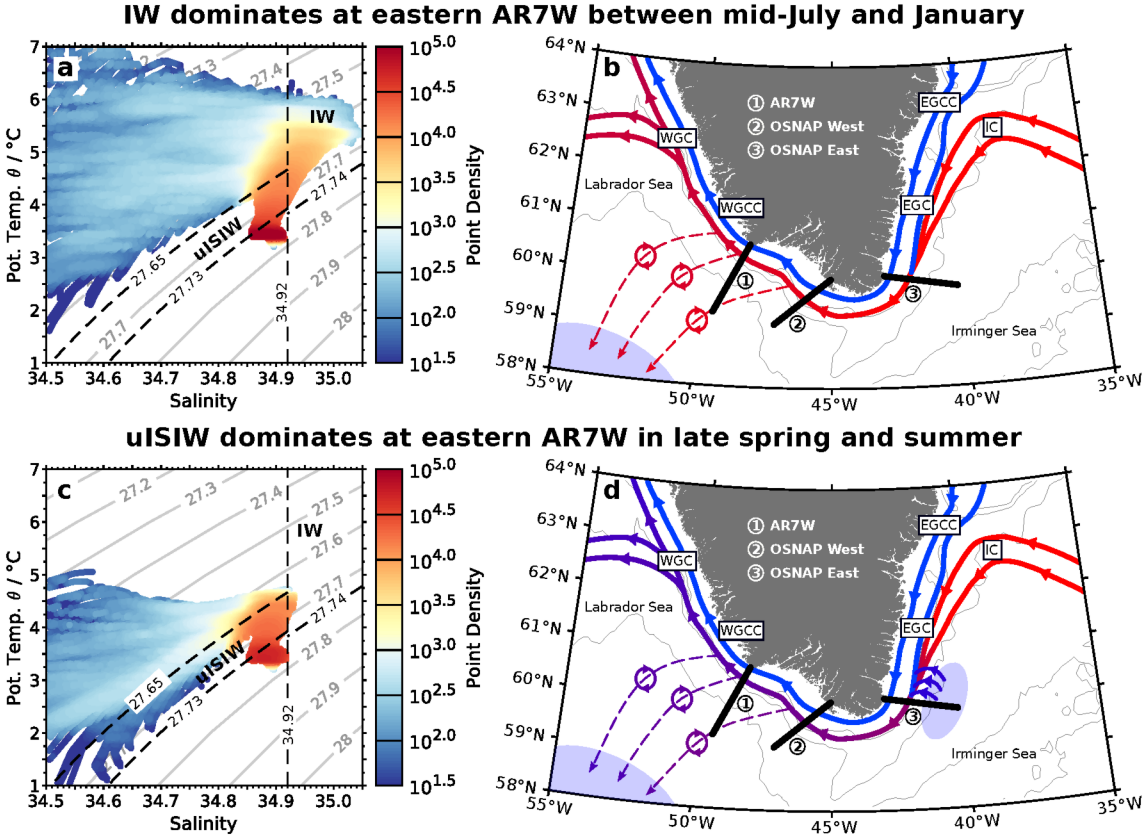

Figure 3.12: T-S diagrams (left column) at eastern AR7W and circulation maps (right column) for times when Irminger Water dominates at eastern AR7W (upper row) and when upper Irminger Sea Intermediate Water dominates at eastern AR7W (lower row) based on the ARMOR3D climatology. Colors in the T-S diagrams denote point densities illustrated as natural logarithmic distributions. Given is the number of points within a box spanning 0.05 °C in temperature and 0.05 in salinity. (b) and (d) show the seasonal circulation state for the respective water mass dominance.

(April, June, July), the area previously covered by IW is now occupied by uISIW (Figure 3.11). The upper uISIW isopycnal ($\sigma_\theta = 27.65\,\mathrm{kg\,m^{-3}}$) ascends to shallower depths, where water characteristics are colder and fresher compared to other months (Figure 3.11). This behavior coincides with a deepening of the lower uISIW isopycnal ($\sigma_\theta = 27.73\,\mathrm{kg\,m^{-3}}$). These results indicate a substantial expansion of the uISIW area that now encompasses shallower depths where IW was not previously identified. These findings align with OSNAP East mooring observations between 2014 and 2016 where Le Bras et al. (2020) identified an outcropping of the isopycnal defining the upper limit of uISIW ($\sigma_\theta = 27.65\,\mathrm{kg\,m^{-3}}$) approximately between January and April (with the most profound MLD in February and March) at the edge of the boundary current. IW exhibits colder and fresher conditions in late spring and summer compared to other

times. As a result, regions downstream of the convection area also experience colder and fresher conditions (Figure 3.12 c, d). These findings are consistent with Pacini et al. (2020), who attributed the seasonal IW variability to winter air-sea interactions in the Irminger Sea.

Within approximately three months, the uISIW is subducted into the boundary current (Le Bras et al., 2020). By the time it reaches the location of eastern AR7W, it typically spans the area beneath the IW down to a depth of about 1,000 m, extending offshore from $\sim$120 to 130 km (Figure 3.3). Conversely, during periods of maximum IW volume transport (mid-July to January), the upper uISIW isopycnal becomes correspondingly depressed, while the lower uISIW isopycnal is elevated (Figure 3.11 c). Analyzing the T-S properties across different seasons suggests that the shape of the upper inflection of IW in fall and winter (Figure 3.12 a) mirrors that of the upper inflection of uISIW in spring and summer (Figure 3.12 c). By applying static thresholds to identify IW, a clear distinction can be made between IW and uISIW. It is important to note that considering thresholds that vary over time might lead to the classification of the warm and saline parts of uISIW as modified IW, as is further explored in Chapter 4.

3.3.4 Interannual and decadal Irminger Water variability

In the following, I analyze the long-term variability of IW covering years between 1993 and 2022. For this purpose, a 10-week and a 2-year running average are applied to the ARMOR3D IW salinity, temperature, velocity, and volume transport time series at eastern AR7W. In order to eliminate higher frequency variability, a Hanning window is applied for all 2-year running average analyses throughout this thesis. It is worth noting that the comparison of ARMOR3D IW properties with those reported by Pacini et al. (2020) has limitations due to the available OSNAP West mooring time series, which spans only four years (2014 - 2018). When analyzing the 10-week running average (Figure 3.13), it becomes apparent that the seasonal variability (Figure 3.8) dominates the amplitude for each parameter, irrespective of the long-term state. The comparison between ARMOR3D and OSNAP West (Pacini et al., 2020) demonstrates the agreement in the timing of the seasonal peaks (Figure 3.13).

The amplitudes of ARMOR3D salinity on interannual time scales slightly exceed those of OSNAP West (Figure 3.13 a). Notably, the OSNAP West salinity minima in summer exhibit higher values, while the salinity maxima are slightly lower. This behavior might

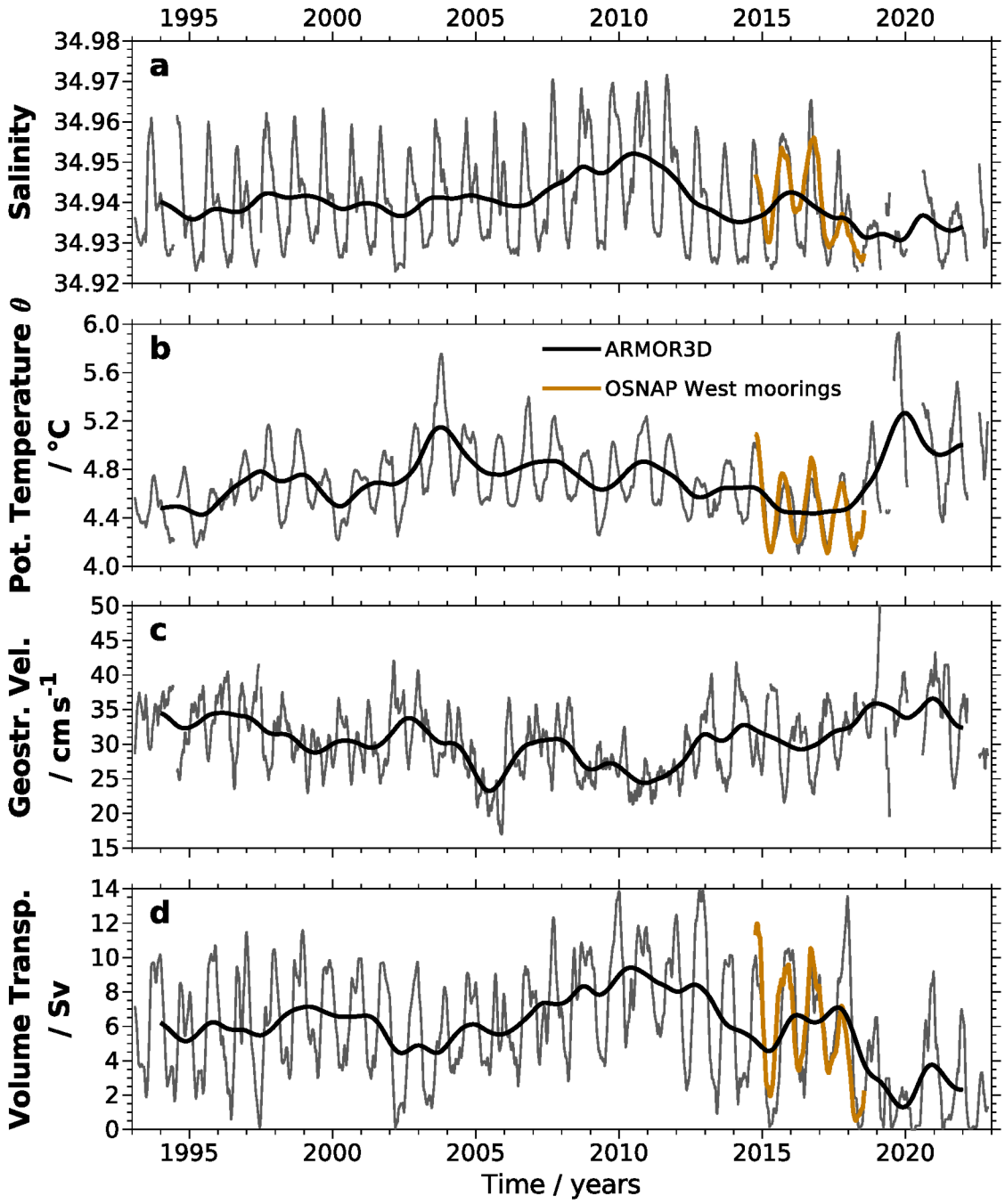

Figure 3.13: Irminger Water properties at eastern AR7W smoothed with a 10-week running average (thin, gray lines) and a 2-year running average including a Hanning window (thick, black lines) in ARMOR3D. OSNAP West mooring observations from Pacini et al. (2020) for a 10-week running average in orange. Gaps in ARMOR3D indicate that Irminger Water was mixed below the fixed thresholds in more than 50 % of the running average range. Properties are salinity (a), potential temperature θ (b), geostrophic velocity (c), volume transport (d).

again be attributed to the vertical resolution of the moorings, which may not provide the detail necessary for a comprehensive analysis of the boundary between the cold and fresh surface waters and the underlying IW. Nevertheless, the trends in interannual changes and the timing of the peaks generally align with those observed in ARMOR3D.

Shifting the focus to the 2-year running average, it becomes evident that there is an overall IW salinity maximum in 2010/2011, contrasting with a minimum in 2019 (Figure 3.13 a). The corresponding IW temperature time series indicates variability at higher frequencies than IW salinity (Figure 3.13 b). 2003 and 2019/2020 saw the highest temperatures, almost reaching or exceeding 5.2 °C, while the lowest temperatures of approximately 4.4 °C occurred in 1995 and from 2015 to 2017. It is worth noting that the peaks of maximum temperatures do not align with those observed for salinity.

Similar to the seasonal variability analysis, the long-term velocity variability exhibits an opposing signal compared to the salinity. Specifically, a velocity minimum was observed in 2010 and 2011, while recent years between 2019 and 2022 witnessed a velocity maximum. Additionally, akin to the findings in the seasonal analysis (Chapter 3.3.1), significant correlations between the 2-year running average of salinity (Figure 3.13 a) and volume transport (Figure 3.13 d) are identified with $r = 0.81$ [0.78, 0.83]. The maximum volume transport of ~ 9 Sv in 2010/2011 aligns with the observations of Ribergaard (2014). Conversely, periods preceding and succeeding 2010/2011 exhibit lower volume transports, reaching minimum values of ~ 4 Sv in 2003, 5 Sv in 2014/2015, and 2 Sv in 2019/2020, indicative of long-term decadal variability. The correlations between volume transport and temperature ($r = -0.38$ [-0.44, -0.32]), as well as between volume transport and velocity ($r = -0.70$ [-0.74, -0.66]), are both significantly negative. This relation suggests that lower temperatures accompany elevated salinities and resulting volume transports over longer time scales. In contrast, high salinities and volume transports correspond to elevated temperatures on seasonal time scales. Consequently, the causes of seasonal and longer-term variability differ substantially.

Myers et al. (2007) analyzed IW at Cape Desolation, located just downstream of eastern AR7W, utilizing ship-based data from late spring and summer. Focusing solely on late spring and summer data (May to July; not shown) within ARMOR3D reveals a similar decline in volume transport aligned with the findings of Myers et al. (2007) between 1993 and 2000. However, between 2000 and 2005, Myers et al. (2007) reported a continuous increase, whereas ARMOR3D depicts a decrease in 2002/2003 followed by

a restrained increase in subsequent years. The ship-based data (Chapter 2.5.1) showed similar results, revealing the highest volume transports around 2010 and the lowest during the 1990s and from 2015 to 2018. Specifically, the mean IW volume transport (with corresponding standard deviation) from ARMOR3D was 6.0 Sv (2.8 Sv) over the entire period, compared to 3.3 Sv (3.3 Sv) obtained from the ship-based data. From 2014 to 2018, ARMOR3D consistently exhibited a higher IW volume transport than OSNAP West. However, for the years 2019 to 2022, the IW volume transport decreased to 2 - 3 Sv, constituting the lowest values within the entire period (Figure 3.13 d and Figure 3.14) due to the freshening of the SPNA. This freshening started in 2015/2016 in the western SPNA, propagated throughout the entirety of the North Atlantic Basin, and freshened the Irminger Sea between 2015 and 2020 (Holliday et al., 2020; Biló et al., 2022). The constrained IW area from 2019 to 2022 only saw partial compensation from uISIW. Instead, the period witnessed the presence of waters characterized by low salinity (Figure 3.14 a), accompanied by relatively high temperatures (Figure 3.14 b) extending to depths between ∼300 and 400 m. Also, the IW velocities increased during these years, akin to the patterns observed during the 1990s (Figure 3.13 c and Figure 3.14 d). In contrast, periods of low IW velocities occurred around 2005 and 2010. Consequently, the behavior of IW velocity appears to be contrary to that of IW salinity and volume transport.

3.3.5 Mechanisms shaping the long-term Irminger Water variability

To address likely causes of long-term IW variability, IW time series are analyzed regarding possible forcing mechanisms in the North Atlantic region. I focus on the NAO and the size and strength of the SPG. I detail how the respective NAO and SPG index time series have been obtained in the following.

The North Atlantic Oscillation Index

For this thesis, I obtained daily NAO index values from NOAA (2023b), which are based on a Rotated Principal Component Analysis (Barnston & Livezey, 1987). A positive/negative NAO index describes an enhanced/weakened gradient of the geopotential height anomaly (500 mb atmospheric pressure) over the North Atlantic. I performed a temporal averaging of the daily NAO index values to match the ARMOR3D's weekly temporal resolution (Figure 3.15 b). The NAO exhibits its most considerable variabil-

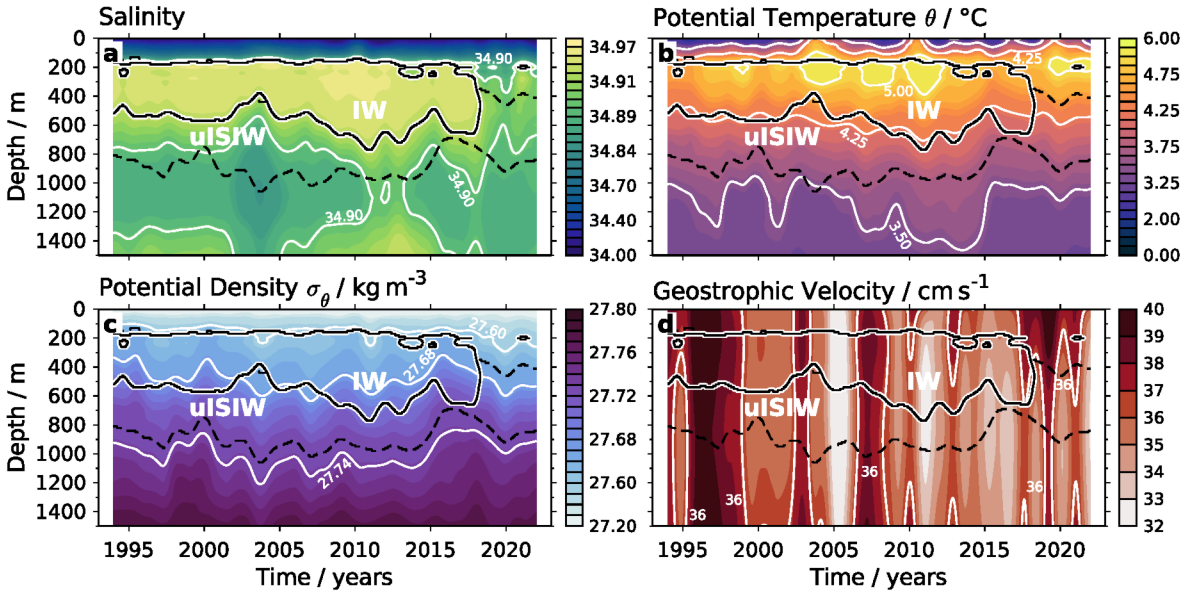

Figure 3.14: ARMOR3D-derived Hovmöller diagrams within the IW core region 40 km offshore from the 300 m at eastern AR7W from 1993 - 2022 with a 2-year running average including a Hanning window. Properties are salinity (a), potential temperature θ (b), potential density σ_θ (c), and geostrophic velocity (d). Thick and solid white lines overlaid with thin and solid black lines encompass Irminger Water. Dashed, black lines encompass upper Irminger Sea Intermediate Water. White lines represent selected isolines.

ity in winter (December to March; Hurrell et al., 2003). During the positive phase of the NAO index, stronger westerly winds bring cold and dry air from the American continent into the region of the western SPG (Lazier et al., 2002) and the Nordic Seas (Sarafanov, 2009).

The Subpolar Gyre Index

Following the approach of Hátún and Chafik (2018), I calculate the SPG index using SSH data (Figure 3.15 b). For consistency within this thesis, I utilize the ARMOR3D geopotential height at the ocean surface. To derive the SPG index, I begin by computing detrended SSH anomalies and then perform empirical orthogonal functions along with their associated principle components within the region defined by 80°W - 0° and 30°N - 65°N (e.g., Hannachi et al., 2007). The SPG index in this analysis corresponds to the first principle component, whereas in Hátún and Chafik (2018), the SPG index corresponds to the second principle component. This difference is likely due to the applied detrending of the SSH time series before conducting the empirical or-

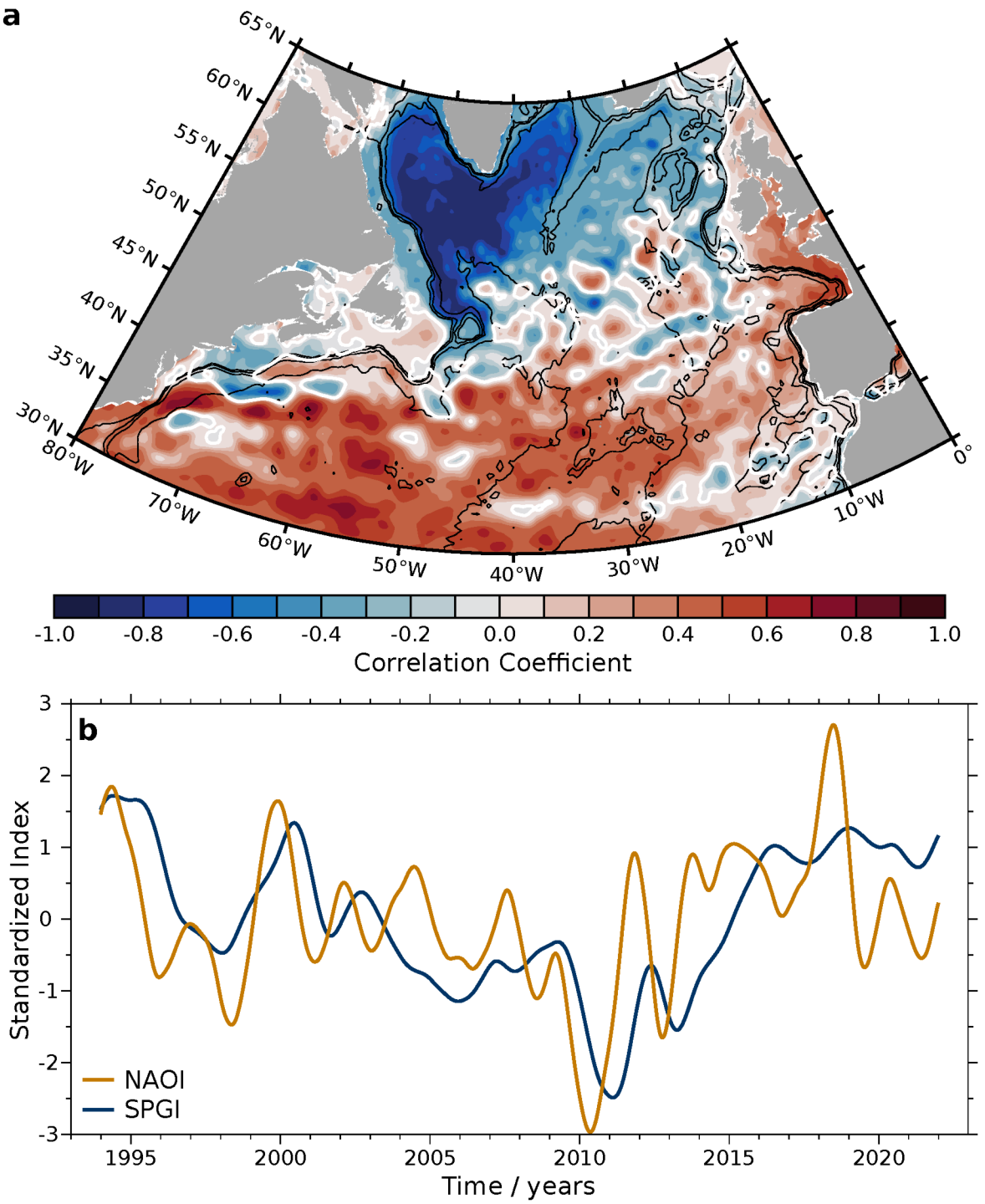

Figure 3.15: (a) Correlation map of the subpolar gyre index (first principle component from the empirical orthogonal function analysis) with ARMOR3D sea surface height field, smoothed with a 2-year running average, including a Hanning window. White contours denote zero correlation. (b) Standardized time series of the North Atlantic Oscillation index (orange) from NOAA (2023b) and the subpolar gyre index (blue) calculated within ARMOR3D, smoothed with a 2-year running average including a Hanning window.

thogonal functions analysis, in contrast to Hátún and Chafik (2018). I find that the detrended weekly ARMOR3D-based SPG index is significantly correlated with the detrended weekly SPG index reported by Hátún and Chafik (2018) and Chafik (2019) with r = 0.83 [0.81, 0.85] when interpolating their time series to the ARMOR3D temporal resolution.

To examine the spatial patterns of correlation, I analyze the relationship between the 2-year running averaged SSH field and the corresponding running averaged SPG index (Figure 3.15). In line with the findings of Hátún and Chafik (2018), it becomes apparent that an expanded gyre (positive SPG index) corresponds to a decrease of SSH within the Irminger and Labrador Seas. This correlation arises from the increased formation of deep waters in these regions (de Jong & de Steur, 2016; Yashayaev & Loder, 2016). The SSH field effectively captures the positions of advective fronts, including the subpolar front. At the same time, the SPG index reflects changes in the spatial expansion and contraction of the SPG. Specifically, an expansion of the SPG is associated with a positive SPG index and a high SSH gradient between the subpolar and subtropical gyre. Conversely, a contraction of the SPG is associated with a negative SPG index and a low SSH gradient between the subpolar and subtropical gyre (e.g., Holliday et al., 2020; Koul et al., 2020).

How do the NAO and SPG affect Irminger Water?

Following Holliday et al. (2020), strong westerly winds during positive phases of the NAO expand the SPG by moving the subpolar front as far south as 45°N. Consequently, the primary branch of the NAC is located anomalously far south and extends the SPG to the east further downstream. This position of the NAC restricts the inflow of substantial amounts of Atlantic-origin waters into the Irminger Sea while enhancing transport into the Arctic. Conversely, during negative phases of the NAO, characterized by weaker westerly winds, the Irminger Sea experiences an increased inflow of Atlantic-origin waters. These variations in the size and strength of the SPG are perceptible through the SPG index (Figure 3.15 b).

Given the analysis of IW at eastern AR7W, I anticipate that periods of a positive NAO would correspond to reduced IW. At the same time, negative NAO phases would lead to increased amounts of IW at eastern AR7W. The timing of such effects relies on the

advection time of signals influenced by the shift of the NAC and other contributing factors. During positive NAO phases, the intensified westerly winds facilitate the transport of cold and dry air from the American continent into the western SPG (Lazier et al., 2002) and the Nordic Seas (Sarafanov, 2009). As a result, I expect that IW during positive NAO phases would exhibit lower temperatures.

Conversely, during negative NAO phases, IW might display warmer characteristics. Such a reversed behavior between the NAO and IW temperature within the Irminger Sea was already shown within a model study from Zhu and Demirov (2011). However, in Zhu and Demirov (2011), the response time of changes in the NAO toward the SPG index (calculated differently than in this thesis) was calculated at a lag of three years between the 1980s and 1990s. Calculating the lag correlation between the 2-year running averaged NAO and SPG index between 1993 and 2022 following Figure 3.15 reveals a maximum lag when the NAO leads the changes in the strength and size of the SPG by 33 weeks ($r = 0.74$ [0.70, 0.78], not shown). These results either suggest that the modeled response between NAO and SPG is generally too slow by about 2.5 years or that large temporal differences in the described relationship between NAO and SPG occur on decadal time scales. Consequently, the first mentioned possible explanation would also result in a delayed response of changes in the NAO on the IW properties by 2.5 years in the model used by Zhu and Demirov (2011).

These wind conditions during positive NAO phases also favor deep convection in the Irminger and Labrador Seas by increasing the occurrence of Greenland tip jet events (Pickart et al., 2003a; Våge et al., 2009). As discussed in Chapter 3.3.3, the convection in the Irminger and Labrador Seas directly influences the hydrographic IW properties in the WGC. Particularly, it leads to lower seasonal IW salinities and temperatures at locations such as eastern AR7W and OSNAP West. Consequently, I expect that changes in the NAO would leave a more pronounced imprint on hydrographic properties compared to IW volume transport, which is likely to be influenced by a combination of both seasonal and long-term NAO variations.

Holliday et al. (2020) found a freshening of the NAC from 2012 to 2016. Over the same period, I identify an increase in the NAO and SPG indices (Figure 3.15 b) along with a corresponding decrease in IW volume transport at eastern AR7W (Figure 3.13 d). When comparing the IW volume transport at eastern AR7W (Figure 3.13 d) with the NAO and SPG index (Figure 3.15 b), it becomes evident that a lagged connection

exists between the forcings in the North Atlantic region and the occurrence at eastern AR7W. Therefore, I conduct a lag correlation analysis for the 2-year running averaged time series, utilizing the maximum possible window length (Figure 3.16). The analysis reveals a significant negative correlation between the IW volume transport and the SPG index with a delay of up to three years (Figure 3.16 d), indicating that the SPG index leads the IW volume transport.

Similarly, a notable relationship is observed between the NAO index and the IW volume transport, particularly within the first three lag years (with the highest correlation at lag 0), highlighting that the NAO index also leads the IW volume transport. The analyses of IW salinity (Figure 3.16 a) and IW temperature (Figure 3.16 b) reveal differences in their respective correlations with the NAO index. While the salinity indicates a strong dependency on the NAO and the SPG, the correlation between the NAO and the temperature is relatively small. As for IW velocity (Figure 3.16 c), the highest correlation appears at a lag of only a few months, coinciding with a minimum correlation in the temperature analysis. These findings strengthen my expectations that local convection in the Irminger and Labrador Seas largely impacts the IW temperature. However, the results also unveiled that changes in salinity are driven by immediate local influences (strongest anti-correlation at zero lag) and effects of advective signals (highly correlated with NAO and SPG up to a lag of three years). Similar to the analysis of seasonal variability, these results on longer time scales are sensitive to the chosen definition for IW.

LSW spreads directly from the Labrador Sea into the Irminger Sea (Paillet et al., 1998; Yashayaev et al., 2007b) and entrains into the Irminger Sea boundary current (Lavender et al., 2000; Chafik et al., 2022). Thereby, it preconditions the water column in the Irminger Sea for winter convection (Yashayaev, 2007a; Yashayaev et al., 2007b, 2007c). I observe minima of IW volume transport in 2003 and 2015. These times align with periods of elevated LSW production in the years 2000 to 2003 and 2014 to 2016 (Yashayaev & Loder, 2016; Garcia-Quintana et al., 2019; Rühs et al., 2021). However, the high production of LSW in 2008 occurred during a year characterized by a relatively strong IW volume transport. The subsequent years, specifically from 2019 to 2022, exhibit the lowest IW volume transport within the last three decades. Low salinities and high temperatures also characterize these years. These characteristics correspond well with the extensive freshening of the SPNA that followed the last phase

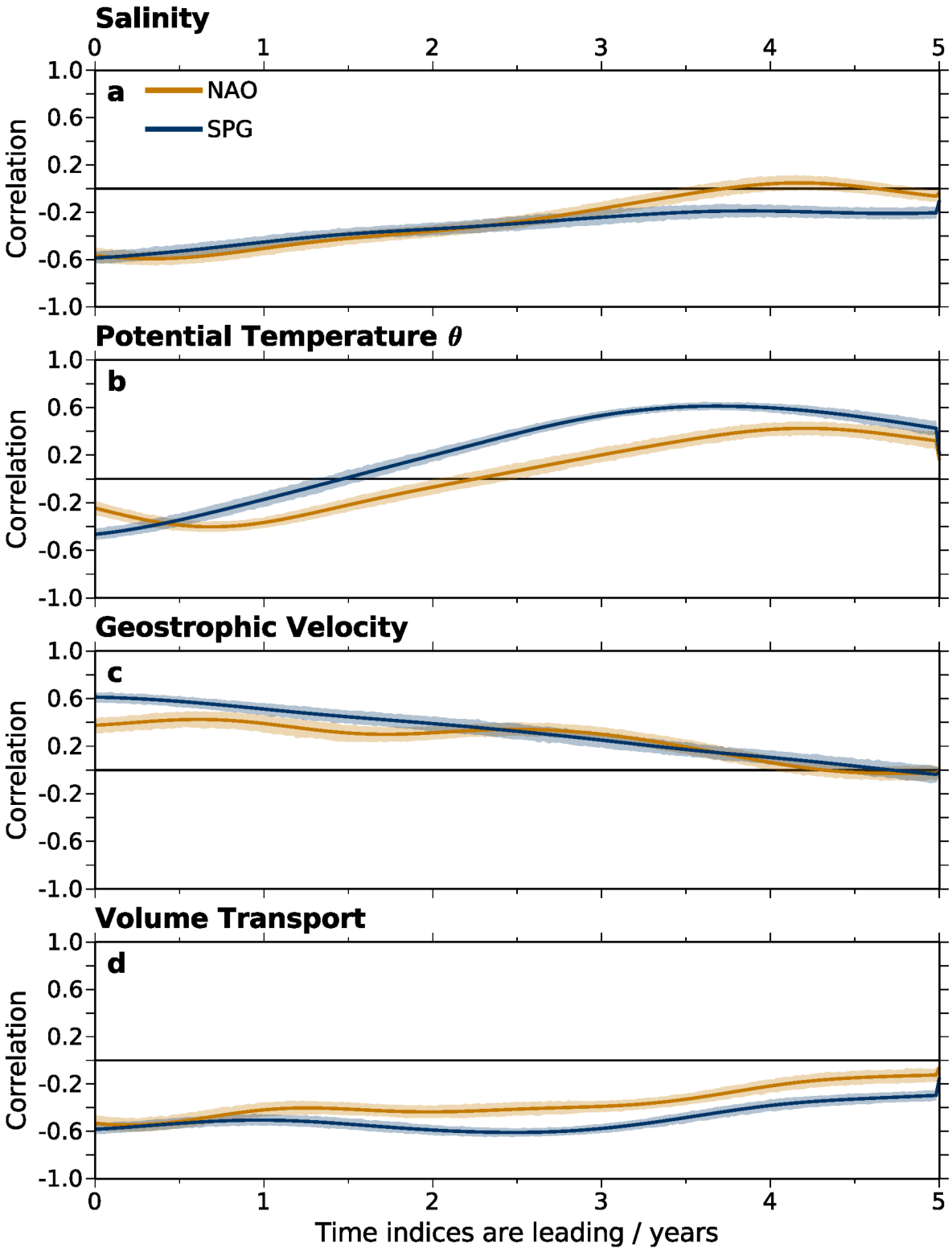

Figure 3.16: Lag correlations of North Atlantic Oscillation index (orange) and subpolar gyre index (blue) with Irminger Water properties at eastern AR7W calculated with a 2-year running average including a Hanning window. Properties are salinity (a), potential temperature θ (b), geostrophic velocity (c), and volume transport (d). Shades denote the two-sided confidence intervals at 1 %.

of strong LSW production between 2014 and 2016 (Holliday et al., 2020; Biló et al., 2022). Given these observations, it is plausible to suggest that this extensive freshening ultimately causes large portions of the IW to become mixed below the defined salinity threshold of S = 34.92.

3.4 Summary and Conclusion

This chapter investigates the temporal variability of IW properties in the BCS on seasonal to decadal time scales. Therefore, I analyze the multi-source observation-based data set ARMOR3D from the Copernicus Marine Environmental Monitoring Service comprising 1/4° gridded hydrographic and geostrophic velocity data with a weekly resolution to achieve this. Previous studies primarily focused on ship-based data collected during late spring and summer (e.g., Myers et al., 2007, 2009; Ribergaard, 2014; Rykova et al., 2015), or relied on temporally limited mooring observations given their jet short timespan from the deployment in 2014 (e.g., Pacini et al., 2020; Le Bras et al., 2020). In contrast, I use the continuous ARMOR3D data set between 1993 and 2022, utilizing the advantages of both remote sensing and in-situ data and providing a means for filling the temporal, vertical, and horizontal gaps that often characterize pure in-situ observations.

For the first time, this allows reconstructing 30 years of IW variability in an observation-based data set, revealing substantial seasonal and interannual to decadal variability. The strongest IW volume transport occurs between mid-July and January, with weaker transport in other months (Figure 3.8 and Figure 3.11). These findings are consistent with observations from OSNAP West moorings (2014 - 2018; Pacini et al., 2020, Chapter 2.5.3) and DOORS (1993 - 2021; Chapter 2.5.2), which incorporates information from Argo floats since the year 2000 and ship-based surveys partly not included in ARMOR3D. Two dominating seasonal states exist at eastern AR7W to the west of Greenland: one with gradually modified IW along the pathway in the BCS (Figure 3.12 a, b), and another with modified uISIW via winter convection in the Irminger and Labrador Seas (Figure 3.12 c, d; Pacini et al., 2020; Le Bras et al., 2020; Falina et al., 2007; Yeager et al., 2021). The colder and fresher uISIW dominates the warmer and more saline IW until mid-July (Figure 3.8).

On interannual and decadal time scales, IW volume transport was strongest in 2010 and weakest at the end of the time series between 2019 and 2022 (Figure 3.13 and Figure 3.14). The period from 2019 to 2022 marked a phase within the available three decades when IW modification was particularly pronounced, resulting in large portions of IW being mixed below the threshold of S = 34.92 (Figure 3.13 d and Figure 3.14). This period coincides with a production of LSW that was among the highest on record (Yashayaev et al., 2022). The SPG's strength and width directly impact the IW volume transport variability on longer time scales. These findings indicate that the SPG variability leads the IW volume transport by up to 3 years (Figure 3.15 and Figure 3.16). An expanded state of the SPG, resulting from a strong NAO, reduces warm and saline waters in the Irminger Sea and vice versa (Holliday et al., 2020). Consequently, a contracted SPG leads to a strong IW volume transport in the boundary currents around Greenland up to 3 years later. Notably, both mechanisms, operating on seasonal or longer time scales, play a crucial role in deep-sea ventilation (Thomas & Zhang, 2022), as the NAO directly impacts deep convection in the Irminger and Labrador Seas due to increased winds (Pickart et al., 2003a; Våge et al., 2009; Paquin et al., 2016).

Fried and de Jong (2022) provide a reanalysis time series from GLORYS (see Chapter 2.2) spanning years from 1993 to 2020, revealing top-to-bottom volume transports of the IC in the eastern Irminger Basin that are reversed to the obtained IW volume transport (Figure 3.13). Periods of strong cooling in the Irminger Sea are accompanied by an increased MLD and a doming of isopycnals during the 1990s and from 2013 to 2015. These changes induced stronger horizontal density gradients, resulting in a more substantial total volume transport. Simultaneously, intensified westerlies, alongside strong winter surface cooling in the Labrador Sea, led to enhanced convection and an expansion of the SPG (Fried & de Jong, 2022). This shift in the SPG led to diminished warm and saline NAC water advection into the Irminger Sea (Sarafanov, 2009). Consequently, I observe a corresponding decrease in IW volume transport at eastern AR7W (Figure 3.13 d).

Furthermore, Holliday et al. (2020) and Biló et al. (2022) note an overall freshening trend in the Irminger Sea starting in 2018. This freshening resulted in an increased local stratification and therefore suppressed convection from 2018 onward. Consequently, the minimum IW volume transport at eastern AR7W between 2019 and 2022 is potentially attributed to a broader freshening of the SPNA below the threshold defining IW.

Through the ARMOR3D-based analysis of inferred IW properties at eastern AR7W, I revisit the research questions previously posed and conclude the following:

1. **How do Irminger Water hydrographic properties and volume transports based on ARMOR3D compare with in-situ observations at eastern AR7W?**

   ARMOR3D realistically represents hydrographic properties in the upper 1,500 m of the water column at eastern AR7W and reproduces the key properties of IW (Figure 3.3, Figure 3.5, and Figure 3.6). The agreement with in-situ data is notably better during periods characterized by a considerable amount of profiling float and ship-based data.

2. **What is the seasonal and long-term variability of Irminger Water at eastern AR7W between 1993 and 2022?**

   IW is the warmest and most saline during fall and winter, accompanied by a maximum volume transport. It becomes coldest and least saline, accompanied by a minimum volume transport, during spring and early summer (Figure 3.8 and Figure 3.11). On multi-year time scales, the IW volume transport reaches its peak in 2010/2011 and reaches its minimum between 2019 and 2022 (Figure 3.13 and Figure 3.14).

3. **What causes Irminger Water temporal variability on different time scales at eastern AR7W?**

   Seasonal variability of the IW volume transport is primarily attributed to local cooling and winter convection in the Irminger and Labrador Seas. Consequently, high IW temperatures accompany high IW salinities and vice versa (Figure 3.8). Large-scale changes occurring in the North Atlantic influence the IW volume transport on multi-year time scales. These include changes in the NAO and the expansion and contraction of the SPG (Figure 3.12 and Figure 3.16). Lower IW temperatures coincide with high salinities (Figure 3.13). Therefore, I deduce that seasonal processes dominate the variability of IW temperature. In contrast, the underlying causes for seasonal and longer-term variability are different.

While this chapter uses static property thresholds for identifying IW and uISIW, other studies have demonstrated how water masses can alter their core properties over time,

driven by large-scale changes in the water column. For instance, Pickart et al. (2003b) and Yashayaev and Loder (2017) identified evolving core densities within the context of LSW. Specifically, LSW produced during the years 2012 to 2016 was observed to be warmer and more saline than LSW produced between 1987 and 1994 (Yashayaev & Loder, 2017). Similarly, a recent study by Le Bras et al. (2022) argued for defining ISIW differently due to the general freshening of the SPNA in recent years (Holliday et al., 2020; Biló et al., 2022). In light of these considerations, the forthcoming step in Chapter 4 involves analyzing such temporal shifts in IW core water mass properties across multi-year and seasonal time scales. This endeavor aims to enhance our comprehension of IW's distribution, from its origin in the Irminger Sea into Baffin Bay and the western Labrador Sea.

"Change is essential for growth. Just as the sun rises and sets, embracing change allows us to experience the full spectrum of life's possibilities."

Mufasa - The Lion King, 1994

Chapter 4

Irminger Water - Influences of large-scale ocean changes

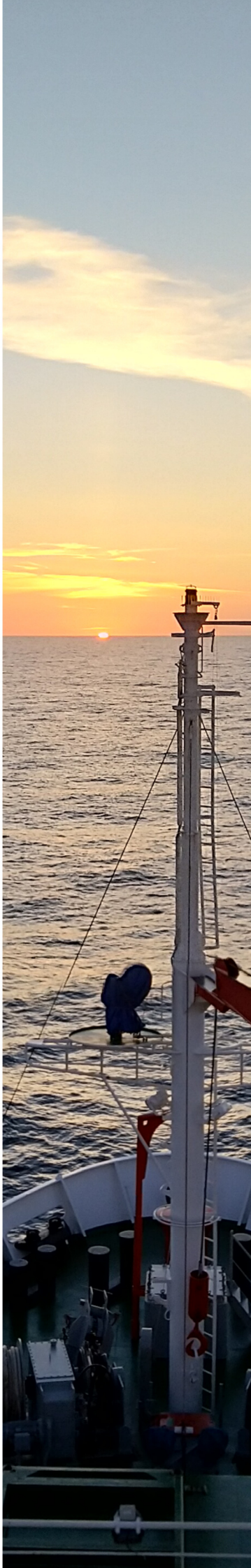

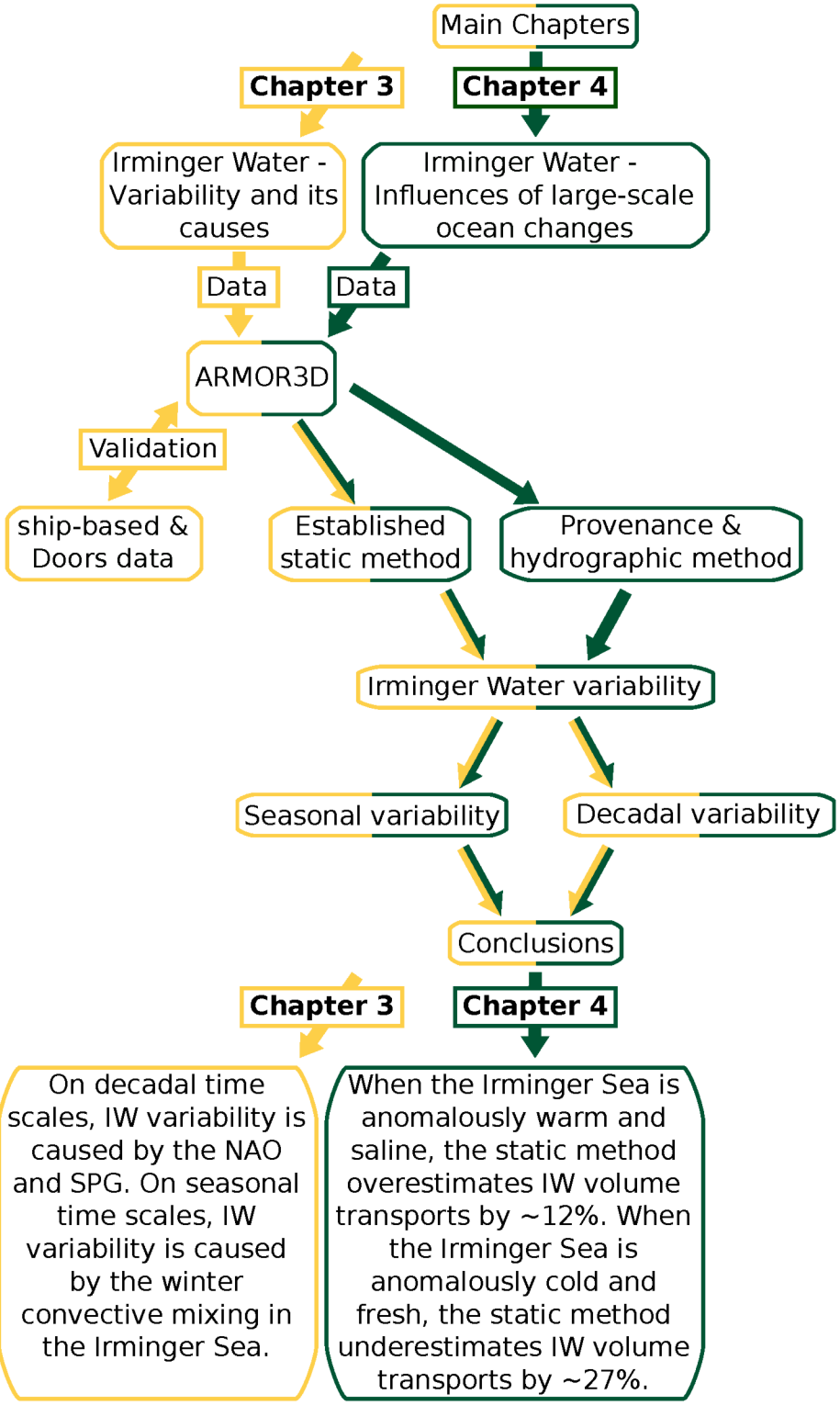

Figure 4.1: Graphical outline of Chapter 4. Content of Chapter 3 is highlighted in yellow, content of Chapter 4 in green. I add more details to the outline in Chapter 5. Eventually, it shows the connection within the main chapters. Following the green colors guides the reader through the present Chapter 4.

This chapter is currently in preparation for publication in the Journal of Geophysical Research: Oceans. The text has been partially adapted to fit the context of this thesis. I was responsible for the calculation, analyses, visualization and writing of the manuscript. Dagmar Kieke, Paul G. Myers, and Igor Yashayaev are co-authors and provided scientific input and helped to revise the text for publication.

4.1 Irminger Water in a changing boundary current system

In the present chapter, I build on Chapter 3 and include temporally and spatially changing IW thresholds when analyzing IW variability. Therefore, by analyzing four sections in detail, I enlarge the region of interest from Chapter 3 to the larger BCS domain. These sections are located in the Irminger Sea, the eastern Labrador Sea, the western Labrador Sea, and Baffin Bay. They are chosen as they represent the bandwidth of vertical variability in the water column within the BCS (Figure 4.2). I incorporate the mentioned large-scale temporal changes in the water column while describing the evolution of IW from the Irminger Sea downstream within the BCS. To analyze potential pathways of IW and investigate it at spatially fixed positions, I also consider spatial changes of IW properties as IW subsequently mixes with colder and fresher ambient waters on its pathway.

I focus on the following objectives in particular:

1. **How can the temporal variability within the water column be included when identifying Irminger Water and tracking its downstream fate?**
2. **How can waters maintaining vertical Irminger Water structures in regions where it is fully mixed below a certain threshold be identified?**
3. **What influences do long-term (temporal) and large-scale (spatial) variability in the water column have on the variability of Irminger Water properties?**

Chapter 4 is structured as follows: I introduce three different methods for identifying IW in Chapter 4.2. The first method represents the commonly used method to identify IW already applied in Chapter 3. In contrast, the following methods represent new approaches developed within this thesis. Chapter 4.3 analyzes IW variability at eastern

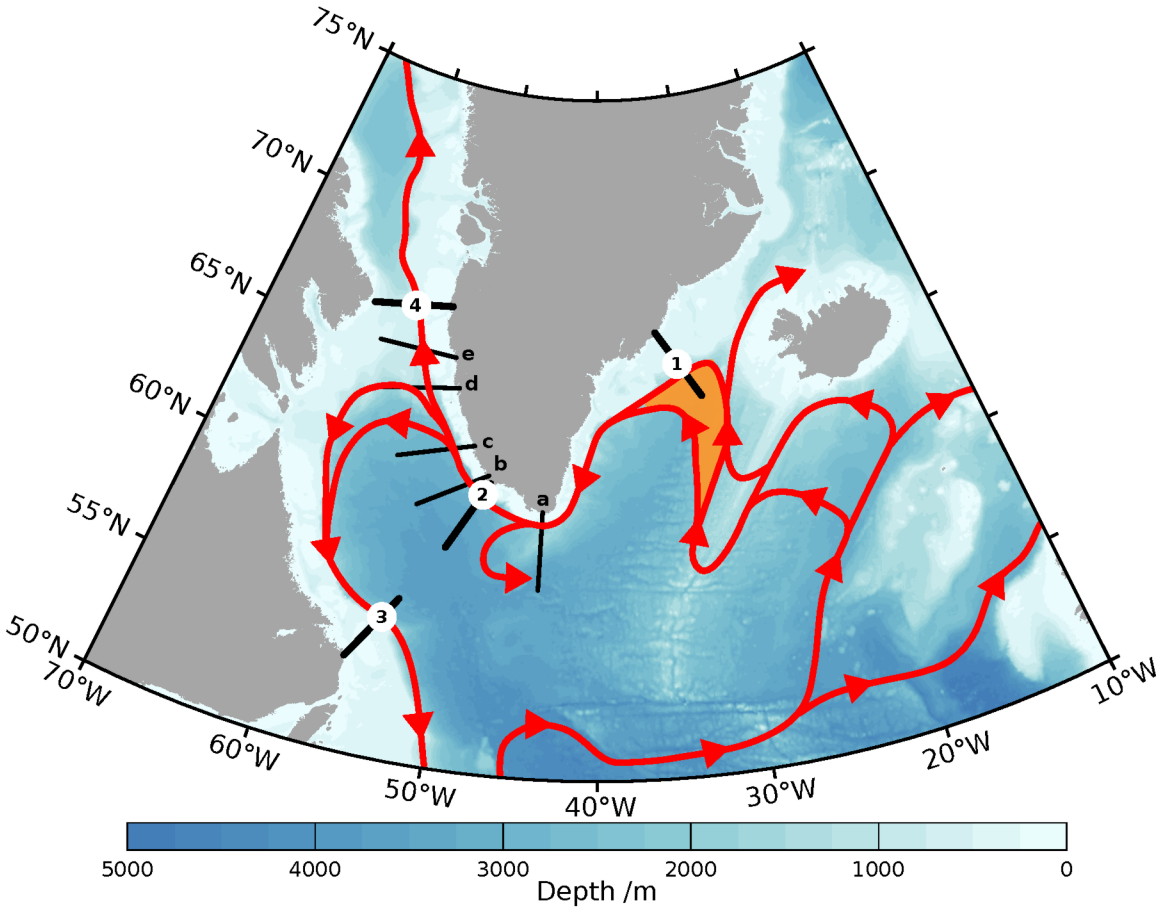

Figure 4.2: Map of the study region around southern Greenland, including the Irminger and Labrador Seas and parts of the Baffin Bay. Background colors denote bathymetry. Red lines represent idealized schematic Irminger Water pathways. Orange highlighted area in the Irminger Sea indicates the Irminger Sea provenance region (see Chapter 4.2.2). Thick black lines indicate the main sections analyzed in this chapter. White circles denote the positions of individually analyzed vertical profiles in Chapter 4.2.3 (1 - Sermiligaaq; 2 - Eastern AR7W; 3 - Western AR7W; 4 - Sisimiut). Thin black lines indicate sections this chapter refers to (a - Cape Farewell; b - Cape Desolation; c - Paamiut; d - Fylla Bank; e - Maniitsoq).

AR7W using these different methods. Chapter 4.4 analyzes the salinity distribution within IW and Chapter 4.5 investigates how the different methods affect the thickness of the identified IW in the SPNA. I close this chapter by summarizing the main results and drawing conclusions based on the findings (Chapter 4.6).

4.2 Identifying Irminger Water: How to?

At eastern AR7W, warm and saline waters occupy depths between ∼200 and 600 m (e.g., Figure 3.3 and Figure 3.14). In Chapter 3 (Table 3.1), static salinity and density thresholds were used to identify IW. This chapter presents different methods for identifying IW beyond the common approach of temporally and spatially static thresholds. These methods go beyond the approaches of Buch (2000), Buch et al. (2004), Myers et al. (2009), and Ribergaard (2014), defining two distinct states of IW. However, this chapter aims to analyze local IW based on changes in the water column at each time step within the ARMOR3D period between 1993 and 2022. Therefore, I analyze the seasonal and decadal variability of the hydrographic IW properties and its volume transport, following the methodology in Chapter 3, and compare differences between the individual methods. I explain the different methods and present the conventions I use throughout this thesis when referring to IW identified using the different methods.

4.2.1 Static method

The first method builds upon static hydrographic thresholds. Hence, this method is referred to as the "static method". IW obtained with the static method is referred to as IW_{stat}. The static method is commonly used to describe IW_{stat} within the BCS. Combined static thresholds of salinity, temperature, or density represent the boundary between IW_{stat} and ambient waters (see Table 4.1). For the static method, the same IW_{stat} thresholds as in Chapter 3 are applied (thresholds given in Table 4.2). These thresholds represent a density range and a lower salinity limit of IW_{stat}. Since IW_{stat} is the most saline water mass in the given density range, there is no upper limit for its salinity. The hypothesis is that such static thresholds do not adequately identify the magnitude of IW_{stat} at certain times since these thresholds do not account for shifts in the large-scale hydrographic state of the water column in the BCS.

4.2.2 Provenance method

The second method builds upon hydrographic properties in a subregion of the Irminger Sea, the provenance of IW. Hence, this method is referred to as the "provenance method". IW obtained with the provenance method is referred to as IW_{prov}. To consider the impact of the large-scale hydrographic state of the water column on changes

Table 4.1: Overview of Irminger Water thresholds based on various studies at different locations and times. Potential temperature θ, salinity S, and potential density σ_θ represent static thresholds used to identify Irminger Water. When two salinity or temperature criteria are listed, the higher values correspond to pure Irminger Water, and the lower values correspond to modified Irminger Water. Abbreviations: CF - Cape Farewell, CD - Cape Desolation, P - Paamiut, FB - Fylla Bank, M - Maniitsoq, S - Sisimiut

Reference	**Data type**	**Location**	**Time**	θ / °C	**S**	σ_θ / kg m^{-3}
Kiilerich (1943)	ship-based data	Southwest Greenland	1930s - 1940s	3.5 - 5.0	34.75 - 35.00	
Lee (1968)	ship-based data	East / West Greenland	1963	4.0 - 6.0	34.95 - 35.10	
Buch (2000)	ship-based data	CF, FB	1981 - 1997	> 4.5 4.0 - 4.5	> 34.95 34.88 - 34.95	
Cuny et al. (2002)	ship-based, float data	FB	1990 - 1999	> 4.5	> 34.95	
Stein (2004)	ship-based data	FB	1946 - 1999	4.0 - 6.0	34.95 - 35.10	
Myers et al. (2007)	ship-based data	CF, CD, P	1984 - 2005	> 3.5	> 34.88	
Myers et al. (2009)	ship-based data	CF, CD, P, FB, M, S	1955 - 2008	> 4.5 3.5 - 4.5	> 34.95 34.88 - 34.95	
Ribergaard (2014)	ship-based data	CF, CD, P, FB, M, S	1993 - 2013	> 4.5 3.5 - 4.5	> 34.95 34.88 - 34.95	
Rykova et al. (2015)	ship-based data	Eastern AR7W	1993 - 2006		> 34.40	
Pacini et al. (2020)	mooring data	Eastern OSNAP West	2014 - 2018		> 34.92	< 27.74
Chapter 3	ARMOR3D	Eastern AR7W	1993 - 2022		> 34.92	< 27.74

in IW_{prov}, this method identifies non-static thresholds that vary in time. Therefore, a region is first identified as a reference area to obtain information about the state of the water column. Since all of IW_{prov} propagates within the IC around the Irminger Sea, a particular subregion in the Irminger Sea that exhibits maximum salinities in the upper ocean, attributed to waters advected from the NAC (orange area in Fig-

ure 4.2), is identified. This region is referred to as the Irminger Sea provenance region. Within the Irminger Sea provenance region, the subsurface salinity maximum in the upper ocean is situated at a depth of ~ 200 m. It is found that maximum salinities of $S > 35$ correspond best with the pathway of the IC obtained from the ARMOR3D geostrophic velocities. Additionally, areas with a water depth < 2000 m are excluded to avoid incorporating dense overflow waters from the Denmark Strait. As the aim is to identify IW_{prov} based on temporal changes, spatial averaging is carried out over the Irminger Sea provenance region for each available time step individually. The average is first calculated over the region in density space and then converted back into pressure space. This averaging results in one spatially averaged vertical profile per time step. The warm and saline Atlantic-origin waters are confined to a depth of $\sim 1{,}000$ m (e.g., García-Ibáñez et al., 2015; Fried & de Jong, 2022). Therefore, a depth range between 100 and 1,000 m is chosen to represent waters of Atlantic-origin in the Irminger Sea provenance region without including influences from the surface. To provide a preliminary understanding of the IW hydrography in the Irminger Sea provenance region, properties of IW_{stat} obtained with the static method are presented as an average over the domain (Figure 4.3).

The IW_{stat} salinity in the Irminger Sea provenance region (Figure 4.3 a) reveals large decadal variability. The region was most saline between 2005 and 2011, which coincided with a period of reduced convection in the Labrador Sea, impacting the hydrography of the SPNA as a whole (e.g., Yashayaev & Loder, 2016). 2018 and 2019 were the freshest within the 30 years (2018 was also the coldest year since 1995), corresponding to the coldest and freshest intermediate layer in the Labrador Sea since 2002 (Yashayaev et

Table 4.2: Water mass criteria (thresholds) for Irminger Water at eastern AR7W based on the static (IW_{stat}), provenance (IW_{prov}), and hydrographic method (IW_{hydro}). The thresholds for IW_{prov} and IW_{hydro} are presented as a range, as they change in time.

	Min. Salinity	**Max. Pot. Dens. / kg m^{-3}**	**Min. Pot. Temp. / °C**	**Downstream Vel. / m s^{-1}**
IW_{stat}	34.92	27.74		> 0
IW_{prov}	~ 34.86 - ~ 34.96		~ 3.64 - ~ 4.40	> 0
IW_{hydro}	~ 34.68 - ~ 34.91		~ 1.22 - ~ 5.91	> 0

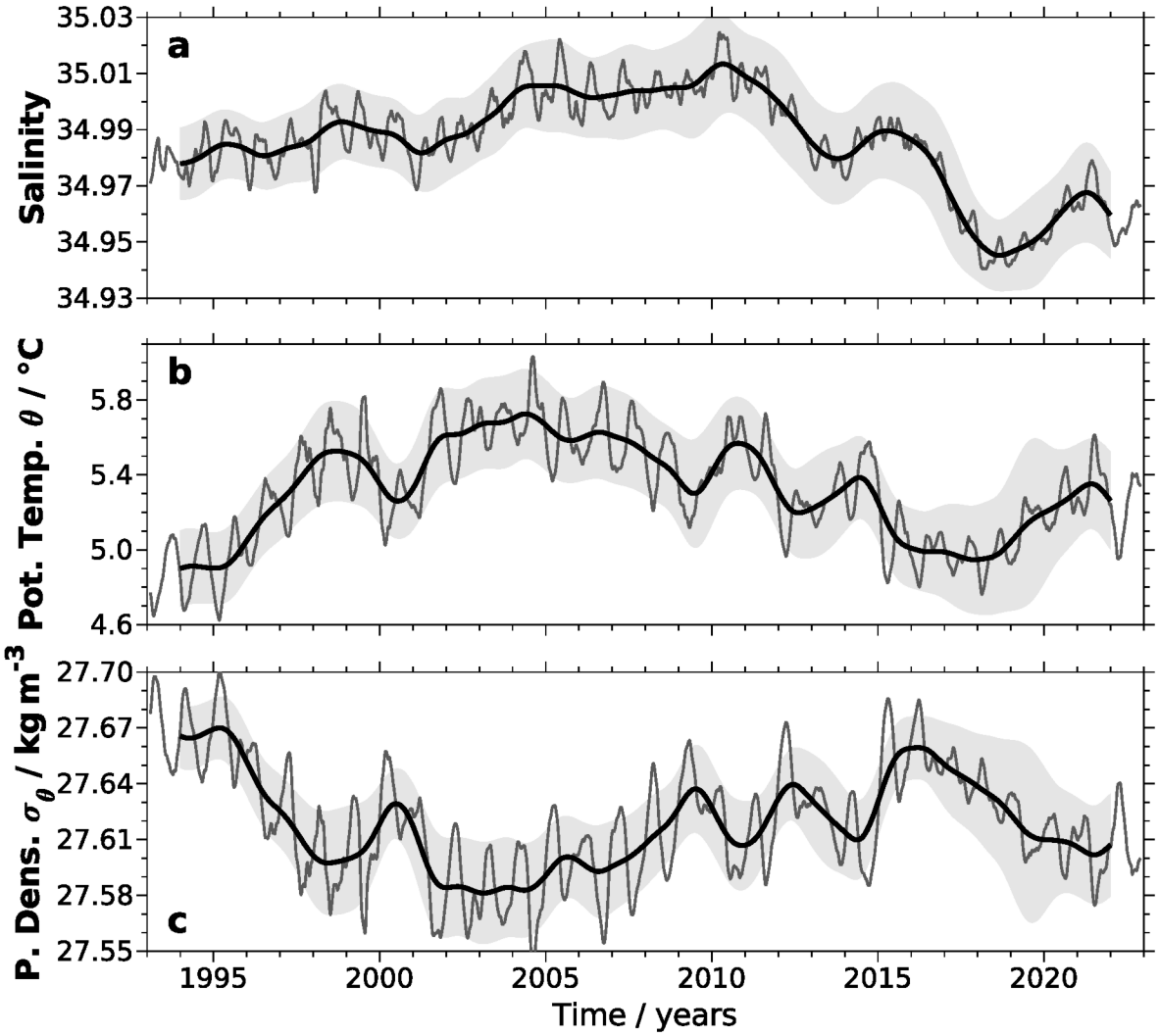

Figure 4.3: Irminger Water properties obtained with the static method in the Irminger Sea provenance region smoothed with a 2-year running average including a Hanning window (thick black line) and with a 10-week running average (thin gray line). Gray shaded background corresponds to the spatial standard deviation for the entire region (orange shade in Figure 4.2). Properties are salinity (a), potential temperature θ (b), potential density σ_θ (c).

al., 2022). The IW_{stat} temperature (Figure 4.3 b) indicates a decadal variability similar to that in the IW_{stat} salinity. However, the maximum occurred in 2004, followed by a minimum from 2016 to 2018. Changes in the IW density in the Irminger Sea provenance region (Figure 4.3 c) strongly mirror the inverted temperature (r = -0.92 [-0.93, -0.91] for the 2-year running averaged time series). The correlation between the IW_{stat} density and salinity is also significant (r = -0.28 [-0.33, -0.23] for the 2-year running averaged time series), although not as strong as the correlation between density and temperature. When comparing the IW_{stat} properties in the Irminger Sea provenance region with those

from eastern AR7W following Chapter 3, the time series exhibit significant correlation (salinity: r = 0.85 [0.83, 0.86], temperature: r = 0.58 [0.53, 0.62], density: r = 0.68 [0.65, 0.71]), when the time lag between the two regions is considered (see Figure 4.4). These results suggest that the chosen Irminger Sea provenance region effectively represents the primary pathway of IW within the IC in ARMOR3D.

For the provenance method, it is assumed that the minimum temperature and salinity of the spatially averaged Irminger Sea provenance region between 100 and 1,000 m represent the cold and fresh limits of IW, thus serving as the lower IW thresholds for each time step individually. Like the static method, upper thresholds are not defined, as IW_{prov} encompasses the most saline waters accompanied by the highest temperatures. To extend the IW_{prov} thresholds from the Irminger Sea provenance region to the cross-slope sections within the BCS, the IW_{prov} thresholds are temporally adjusted based on the advection time between the Irminger Sea provenance region and the individual cross-slope sections (Figure 4.4). This adjustment is achieved by assuming a constant velocity within the BCS. Subsequently, lag correlations are calculated between the IW_{stat} salinity in the Irminger Sea provenance region (Figure 4.4) and the IW_{stat} salinity at the individual sections (all used sections are presented in Figure 5.2 and Table 5.1), following Chapter 3. The lag corresponding to the highest correlation determines the advection time.

In total, 25 cross-slope sections are included, primarily representing sections from previous measurement campaigns (e.g., Myers et al., 2007, 2009; Ribergaard, 2014). Additional sections were added to cover the entire BCS, spanning from its northernmost location in the Irminger Sea to 75°N in Baffin Bay and 52°N on the Labrador continental slope (a comprehensive description of the cross-slope section array is given in Chapter 5.1, see Figure 5.2). Correlations exhibit a sharp decrease downstream of Paamiut. Paamiut is the last section before the bifurcation of the BCS into the Baffin Bay and Labrador Sea branches. Downstream of Paamiut, IW_{stat} becomes seasonally mixed below the IW_{stat} salinity threshold, which could contribute to the reduced correlation. Furthermore, the calculated advection times display larger deviations from the previous linear behavior. Consequently, calculating a linear regression is restricted to sections from Sermiligaaq toward Paamiut. Within this range, one profile falls outside of the one-sided 1 % confidence interval. Therefore, it is not considered for the final calculation of the linear fit.

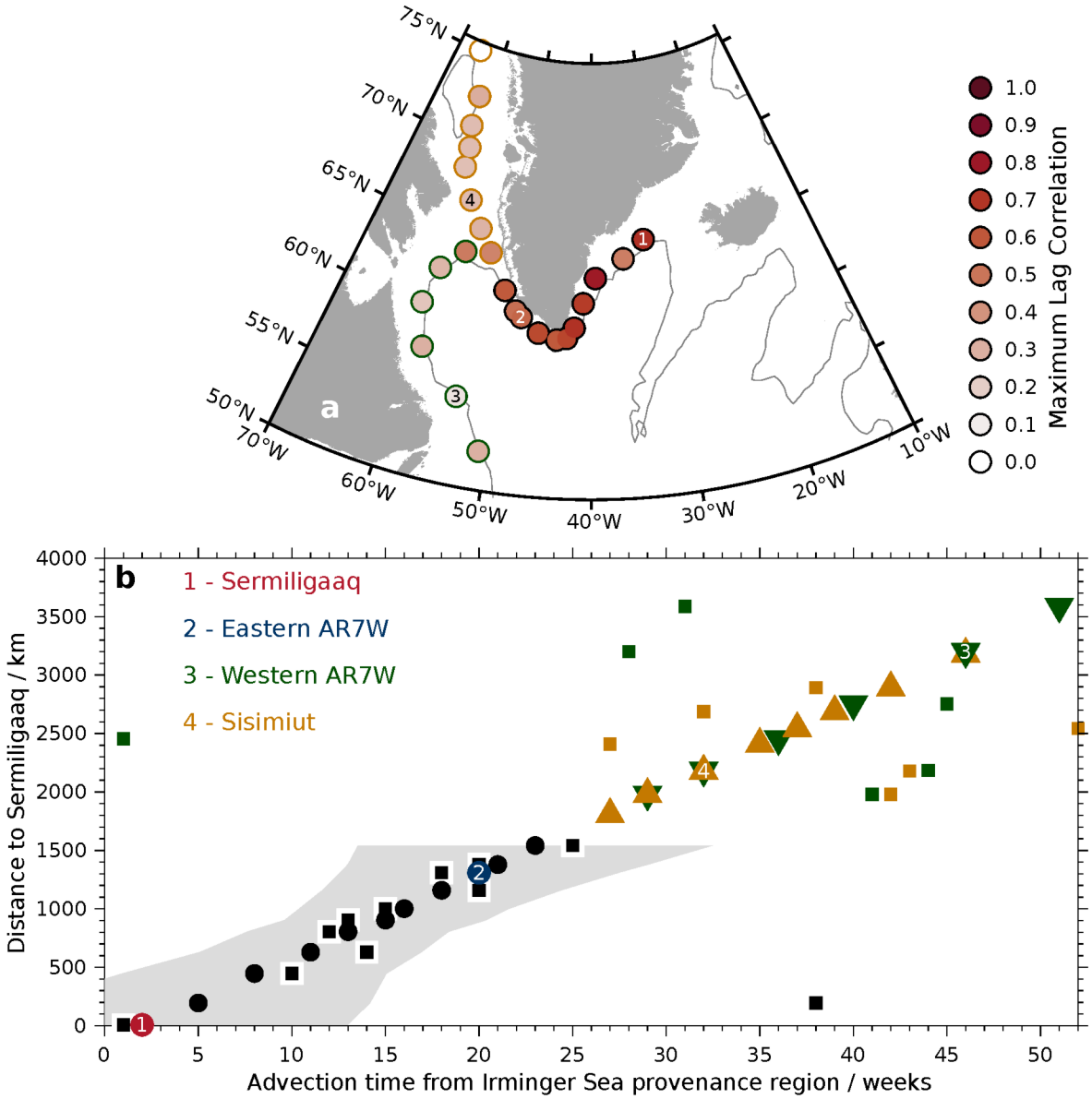

Figure 4.4: (a) Circles indicate locations of the Irminger Water core at individual sections (Irminger Sea to Paamiut: black, Paamiut to Baffin Bay: orange, and Paamiut to Labrador Sea: green). The circle's filling represents the maximum lag correlation between the static Irminger Water salinity in the Irminger Sea provenance region and the respective section. Gray lines follow the smoothed 2,000 m isobath. (b) Downstream advection time of Irminger Water with increasing distance from Sermiligaaq (Figure 4.2). Squares represent originally calculated advection times, circles and triangles the advection times after applying a linear regression (Irminger Sea to Paamiut: black, Paamiut to Baffin Bay: orange, and Paamiut to Labrador Sea: green). A linear fit is limited from Sermiligaaq to Paamiut; times further downstream have been linearly extrapolated. Gray shading highlights confidence intervals at a 1 % significance level. Numbered circles represent the four sections that are analyzed in detail within this chapter (see Chapter 4.2.3.1).

By linearly extrapolating the advection times into the two downstream branches, advection times between the Irminger Sea provenance region and Baffin Bay (75 °N) are estimated to be 51 weeks and between the Irminger Sea provenance region and the southwestern Labrador Sea ($\sim$52.3 °N; $\sim$50.8 °W) are estimated to be 46 weeks. These advection times correspond to an average IW velocity of $\sim 0.11\,\mathrm{m\,s^{-1}}$ in the BCS. Generally, these calculated advection times are consistent with observations by Grist et al. (2014). Utilizing the ORCA12 data set, they found advection times of about three to four months within the WGC between Cape Desolation and Aasiaat by tracking the maximum temperature signal. ARMOR3D indicates an advection time of 15 weeks between these two sections after applying the linear regression.

By adjusting the $\mathrm{IW_{prov}}$ thresholds from the Irminger Sea provenance region based on the advection time at the individual sections, simultaneous thresholds are derived along the BCS pathway. However, these thresholds still rely on the local hydrography in the Irminger Sea provenance region. In regions further downstream, warm and saline waters might still mix below these thresholds, despite the water column resembling typical IW characteristics. To address this problem, a third method is developed.

4.2.3 Hydrographic method

The third method builds upon the local hydrographic properties: temperature and salinity. Hence, this method is referred to as the "hydrographic method". IW obtained with the hydrographic method is referred to as $\mathrm{IW_{hydro}}$. The static and provenance methods fail to identify the respective IW in regions where all waters are mixed below the corresponding thresholds. However, the vertical structure of the water column in these regions still suggests the presence of waters originating from the Irminger Sea, as evidenced by the simultaneous subsurface maximum temperature and salinity characteristics. Therefore, the hydrographic method aims to identify these distinct warm and saline waters, which are remnants of IW, even when they are mixed below the $\mathrm{IW_{stat}}$ and $\mathrm{IW_{prov}}$ thresholds. Consequently, $\mathrm{IW_{hydro}}$ contains waters that have been identified as $\mathrm{IW_{stat}}$ or $\mathrm{IW_{prov}}$ in upstream regions but are now mixed with colder and fresher waters. As a result, $\mathrm{IW_{hydro}}$ is not interpreted as a distinct water mass but rather as a layer preserving the structural characteristics of IW. Therefore, the objective is not to compare magnitudes of, for example, the $\mathrm{IW_{hydro}}$ volume transport but to analyze its variability and trends within the resulting time series.

4.2.3.1 From local hydrography to Irminger Water thresholds

As mentioned earlier, the hydrographic method identifies waters exhibiting a simultaneous subsurface temperature and salinity maximum. IW_{hydro} is identified by establishing temperature and salinity thresholds based on percentiles for the SPNA region, including the Irminger Sea, the Labrador Sea, and parts of Baffin Bay. The percentiles for temperature and salinity thresholds are derived from the analysis within the IW core (see Chapter 3.3.2) at four cross-slope sections (see Figure 4.2) that display distinct water column structures within the BCS. These four sections have been selected to represent a comprehensive range of variability in the BCS.

The sections include Sermiligaaq in the Irminger Sea, eastern AR7W in the eastern Labrador Sea, western AR7W in the western Labrador Sea, and Sisimiut in Baffin Bay. Afterward, the determined percentiles are applied to the SPNA domain. In the following, the detailed steps for identifying IW_{hydro} are outlined in detail:

1. Temperature and salinity profiles are extracted at Sermiligaaq, eastern AR7W, western AR7W, and Sisimiut within the IW core. Individual grid points at these sections, along with their nearest neighbors, are selected, resulting in an averaged profile over 3×3 grid points (Figure 4.2 indicates the location of the averaged profiles, while Figure 4.5 displays the profiles).

2. Since IW is confined to the upper 1,000 m (García-Ibáñez et al., 2015; Fried & de Jong, 2022, Chapter 3), the respective ranges from minimum to maximum values for each parameter X are calculated within the upper 1,000 m: $X_{range} = X_{max} - X_{min}$, where X represents either salinity S or temperature T. Recognizing that seasonal effects such as surface warming during summer impact the temperature close to the surface and consequently influence this range, the upper 100 m are excluded when determining T_{range}. Similar effects for salinity have been tested but are negligible. This approach ensures that only seasonal variability within the IW is considered.

3. Since I aim to determine percentiles for use in the BCS, spanning from the Irminger Sea into Baffin Bay and the western Labrador Sea, I encounter water columns with highly diverse structures. In the Irminger Sea, the salinity range is relatively small, on the order of $\mathcal{O}(0.1)$. In contrast, in Baffin Bay, it

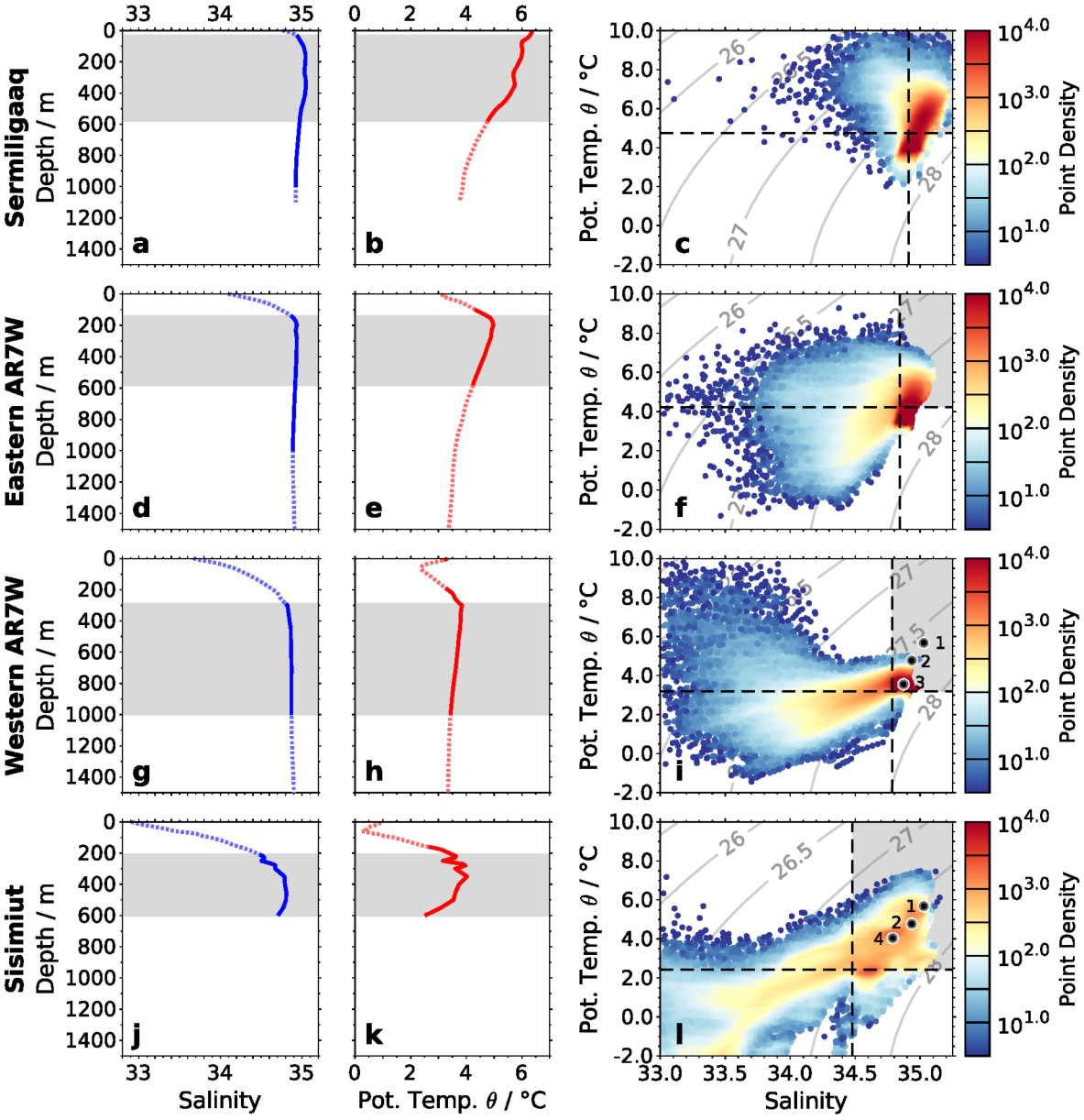

Figure 4.5: Salinity (left column) and temperature profiles (middle column) at four different cross-slope sections within the core of the BCS (circles in Figure 4.2), averaged from 1993 - 2022 as dashed colored lines. Sections from top to bottom: Sermiligaaq, eastern AR7W, western AR7W, Sisimiut. Overlaid solid lines denote the same profiles with identified IW_{hydro} for the respective parameter. The gray background highlights the depth range of the finally identified IW_{hydro}. Right column: T-S diagrams for the specific regions for the entire period with vertical resolutions of 10 m. Isotherm and isohalines represent respective local IW_{hydro} thresholds. Marker colors show point densities as natural logarithmic distributions. The point density represents the number of points within a box spanning 0.1 °C in temperature and 0.1 in salinity. Gray-scaled markers indicate the T-S path or modification trajectory of IW_{hydro} following the illustration in Yashayaev and Seidov (2015a, their Figure 16)

is larger by one magnitude, on the order of $\mathcal{O}(1.0)$. The full range falls between these regions in the Labrador Sea, depending on whether the analysis pertains to the eastern (smaller range) or western Labrador Sea (larger range). I incorporate weighting factors into the determined ranges to calculate the thresholds for these distinct ranges. The equations used to derive the thresholds are as follows:

$$\text{if } X_{range} < 1\text{: } X_{threshold} = X_{min} + p_X \cdot {X_{range}}^{e_{X_{range}<1}} \text{ and}$$

$$\text{if } X_{range} \geq 1\text{: } X_{threshold} = X_{min} + p_X \cdot {X_{range}}^{e_{X_{range}\geq 1}},$$

with the percentile p_X corresponding to parameter X and the weighting exponent e. As p_X, $e_{X_{range}<1}$, and $e_{X_{range}\geq 1}$ are unknown, exponents and percentiles for temperature and salinity are empirically determined. This yields the calculation of $\mathrm{IW_{hydro}}$:

$$\text{if } X_{range} < 1\text{: } X_{threshold} = X_{min} + p_x \cdot {X_{range}}^{1.5} \text{ and}$$

$$\text{if } X_{range} \geq 1\text{: } X_{threshold} = X_{min} + p_x \cdot {X_{range}}^{0.75}.$$

The percentiles of $p_S = 0.97$ for salinity and $\mathrm{p}_T = 0.50$ for temperature are empirically obtained through the analysis of the four regions. These percentiles are used to calculate the lower thresholds for $\mathrm{IW_{hydro}}$. Like the static and provenance methods, upper thresholds are not defined for $\mathrm{IW_{hydro}}$, as it encompasses the most saline waters when accompanied by the highest temperatures. As $\mathrm{IW_{hydro}}$ incorporates both IW and colder, fresher ambient waters, it is not considered a distinct water mass but a layer characterized by simultaneous subsurface temperature and salinity maxima.

Sermiligaaq

At Sermiligaaq (Figure 4.5 a - c), the water column between $\sim$20 m and 600 m comprises warm ($\mathrm{T} > 4.8\,^{\circ}\mathrm{C}$) and saline ($\mathrm{S} > 34.95$) waters. In this location, the salinity threshold identifies $\mathrm{IW_{hydro}}$ down to a maximum depth of 1,000 m (as defined for $\mathrm{IW_{hydro}}$). However, the temperature criterion only identifies $\mathrm{IW_{hydro}}$ in the upper 600 m, thus determining the maximal depth of $\mathrm{IW_{hydro}}$.

Eastern AR7W

Further downstream at eastern AR7W, $\mathrm{IW_{hydro}}$ is identified in the depth range of 150 to 650 m (Figure 4.5 d - f). Like Sermiligaaq, the salinity threshold alone identifies $\mathrm{IW_{hydro}}$

down to a depth of 1,000 m. However, the temperature threshold identifies IW_{hydro} between 150 and 600 m. When comparing the T-S diagram at eastern AR7W (Figure 4.5 f), which includes all time steps within the years 1993 to 2022 climatology to the T-S diagram from Sermiligaaq (Figure 4.5 c), an expected cooling and freshening between these two sections is observed.

Western AR7W

At western AR7W (Figure 4.5 g - i), similar to the profiles analyzed earlier, the upper limit of the IW_{hydro} is defined by salinity, while the lower limit is determined by temperature.

Sisimiut

At Sisimiut (Figure 4.5 j - l), water between 200 and 550 m is identified as IW_{hydro}. The profile suggests that the characteristic structure of IW is preserved despite the maximum salinity being mixed below the static threshold of $S = 34.92$ ($S_{max} \approx 34.80$). The simultaneous subsurface temperature and salinity maximum, which is characteristic for IW (e.g., Myers et al., 2007; Pacini et al., 2020, Chapter 3), is situated at a depth between $\sim$300 and 400 m. Consequently, it can be inferred that substantial portions of the water column at Sisimiut either originate in the Irminger Sea or have been into contact with IW previously.

Yashayaev and Seidov (2015a) presented a similar modification and transformation utilizing T-S properties to analyze the fate of warm and saline Atlantic Water along the Norwegian Coast. They introduced a T-S path, also referred to as transformation trajectory, within their T-S diagrams, which illustrates the rate of cooling and freshening of Atlantic Water. I have incorporated a similar illustration into Figure 4.5, where the points corresponding to the individual profiles result from averaging over all data points identified as IW_{hydro}. This way, I demonstrate the modification of IW_{hydro} into a colder and fresher state along its downstream pathway within the BCS.

4.2.3.2 Where can hydrographic Irminger Water be identified?

The hydrographic method is designed to identify IW_{hydro} within the BCS of Greenland and Labrador. However, since the hydrographic method is applied to individual grid points in ARMOR3D, it enables the analysis of IW_{hydro} across the entire chosen domain of the SPNA. Therefore, I test whether the method is confined solely to the BCS or if it can also successfully identify IW_{hydro} in the interior Irminger and Labrador Basins and even further upstream within the NAC.

Similar to the provenance method, I utilize the weekly temporal resolution of ARMOR3D and apply the method for each time step individually to capture temporal variability within the water column. The analysis of IW_{stat} variability between 1993 and 2022 (Chapter 3) revealed that IW_{stat} volume transports at eastern AR7W exhibited a maximum in 2010 and a minimum in 2019. In order to gain an understanding of the large-scale conditions of the SPNA during these years, I examine the newly calculated IW_{hydro} salinity (Figure 4.6 a, b) and temperature (Figure 4.6 d, e) thresholds for the yearly averages of 2010 and 2019, respectively. Furthermore, I present the differences between the two years (Figure 4.6 c, f). Additionally, I analyze the resulting IW_{hydro} layer thickness for the respective years, as well as their differences (Figure 4.6 g - i).

As expected, the pattern of the IW_{hydro} temperature and salinity thresholds closely approximate the warm and saline ocean currents. The highest values are evident within the primary paths of the NAC and IC. Additionally, high values occur in the shallow areas in the eastern SPNA. In this region, T_{range} is smaller than the basin interior due to the typical decrease in temperature with depth, resulting in higher IW_{hydro} temperature thresholds in the shallow regions. Higher values extend into the Irminger Sea and the EGC along the onshore side of the 2,000 m isobath. Further downstream, as the WGC curves around the Labrador Sea, the temperature thresholds exhibit higher values along the 2,000 m isobath (Figure 4.6 d, e). In Baffin Bay, higher salinity thresholds are identified, filling the deeper troughs in the Greenland shelf (Figure 4.6 a, b). This characteristic indicates that IW_{hydro} is being advected within these channels and that the hydrographic method can effectively identify these waters. Along these pathways, the thresholds decrease as the warm and saline Atlantic-origin waters mix with ambient waters. This process was described by Buch (2000), Buch et al. (2004), Myers et al.

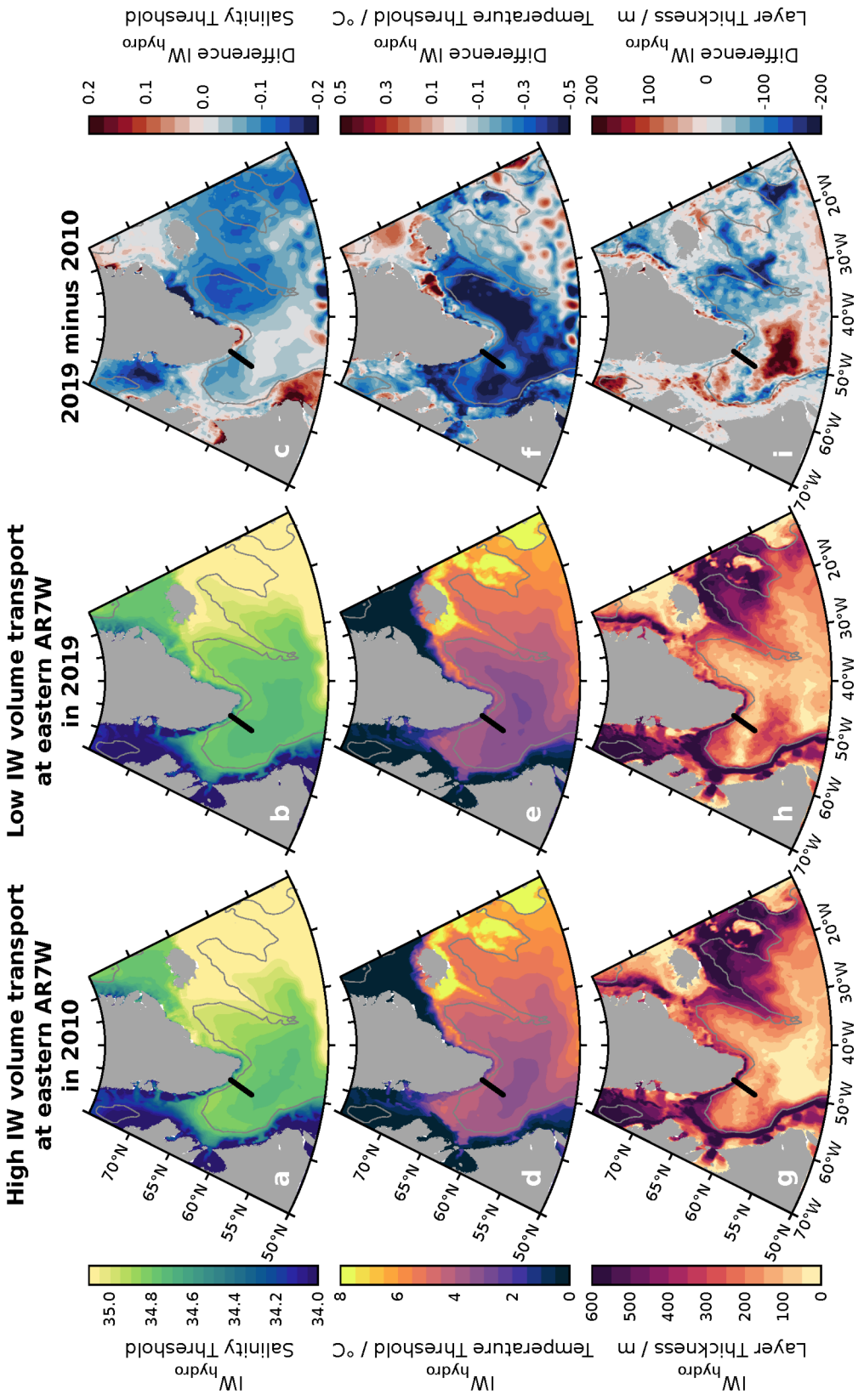

Figure 4.6: Yearly averaged hydrographic salinity (upper row), temperature thresholds (middle row), and IW_{hydro} layer thickness (lower row) in 2010 (left column) and 2019 (middle column) and their difference (2019 minus 2010, right column). Gray lines follow the smoothed 2,000 m isobath. The black line represents eastern AR7W.

(2009), and Ribergaard (2014). The reduction in IW_{hydro} thresholds along the main pathway within the BCS highlights the effectiveness of the hydrographic method. As the previously pure IW becomes mixed, the thresholds decrease, ensuring the ability to identify these now colder and fresher waters as remnants of the original pure water mass.

The layer thickness provides insight into the spatial distribution of IW_{hydro} within the SPNA. Once again, larger quantities of IW_{hydro} are identified in regions such as the BCS, Baffin Bay, the Labrador continental slope, along the Reykjanes Ridge, and in the eastern SPNA, where the NAC extends further eastward (compare to Figure 4.2). However, IW_{hydro} layer thicknesses are relatively small within the primary NAC pathway further upstream. Examination of individual profiles in the central SPNA along 52°N indicates a rapid temperature decrease within the upper 400 m. In this region, the hydrographic method identifies IW_{hydro} only at depths between 100 and 250 m. Moving downstream into the eastern SPNA, individual profiles reveal a more gradual temperature decrease with depth. Consequently, IW_{hydro} is identified within the upper 600 m in this region.

Initially, the IW_{hydro} temperature and salinity thresholds, as well as the IW_{hydro} layer thickness appear similar in 2010 and 2019. However, substantial differences emerge after calculating the differences between the two years (Figure 4.6, right column). Across the entire SPNA (excluding shelf areas), lower IW_{hydro} salinity ($\Delta S \sim 0.2$) and temperature ($\Delta T \sim 0.5$) thresholds are observed in 2019 compared to 2010. These lower thresholds likely result from the general freshening of the SPNA during the 2010s (Holliday et al., 2020), which reached the Irminger Sea by 2018 (Biló et al., 2022; Fried & de Jong, 2022). However, differences in the IW_{hydro} layer thickness remain relatively small in regions where the thresholds reveal larger differences.

The reasons for the lower thresholds align with the findings of Buch et al. (2004), who proposed that transitions between dominant pure or modified IW are influenced by large-scale changes in the water column that affect the entire SPNA. Notably, the largest differences in the IW_{hydro} layer thickness are concentrated in the characteristic convection region of the Labrador Sea (e.g., Pickart et al., 2003a; Våge et al., 2008a). In this region, the IW_{hydro} layer thickness is larger by up to > 200 m in the yearly average of 2019 compared to 2010. In 2019, there was a pronounced formation of LSW as opposed to 2010 (Yashayaev et al., 2022). An evaluation of the MLD provided

within ARMOR3D indicates that the MLD in 2019 was deeper by $\sim$200 m in the above-mentioned convection region in the Labrador Sea compared to 2010. This result offers additional insights into the mechanisms of the hydrographic method in identifying remnants of IW, particularly when mixed with ambient waters. In the deep convection region, where warm and saline waters mix over greater depths, the method successfully identifies IW_{hydro} within this expanded depth range.

Analyzing IW_{hydro} thresholds and their resulting layer thicknesses in the SPNA reveals that this method should not be used upstream from the IC. Within the main pathway of the NAC, the hydrographic method does not identify the entire warm and saline Atlantic-origin waters. Only in the eastern North Atlantic, specifically in the Iceland Basin, the water column exhibits a similar structure regarding vertical temperature and salinity gradients, and, thus, enlarged IW_{hydro} layer thicknesses are identified. This body of identified IW_{hydro} can be compared with the subpolar mode water (e.g., Brambilla & Talley, 2008; Brambilla et al., 2008b; Stendardo et al., in revision). Therefore, I posit that the hydrographic method for identifying IW_{hydro} can also be used to identify waters characterized by similar vertical structures in the water column, as seen for subpolar mode water. The analysis also reveals that IW_{hydro} is identified in the interior Irminger and Labrador Seas. The variability between the two years resembles changes in the MLD due to convection.

4.2.4 Variability of the obtained Irminger Water salinity thresholds

The water column in the BCS experiences substantial variability across different time scales. To illustrate this variability and demonstrate how the provenance and hydrographic methods account for it when identifying IW, I present both seasonal (Figure 4.7) and decadal variability (Figure 4.8) of the obtained salinity threshold. These changes are highlighted for the four sections (see Figure 4.2) that have been utilized to derive the percentiles for the hydrographic method (Chapter 4.2.3.1). Since the thresholds for the provenance method are derived in the Irminger Sea provenance region and are merely temporally adjusted based on the advection time between the Irminger Sea provenance region and the respective section in the BCS, the variability remains consistent across all analyzed sections. In regions with seasonal sea ice cover, the salinity thresholds derived using the hydrographic method agree with the local sea ice concentration from the National Snow and Ice Data Center (DiGirolamo et al., 2022).

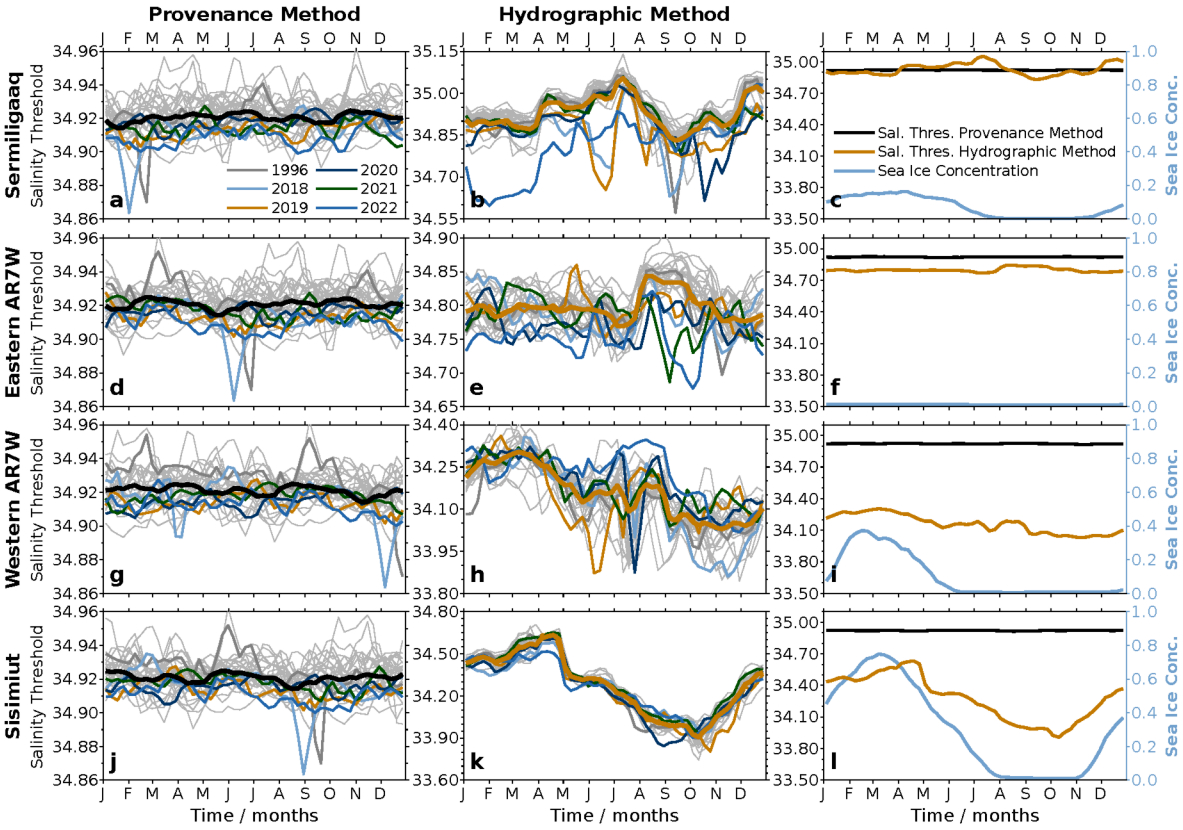

Figure 4.7: Seasonal salinity thresholds at different sections for the provenance (left column, black) and hydrographic method (middle column, orange) climatologically averaged between 1993 and 2022. Individual years in thin gray lines, some are highlighted in colors. The right column repeats the climatological results from both methods using the same y-axis. Sea ice concentrations from the National Snow and Ice Data Center in blue (DiGirolamo et al., 2022). Rows indicate the spatial averages for individual sections (top to bottom: Sermiligaaq, eastern AR7W, western AR7W, Sisimiut).

Seasonal variability

As detailed in Chapter 4.2.2, I have calculated the advection time between the Irminger Sea provenance region and the respective cross-slope sections based on the lag correlation of the IW_{stat} salinity (Figure 4.4). Comparing the climatological thresholds for the provenance method at the four main sections reveals the advection times between these sections by comparing shifts within the climatologies (Figure 4.7, left column). IW_{prov} requires four months to propagate from Sermiligaaq (Figure 4.7 a) to eastern AR7W (Figure 4.7 d). After six months, it reaches western AR7W (Figure 4.7 g). Similarly, the advection time between eastern AR7W and Sisimiut (Figure 4.7 j) is approximately three months.

The salinity thresholds for the provenance method exhibit only small seasonal variability (Figure 4.7, left column). 1996 and 2018 stand out; during these years, anomalously low salinity thresholds occurred at Sermiligaaq in winter (Figure 4.7 a). These periods of low thresholds are short-lived, lasting only two to three weeks. Based on the advection time between the sections, these instances of low salinity thresholds reached eastern AR7W in early summer (Figure 4.7 d), western AR7W in winter (Figure 4.7 g) and Sisimiut in late summer and early fall (Figure 4.7 j).

When averaging across all years, the salinity threshold at eastern AR7W still indicates its lowest values in spring and its highest values in fall. This pattern of low salinity thresholds at eastern AR7W corresponds to the arrival of uISIW, which forms through air-sea interaction in the Irminger Sea during winter (Le Bras et al., 2020, Chapter 3). Analysis of output from an Earth System Model with a 5 km horizontal resolution by Gutjahr et al. (2022) revealed that katabatic storms contribute to the formation of uISIW along the boundary current and on the southeast Greenland shelf.

By comparing the seasonal evolution of salinity thresholds for the provenance method and the hydrographic method, it becomes evident that the latter exhibits a generally larger amplitude (Figure 4.7, right column). Given that the hydrographic method includes not only pure IW but also ambient waters, I anticipate larger influences on the amplitude of the salinity threshold. Consequently, the hydrographic method demonstrates stronger seasonal variability in the salinity thresholds than the provenance method.

Furthermore, variations in salinity thresholds are apparent within the individual sections. At Sermiligaaq, biannual variability reveals high salinity thresholds > 35.0 in July and December, along with a low salinity threshold < 34.85 in September (Figure 4.7 b). At eastern AR7W, the seasonal salinity threshold signal aligns with the IW salinity identified using the static method at the same location, as demonstrated in Chapter 3. Here, a minimum in July is followed by a rapid increase to a maximum in August (Figure 4.7 e). 2021 and 2022 stand out with anomalously low salinity thresholds in September and October. These two years warrant further attention, particularly because September and October typically represent the highest annual values in the climatology.

Further investigation reveals that these anomalies of low salinities at eastern AR7W in 2021 and 2022 can be attributed to unusually substantial amounts of cold and fresh surface waters or an exceptionally strong displacement of these waters from the shelf further offshore. Additionally, the entire southeast and southwest Greenland shelves exhibit minimal values for the salinity thresholds during the falls of 2021 and 2022 (not shown). The primary source of fresher waters in these areas are the cold and fresh surface waters originating from Arctic runoff and east Greenland melting glaciers (Rysgaard et al., 2020). Dukhovskoy et al. (2019) presents annual Greenland freshwater fluxes from (Bamber et al., 2018), indicating that the peak seasonal melting of the Greenland Ice Sheet takes place in July. A similar timing of maximum melting was noted for the region spanning from Fylla Bank to Disko Bay (van den Broeke et al., 2011). Thus, I posit that the anomalies observed at eastern AR7W in 2021 and 2022 stem from anomalously large amounts of these cold and fresh surface waters and an exceptionally pronounced displacement of these waters from the shelf to areas farther offshore.

Exploring the impact of seasonal sea ice on the salinity thresholds reveals that the salinity threshold at western AR7W corresponds closely to the local sea ice concentration from the National Snow and Ice Data Center (Figure 4.7 h, i). A maximum salinity threshold is observed in February and March, while a minimum occurs in October and November, aligning with the period of highest sea ice concentrations, which can reach up to 0.4 in February. Similarly, Sisimiut displays distinct variability in the seasonal salinity threshold (Figure 4.7 k, l). A maximum in April is followed by a minimum spanning from August to October. Like at western AR7W, the seasonal cycle at Sisimiut mirrors the local sea ice concentration. Notably, Sisimiut remains free of sea ice between August and October, while the sea ice concentration peaks at 0.7 in March. Consequently, especially at Sisimiut, the salinity threshold is primarily influenced by the sea ice formation and melting, resulting in salt accumulation due to brine rejection and freshwater input. It is worth reiterating that ARMOR3D's accuracy and precision experience larger errors and uncertainties in the presence of sea ice.

Decadal variability

The decadal variability of the salinity thresholds obtained with the provenance method (Figure 4.8, left column) follows the variability of the IW_{stat} salinity at eastern AR7W

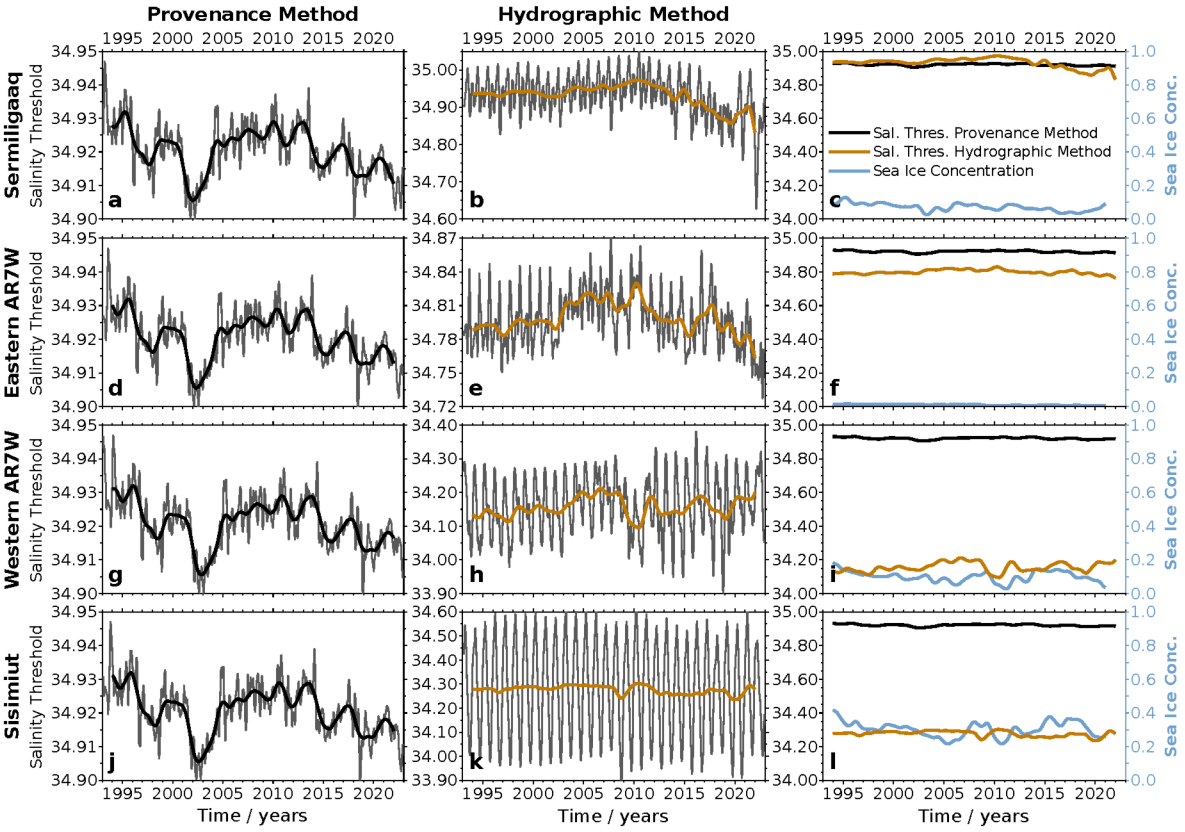

Figure 4.8: Salinity thresholds at different sections for the provenance (left column, black) and hydrographic method (middle column, orange) between 1993 and 2022. The thin gray line represents a 10-week running average, thick black and orange lines a 2-year running average, including a Hanning window. Note that the time series of the provenance method origins in the Irminger Sea provenance region that are shifted according to the different advection times. The right column repeats both methods using the same y-axis. 2-year running averaged (including Hanning window) sea ice concentrations from the National Snow and Ice Data Center in blue (DiGirolamo et al., 2022). Rows indicate the spatial averages for individual sections (top to bottom: Sermiligaaq, eastern AR7W, western AR7W, Sisimiut).

(Chapter 3) and in the Irminger Sea provenance region (Figure 4.3 a). The only major differences are the maximum salinity thresholds in the 1990s, followed by a minimum in the early 2000s. During these times, the Irminger Sea provenance region salinities are at a medium level. In contrast, from 2018 to 2019, when the salinities in the Irminger Sea provenance region were minimal, the IW_{prov} salinity thresholds were low but still higher compared to the early 2000s. The difference between these periods, the early 2000s and from 2018 to 2019, is that in the latter, the effects of the overall freshening of the SPNA (e.g., Holliday et al., 2020; Biló et al., 2022) had their largest imprint for smaller depths. Thus, these years represented the freshest within a depth range

from 100 to 500 m (not shown), while the early 2000s represented the freshest years at a depth of 1,000 m (not shown), which represented the freshest limit of IW and hence determined its salinity threshold.

Averaging the salinity thresholds obtained with the provenance method over the entire period from 1993 to 2022 reveals a mean value of $S \approx 34.921$. Therefore, the mean difference compared to the IW_{stat} salinity threshold of $S = 34.920$ following Pacini et al. (2020) and Chapter 3 is negligible. I conclude that using the static method to analyze the average of IW_{stat} over a larger period of, for example, thirty years reveals physically meaningful results. Also, analyzing IW_{stat} for small periods, such as during a specific scientific cruise, is suggested to reveal meaningful results. In this case, the IW_{stat} thresholds should be determined individually at different times. However, when using a static threshold over a larger period and it is desired to quantify magnitudes within multi-year variability, I suggest adjusting the thresholds to the large-scale state of the water column.

The general multi-year variability of the salinity thresholds indicates that the provenance method is appropriate for considering the large-scale changes in the water column in the Irminger Sea provenance region to evaluate IW_{prov}. For the hydrographic method, the salinity threshold at Sermiligaaq (Figure 4.8 b) is similar to the one from the provenance method. Starting from 2015, the hydrographic method yielded lower salinity thresholds than the provenance method (Figure 4.8 c). At eastern AR7W (Figure 4.8 e), the IW_{hydro} salinity threshold exhibited a long-term maximum similar to Sermiligaaq in 2010. However, the subsequent years until 2022 exhibited differences from Sermiligaaq. A distinct minimum of the hydrographic salinity threshold cannot be identified. Instead, the IW_{hydro} salinity threshold decreased until the end of the time series.

The two sections further downstream indicate a very different variability. At western AR7W (Figure 4.8 h), the IW_{hydro} salinity threshold showed an increase between 1993 and 2008, followed by a rapid decrease until 2010 and a subsequent increase. At Sisimiut (Figure 4.8 k), the IW_{hydro} salinity threshold remained almost constant over time, indicating little influence from changing properties in the water column on decadal time scales. Here, the amplitude of the seasonal variability, likely driven by the local sea ice cover, exceeds the relatively small decadal changes.

Comparing the order of the salinity threshold within the individual sections highlights the intended mechanism of the hydrographic method. The further downstream within the BCS, the fresher the water column becomes, either due to local mixing with ambient waters or as a result of large-scale changes in the water column (Figure 4.8, right column). Hence, the IW_{hydro} salinity threshold also decreases further downstream. The variability at the two most downstream sections indicates that other variabilities dominate apart from the one imprinted by the IW. However, the water column still exhibits features resembling the characteristic vertical structure of IW: the simultaneous subsurface temperature and salinity maximum (Figure 4.5). These characteristics imply that the waters have been in contact with IW previously.

4.3 Irminger Water variability for different methods

In the following, I analyze the resulting variability of the different IW types. Previously, I presented that the IW_{prov} and the IW_{hydro} salinity thresholds exhibit pronounced temporal changes on seasonal (Figure 4.7) and multi-year time scales (Figure 4.8). These temporal changes also impact the resulting properties and volume transports for IW_{prov} and IW_{hydro}. To analyze the consequences of the varying thresholds, I compare the IW_{stat}, IW_{prov}, and IW_{hydro} salinity, temperature, geostrophic velocity, and volume transport at eastern AR7W (Figure 4.9).

The static method

For the static method (Figure 4.9, left column), I obtain multi-year IW_{stat} salinity variability at eastern AR7W, indicating maximum salinities in 2010 and minimum salinities in 2019 (Figure 4.9 a). The period can be divided into two parts where the salinity first increased from the beginning to its maximum and decreased afterward. This behavior differs for the temperature (Figure 4.9 d). Here, maximum temperatures occurred in 2003 and from 2019 to 2020, while minimum temperatures occurred in 1995 and 2015 to 2017. For the geostrophic velocity (Figure 4.9 g), the highest values occurred from 1996 to 1997 and 2018 to 2020, lowest values in 2005 and 2011. As shown in Chapter 3, this is due to a horizontal shift of the IW perpendicular to the slope. In more saline years, IW is observed further offshore in regions with lower velocities than at the continental slope. Hence, the averaged geostrophic velocities consisted of higher values

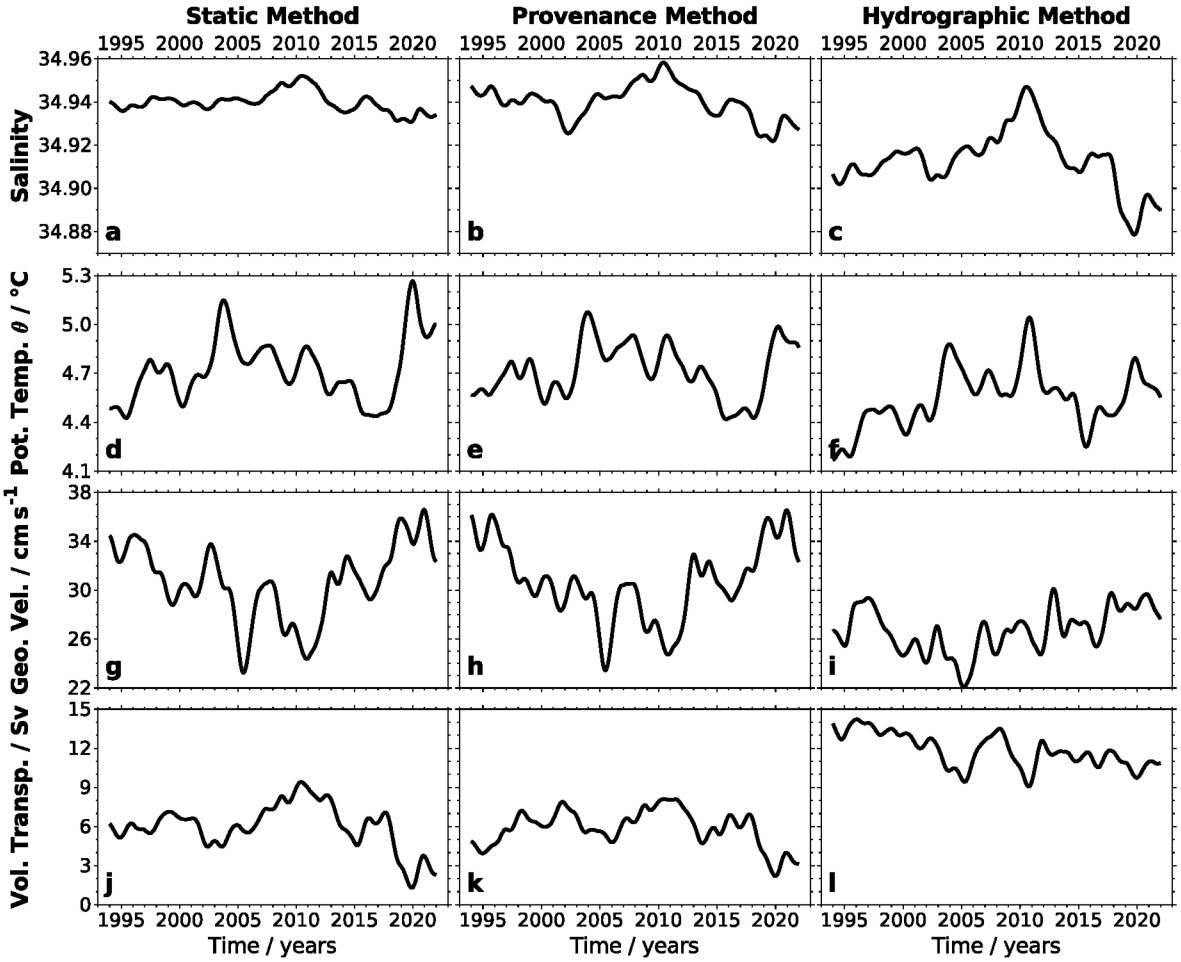

Figure 4.9: Multi-year variability of Irminger Water properties (top to bottom: salinity, potential temperature θ, geostrophic velocity, volume transport) at eastern AR7W smoothed with a 2-year running average including a Hanning window: Columns show different methods (left to right: static, provenance, hydrographic method).

close to the slope and lower velocities further offshore. The multi-year variability of the volume transport (Figure 4.9 j) is similar to the salinity, showing a maximum of almost 10 Sv in 2010 and a minimum of less than 2 Sv from 2019 to 2020. The IW volume transport variability agrees with the IW_{hydro} salinity thresholds (Figure 4.8).

The provenance method

The variability of all analyzed IW_{prov} properties matches the variability of IW_{stat} properties: salinity (Figure 4.9 b, correlation between IW_{stat} and IW_{prov}: $r = 0.84$ [0.82, 0.86] calculated for the 2-year running average), temperature (Figure 4.9 e, $r = 0.91$ [0.89, 0.92]), velocity (Figure 4.9 h, $r = 0.96$ [0.95, 0.96]), and volume transport (Figure 4.9 k, $r = 0.81$ [0.77, 0.83]). On average, the volume transports of IW_{stat} and IW_{prov}

are similar at 6.0 Sv and 5.9 Sv, respectively. These close results were expected, as the thresholds for the static and provenance methods are, on average, very similar with $IW_{stat} = 34.920$ and $IW_{prov} \approx 34.921$ (see Chapter 4.2.4). The differences in the volume transports between the static and provenance methods occur in their respective timing. The IW_{stat} volume transport dominates in years when the Irminger Sea provenance region is anomalously warm and saline (Figure 4.3), for example, between 2008 and 2012 (static: 8.5 Sv; provenance: 7.5 Sv, difference: $\sim 12\,\%$). The IW_{prov} volume transport dominates in years when the Irminger Sea provenance region is anomalously cold and fresh, for example, between 2019 and 2022 (static: 2.2 Sv; provenance: 3.0 Sv, difference: $\sim 27\,\%$). For a better direct comparison of the variability within the applied methods, I present the time series from Figure 4.9 individually standardized in Figure 4.10.

The hydrographic method

Applying the hydrographic method, the IW_{hydro} salinity at eastern AR7W (Figure 4.9 c) is consistently lower throughout the entire 30-year period compared to the two previously analyzed methods. The IW_{hydro} salinity maximum in 2010 and minimum in 2019 agree with the previously discussed methods, with the multi-year variability being similar compared to the static ($r = 0.90$ [0.88, 0.91]) and the provenance method ($r = 0.88$ [0.86, 0.90]). Similar to the IW_{hydro} salinity, the IW_{hydro} temperature (Figure 4.9 f) is consistently lower than the IW_{stat} and IW_{prov} temperature, except around the overall maximum in 2010. At the same time, the variability is similar to the previous methods (static: $r = 0.74$ [0.72, 0.77]; provenance: $r = 0.83$ [0.81, 0.85]). In contrast to the IW_{hydro} temperature and salinity, the IW_{hydro} volume transport at eastern AR7W (Figure 4.9 l) exhibits large differences compared to the volume transport obtained with the previous methods. The IW_{hydro} volume transport is not significantly correlated with the IW_{stat} and the IW_{prov} volume transport (static: $r = 0.03$ [-0.05, 0.10], provenance: $r = -0.03$ [-0.09, 0.05]). A linear trend calculated over the entire period reveals a decrease in IW_{hydro} of -1.22 Sv per decade. Accompanying this negative trend in the volume transport is a positive trend of $0.96\,m\,s^{-1}$ per decade in the IW_{hydro} velocity. Thus, a reduced IW_{hydro} area must be responsible for the decay in volume transport. Calculating decadal trends for temperature and salinity results in a slight warming trend of 0.10 °C per decade and a freshening of 0.004 per decade. All these trends are

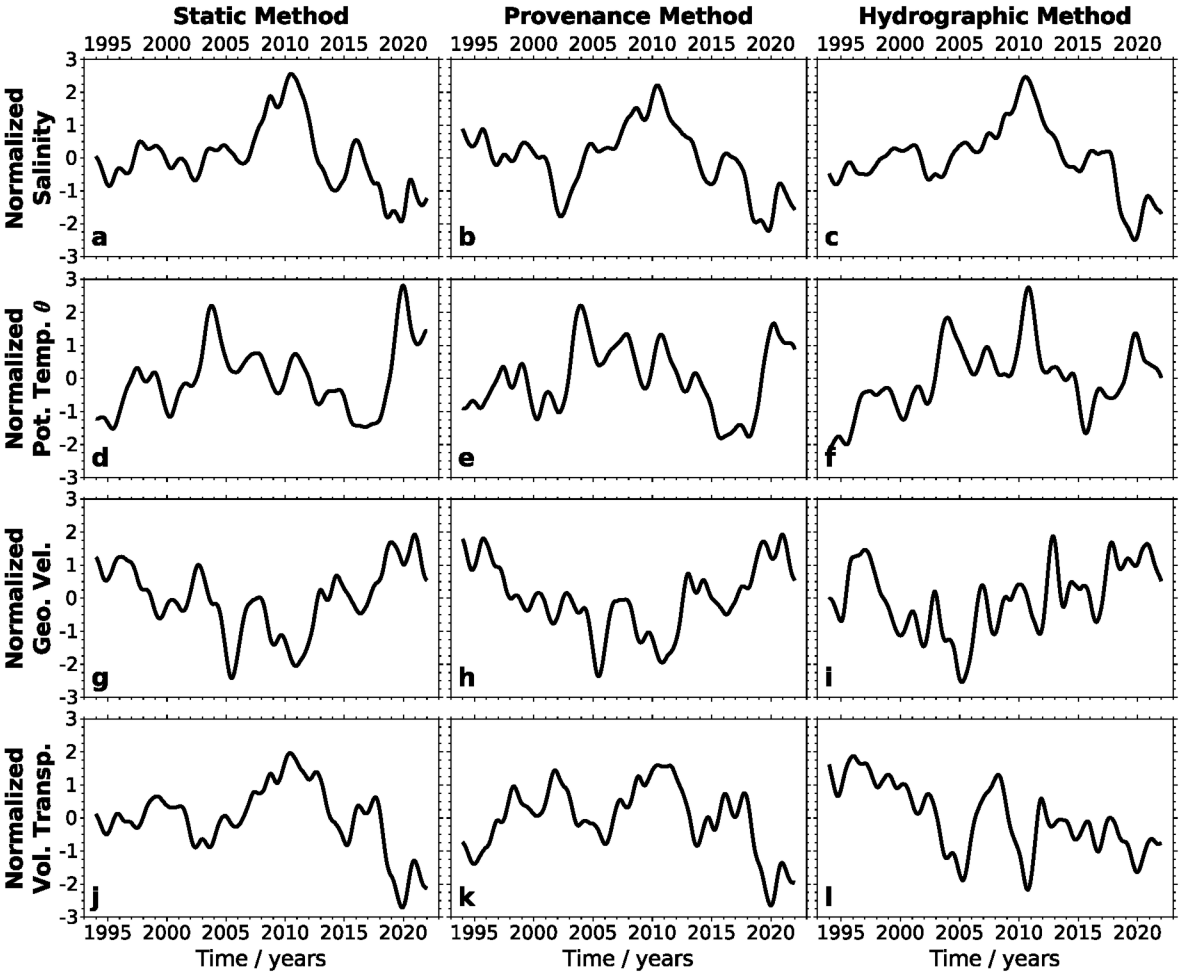

Figure 4.10: Similar to Figure 4.9 but with standardized time series.
Standardized multi-year variability of Irminger Water properties (top to bottom: salinity, potential temperature θ, geostrophic velocity, volume transport) at eastern AR7W smoothed with a 2-year running average including a Hanning window: Columns show different methods (left to right: static, provenance, hydrographic method).

significant. However, the freshening trend is dominated by the fresher years from 2018 to 2022. As the hydrographic method only considers the hydrography at the given location, the trends reveal a clear warming and slight freshening of the $\mathrm{IW}_{\mathrm{hydro}}$ within the WGC at eastern AR7W.

4.4 Irminger Water salinity distribution

The volume transports obtained with the three different methods showed the expected results. The water column in the Irminger Sea provenance region was anomalously saline around 2010, while it was anomalously fresh from 2018 to 2019 (Figure 4.3 a). With the static method, the $\mathrm{IW}_{\mathrm{stat}}$ volume transport is overestimated in years with

a warm and saline water column and underestimated in years with a cold and fresh water column. Additionally, the static method delivers a strong boundary between IW_{stat} and ambient waters at its fresher limit. Analyzing the IW area covered by specific salinity bins within the IW indicates that a slight shift of the static threshold of $S = 34.92$ would result in larger IW volume transport changes (Figure 4.11, left column). This behavior is particularly evident when investigating further upstream sections, such as Sermiligaaq and eastern AR7W (Figure 4.11 a, d, respectively), where the IW_{stat} salinities are unrealistically truncated when falling below the static threshold. At western AR7W (Figure 4.11 g), the areas filled with IW_{stat} salinities of particular strength are so sparse that interpretations about long-term variability are not possible. At Sisimiut, the data for IW_{stat} are not as sparse as at western AR7W. However, here the individual salinity bins rely on a minimal area. Especially at these two downstream sections, IW_{stat} is almost entirely mixed with colder and fresher ambient waters, as stated by e.g., Buch (2000), Buch et al. (2004), Myers et al. (2009), and Ribergaard (2014). Hence, only small remnants of IW_{stat} reach these sections.

For the provenance (Figure 4.11, middle column) and hydrographic methods (Figure 4.11, right column), the thresholds used to identify IW are non-static and allow for considering large-scale temporal changes of the water column, either in the Irminger Sea provenance region or locally in the BCS. Hence, the properties of the fresh limits of IW_{prov} and IW_{hydro} exhibit multi-year variability just like the saline limits. The multi-year variability of the IW_{prov} salinity distribution follows the salinity variability in the Irminger Sea provenance region (Figure 4.3 a) and the salinity variability obtained with all three methods (Figure 4.9). Analyzing the two downstream sections reveals only small differences between the provenance and static methods. When reaching these regions, the IW_{prov} is almost fully diluted, just like the IW_{stat}. Hence, the provenance method does not improve the analysis of multi-year IW_{prov} variability in Baffin Bay and the western Labrador Sea.

Analyzing the IW_{hydro}, the salinity distribution reveals differences for all four sections. At Sermiligaaq (Figure 4.11 c), the hydrographic method consistently reveals higher salinities, on average, than the other two methods. I identify smaller areas of IW_{hydro} salinities at their fresher limit due to higher thresholds obtained using the percentiles. For all three other sections, the hydrographic method consistently reveals salinities below those obtained from the other methods. At eastern AR7W (Figure 4.11 f), the

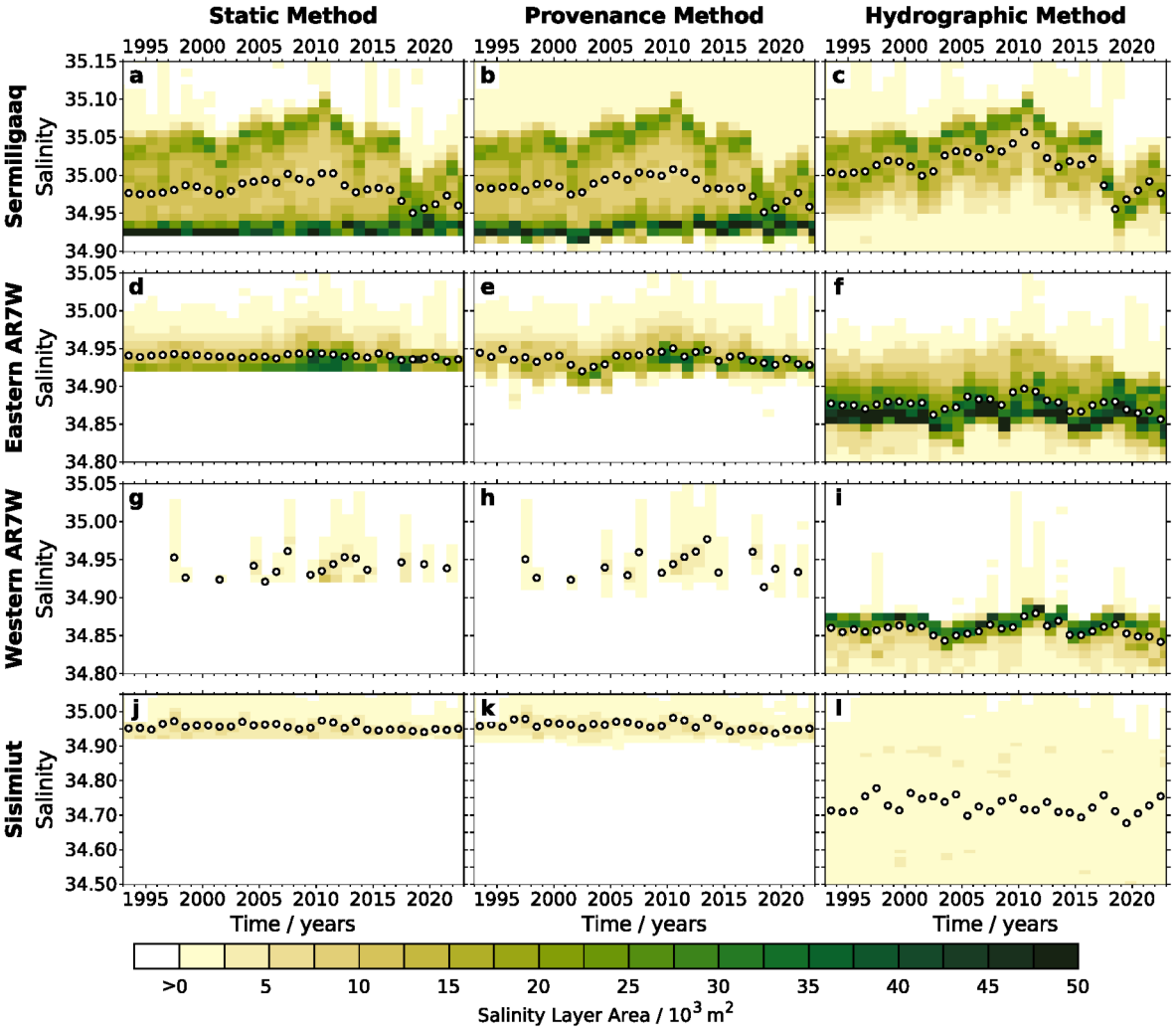

Figure 4.11: Yearly mean layer area for individual salinity bins for different methods (left to right: static, provenance, hydrographic method). Rows denote individually analyzed sections (top to bottom: Sermiligaaq, eastern AR7W, western AR7W, Sisimiut). Circles denote yearly averaged salinities for the respective Irminger Water type.

largest areas occur at salinities between 34.85 and 34.90. The multi-year variability still follows the variability from the other two methods. The most notable differences using the hydrographic method occur at western AR7W (Figure 4.11 i) and Sisimiut (Figure 4.11 l). At western AR7W, I have identified a sparse salinity distribution for the static and provenance methods. However, the hydrographic method reveals a clear signal of multi-year variability that matches further upstream at eastern AR7W and Sermiligaaq. The salinities are slightly lower than at eastern AR7W, and the individual salinity bins cover a smaller area. At Sisimiut, IW_{hydro} comprises lower salinities and is thus built on more salinity information. The highest salinities occurred in the late 1990s and early 2000s, decreasing afterward. This freshening trend agrees with analyses

from Curry et al. (2014), who found a decreasing salinity in the layer of Atlantic-origin waters at Davis Strait just north of Sisimiut by analyzing mooring observations.

Additionally, the results agree with Myers et al. (2009) for those years when the analyzing periods overlap. Myers et al. (2009) also found a maximum salinity at Sisimiut in the early 2000s and lower salinities before and after. However, they did not further analyze possible reasons for such variability. To get a better understanding of the causes for such salinity variability at Sisimiut, I analyzed the salinity distribution for additional cross-slope sections between eastern AR7W and Sisimiut (not shown), following the investigated sections in Myers et al. (2009) (see Figure 4.2). I find multi-year salinity variability close to what is identified at eastern AR7W further downstream in the WGC until Fylla Bank. Even further downstream, at Maniitsoq, the decadal signal observed at Sisimiut becomes dominant. At Fylla Bank, the characteristic salinity maximum from Sisimiut was identified in the early 2000s. However, the characteristic salinity maximum from eastern AR7W was also identified around 2010. Therefore, I conclude that major parts of the IW_{hydro} recirculate within the Labrador Sea south of Fylla Bank. The bathymetry holds back these waters from entering Baffin Bay, where only the upper branches of IW_{hydro} that shape a different multi-year and decadal variability are identified. Gou et al. (2022) found the largest exchange between the WGC and the interior Labrador Sea between Cape Desolation and Fylla Bank. Combining the results from Gou et al. (2022) and this chapter, I conclude that the region south of Fylla Bank forms a transition region that serves as the gateway into Baffin Bay.

4.5 How do the methods impact Irminger Water thickness?

Regarding how much IW is located in the water column, its thickness is the first quantity to analyze. In the following, I compare the thickness of IW_{stat} and IW_{hydro} averaged over 1993 to 2022 in the entire SPNA. For IW_{prov}, analyses are restricted to individual sections; thus, a basin-wide analysis is not possible. In the case of the static method (Figure 4.12 a), the highest IW_{stat} thickness is observed in the eastern SPNA, along the Reykjanes Ridge, following the IC into the BCS, where the IW_{stat} thickness decreases further downstream.

Following the hydrographic method (Figure 4.12 b), the highest IW_{hydro} layer thicknesses also occur in the eastern SPNA south of Iceland. However, in contrast to the

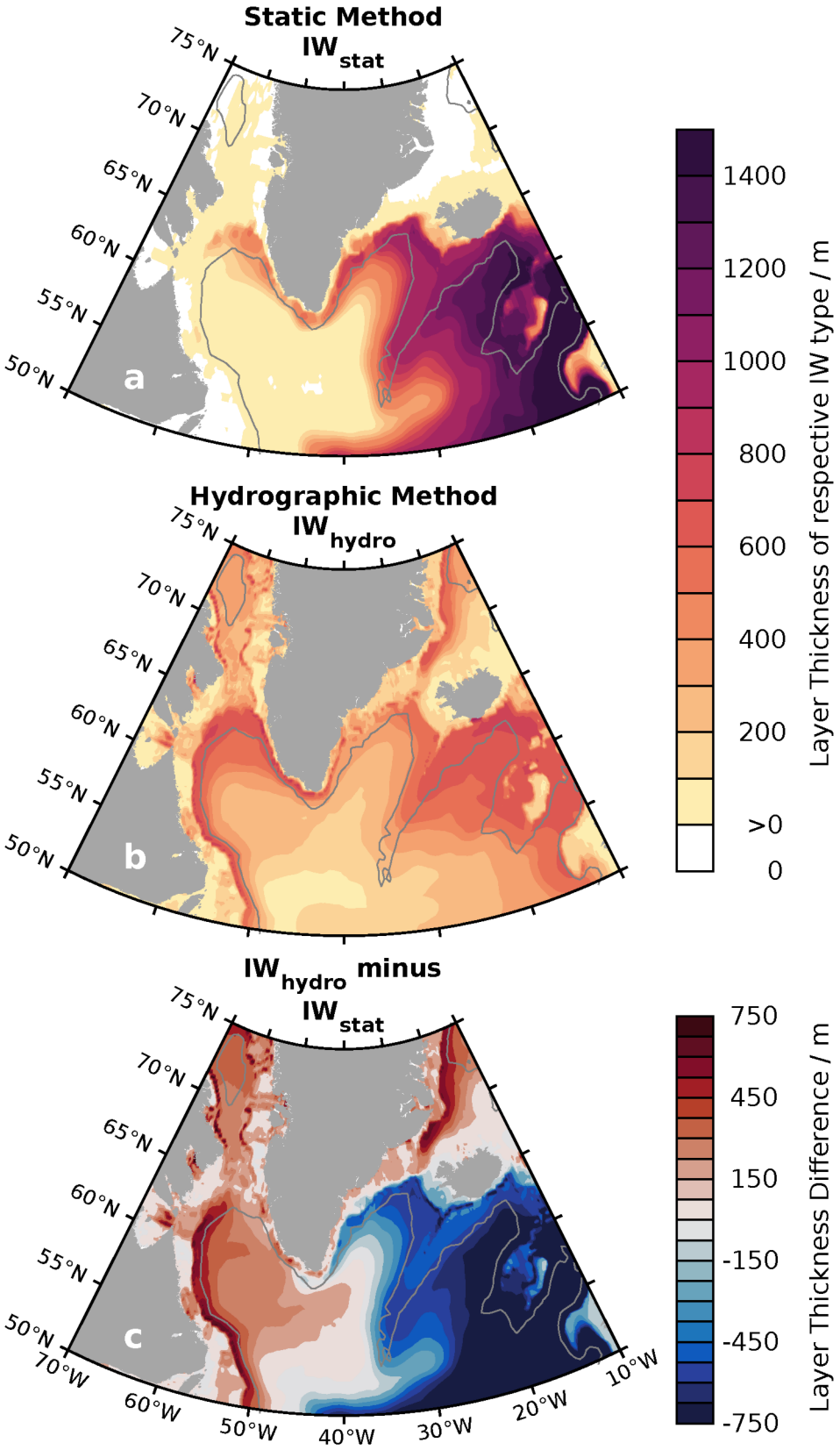

Figure 4.12: Mean layer thickness of the respective IW type obtained from the static (a) and hydrographic method (b) from 1993 - 2022 and the difference between the two methods (c). Gray lines follow the smoothed 2,000 m isobath.

static method, the layer thicknesses in the Irminger Sea, Labrador Sea, and Baffin Bay are relatively similar. A domain with higher layer thicknesses occurs in the Labrador Sea along the WGC and the recirculation along the Labrador continental slope. These results for the 30-year average resemble the general pattern that was previously described for two individual years (Figure 4.6), indicating a persistent background pattern of IW_{hydro} thickness in the SPNA.

The difference between IW_{stat} and IW_{hydro} thickness reveals a contrast between the eastern and western SPNA (Figure 4.12 c). As intended, the hydrographic method identifies more IW_{hydro} in the Labrador Sea and Baffin Bay compared to the static method, as it accounts for mixing IW with colder and fresher ambient waters. Simultaneously, the hydrographic method reveals higher IW_{hydro} salinity thresholds in the eastern SPNA and thus identifies less IW_{hydro} compared to the static method.

4.6 Summary and Conclusion

In this chapter, I present three approaches to identify IW in the BCS downstream of the Irminger Sea. Subsequently, I study differences between the established method for identifying IW and the two newly developed approaches regarding IW's seasonal and multi-year variability. These two methods include either the temporal variability of the water column (provenance method) or the temporal and spatial variability (hydrographic method). The endeavor to include temporally varying water mass properties was already applied to LSW (Pickart et al., 2003b; Yashayaev & Loder, 2017) and was suggested for ISIW (Le Bras et al., 2022). Especially when analyzing IW over a larger period, here 30 years, temporal hydrographic changes in the water column and temporally varying thresholds to identify IW contribute to a more realistic representation of the water mass (Figure 4.11).

In the following, I summarize the different methods to identify IW in this chapter:

Static method

The static method identifies IW_{stat} based on static thresholds. When IW_{stat} mixes with ambient waters, it cannot be identified anymore at sections far downstream from the Irminger Sea. Different static thresholds were used in previous studies (see Table 4.1).

Provenance method

The provenance method identifies IW_{prov} based on the temporally changing hydrography in the Irminger Sea provenance region, which I assume is the source region for IW_{prov}. This method considers changes in the water column, which can become colder and fresher or warmer and more saline during certain periods. Nevertheless, the water can still be mixed below these thresholds for sections far downstream from the Irminger Sea provenance region as they are spatially constant.

Hydrographic method

The hydrographic method identifies IW_{hydro} assuming that it maintains the vertical structure of the water column, the characteristic subsurface temperature, and salinity maximum. Hence, this method allows for identifying IW_{hydro} in regions where this coherence of temperature and salinity still exists, even though the waters are mixed below the thresholds of the static or provenance methods. In contrast to IW_{stat} and IW_{prov}, I do not consider IW_{hydro} as a distinct water mass.

Applying the provenance method, I obtain larger amplitudes of IW_{prov} salinity variability compared to the static method. Especially in 2010, where the BCS was anomalously saline, IW_{stat} volume transport estimates included ambient waters that were also more saline. The provenance method takes such variability into account and suggests less IW_{prov} volume transport at eastern AR7W in 2010 (Figure 4.9). The multi-year variability between 1993 and 2022 is similar for both methods. Applying the static method creates a strong boundary between IW_{stat} and ambient waters at the fresher IW_{stat} limit (Figure 4.11 left column). This boundary may impose or modulate unrealistic changes in the IW_{stat} volume transport simply because the actual boundary of IW_{stat} does not coincide with a certain isohaline. The provenance method resolves this issue by considering long-term changes in the water column (Figure 4.11, middle column). Therefore, this chapter considers long-term hydrographic changes in the Irminger Sea provenance region for the seasonal and multi-year analysis of IW_{prov} variability in the BCS.

Additionally, I consider spatial changes of the Atlantic-origin waters along its pathway in the BCS. With the hydrographic method, I can follow the subsurface temperature and salinity maximum characteristic of Atlantic-origin waters within the BCS on its way into Baffin Bay and the western Labrador Sea. Estimates of its hydrographic prop-

erties and volume transport include IW originating in the Irminger Sea and ambient waters mixed with IW without diluting its vertical structure in the water column. All the ambient waters are colder and fresher than IW. Hence, IW_{hydro} temperature and salinity are also lower compared to IW_{stat} and IW_{prov}.

Attempts to consider such mixing of IW along the pathway in the BCS have been made previously (Buch, 2000; Buch et al., 2004; Myers et al., 2009; Ribergaard, 2014). They differentiated between pure and modified IW, allowing them to analyze IW variability even though it was mixed with ambient waters to a certain degree. However, the authors only set lower static thresholds for identifying the modified IW and kept these thresholds constant over time. This way, the modified IW might still get mixed below the newly defined lower threshold, and long-term changes in the water column are not considered. The newly developed hydrographic method builds on the general idea of analyzing a modified IW following Buch (2000), Buch et al. (2004), Myers et al. (2009), and Ribergaard (2014). In addition, I consider the lower IW_{hydro} threshold to decrease for regions further downstream in the BCS, allowing for identification of IW_{hydro} as long as the vertical structure of the water column is preserved. The method also considers changes in the water column. It accounts for short-term processes affecting IW, like modification due to vertical mixing and convection (e.g., Le Bras et al., 2020; Gutjahr et al., 2022) or long-term processes like changes in size and strength of the SPG (Buch et al., 2004; Holliday et al., 2020, Chapter 3).

The IW_{hydro} volume transport at eastern AR7W does not reveal considerable decadal variability. It is generally higher than the volume transport of IW_{stat} and IW_{prov} (Figure 4.9l). Therefore, I suggest that the variability within the warm and saline water layer dominates the multi-year variability of IW_{stat} and IW_{prov} volume transports at eastern AR7W. The ambient waters that mix with IW dampen the multi-year variability of IW_{hydro}. Hence, I conclude that there is less multi-year variability of the IW_{hydro} volume transport compared to the volume transports of IW_{prov} and IW_{stat}.

From the analysis to determine IW, including temporally varying thresholds (IW_{prov}), as well as temporally and spatially varying thresholds (IW_{hydro}), I answer the previously stated research questions and draw the following conclusions:

1. **How can the temporal variability within the water column be included when identifying Irminger Water and tracking its downstream fate?**

   Using temporal temperature and salinity changes in the Irminger Sea provenance region as a proxy for IW variability allows accounting for temporal variability in the water column of the BCS when identifying IW.

2. **How can waters maintaining vertical Irminger Water structures in regions where it is fully mixed below a certain threshold be identified?**

   The hydrographic method builds on analyzing percentiles of water mass properties in the water column. It identifies waters with Irminger Sea origin in regions where IW_{stat} is mixed below spatially static thresholds, for example, in Baffin Bay and the western Labrador Sea.

3. **What influences do long-term (temporal) and large-scale (spatial) variability in the water column have on the variability of Irminger Water properties?**

   The provenance method resolves the issue of having a too strong boundary between IW_{stat} and ambient waters. Hence, it resembles temporal variability in the IW_{prov} volume transport more realistically. Consequently, in anomalously warm and saline years, the volume transport of IW_{stat} is overestimated compared to IW_{prov} by 1.3 Sv. In anomalously cold and fresh years, the volume transport of IW_{stat} is underestimated compared to IW_{prov} by 0.9 Sv. Temporal variability of the IW_{hydro} volume transport is mainly caused by the warmest and most saline waters in the water column. Fresher and less saline ambient waters resembling a vertical structure like IW dampen the multi-year variability. In Baffin Bay and the western Labrador Sea, I found a similar multi-year variability for IW_{hydro} compared to IW obtained from the other methods in regions further upstream. On seasonal time scales, the local effects of sea ice play a larger role.

A better understanding of IW_{stat}, IW_{prov}, and IW_{hydro} pathways and the local variability can increase the estimates of their influence on local buoyancy changes to either favor or inhibit convection in the Irminger and Labrador Seas. The provenance method considers hydrographic changes in the Irminger Sea provenance region. One possible next step could be to follow IW_{prov} from the Irminger Sea along the EGC and WGC into

either Baffin Bay or the western Labrador Sea. For regions not reached by IW_{prov}, the hydrographic method allows for evaluating local variability of IW_{hydro}. Both suggested analyses follow in Chapter 5.

"Observations provide the ground truth against which I can evaluate and improve climate models, helping us to better understand and prepare for the impacts of climate change."

Michael Evan Mann - Climatologist and geophysicist;
Professor of Earth & Environmental Science at the
University of Pennsylvania

Chapter 5

Irminger Water - Variability in multiple data sets

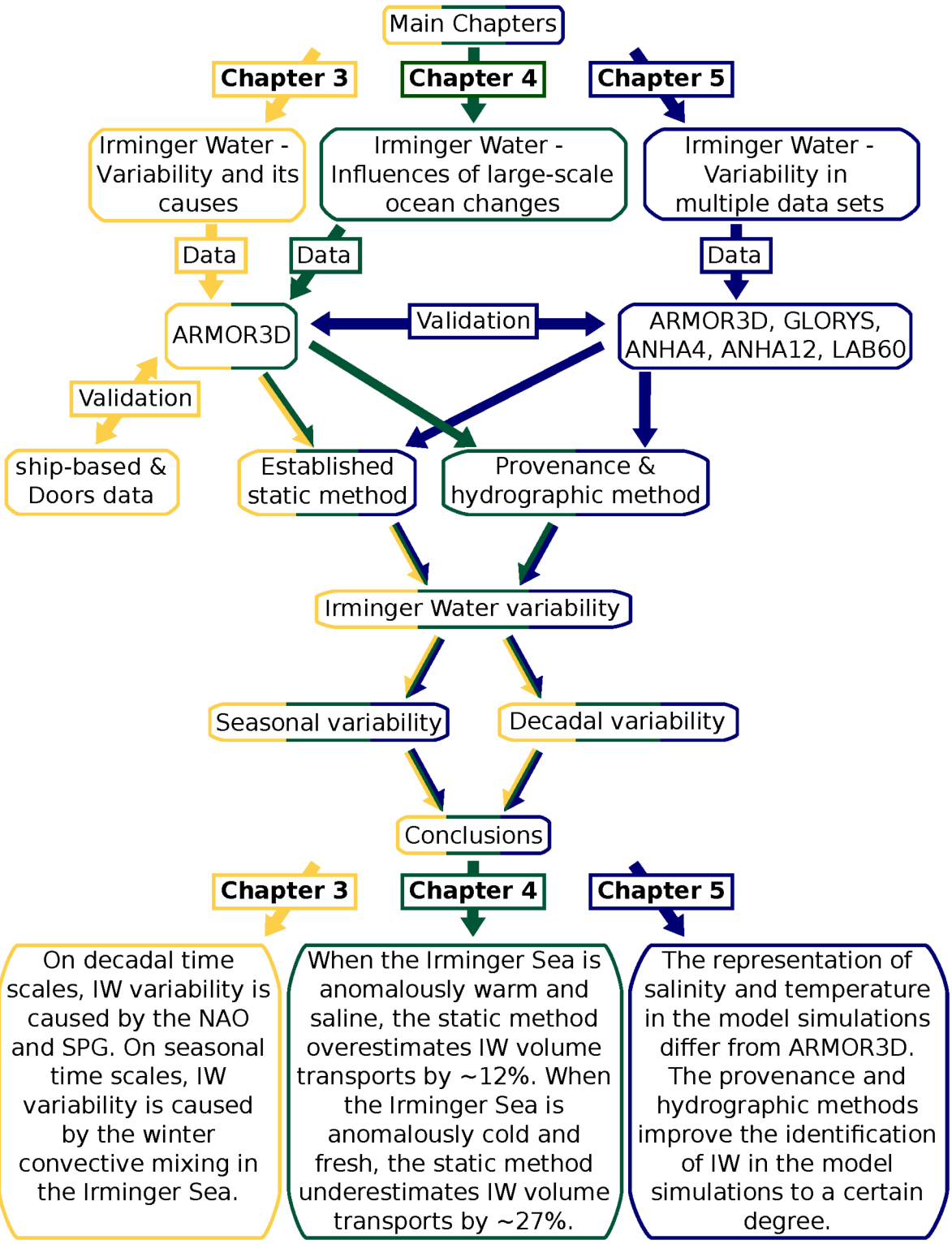

Figure 5.1: Graphical outline of Chapter 5. The content of Chapter 3 is highlighted in yellow, the content of Chapter 4 in green, the content of Chapter 5 in blue. Following the blue colors guides the reader through the present Chapter 5.

5.1 The boundary current system off Greenland and Labrador

In the previous chapters, I focused on analyzing IW using the multi-source observation-based data set ARMOR3D at a small set of cross-slope sections. In the following, I analyze IW in additional data sets introduced in Chapter 2.2 and Chapter 2.3. The results are compared with those previously obtained using ARMOR3D. I identify differences in the IW properties by comparing IW in ARMOR3D with IW in GLORYS, ANHA4, ANHA12, and LAB60. These differences result only partly from the varying horizontal resolution of the individual data sets. Additionally, the general vertical structure of the water column differs within the data sets.

In Chapter 3, the analysis was focused on one cross-slope section in the BCS, eastern AR7W. To develop the hydrographic method, I extended the analysis to four sections spanning the BCS in the Irminger Sea, eastern Labrador Sea, western Labrador Sea, and Baffin Bay in Chapter 4. In the following Chapter 5, I build on the previous chapters and construct an array of 25 cross-slope sections (Figure 5.2). The sections selected for the analysis primarily follow existing measurement campaigns (e.g., Myers et al., 2009; Ribergaard, 2014; Kieke & Yashayaev, 2015) and have been extended to cover the entire study region. I refer to the individual sections by their given numbers and names as per Table 5.1. Sections 1 to 11 follow the BCS within the EGC and WGC. Subsequent sections 12 to 19 continue within the WGC into Baffin Bay. Sections 20 to 25 follow the recirculation along the boundary of the continental slope in the western Labrador Sea. To provide an impression of the salinity distribution across this extensive array of individual sections, I present all sections in Figure C.1. Analyzing the hydrography and resulting IW properties at these 25 sections provides detailed insights about spatial variability in the BCS, including differences within the individual data sets.

The described array of individual cross-slope sections allows me to analyze the horizontal extent of the BCS. It facilitates the determination of the area covered by IW and, including the cross-slope velocity, calculating IW volume transports. I combine the results from the multiple sections to analyze the spatial evolution of IW properties from the Irminger Sea along its pathway in the BCS into Baffin Bay and the western Labrador Sea. However, the sections only represent spatial snapshots as they come with a distance of $\sim 200\,\mathrm{km}$ from each other. Hence, the array might not capture all

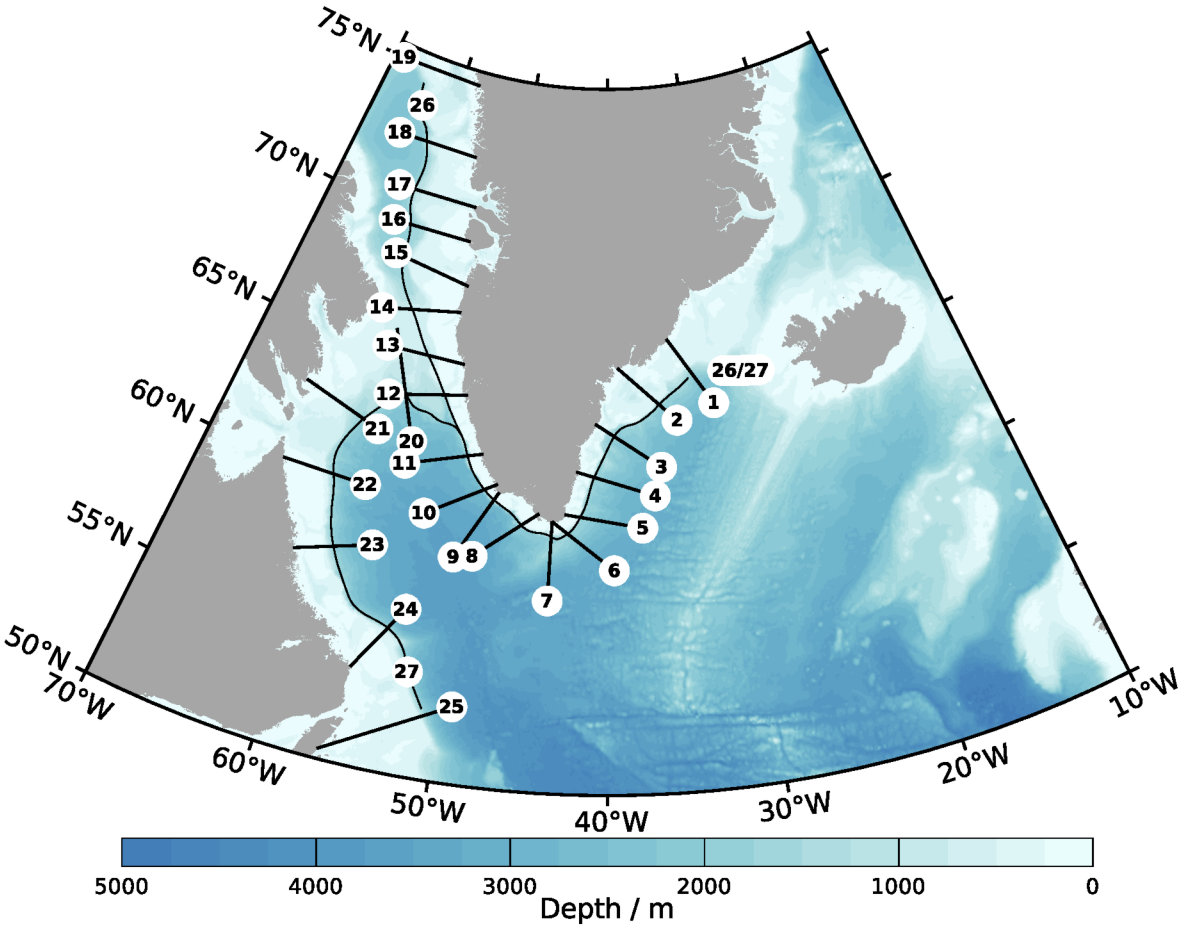

Figure 5.2: Map of the study region around southern Greenland, including the Irminger and Labrador Seas, and parts of the Baffin Bay. Colors denote bathymetry. Thick black lines crossing the continental slope indicate cross-slope sections analyzed in this chapter (Sections 1 - 25). The two thin black lines indicate along-slope sections following the 1,500 m isobath spanning from the Irminger Sea into Baffin Bay (Section 26) and the western Labrador Sea (Section 27). The given number for each section refers to the respective section name in Table 5.1.

spatial variability, for example, due to changing topography (e.g., Buch, 2002), the influences of local currents that leave the BCS (e.g., Holliday et al., 2007), or eddies that are shed off from the BCS and transported further offshore (Garcia-Quintana et al., 2019; Pennelly & Myers, 2020; Gou et al., 2023). To overcome these problems, I have extracted two along-slope sections that follow the 1,500 m isobath within the BCS, allowing for a spatially continuous analysis of IW properties.

In this chapter, I focus on the following objectives in particular:

1. **How do the hydrography in GLORYS and different model simulations compare with ARMOR3D in the BCS?**
2. **How are Irminger Water properties changing along their pathway from the Irminger Sea in the boundary current system?**
3. **Can different methods to identify Irminger Water be used to overcome differences in individual data sets?**

Chapter 5 is structured as follows: In Chapter 5.2, I present hydrographic differences between the individual data sets, focusing first on eastern AR7W and then on different cross-slope sections in the BCS. Following, I address the provenance and hydrographic methods to identify IW within the individual data sets (Chapter 5.3). Chapter 5.4 presents a detailed analysis of IW at eastern AR7W, starting with local hydrographic differences, presenting the obtained IW thresholds, and closing with the calculated variability of IW properties on seasonal and multi-year time scales. In Chapter 5.5, I

Table 5.1: List of the analyzed cross-slope (1 - 25) and along-slope (26, 27) sections. The table includes the section number given in Figure 5.2 and the corresponding section name.

Number	Section name	Number	Section name
1	Sermiligaaq	15	Aasiaat
2	Suunikajik	16	Kangerluk
3	Sermersooq	17	Nuussuaq
4	Uttorsiutit	18	Upernavik
5	OSNAP East	19	Qimusseriarsuaq
6	CF - Irminger	20	Northern Labrador Sea (LS)
7	44° West	21	Hudson Strait Inlet
8	OSNAP West	22	Hudson Strait Outlet
9	Eastern AR7W	23	Nain
10	Cape Desolation	24	Western AR7W
11	Paamiut	25	Northern Peninsula
12	Fylla Bank	26	Irminger Sea - Baffin Bay
13	Maniitsoq	27	Irminger Sea - Labrador Sea
14	Sisimiut		

extend the analysis to examine the BCS from the northern Irminger Sea into Baffin Bay and the western Labrador Sea. I present the hydrography along the entire pathway of the BCS and analyze the salinity distribution at individual sections. Afterward, I present IW properties along the BCS pathway and analyze the obtained IW thickness in the entire SPNA for the individual data sets. The chapter closes with a summary and conclusion (Chapter 5.6).

5.2 Hydrographic differences between the individual data sets

5.2.1 A detailed comparison at eastern AR7W

I analyzed eastern AR7W using ARMOR3D and validated it with different in-situ data in Chapter 3. In the following, I compare the vertical structure of the water column at eastern AR7W between ARMOR3D and the additional data sets, including GLORYS and different ANHA simulations (Figure 5.3). The main text focuses on the comparison based on salinity. Temperature, density, and geostrophic velocity comparisons can be found in Appendix E. As previously stated in Chapter 2.4, each data set was treated equally in terms of interpolating the individual sections on the same spatial resolution of $\Delta x = 1\,km$, and $\Delta z = 10\,m$.

All additional data sets share the common feature of having lower salinities at the Greenland shelf compared to ARMOR3D (Figure 5.3). This difference indicates that reanalysis and model simulations overestimate the signals of the fresher shelf waters originating in the Arctic Ocean or from Greenland's melting glaciers. Another explanation could be that ARMOR3D has an excessively high salinity on the shelf. Other differing features within the various data sets are analyzed separately in the following.

GLORYS

In GLORYS (Figure 5.3 c, d), the largest differences in comparison to ARMOR3D occur in the upper 100 m offshore from the shelf break. Here, GLORYS is more saline, while it is fresher further offshore. At the continental slope, the vertical salinity structure indicates fundamental differences compared to ARMOR3D. Higher salinities stretch along the entire slope into greater depths. Further offshore, the isohalines shape a mirrored 'C', allowing fresher water to reach closer to the slope at a depth of 1,000 m. This structure is more pronounced in ARMOR3D, where individual isohalines with

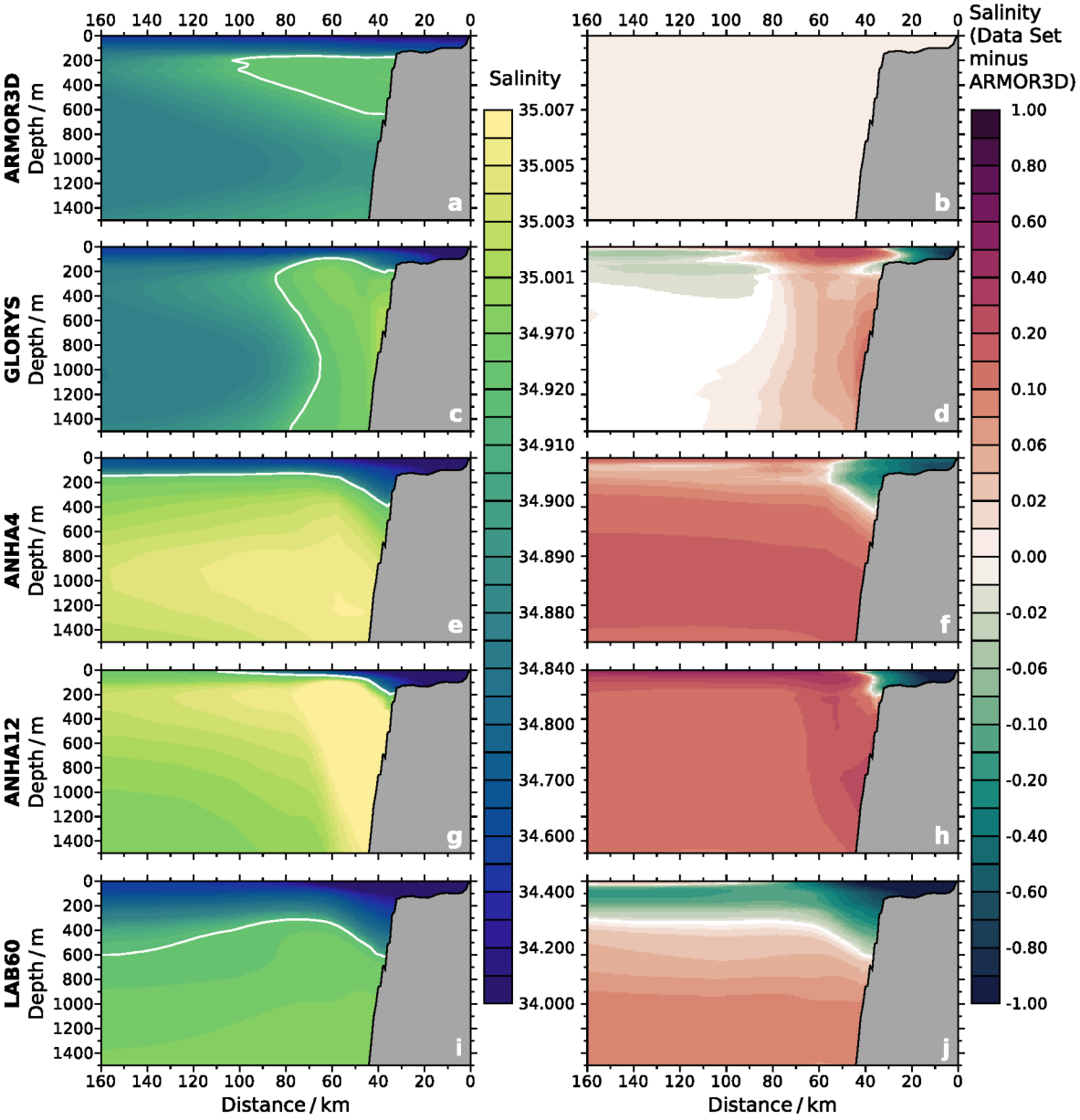

Figure 5.3: Salinity at eastern AR7W in the upper 1,500 m from the coast to a distance 160 km offshore averaged from 2002 - 2020. The left column indicates data from the individual data sets (top to bottom: ARMOR3D, GLORYS, ANHA4, ANHA12, LAB60 from 2004 - 2018). The white contour describes the 34.92 isohaline that defines the IW_{stat} salinity threshold (Chapter 3.2, Table 3.1). The right column indicates the difference to ARMOR3D (data set minus ARMOR3D).

$S > 34.895$ reach the slope for depths greater than 600 m and isolate the high IW salinities from the high salinities of deeper water masses.

ANHA4

In ANHA4 (Figure 5.3 e, f), the section exhibits a generally higher salinity, except for the fresher shelf area. The area of maximum salinity is located at 1,200 m depth and is much deeper than ARMOR3D (Figure 5.3 a). Since the subsurface salinity maximum is characteristic of IW, IW is consequently also located at greater depths in ANHA4 compared to ARMOR3D or the previously analyzed in-situ measurements (Chapter 3).

ANHA12

ANHA12 (Figure 5.3 g, h) presents a similar picture as ANHA4. The only notable difference is that the area of the largest salinity difference compared to ARMOR3D is confined to the continental slope. Disregarding the generally higher salinities in ANHA12, the location of the maximum salinity lies within depths between 200 and 600 m at an offshore distance of 40 to 60 km detached from the continental slope (not visible), agreeing with the definition of the IW core in Chapter 3 based on ARMOR3D. Further offshore, GLORYS and ARMOR3D exhibit similar characteristics, while ANHA12 shows an almost constant decrease in salinity with increasing depth.

LAB60

LAB60 (Figure 5.3 i, j) indicates lower salinities compared to ARMOR3D above 400 m (600 m at the continental slope) and higher salinities below. The differences in higher salinities in LAB60 compared to ARMOR3D do not exceed 0.1 (Figure 5.3 j), as for ANHA4 and ANHA12 (Figure 5.3 f, h). However, there is no distinct area of a maximum salinity. IW is more described as a layer, aligning with findings from (Gou et al., 2023). Therefore, it is important to use caution when interpreting IW within LAB60.

At eastern AR7W, minor and major differences between the analyzed data sets become apparent. Only in ARMOR3D is the subsurface salinity maximum, a major characteristic of IW, restricted to the upper 600 m close to the continental slope. In GLORYS and ANHA12, the maximum salinity reaches greater depths, while in ANHA4, it is

confined to greater depths. This vertical structure makes it more challenging to separate IW from deeper waters expressing higher salinities. At eastern AR7W, this might correspond to North East Atlantic Deep Water (NEADW) that can reach depths of 1,000 to 1,500 m at the continental slopes of AR7W (Yashayaev & Loder, 2017).

5.2.2 Comparing different cross-slope sections in the boundary currents

In the following, I extend the comparison of salinity between ARMOR3D and the other data sets from eastern AR7W to the four cross-slope sections analyzed in Chapter 4 (see positions of the sections in Figure 4.2 and Figure 5.2). These sections are Sermiligaaq (1) in the northwestern Irminger Sea, western AR7W (24) in the western Labrador Sea, and Sisimiut (14) in Baffin Bay. As stated in Chapter 2.4, LAB60 is only analyzed at eastern AR7W. Hence, I focus on the intercomparison of ARMOR3D, GLORYS, ANHA4, and ANHA12 by first analyzing the salinity in ARMOR3D at the mentioned sections (Figure 5.4) and discussing the differences compared to the other data sets subsequently (Figure 5.5, Figure 5.6, and Figure 5.7). Differences between the individual data sets at eastern AR7W have already been discussed in Chapter 5.2.1. For completeness, I present the results for eastern AR7W again in Figure 5.4, Figure 5.5, Figure 5.6, and Figure 5.7 but do not repeat the analysis. The cross-slope sections are always displayed with the continental slope to the right, simulating a downstream flow direction into the plane.

ARMOR3D

In ARMOR3D, Sermiligaaq (Figure 5.4 a) reveals an area of high salinities near the shelf break. This area stretches further offshore into the central Irminger Sea, outcropping at the surface at a distance of 150 km from the coast. The entire area of high salinities lies within the major pathway of the IC transporting IW (see Figure 4.2 and Figure 5.4 a). Hence, the entire area of high salinities represents pure IW that has recently entered the EGC and, therefore, has not mixed with ambient waters. Further onshore, fresher waters occupy the upper 150 m on the east Greenland shelf. The spatial extent of the west Greenland shelf is generally smaller than the east Greenland shelf (compare all 25 cross-slope sections in the Appendix, Figure C.1). While the shelf break at Sermiligaaq is located 130 km offshore from the Greenland coast, it is only 30 km offshore from the coast at eastern AR7W (Figure 5.4 b).

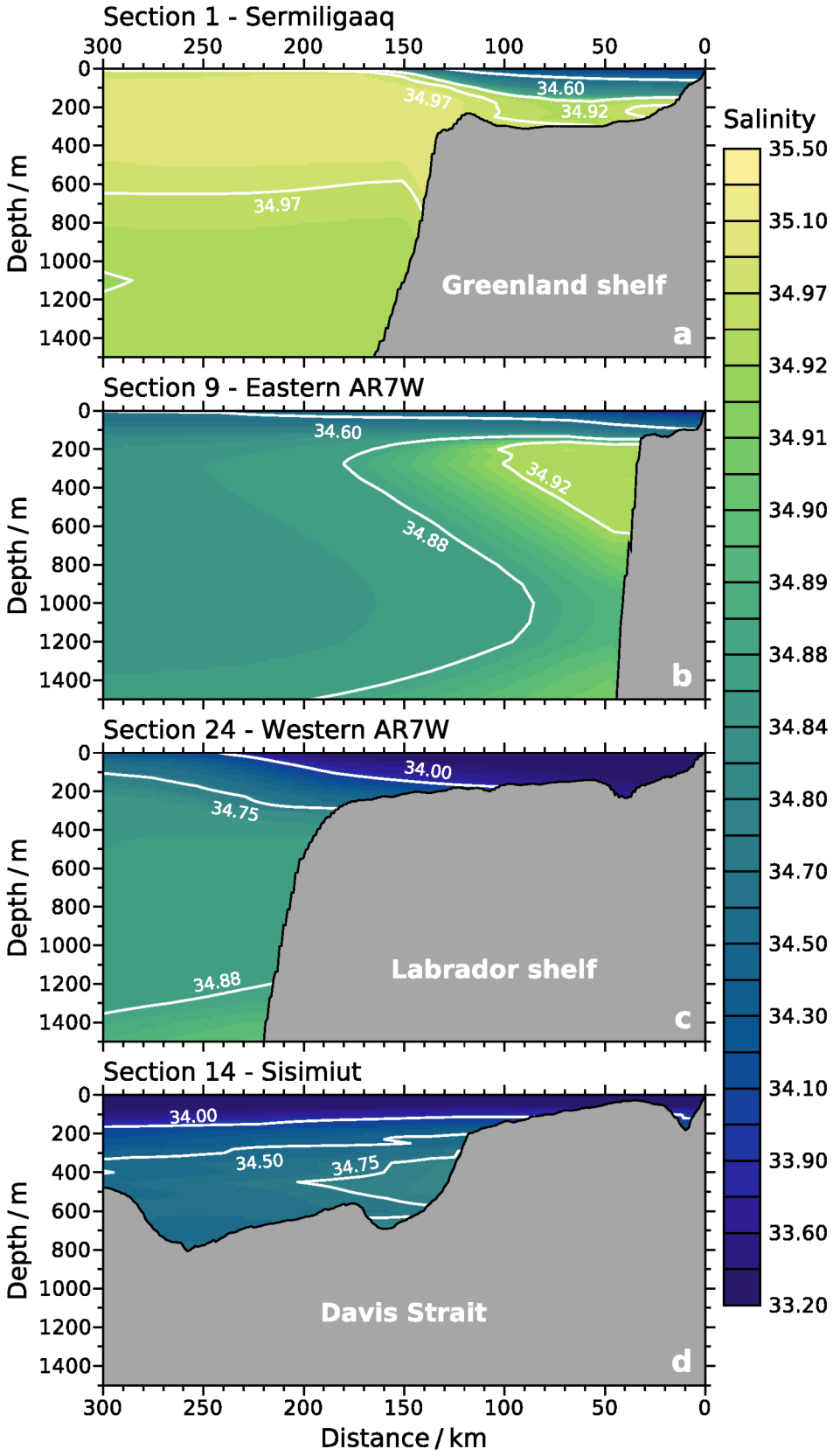

Figure 5.4: ARMOR3D salinity in the upper 1,500 m from the coast to a distance 300 km offshore averaged from 2002 - 2020. Sections from top to bottom: Sermiligaaq, Eastern AR7W, Western AR7W, and Sisimiut.

In the western Labrador Sea, at western AR7W (Figure 5.4 c), the salinity continuously increases with depth. The fresher waters on the 200 km wide shelf originate from the high latitudes (Loder et al., 1998), primarily from within Baffin Bay (Khatiwala & Fairbanks, 1999) and the Canadian archipelago (e.g., Yashayaev, 2007a). Below and further offshore from the shelf break are waters that have recirculated south of Davis Strait and constitute the same waters as at eastern AR7W. However, these waters had more time compared to the waters at eastern AR7W to subsequently mix with ambient waters along the pathway in the BCS and with LSW from the interior (e.g., Yashayaev & Loder, 2016).

Similar to western AR7W, at Sisimiut (Figure 5.4 d), the saline waters are already strongly mixed with fresher ambient waters. Across the entire Baffin Bay, fresher waters occupy approximately the upper 200 m. However, like at eastern AR7W, a subsurface salinity maximum is identified at the continental slope. This maximum salinity has been mixed far below the static threshold of 34.92 (Chapter 4.2.1) and represents the IW_{hydro} introduced in Chapter 4.2.3. Thus, the static method would identify no IW_{stat}. Only by applying the hydrographic method would it be possible to conduct further variability analysis of IW_{hydro}.

GLORYS

In GLORYS, the largest differences at Sermiligaaq compared to ARMOR3D are on the shelf (Figure 5.5 a, b). Here, GLORYS is fresher by more than 0.6. GLORYS is slightly more saline offshore from the shelf break, with differences not exceeding 0.1. At western AR7W (Figure 5.5 e, f), GLORYS reveals lower salinities on the shelf, similar to Sermiligaaq. Higher salinities occur offshore from the shelf break, similar to Sermiligaaq and eastern AR7W.

Particularly noteworthy is the intensification of high salinities along the continental slope at eastern and western AR7W, indicating generally higher salinities in the core of the boundary current in GLORYS. Furthermore, the cross-slope velocities in the core of the boundary current are considerably higher in GLORYS by more than 15 $cm\,s^{-1}$ (Figure E.3 d for eastern AR7W). Another area of higher salinities (and higher densities, not shown) in GLORYS compared to ARMOR3D is at western AR7W, only 40 km offshore from the coast, within a sill on the Labrador shelf. Given that this location is

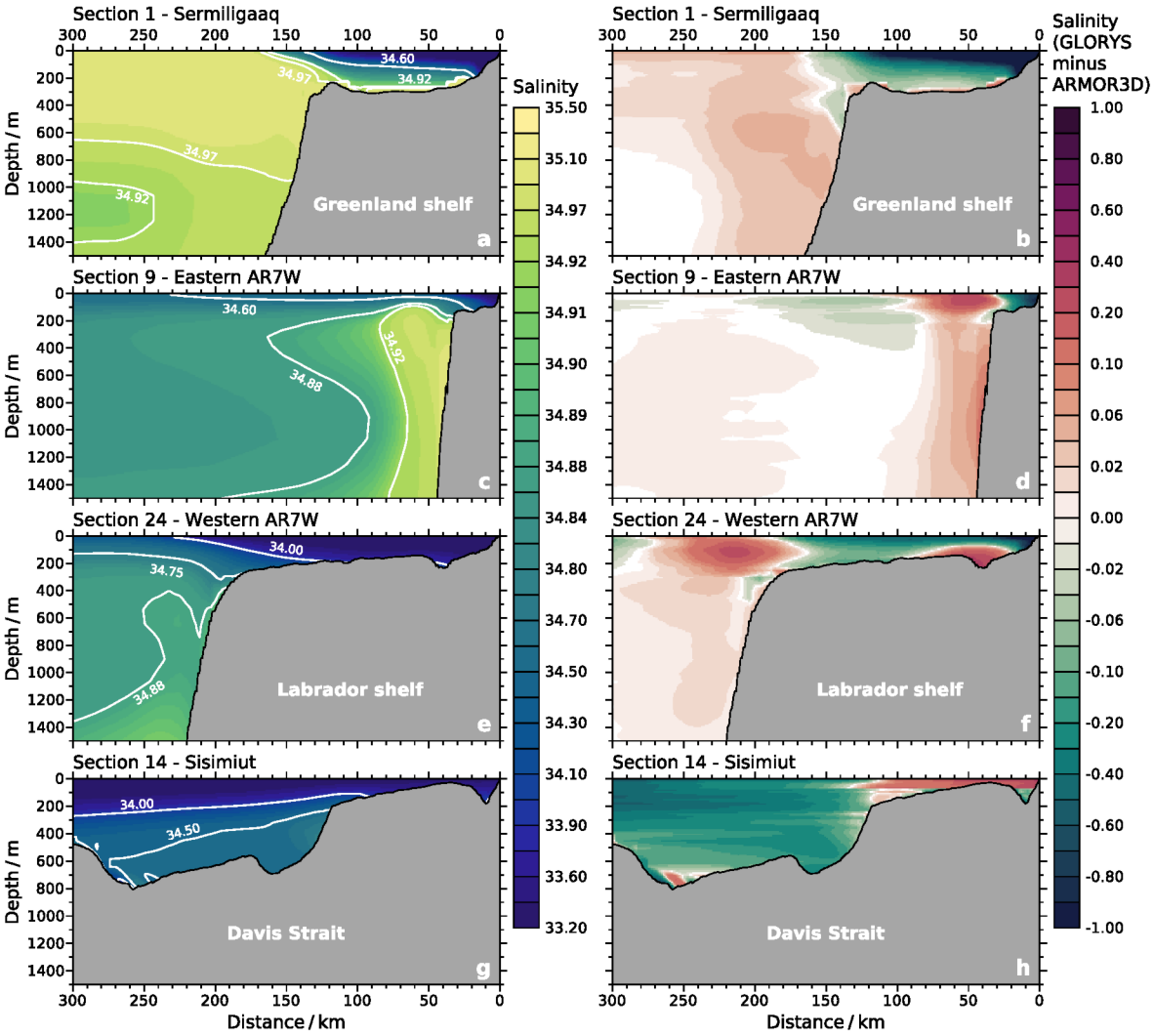

Figure 5.5: GLORYS salinity in the upper 1,500 m from the coast to a distance 300 km offshore averaged from 2002 - 2020 (left column). Anomalies with respect to ARMOR3D (right column). Sections from top to bottom: Sermiligaaq, Eastern AR7W, Western AR7W, and Sisimiut.

seasonally covered with sea ice (Figure D.1), I propose that this sill is filled with denser, more saline water resulting from brine rejection during the formation process of the sea ice. This hypothesis aligns with the low salinities on the shelf, which may also result from local sea ice melt and freshwater export from higher latitudes. ARMOR3D heavily relies on satellite measurements, especially in shallower shelf regions where penetration through sea ice is limited, such processes might not be represented in ARMOR3D. However, they are parameterized in the sea ice model, and may also be incorporated through the assimilation, in GLORYS (Drévillon et al., 2022b).

At Sisimiut (Figure 5.5 g, h), the difference between GLORYS and ARMOR3D is opposite to that of the previously analyzed sections. Here, the area on the Greenland shelf exhibits higher salinities in GLORYS, and further offshore, GLORYS reveals lower salinities, each differing by about 0.2. The shelf break region serves as a narrow transition zone where the salinities of the two data sets are similar.

ANHA4

In ANHA4, Sermiligaaq (Figure 5.6 a, b), eastern AR7W (Figure 5.6 c, d), and western AR7W (Figure 5.6 e, f) indicate similar salinity differences compared to ARMOR3D. ANHA4 is fresher on the shelves at these three locations by nearly 1.0. However, offshore from the shelf break, ANHA4 is more saline by up to 0.3. The transition zone between negative and positive salinity biases is located at the shelf break, distinctly separating a shelf and an offshore regime. Especially for identifying IW, using the static method with the same thresholds used for ARMOR3D would result in major problems. Based on its salinity, the entire water column (below the still fresher surface layer) would be identified as IW. Only the additional density criterion would limit the IW extent to even greater depths. I demonstrate in Chapter 5.4 and Chapter 5.5 how the provenance and hydrographic methods automatically correct for parts of such systematic biases in the model simulations compared to ARMOR3D. At Sisimiut (Figure 5.6 g, h), the salinity difference between ANHA4 and ARMOR3D is opposite compared to the three previously analyzed sections. Here, ANHA4 is more saline on the shelf and fresher further offshore, similar to GLORYS (Figure 5.5 h).

ANHA12

In ANHA12, a similar model bias toward higher salinities as in ANHA4 is identified. Similarly, the salinities are lower on the shelves compared to ARMOR3D at Sermiligaaq (Figure 5.7 a, b), eastern AR7W (Figure 5.7 c, d), and western AR7W (Figure 5.7 e, f). Simultaneously, regions further offshore are more saline. Also, the offset compared to ARMOR3D is similar at $\sim$0.3 in the offshore regions. The only difference compared to ANHA4 is that the higher salinities reach further onshore. The isohalines (and isopycnals; not shown) are less vertical, indicating higher stratification, especially at Sermiligaaq and western AR7W with wider shelves. This vertical structure allows the

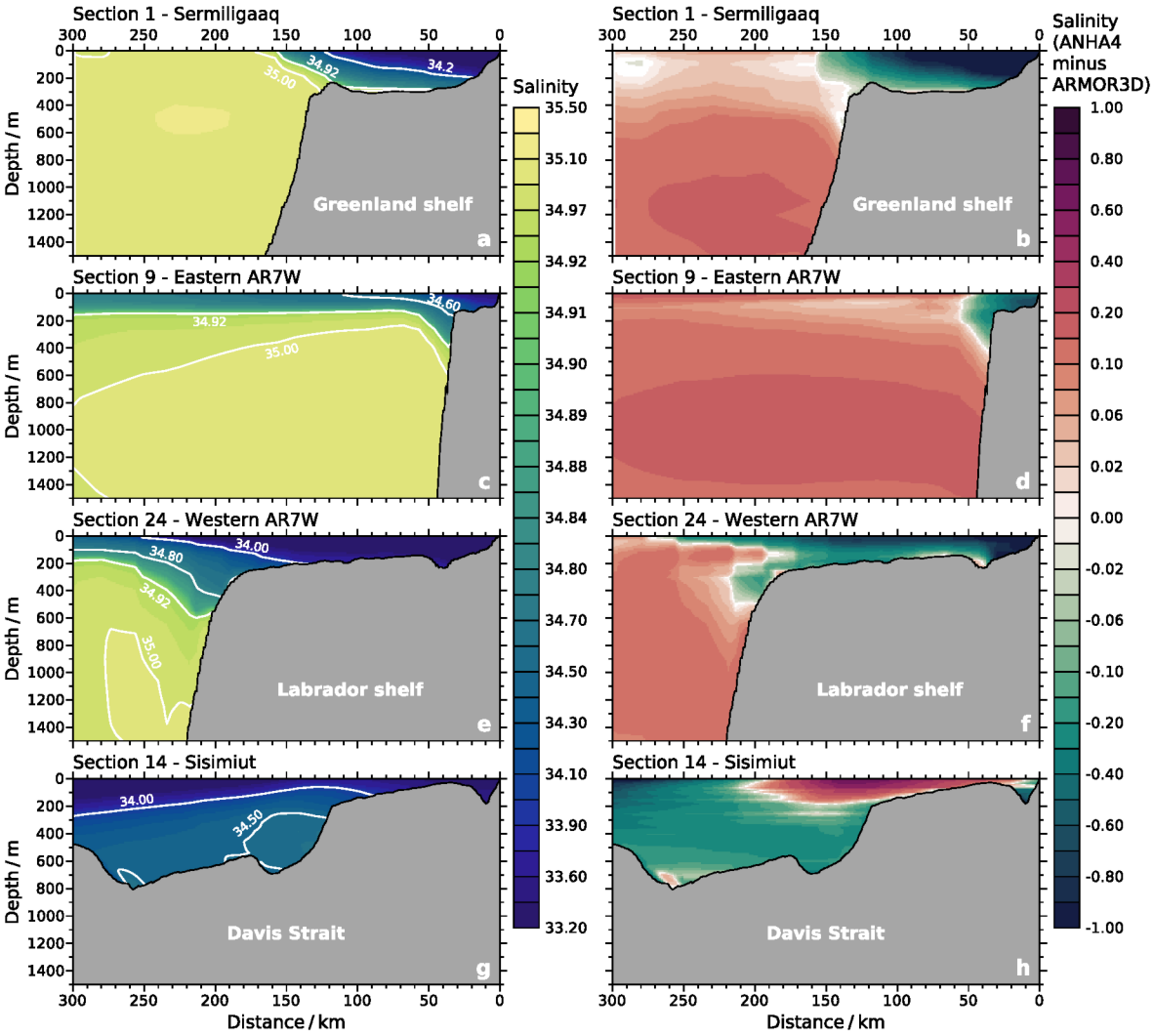

Figure 5.6: Similar to Figure 5.5 but for ANHA4.
ANHA4 salinity in the upper 1,500 m from the coast to a distance 300 km offshore averaged from 2002 - 2020 (left column). Anomalies with respect to ARMOR3D (right column). Sections from top to bottom: Sermiligaaq, Eastern AR7W, Western AR7W, and Sisimiut.

presence of waters with higher salinities in deeper layers on the shelves. At Sisimiut (Figure 5.6 g, h), an area with high salinities is located on the continental slope. This small area represents the only region with higher salinities than ARMOR3D. Further offshore and onshore on the shelf, the salinities are lower.

For temperature at eastern AR7W (Figure E.1), the differences of the individual data sets compared to ARMOR3D resemble a similar pattern as the salinity, indicating that the influence of warm and saline waters is generally higher in the other data sets. GLORYS is warmer compared to ARMOR3D within the fast core of the WBC (see GLORYS

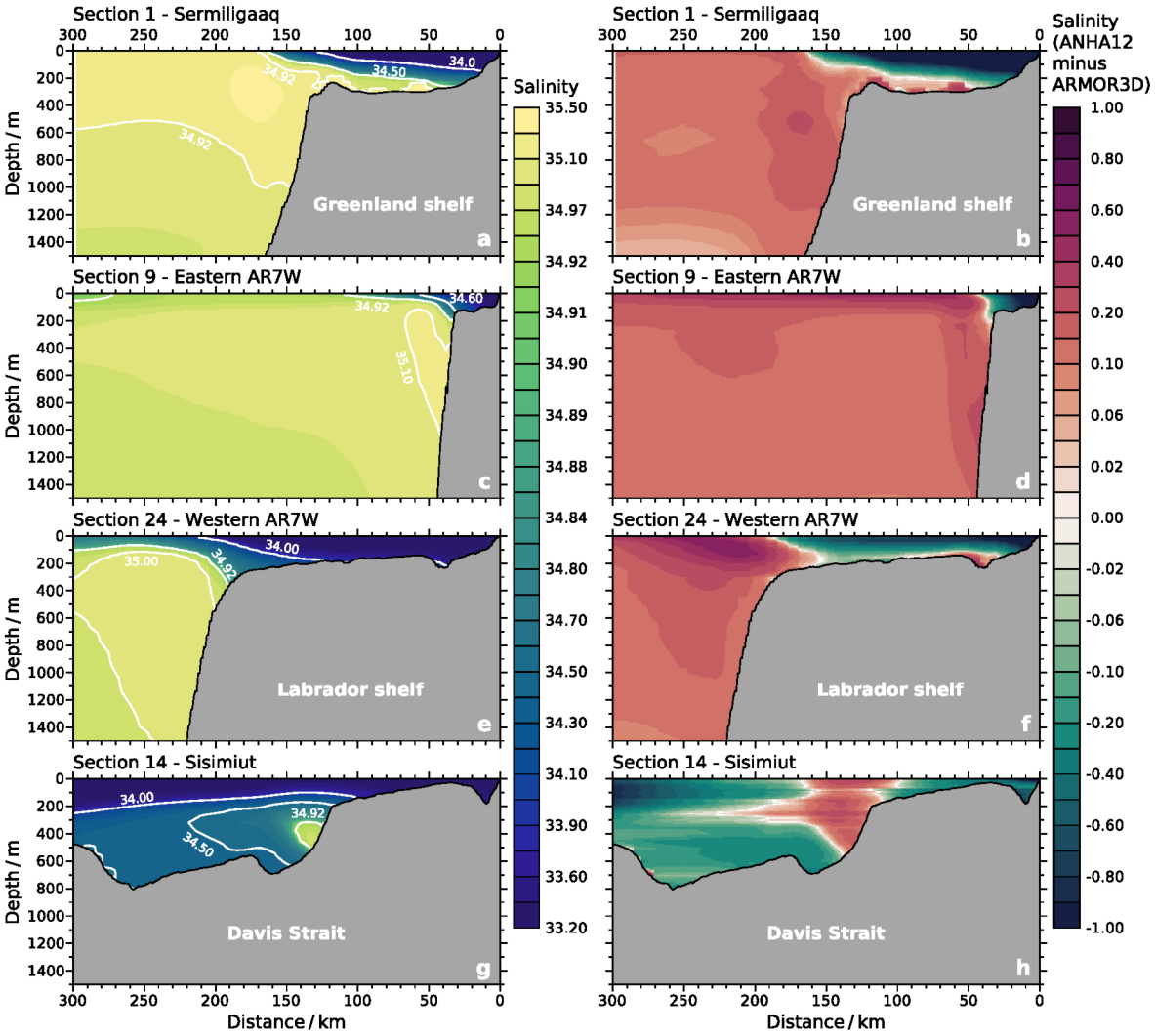

Figure 5.7: Similar to Figure 5.5 but for ANHA12.
ANHA12 salinity in the upper 1,500 m from the coast to a distance 300 km offshore averaged from 2002 - 2020 (left column). Anomalies with respect to ARMOR3D (right column). Sections from top to bottom: Sermiligaaq, Eastern AR7W, Western AR7W, and Sisimiut.

velocity at eastern AR7W in Figure E.3 c). Further offshore, when the velocities approach zero, GLORYS exhibits lower temperatures than ARMOR3D (Figure E.3 c and Figure E.1 d). ANHA4 and ANHA12 are warmer than ARMOR3D offshore from the shelf break by more than 1.5 °C at individual locations (Figure E.1). Notably, LAB60 reveals a distinct subsurface temperature maximum at the same location as GLORYS, ANHA4, and ANHA12 between ~100 and 600 m just offshore from the continental slope. In comparison, the maximum temperatures in ARMOR3D are more confined to a depth of ~200 m. The cross-section velocity fields are comparable across all data sets, with a strong WGC along the continental slope and decreasing velocities further

offshore (Figure E.3). However, the individual strengths of the WGC differ, and so does the comparison to ARMOR3D. All data sets exhibit higher velocities close to the continental slope compared to ARMOR3D and lower velocities further offshore. In ANHA4, the area of higher velocities is limited to the shelf break. At the same time, it is an isolated area in the upper 600 m isolated from the continental slope in LAB60. These differences, especially in temperature and velocity, must be considered when estimating the influence of IW on marine-terminating glaciers. However, a direct comparison between IW properties and melting rates of these glaciers is beyond the scope of this thesis.

5.3 Addressing the provenance and hydrographic methods

In the following, I present analyses that are required to apply the provenance and hydrographic methods in GLORYS, ANHA4, and ANHA12 for the analyses in Chapter 5.4 and Chapter 5.5.

5.3.1 The Irminger Sea as origin of Irminger Water

Following Chapter 4.2.2, I interpret the Irminger Sea provenance region as the origin of IW in the Irminger Sea. I have identified the Irminger Sea provenance region using ARMOR3D by isolating the area with higher salinities between 100 and 1,000 m depth in the averaged fields between 1993 and 2022. To gain a preliminary understanding of how the different data sets represent salinity in the SPNA, I initially compare the spatial distribution of the subsurface salinity maximum within the different data sets (Figure 5.8).

ARMOR3D

Analyzing the salinity maximum between 100 and 1,000 m in ARMOR3D (Figure 5.8 a) allows identifying the subpolar front that defines the boundary between the subpolar and subtropical gyre. Thus, the maximum salinities are low to the north and west of the subpolar front and high to the south and east of the subpolar front. The Davis Strait, separating the Labrador Sea and Baffin Bay, reveals another major horizontal front in the maximum salinity distribution. The difference between the maximum salinities in the Labrador Sea and Baffin Bay arises from the bathymetry. Since the primary path-

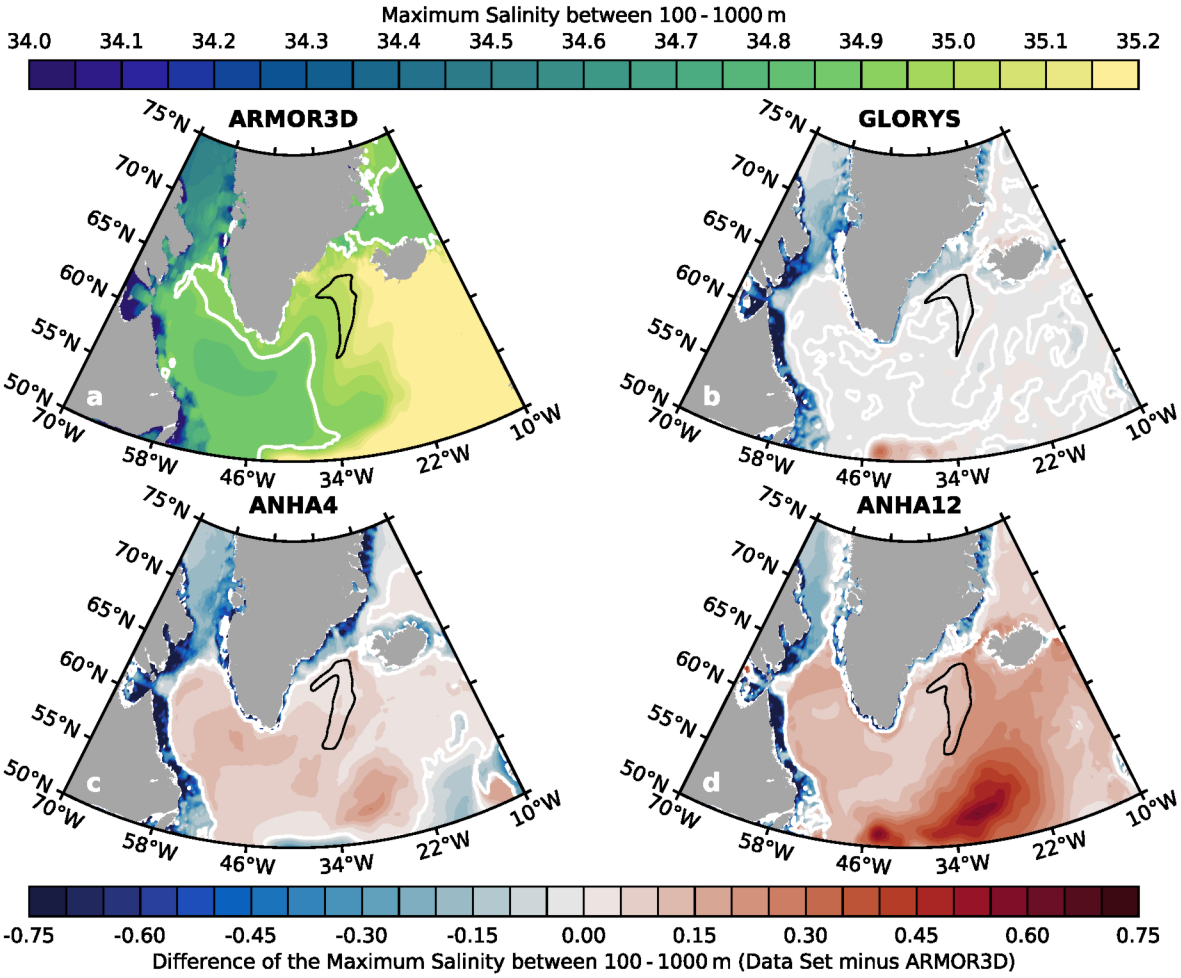

Figure 5.8: (a) Maximum ARMOR3D salinity within the water column from 100 - 1,000 m temporally averaged from 2002 - 2020. The other maps indicate differences between ARMOR3D and GLORYS (b), ANHA4 (c), ANHA12 (d), data set minus ARMOR3D. Black encompassed areas indicate the Irminger Sea provenance region (see Chapter 4.2.2). The white contour (a) denotes the 34.92 isohaline representing the IW_{stat} salinity threshold. The white contours (b - d) denote the line of zero difference between the salinity of the individual data sets and ARMOR3D.

way of the WGC follows the bathymetry and recirculates west- and southward in the Labrador Sea, only the upper and fresher portions of the WGC extend further northward into Baffin Bay (see, e.g., Chapter 4.4 and Figure 4.11). However, higher salinity maxima still exist along the deeper troughs in the Greenland shelf north of Davis Strait. I did not study these deep troughs in detail within this thesis. Thus, I cannot exclude that higher salinities in the troughs appear as artifacts within ARMOR3D. However, high salinities in these troughs align with observations from Holland et al. (2008) and Myers and Ribergaard (2013). I would expect that the seasonal coverage with sea ice is the major contribution to artificial signals in Baffin Bay. As the maximum seasonal

salinity within the cross-slope sections in Baffin Bay is aligned with the local sea ice concentration, further analyses would be needed to further elaborate of the high salinities in the deep troughs are an artifact or a physically meaningful signal inherited in ARMOR3D.

GLORYS

Comparing the ARMOR3D maximum salinity field in the North Atlantic with GLORYS (Figure 5.8 b) reveals only minor differences. Higher salinities in GLORYS are evident along the primary pathway of the NAC in the southern SPNA. Other parts of the SPNA are slightly more saline (< 0.05) in GLORYS than ARMOR3D. Noticeable differences are observed in the shelf areas where GLORYS is fresher by up to 0.75 in specific regions and between 0.1 and 0.4 in Baffin Bay and its adjacent fjords. It is striking that GLORYS, ANHA4, and ANHA12 reveal larger areas without data in shelf regions than ARMOR3D, although they have a higher horizontal resolution. This difference is either due to the higher vertical resolution of ARMOR3D at depths around 100 m as stated in Chapter 2.4 (Figure 2.2) or results from the process of interpolating the GLORYS, ANHA4, and ANHA12 fields toward the ARMOR3D grid to calculate the differences.

ANHA4

ANHA4 (Figure 5.8 c) exhibits both similarities and differences when compared to ARMOR3D. It exhibits higher salinities in the ocean basins than ARMOR3D and lower salinities in the shelf regions and Baffin Bay. However, the differences compared to ARMOR3D in the open ocean are more pronounced compared to GLORYS, reaching an average of 0.1 and up to 0.2 at the subpolar front around 30 °W.

ANHA12

The overall pattern of the subsurface salinity maximum in ANHA12 (Figure 5.8 d) is similar to that obtained in ANHA4. However, the differences compared to ARMOR3D in the open basins are larger than those in ANHA4, reaching values of 0.15 to 0.20 in the SPNA. The main pathway of the NAC exhibits even more substantial salinity differences. In this region, ANHA12 is more saline by up to 0.5 compared to ARMOR3D.

5.3.2 Irminger Water variability in the Irminger Sea provenance region

The salinity difference between the two ANHA simulations and ARMOR3D in the SPNA was expected. Garcia-Quintana et al. (2019) discussed a mean salinity model-observation difference of 0.1 to 0.2 for the ANHA4 and ANHA12 simulations within the Labrador Sea based on Yashayaev and Loder (2016) (their Figure 1 c). Differences of 0.2 have also been observed when comparing ship-based observations at Fylla Bank from Ribergaard (2014) to ANHA4 and ANHA12 simulations (Gillard, 2020). It is important to consider that a positive salinity bias resulting from model drift towards higher salinities (Treguier et al., 2005; Rattan et al., 2010) is to be expected. Notably, the higher maximum salinities in the Irminger Sea strongly influence the identification of the Irminger Sea provenance region when applying the provenance method (Chapter 4.2.2) to ANHA4 and ANHA12. As outlined in Chapter 4.2.2, the initial criterion to identify the Irminger Sea provenance region is to include areas with a subsurface salinity maximum of $S > 35.0$ between 100 and 1,000 m. Given the minor differences between GLORYS and ARMOR3D, the same criterion is applied in GLORYS. However, due to the higher salinities in ANHA4 and ANHA12, this criterion would encompass larger parts of the interior and southwestern Irminger Sea using the two model simulations. Consequently, I adjusted the minimum salinity to obtain the Irminger Sea provenance region based on the difference with ARMOR3D. I found that salinities of 35.05 for ANHA4 and 35.10 for ANHA12 more realistically represent the main IC path.

The Irminger Sea provenance regions exhibit slight variations across the individual data sets. In all data sets, the eastern and northern boundaries of the Irminger Sea provenance region follow the bathymetry of the Irminger Basin. This behavior excludes areas with a water depth $< 2{,}000$ m as described in Chapter 4.2.2. Toward the northwest, the Irminger Sea provenance region stretches, aligning with the main pathway of the IC (Figure 4.2 and Figure 5.8). In both ARMOR3D and GLORYS, the Irminger Sea provenance region does not extend far into the central Irminger Basin. As a result, it thus forms a more distinct tail along its southern boundary along Reykjanes Ridge. Similarly, in ANHA4 and ANHA12, the southern edge of the Irminger Sea provenance region includes a tail along Reykjanes Ridge, which is generally wider than what is observed in ARMOR3D and GLORYS. Across all data sets, the identified Irminger Sea provenance region closely resembles the major pathways of the IC. Therefore, these regions are utilized to apply the provenance method in the subsequent analyses.

To gain an initial understanding of IW variability in the Irminger Sea provenance region, I begin by analyzing IW properties using the static method (IW_{stat}) following Chapter 4.2.1 (Figure 4.3). The derived IW_{stat} properties in the respective Irminger Sea provenance regions exhibit distinct characteristics across the individual data sets (Figure 5.9).

ARMOR3D

In particular, ARMOR3D resembles the presence of the coldest and freshest IW_{stat} (Figure 5.9 a, b). Given that temperature predominantly influences density in the Irminger Sea, ARMOR3D has the highest densities compared to the other data sets (Figure 5.9 c).

GLORYS

The hydrography in GLORYS closely resembles that of ARMOR3D. In the 2010s, the salinity in GLORYS is comparable to ARMOR3D (Figure 5.9 a). However, during the 2000s, GLORYS shows a slightly higher salinity by about ~ 0.02. In the 1990s, GLORYS exhibits occasional fresher periods, displaying a higher level of multi-year variability. While the temperature in GLORYS is more similar to ARMOR3D when compared to ANHA4 and ANHA12, it remains warmer over the entire period, with differences reaching up to $\sim 0.3\,°C$ in the 1990s and 2000s (Figure 5.9 b). Notably, the differences compared to ARMOR3D become smaller in the late 2010s, reaching around $\sim 0.1\,°C$. Consequently, the largest positive difference (indicating warmer and more saline conditions) compared to ARMOR3D occurs during periods when the Irminger Sea provenance region experiences anomalously warm and saline conditions.

ANHA4 and ANHA12

The IW_{stat} properties of the two model simulations, ANHA4 and ANHA12, exhibit similar variability compared to ARMOR3D and GLORYS. Both simulations are characterized by higher salinities compared to ARMOR3D (ANHA4 by ~ 0.09, ANHA12 by ~ 0.13). These results align with the large-scale salinity analysis in the SPNA (Figure 5.8). Furthermore, both model simulations exhibit warmer conditions compared to ARMOR3D (ANHA4 by $\sim 0.7\,°C$, ANHA12 by by $\sim 1.1\,°C$). Their densities remain

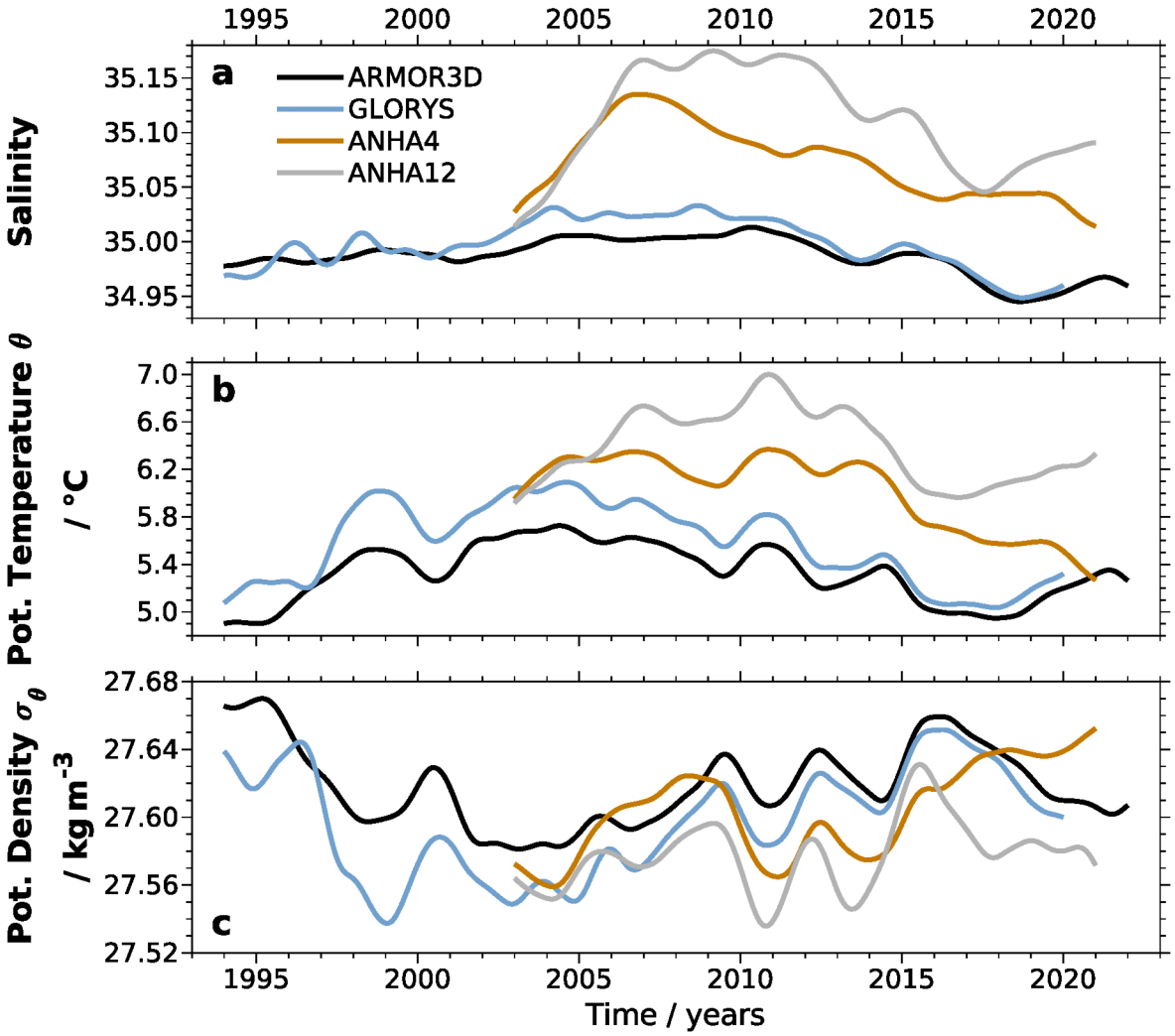

Figure 5.9: Irminger Water properties obtained with the static method in the Irminger Sea provenance region smoothed with a 2-year running average including a Hanning window. IW_{stat} from top to bottom: salinity, potential temperature θ, potential density σ_θ. Colors denote properties for different data sets: ARMOR3D (black), GLORYS (blue), ANHA4 (orange), ANHA12 (gray).

lower compared to ARMOR3D for most of the period, except for ANHA4 between 2006 and 2009, when the model salinity peaks and temporally exceeds the temperature contribution to density variations (Figure 5.9 c).

Despite the substantial hydrographic differences between ANHA4 and ANHA12 compared to ARMOR3D (and GLORYS), their decadal and multi-year variability exhibits similarities throughout the entire model period. All the analyzed data sets suggest peak salinities and temperatures in the late 2000s, followed by a decline until the late 2010s. This multi-year variability also agrees with the timing observed within the in-

dividual data sets and mirrors the density variations. As I have shown in Chapter 3, the multi-year variability of IW_{stat} at eastern AR7W is primarily shaped by the NAO and changes in size and strength of the SPG. According to the similar representation of IW_{stat} in the Irminger Sea provenance region across the different data sets, I suggest that these large-scale changes in the NAO and SPG are represented in all data sets. The differences in the magnitude are attributed to the general bias toward higher temperatures and salinities of ANHA4 and ANHA12 compared to ARMOR3D and GLORYS, as already shown in Figure 5.8.

5.3.3 From the Irminger Sea into the boundary current system

As discussed in Chapter 4.2.2, the provenance method relies on the calculation of the advection time between the Irminger Sea provenance region and the individual cross-slope sections. In this context, I extend the advection times analysis, previously performed for ARMOR3D (Chapter 4.2.2, Figure 4.4), to GLORYS, ANHA4, and ANHA12 (Figure 5.10). The estimation of advection times builds on addressing lag correlations for IW_{stat} salinity between the Irminger Sea provenance region and the individual cross-slope sections. The outcomes of these advection time calculations highlight notable differences among the four analyzed data sets.

GLORYS

In GLORYS (Figure 5.10 b), the advection times from the Irminger Sea provenance region to the individual cross-slope sections display a less linear behavior compared to those obtained in ARMOR3D (Figure 5.10 a; detailed analysis in Chapter 4.2.2). From the Irminger Sea provenance region to Maniitsoq (Section 13), GLORYS suggests an advection time of only 42 days (203 days for the linear regression in ARMOR3D). This advection time in GLORYS implies an average IW velocity of $\sim 0.55\,\mathrm{m\,s^{-1}}$. Such high velocities are reasonable for the BCS core but seem overestimated considering that the analyzed signal is averaged over the entire IW area encompassing regions with lower velocities further offshore. Moreover, these advection times raise questions, particularly given that an advection time of 341 days was calculated from the Irminger Sea provenance region to Aasiaat (Section 15, 245 days for the linear regression in ARMOR3D), which is only $\sim 400\,\mathrm{km}$ downstream of Maniitsoq. Furthermore, northward in Baffin Bay, the IW_{stat} is already fully mixed below the static threshold, rendering the

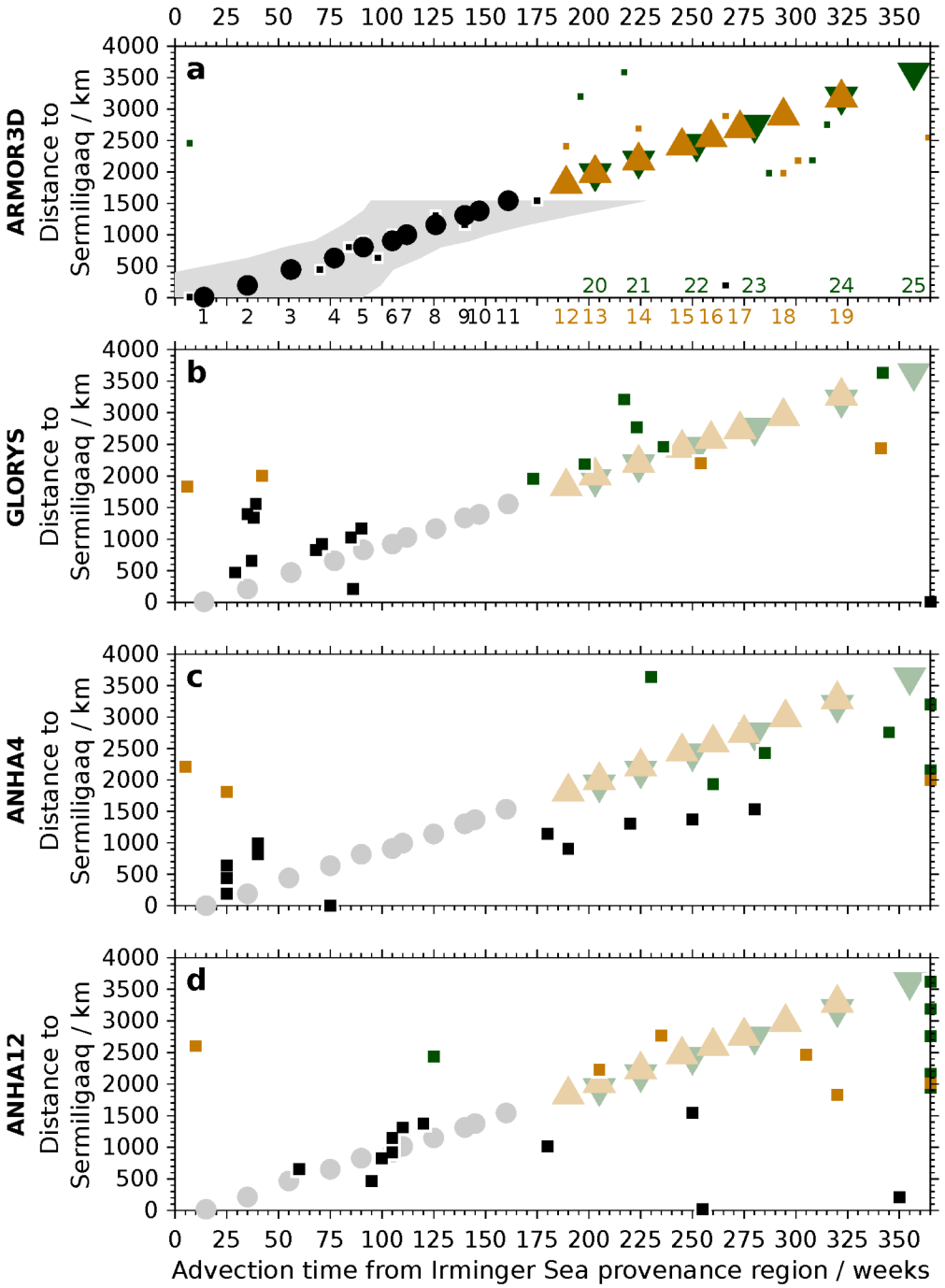

Figure 5.10: Advection times between the Irminger Sea provenance region (Figure 5.8) and individual cross-slope sections within the boundary current system into Baffin Bay and the western Labrador Sea. Rows denote different data sets (top to bottom: ARMOR3D, GLORYS, ANHA4, ANHA12). Squares indicate unfiltered advection times obtained following Chapter 4.2.2, Figure 4.4 (black: Sermiligaaq to Paamiut, orange: into Baffin Bay, green: into the western Labrador Sea). Circles and triangles indicate final advection times after applying a linear regression. The bottom numbers in (a) indicate the section number corresponding to the calculated advection time (see Table 5.1, Figure 5.2). The results obtained from the linear regression in ARMOR3D are repeated for GLORYS, ANHA4, and ANHA12 as opaque symbols and serve as their respective advection times.

calculation of advection times unfeasible. In contrast, the branch from the bifurcation at Paamiut (Section 11) into the Labrador Sea exhibits advection times and inferred current velocities that are more realistic. However, even in these cases, the calculated advection times also do not exhibit a clear increase with distance. Consequently, for subsequent analyses applying the provenance method in GLORYS, I have chosen to use the advection times calculated in ARMOR3D (Chapter 4.2.2).

ANHA4

In ANHA4 (Figure 5.10 c), the advection times calculated for the individual sections do not show any realistic pattern. For Sisimiut, an advection time of only one time step (here, five days) is estimated. These advection times would result in an averaged IW velocity of $\sim 5.1\,\mathrm{m\,s^{-1}}$ between the Irminger Sea provenance region and Sisimiut. That is one order of magnitude higher compared to ARMOR3D and GLORYS. Between individual sections, the advection times are more realistic. To reach eastern AR7W, for example, an advection time of 220 days (161 days for the linear regression in ARMOR3D), an equivalent of a mean IW velocity of $\sim 0.07\,\mathrm{m\,s^{-1}}$ is estimated. However, the overall calculated advection times at the individual sections do not fit. Consequently, I conclude that estimating advection times by calculating lag correlations between the $\mathrm{IW_{stat}}$ salinity in the Irminger Sea provenance region and the individual sections does not work in ANHA4. Consequently, similar to GLORYS, I have decided to use the advection times calculated in ARMOR3D (Chapter 4.2.2) when applying the provenance method in ANHA4 for future analyses.

ANHA12

Similar to ANHA4, the advection pattern in ANHA12 (Figure 5.10 d) does not show physically meaningful results. The advection times for the individual sections seem almost randomly distributed. Most sections downstream of Fylla Bank indicate advection times larger than one year. However, the entire pattern is questionable. Therefore, similar to GLORYS and ANHA4, I use the advection times calculated in ARMOR3D (Chapter 4.2.2) when applying the provenance method in ANHA12 for future analyses.

I suggest that the unrealistic advection times in the two model simulations indicate that the also unrealistic advection times in GLORYS result from the data assimilation. I can only speculate why the method of calculating advection times does not work for GLORYS, ANHA4, and ANHA12. As shown in Figure 5.9, the multi-year variability of the IW_{stat} properties in the Irminger Sea provenance region aligns across the individual data sets. The major differences between the data sets in calculating the advection times are their respective temporal resolutions. While ARMOR3D has a weekly temporal resolution, it is higher in GLORYS (daily) and the ANHA simulations (5 days). Consequently, the lag correlation analyses were conducted with data of different temporal resolutions, which might have been more vulnerable for temporal variability on smaller time scales. However, checking the correlations for all lags does not suggest such influences, as the maximum correlations were always clearly distinct from surrounding times (not shown). Thus, I cannot answer why calculating the advection times does not work for GLORYS, ANHA4, and ANHA12. Possible influences for following analyses are restricted, especially to the seasonal variability when analyzing the provenance method. On longer time scales, the effects of potentially wrongly attributed advection times are negligible.

5.3.4 Assessing the percentiles for the hydrographic method

The hydrographic method is based on specific percentiles that define the portions of the water column identified as IW_{hydro} (see Chapter 4.2.3.1). In the following, the performance of the percentiles, which has been optimized for ARMOR3D, is tested for GLORYS, ANHA4, and ANHA12 (Figure 5.11).

Overall, the temperature and salinity profiles at the four example sections (Sermiligaaq, eastern AR7W, western AR7W, and Sisimiut), averaged between 2002 and 2020, resemble each other across the individual data sets. The profiles agree with previous findings that highlight salinity differences in the data sets (e.g., Chapter 5.3.1 and Chapter 5.3.2). At Sermiligaaq, eastern AR7W, and western AR7W, ARMOR3D exhibits the coldest and freshest water column, followed by GLORYS, ANHA4, and ANHA12. Meanwhile, at Sisimiut, GLORYS and ANHA4 are colder and fresher than ARMOR3D. At the same time, ANHA12 remains the most saline and warmest data set at this location.

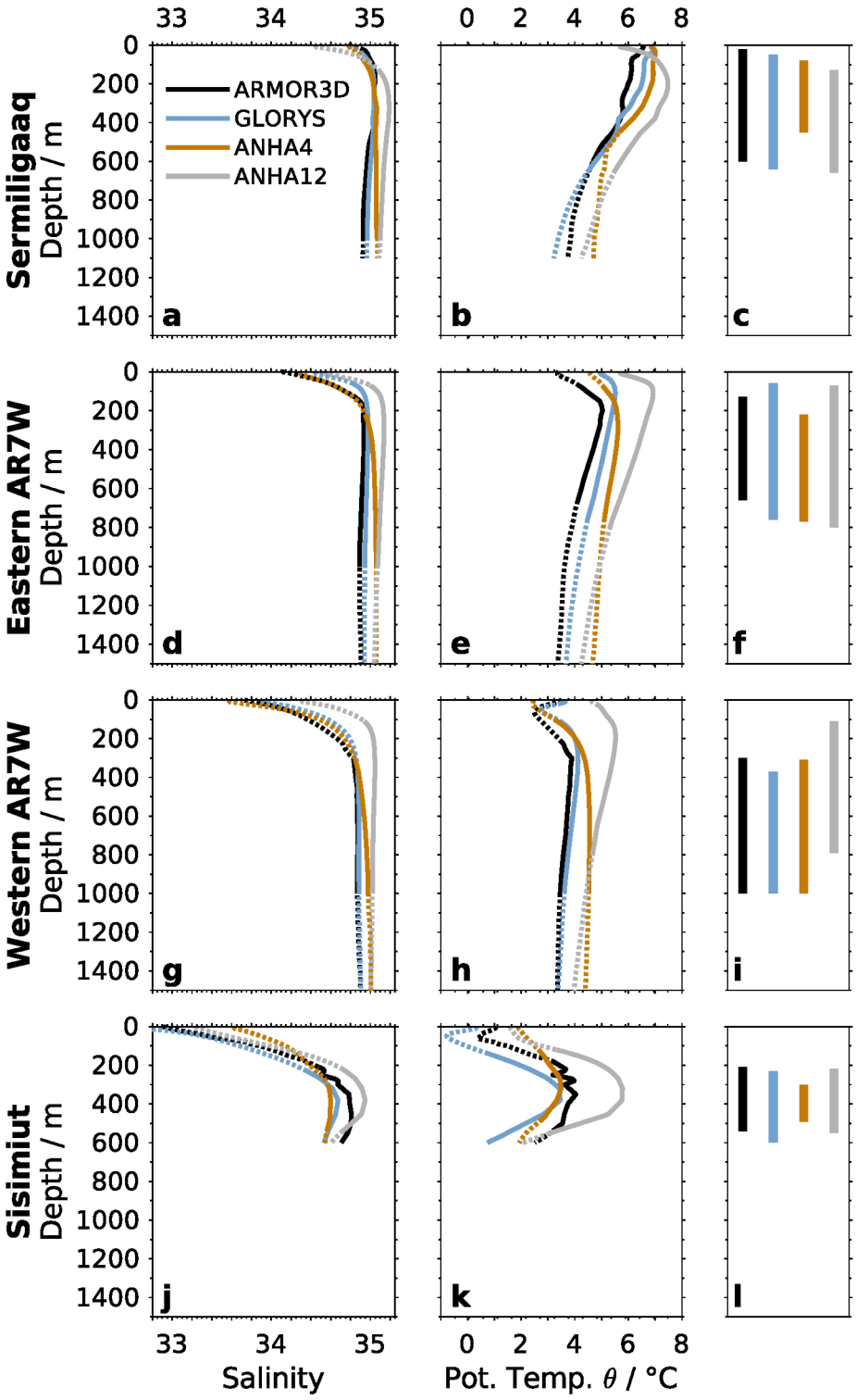

Figure 5.11: Based on Figure 4.5. Salinity (left column) and temperature (middle column) profiles averaged from 2002 - 2020 are shown as dashed colored lines. Overlaid solid lines denote identified IW_{hydro}. Colors indicate different data sets: ARMOR3D (black), GLORYS (blue), ANHA4 (orange), ANHA12 (gray). The right column denotes the depth range of the finally identified IW_{hydro} according to both thresholds. Rows show positions at the IW core from different sections (top to bottom: Sermiligaaq, eastern AR7W, western AR7W, Sisimiut).

The hydrographic method requires the identification of IW_{hydro} based on temperature and salinity (Chapter 4.2.3). When comparing the depths at which IW_{hydro} is identified, the smallest differences among the data sets are observed at eastern AR7W (Figure 5.11 f). In this region, IW_{hydro} extends over a depth of $\sim$500 m in ARMOR3D and ANHA4, and $\sim$650 m in GLORYS and ANHA12.

Further upstream in the BCS, at Sermiligaaq (Figure 5.11 c), ANHA4 reveals the lowest IW_{hydro} depth range ($\sim$300 m) compared to ARMOR3D, GLORYS, and ANHA12 ($\sim$600 m). This anomaly in ANHA4 may be attributed to the relatively high temperatures at greater depths (Figure 5.11 b and Figure F.4), which results in a reduced temperature range across the entire water column (Figure 5.11 b). Consequently, the temperature threshold, optimized for ARMOR3D with a larger vertical temperature range, confines the identification of IW_{hydro} to the upper $\sim$400 m at Sermiligaaq in ANHA4.

A similar reason is responsible for the IW_{hydro} representation at Sisimiut (Figure 5.11 j - l). Here, ARMOR3D, GLORYS, and ANHA12 again reveal a similar IW_{hydro} depth that stretches over $\sim$300 to 400 m (Figure 5.11 l). However, in ANHA4, IW only stretches over $\sim$200 m depth. The reasons for this small IW thickness are high near-surface temperatures accompanied by low temperatures at $\sim$400 m depth compared to the other data sets. Thus, the temperature range over the entire water column (Figure 5.11 k) is small and limits the representation of IW_{hydro}.

At the Labrador shelf, exemplified at western AR7W, the IW_{hydro} depth range expresses the largest differences within the individual data sets (Figure 5.11 i). For ARMOR3D, GLORYS, and ANHA4, IW_{hydro} is limited to the upper 1,000 m as defined in the hydrographic method (Chapter 4.2.3.1). Only in ANHA12 is IW_{hydro} limited to shallower depths (100 - 800 m). Here, the temperature profile differs strongly from the other data sets expressing a near-surface ($\sim$50 m) temperature minimum. ANHA12 does not exhibit such a temperature minimum, resulting in a relatively small temperature range and limiting IW_{hydro} to the upper 800 m.

5.4 Irminger Water at eastern AR7W

After studying hydrography at eastern AR7W within the individual data sets (Chapter 5.2) and discussing the mechanisms of the different methods to identify IW (Chap-

ter 5.3), I analyze IW properties at eastern AR7W in detail in the following. This analysis will explain how IW is characterized in the different data sets regarding water mass properties. As there will be differences across the data sets when utilizing the static method according to the general bias to higher temperatures and salinities, the following analyses will also show how the different methods deal with such large-scale biases. First, I analyze temperature and salinity at eastern AR7W by comparing T-S diagrams for the individual data sets (Figure 5.12). Afterward, I present the resulting salinity (Figure 5.13) and temperature (Figure 5.14) thresholds for the provenance and hydrographic methods. Following this, I present the IW frequencies at eastern AR7W, similar to Chapter 3.2 (Figure 3.4), for the individual data sets (Figure 5.15). Additionally, in line with Chapter 3.2, I present the IW frequencies for the three methods to identify IW. This 2-D analysis serves to understand better the functioning of the different methods to identify IW in the water column. Finally, I analyze the seasonal (Figure 5.16) and decadal variability (Figure 5.17) of IW properties obtained with the different methods and data sets.

5.4.1 Differences in temperature and salinity properties

I have compared the salinity at eastern AR7W among different data sets in Chapter 5.2 (Figure 5.3) and have found substantial differences. In the following, I focus on local hydrographic differences within the different data sets analyzing T-S diagrams of the upper 1,500 m (Figure 5.12). This analysis allows for examining the previously discussed salinity differences in the context of temperature differences and their consequences for water mass analyses at eastern AR7W. I address the T-S space for the entire climatology (Figure 5.12, left column) and for subperiods that describe times when IW_{stat} dominates the water column at eastern AR7W between mid-July and January (Figure 5.12, middle column) and when uISIW dominates the water column at eastern AR7W between March and mid-July (Figure 5.12, right column), following Chapter 3.3.3 (Figure 3.12).

ARMOR3D

The climatological analysis for ARMOR3D (Figure 5.12 a) indicates a distinct upper inflection of IW. The warmest and most saline IW has temperatures between 5.5 and 6.0 °C and salinities of 35.05. The highest point density, which is the number of neigh-

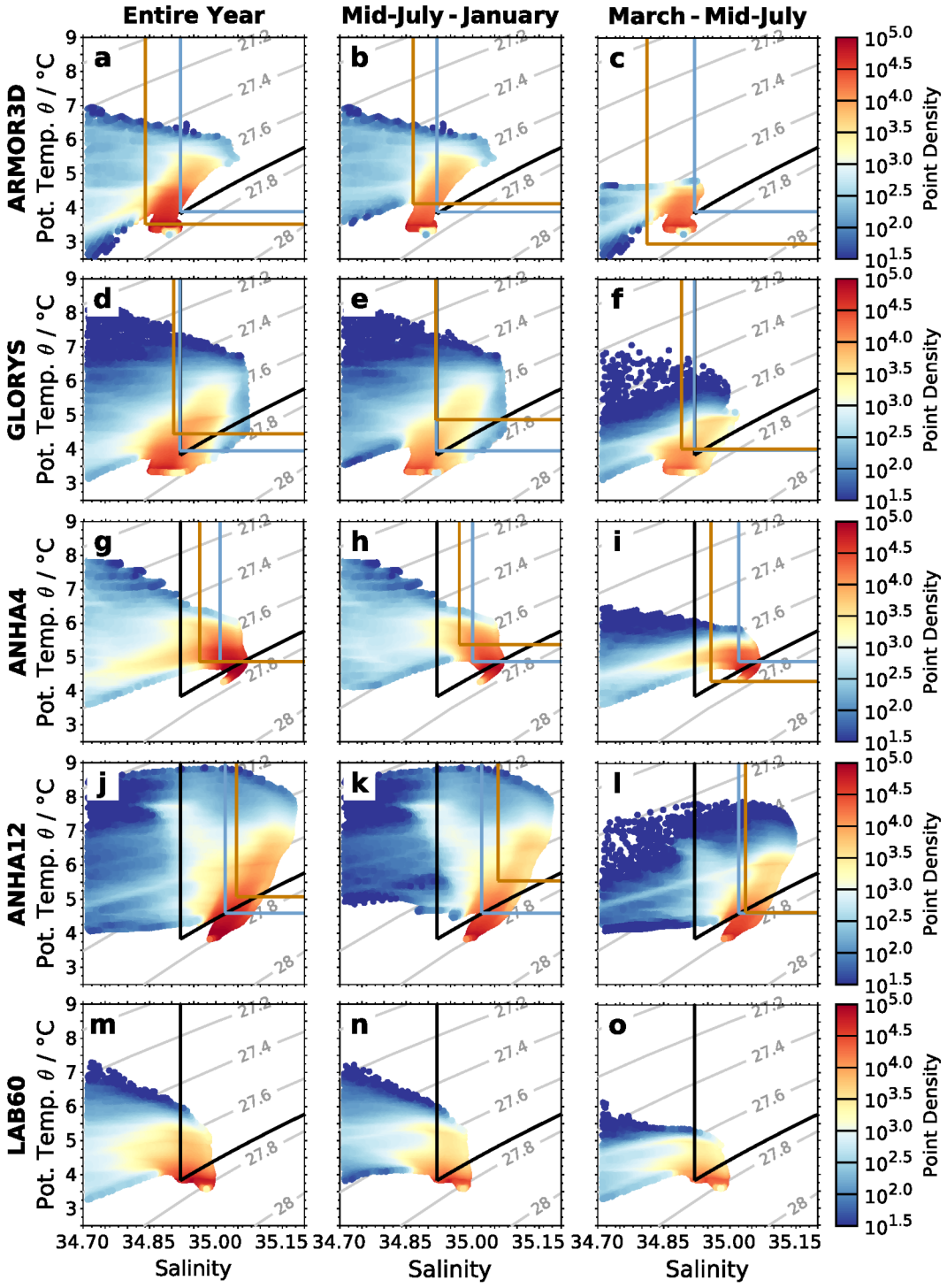

Figure 5.12: Climatological T-S diagrams at eastern AR7W from 2002 to 2020 (2004 to 2018 for LAB60) with vertical resolutions of 10 m. Isolines represent Irminger Water thresholds (IW_{stat}: black, IW_{prov}: blue, IW_{hydro}: orange). Marker colors show point densities as natural logarithmic distributions. The point density represents the number of points within a box spanning 0.05 °C in temperature and 0.05 in salinity. Rows denote individual data sets (top to bottom: ARMOR3D, GLORYS, ANHA4, ANHA12, LAB60). Columns denote different times of the year (left to right: entire year, mid-July to January, March to mid-July). Only every tenth point is plotted for GLORYS and LAB60.

boring points within a distance of 0.05 °C for temperature and 0.05 for salinity in T-S space, is identified for the deeper parts of uISIW (Le Bras et al., 2020), LSW (Kieke, 2005), and NEADW (Pacini et al., 2020). When comparing the periods mid-July to January, and March to mid-July, large differences in the hydrographic method are observed. In this context, the latter period includes the waters with the highest point densities. Consequently, the hydrographic method identifies parts of uISIW, LSW, and NEADW as IW_{hydro} as the maximum salinities and temperatures of IW are lowest in March - mid-July due to the modification caused by winter convective mixing in the Irminger and Labrador Seas (Le Bras et al., 2020, Chapter 3.3.3). In contrast, the static and provenance methods identify only a small amount of IW_{stat} and IW_{prov}. Consequently, the temperature and salinity ranges at eastern AR7W become smaller, and the water column colder and fresher. As a result, ambient waters (namely, uISIW, LSW, and NEADW) are identified as IW_{hydro}.

GLORYS

The GLORYS climatology exhibits a broader range of high salinity IW at lower temperatures (Figure 5.12 d). Consequently, IW is not as distinctly characterized in T-S space as in ARMOR3D with its upper inflection. The area of highest point densities is found within uISIW and LSW. However, in contrast to ARMOR3D, waters with high densities ($\sigma_\theta > 27.74$) also correspond to high salinities. Applying the density criterion to distinguish IW and ambient waters, as outlined by Pacini et al. (2020) and discussed in Chapter 3, might lead to misinterpretation between IW and NEADW since both exhibit high salinities but at different density levels.

ANHA4

In ANHA4 (Figure 5.12 g), the representation of IW in T-S space differs substantially from that in ARMOR3D and GLORYS. ANHA4 presents a similar T-S distribution of IW for high temperatures and salinities. However, waters with high point densities exhibit larger salinities. The highest point densities encompass IW, NEADW, and LSW. However, observed maximum salinities for LSW are within $S < 34.92$ (Yashayaev & Loder, 2017). In ANHA4, they exceed values of 35.05. Furthermore, fresher waters coincide with higher temperatures in ANHA4, resulting in the absence of uISIW.

ANHA12

ANHA12 differs from ARMOR3D and GLORYS in its representation of IW in T-S space (Figure 5.12 j). Like ANHA4, ANHA12 reveals LSW and NEADW with excessively high salinities and minimal uISIW presence. In general, eastern AR7W exhibits higher temperatures (reaching almost 9 °C) and salinities (approaching 35.2) in comparison to all other data sets.

Focusing on the period from mid-July to January, when IW_{stat} dominates at eastern AR7W, exposes minimal differences in higher temperatures and salinities compared to the entire climatology (Figure 5.12 middle column). This behavior is expected since the dominant IW_{stat} represents the region's warmest and most saline water mass. Therefore, deviations from the overall climatology only manifest in lower temperatures and salinities. These differences are evident across all data sets. In addition, all data sets indicate a minor reduction in point density, particularly noticeable for temperatures and salinities exhibiting the highest point densities.

Comparing the climatologies calculated for all months and for the subperiod between March and mid-July, when uISIW dominates the water column at eastern AR7W (Figure 3.12), indicates larger differences across all data sets (Figure 5.12 right column). As discussed in Chapter 3.3.1, Chapter 3.3.2, and Chapter 3.3.3, salinities decrease and almost fall below the IW_{stat} salinity threshold of $S = 34.92$ (Chapter 3.2 and Chapter 4.2.1). The same holds for the highest temperatures, which fall below 5 °C. Therefore, Atlantic-origin waters are colder and fresher between March and mid-July compared to the entire year. The presence of these waters when applying the static and provenance methods is limited.

In GLORYS (Figure 5.12 f), similar cooling and freshening occur from March to mid-July. However, numerous T-S points still fall within the IW domain. A possible explanation could be attributed to less modification to lower temperatures and salinities due to underestimated convection in the Irminger and Labrador Seas, which shapes IW variability on seasonal time scales (Pacini et al., 2020; Le Bras et al., 2020, Chapter 3). Another explanation could be linked to higher salinities in GLORYS compared to ARMOR3D along the continental slope at eastern AR7W (Figure 5.5 c, d). In the latter case, winter convection might still influence the cooling and freshening observed

in T-S space. However, it may not mix IW below the static salinity threshold. However, these possible explanations are speculative and require further analysis. ANHA4 (Figure 5.12 i) and ANHA12 (Figure 5.12 l) exhibit similar T-S patterns as GLORYS. However, ANHA4 is colder and more saline, while ANHA12 is warmer and more saline than GLORYS. LAB60 (Figure 5.12 f) shows the least differences between the different times of the year. As seen in Figure 5.3, LAB60 represents the coldest and freshest eastern AR7W compared to ANHA4 and ANHA12. Additionally, the T-S diagrams illustrate that IW is not realistically represented in LAB60. While ARMOR3D displays a distinct upper inflection, LAB60 lacks data showing a clear signal of simultaneous temperature and salinity maxima, aligning with previous analyses (Figure 5.3).

5.4.2 Irminger Water thresholds

In order to analyze the IW properties in the different data sets using different methods, I introduce the variability of the temperature and salinity thresholds for both the provenance and hydrographic methods at eastern AR7W. The salinity variability is shown in Figure 5.13, while the temperature variability is depicted in Figure 5.14. Their variability provides a better understanding of the variability of IW properties.

Provenance Method

The salinity thresholds for the provenance method (Figure 5.13, left column) indicate substantial differences within the different data sets on both seasonal (Figure 5.13 a) and multi-year time scales (Figure 5.13 b). On seasonal time scales (climatologically averaged between 2002 and 2020), the IW_{prov} salinity thresholds show few agreements within the individual data sets (Figure 5.13 a). In ARMOR3D, the yearly IW_{prov} salinity threshold minimum occurs in April and increases until its maximum in November. In GLORYS, the IW_{prov} salinity threshold minimum emerges in November, January, and February, and the maximum in August. Between August and November, the salinity thresholds of ARMOR3D and GLORYS evolve in reverse. The seasonality in ANHA4 differs from ARMOR3D and GLORYS. The minimum occurs in July/August, and the maximum emerges in April. The magnitude and amplitude exceed ARMOR3D and GLORYS. In ANHA12, the seasonal timing is closest to ARMOR3D, indicating a minimum in July and a maximum in December, while the amplitude in ANHA12 is smaller than in ANHA4 but similar to ARMOR3D and GLORYS. Like ANHA4, the

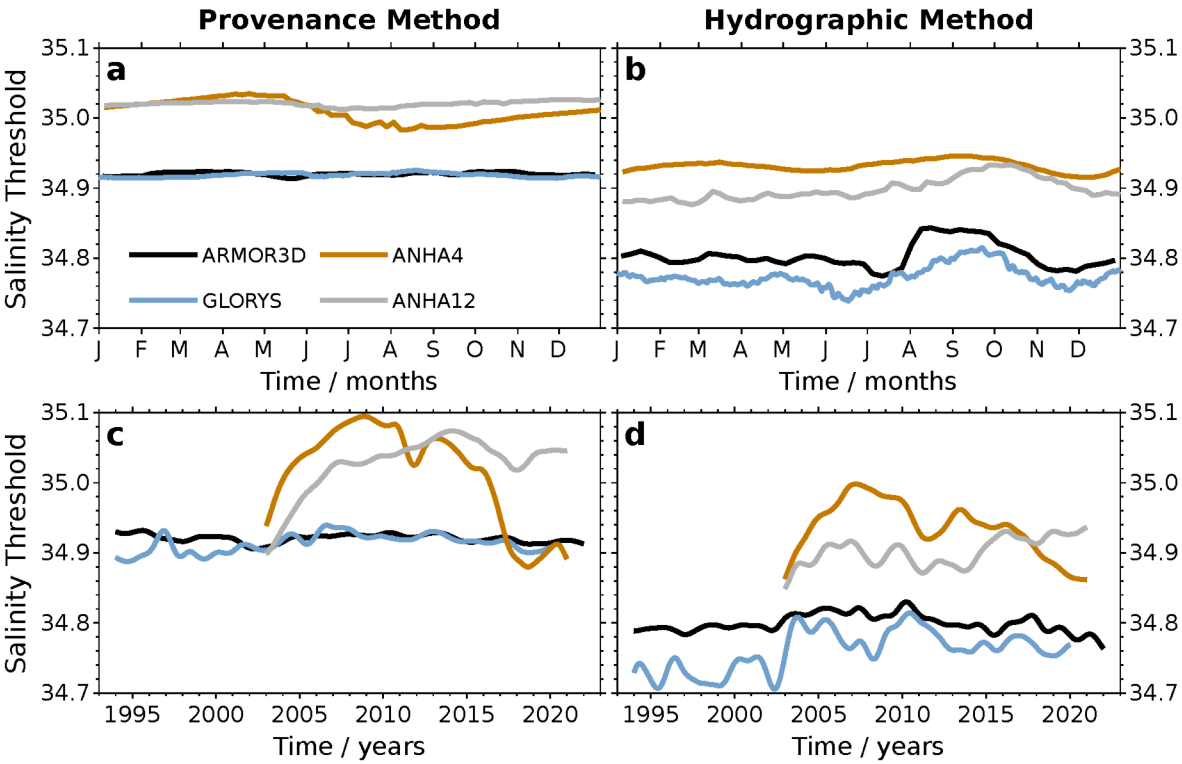

Figure 5.13: Irminger Water salinity thresholds at eastern AR7W for individual data sets: ARMOR3D (black), GLORYS (blue), ANHA4 (orange), ANHA12 (gray). Columns denote the Irminger Water salinity thresholds for the provenance (left column) and hydrographic method (right column). The upper row denotes seasonal variability climatologically averaged from 2002 - 2020, the lower row denotes multi-year variability.

magnitude in ANHA12 is higher than in ARMOR3D and GLORYS by ~ 0.1. However, this difference in magnitude between the two model simulations on the one side and ARMOR3D and GLORYS on the other side is expected, as I have shown before that the two ANHA simulations are more saline compared to ARMOR3D and GLORYS (e.g., Figure 5.3) at eastern AR7W. Additionally, within the entire SPNA, ANHA4 and ANHA12 are more saline. Thus, the Irminger Sea provenance region has been identified with already higher salinity criteria in ANHA4 and ANHA12 (Chapter 5.3.1, Figure 5.8), which is reflected in the higher salinity thresholds.

Although ARMOR3D and GLORYS show distinct multi-year variability (more clearly visible for ARMOR3D in Figure 4.8), the variability remains small compared to ANHA4 and ANHA12 (Figure 5.13 c). As indicated by the salinity difference in the Irminger Sea provenance region (Figure 5.8 and Figure 5.9), the two ANHA simulations are more saline compared to ARMOR3D and GLORYS. This difference is also reflected in the $\mathrm{IW}_{\mathrm{prov}}$ salinity threshold, where ANHA12 reveals a higher threshold throughout

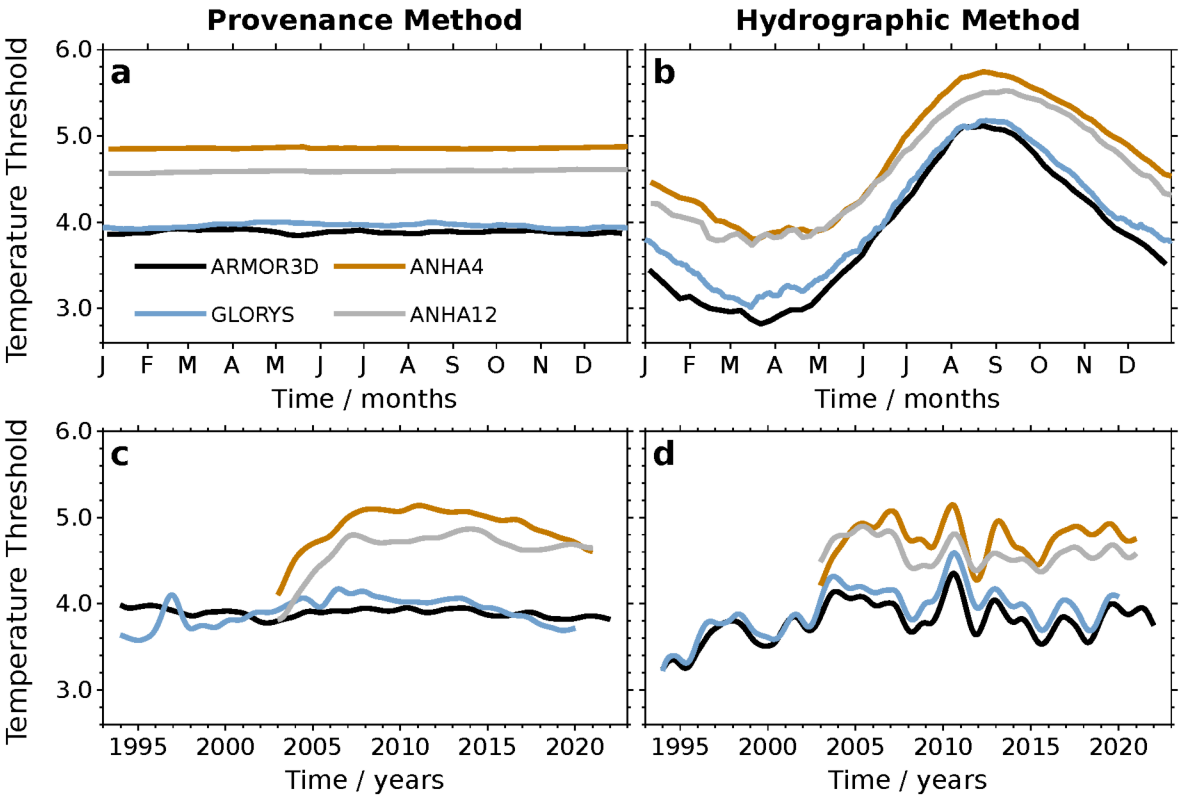

Figure 5.14: Similar to Figure 5.13 but for the temperature thresholds.
Irminger Water temperature thresholds at eastern AR7W for individual data sets: ARMOR3D (black), GLORYS (blue), ANHA4 (orange), ANHA12 (gray). Columns denote the Irminger Water salinity thresholds for the provenance (left column) and hydrographic method (right column). The upper row denotes seasonal variability climatologically averaged from 2002 - 2020, the lower row denotes multi-year variability.

the entire period. However, the salinity threshold of ANHA4 is only higher than ARMOR3D until 2017. After that, it becomes lower for the remaining time. This difference between ANHA4 and ANHA12 serves as another indicator that both reveal different salinity patterns in the Irminger Sea provenance region.

Hydrographic Method

The salinity thresholds for the hydrographic method (Figure 5.13, right column) indicate similar magnitude differences throughout both seasonal (Figure 5.13 b) and multi-year time scales (Figure 5.13 d). In contrast to the provenance method, the seasonal variability of the different data sets agrees better with the hydrographic method. The variability between ARMOR3D and GLORYS is alike. The IW_{hydro} salinity threshold in ARMOR3D indicates a rapid increase in July and August that agrees with the simultaneous increase of the IW_{stat} salinity shown in Chapter 3.3.1 (Figure 3.8).

On multi-year time scales, the large interannual variability within GLORYS in the 1990s is noticeable, as ARMOR3D only indicates low variability over that period. Compared to the provenance method, ANHA4 indicates a higher threshold than ARMOR3D and GLORYS throughout the period. Its salinity threshold exceeds those from ANHA12 by up to ~ 0.1 in the mid-to-late 2000s. This difference between ANHA4 and ANHA12 is explained by a more homogeneous water column at eastern AR7W in ANHA4 (Figure 5.11 d, e). Consequently, identifying the salinity thresholds via the percentiles results in lower values in ANHA12 than in ANHA4.

Temperature thresholds

The results for the temperature thresholds obtained using the provenance and hydrographic methods are presented in the following (Figure 5.14). On seasonal time scales, the IW_{prov} temperature thresholds in all data sets exhibit almost no variability (Figure 5.14 a). In contrast, the IW_{hydro} temperature threshold exhibits a large amplitude between a minimum in March and a maximum in August for all data sets (Figure 5.14 b). Like the salinity thresholds, the temperature thresholds are also higher in ANHA4 and ANHA12 than in ARMOR3D and GLORYS. The differences between the two ANHA simulations and ARMOR3D and GLORYS are larger at the times of the seasonal minimum ($\Delta T < 1\,°C$) compared to the times of the seasonal maximum ($\Delta T \sim 0.5\,°C$). On multi-year time scales, the variability of the IW_{prov} temperature thresholds (Figure 5.14 c) in GLORYS agrees best with ANHA12, showing a constant decrease from the late 2000s. However, the magnitude of the IW_{prov} temperature threshold in GLORYS is closer to ARMOR3D. For the hydrographic method (Figure 5.14 d), the variability of the IW_{hydro} temperature thresholds is similar across all data sets, with larger magnitudes in ANHA4 and ANHA12.

5.4.3 Irminger Water frequencies

Analyzing the IW frequencies illustrates the temporal distribution of IW at the given cross-slope section. In Chapter 3.3.1 (Figure 3.9), I used this illustration to depict differences in the positioning and occurrence of IW at eastern AR7W during two different times of the year. In the following, I use the IW frequencies between 2002 and 2020 to describe the differences in IW positioning and occurrence for the different methods and data sets at eastern AR7W (Figure 5.15).

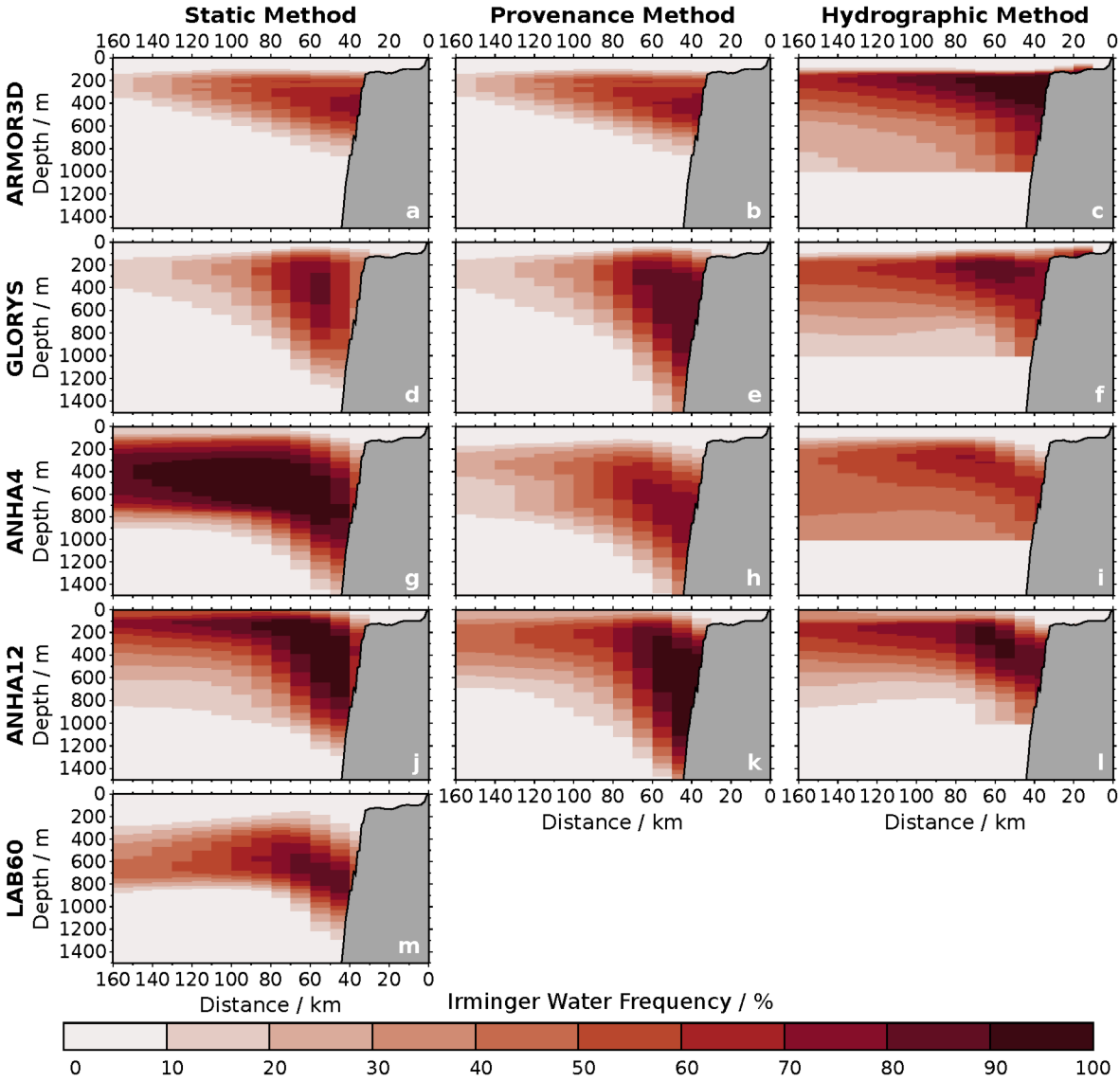

Figure 5.15: Irminger Water frequency (%) at eastern AR7W from 2002 - 2020 (2004 - 2018 for LAB60). Columns denote different methods (left to right: static, provenance, hydrographic method). Rows denote different data sets (top to bottom: ARMOR3D, GLORYS, ANHA4, ANHA12, LAB60).

ARMOR3D

Within ARMOR3D, the differences in the 2-D distribution of the IW_{stat} (Figure 5.15 a) and IW_{prov} (Figure 5.15 b) frequencies at eastern AR7W are negligible. This similarity is due to the temporal average of the IW_{prov} salinity threshold between 2002 and 2020 of $S \approx 34.9201$, which is only slightly higher compared to the static threshold of $S = 34.92$. The results are another indicator that the provenance method using temperature as the second IW_{prov} threshold provides physically meaningful results that resemble the results obtained with the static method using density as the second IW_{stat} threshold.

The IW_{hydro} frequencies are higher compared to IW_{stat} and IW_{prov} (Figure 5.15 c). As described previously (e.g., Chapter 4.2.3), the hydrographic method identifies waters with a simultaneous subsurface temperature and salinity maximum. Thus, I conclude that the IW_{hydro} frequencies of almost 100 % between 200 and 400 m depth close to the shelf break reveal that locally the vertical structure of the water column is preserved throughout the entire year. In addition, IW_{hydro} includes IW and ambient waters. This conclusion also holds when the water column is fresher in late spring and fall (Chapter 3.3.1). Thus, it becomes obvious that the hydrographic method describes a layer of maximum temperature and salinity. The identified IW_{hydro} is cut off at 1,000 m depth. This feature is due to the requirement not to allow IW_{hydro} below 1,000 m (see Chapter 4.2.3). Such a cutoff would be unphysical in the context of water mass analyses, as I have elaborated on the unrealistic cutoff of lower salinities in the static method (Chapter 4.4, Figure 4.11). However, IW_{hydro} as defined here does not represent a water mass but serves to describe the preserved vertical structure of the subsurface temperature and salinity maximum. Thus, the cutoff at 1,000 m depth does not affect the analysis or alter any conclusions about IW_{hydro}.

GLORYS

In GLORYS (Figure 5.15), the highest IW frequencies for the static and provenance methods follow the continental slope, agreeing with the high salinities (Figure 5.5). The general shape of the IW_{stat} (Figure 5.15 d) and IW_{prov} (Figure 5.15 e) frequencies is alike and similar to ARMOR3D. Both are identified to depths of almost 1,500 m close to the continental slope, while they are limited to the upper 800 m in ARMOR3D. However, the highest values are detached from the continental slope for the static method. In contrast, they are attached to the slope for the provenance method, where the area of high IW_{prov} frequencies is enlarged. The temporally averaged IW_{prov} salinity threshold between 2002 and 2020 is $S \approx 34.918$ and therefore, similar to ARMOR3D, close to the static threshold ($S = 34.92$). Consequently, the IW_{prov} frequencies are slightly higher than IW_{stat}. Like ARMOR3D, the hydrographic method also reveals a warm and saline subsurface water layer (Figure 5.15 f). The criterion that does not allow IW_{hydro} below 1,000 m cuts off the waters that follow the continental slope to greater depths. Here, the different methods reveal their largest differences compared to each other. According to the vertical salinity structure at eastern AR7W (Figure 5.3 c), the large amounts

of IW_{stat} and IW_{prov} at greater depths close to the continental slope may represent NEADW. As a result, local NEADW would be falsely identified as IW_{stat} and IW_{prov} due to the higher salinity at greater depths close to the continental slope compared to ARMOR3D. Therefore, it might be questioned if GLORYS realistically represents the vertical structure of the water column in terms of temperature and salinity.

ANHA4

ANHA4 reveals IW_{stat} frequencies between 90 and 100 % in depths from 200 to 800 m in the core region of the WGC, which is detached from the continental slope (Figure 5.15 g). This region of high IW_{stat} frequencies extends further offshore, up to 150 km and corresponds to a layer of warm and saline waters rather than a distinct water mass. The provenance method gives IW_{prov} frequencies rather similar to GLORYS than to ARMOR3D (Figure 5.15 h). Thus, the method can identify IW_{prov} in a physically reasonable area and occurrence but is also likely to include minor parts of NEADW at greater depths at the continental slope. The highest IW_{prov} frequencies are either located at the deeper subsurface salinity (Figure 5.3 e) or shallower temperature maximum (Figure E.1 e). Thus, the provenance method identifies IW_{prov} at depths between the respective maxima where both thresholds are fulfilled. The hydrographic method reveals IW frequencies that resemble a core of high values at a depth of 300 m, similar to GLORYS (Figure 5.15 i). ANHA4 still provides the highest IW frequencies at greater depths, indicating that more ambient waters are attributed to IW_{hydro}. The cutoff at 1,000 m in ANHA4 reveals the strongest boundary between IW_{hydro} and ambient waters compared to the other data sets.

ANHA12

For ANHA12, the IW_{stat} frequencies represent a mix between GLORYS and ANHA4 (Figure 5.15 j). An area with high frequencies close to the continental slope between ~200 and 800 m depth represents the IW core area as in GLORYS. However, high IW frequencies 160 km offshore in the upper ~ 400 m indicate a similar representation as in ANHA4, while the values decrease faster with increasing depth in ANHA12. For the provenance method, ANHA12 reveals similar IW_{prov} frequencies as GLORYS and ANHA4, especially close to the continental slope (Figure 5.15 k), where the frequencies

are the highest among all data sets. The IW_{hydro} frequencies are similar to GLORYS. An area of high frequencies at the upper continental slope and a tail reaching further offshore illustrate a layer of warm and saline waters. Like ANHA4, ANHA12 reveals extraordinarily high salinities at the continental slope of eastern AR7W (Figure 5.3 g). Hence, for ANHA12 as well, a realistic representation of the vertical structure of the water column might be questioned.

LAB60

For LAB60, only the IW_{stat} frequencies can be analyzed (Figure 5.15 m), as I have only extracted eastern AR7W from the LAB60 fields. The vertical shape of IW_{stat} compares well with ANHA4 and ANHA12. Thus, the core of IW_{stat} is located at greater depths compared to ARMOR3D and GLORYS. Horizontally, IW_{stat} follows the isohalines identified previously (Figure 5.3 i), forming a tail of lower frequencies further offshore. Although LAB60 does not reveal the excessive salinities that ANHA4 and ANHA12 show, the vertical structure of the water column does not resemble ARMOR3D (Figure 5.3 j) and other in-situ observations (Figure 3.4 a and Figure A.1).

The analysis of IW frequencies in the different data sets at eastern AR7W illustrates that a given static IW threshold provides fundamentally different results when applied to the individual data sets with varying representations of salinity. Here, ANHA4 and ANHA12 generally exhibit higher salinities than ARMOR3D and GLORYS. Consequently, similar static salinity thresholds identify more IW_{stat} in ANHA4 and ANHA12. Therefore, when using static thresholds is desired, these thresholds should be chosen specifically for the individual data set. However, similar to the results in Chapter 4.3 for ARMOR3D, the provenance method can identify IW_{prov} in a physically reasonable space and time. As the provenance method gets the threshold from the analyzed data set, it automatically corrects for systematic hydrographic biases, assuming they are spatially uniform. However, each method still depends on the correct representation of the water column structure, especially the hydrographic method. The IW_{hydro} frequencies already indicate similar distributions across the different data sets. The remaining differences could be corrected for, when slightly adjusting the percentiles for each data set individually.

5.4.4 Irminger Water properties

Analyzing the IW frequencies showed the spatial extent of the different IW types and their rate of occurrence at eastern AR7W. However, the analysis did not provide insights into the temporal variability of the IW properties, such as salinity, temperature, geostrophic velocity, and volume transport. Therefore, I present seasonal and multi-year variability of IW properties in the following focusing at eastern AR7W. In Chapter 3.3, I presented such results only for ARMOR3D and the static method. Chapter 4.3 added results from ARMOR3D for the provenance and hydrographic methods. The next step is to compare these results obtained with ARMOR3D to the other data sets - GLORYS, ANHA4, and ANHA12 (and LAB60 only for the static method). First, I analyze the seasonal variability of IW properties (Figure 5.16), followed by the analysis of multi-year variability (Figure 5.17).

5.4.4.1 Seasonal variability

As emphasized in previous analyses, ANHA4 and ANHA12 are generally warmer (Figure E.1) and more saline (Figure 5.3) compared to the other data sets at eastern AR7W. Similarly, when analyzing the resulting IW salinities and temperatures (Figure 5.16 and Figure 5.17), ANHA4 and ANHA12 generally reveal higher values. These differences, compared to ARMOR3D, GLORYS, and also LAB60, occur for all three different methods. Additionally, GLORYS is warmer and more saline than ARMOR3D, although the difference is smaller compared to ANHA4 and ANHA12.

Static Method

For the static method, IW_{stat} (Figure 5.16 a) salinities in ARMOR3D, GLORYS, and ANHA12 indicate a similar seasonality with the lowest salinities in late spring and summer and the highest salinities in fall and winter. However, only ARMOR3D reveals the previously sharp increase in July/August (see Chapter 3.3.1, Figure 3.8), while GLORYS and ANHA12 indicate a smooth increase between the seasonal minimum and maximum. As previously described in Chapter 3.3.1, I cannot prove or disprove whether this rapid salinity jump in ARMOR3D is a valid signal. The seasonal variability in ANHA4 does not agree with the other data sets. IW_{stat} salinities in ANHA4 exhibit a plateau of the highest seasonal values between May and October.

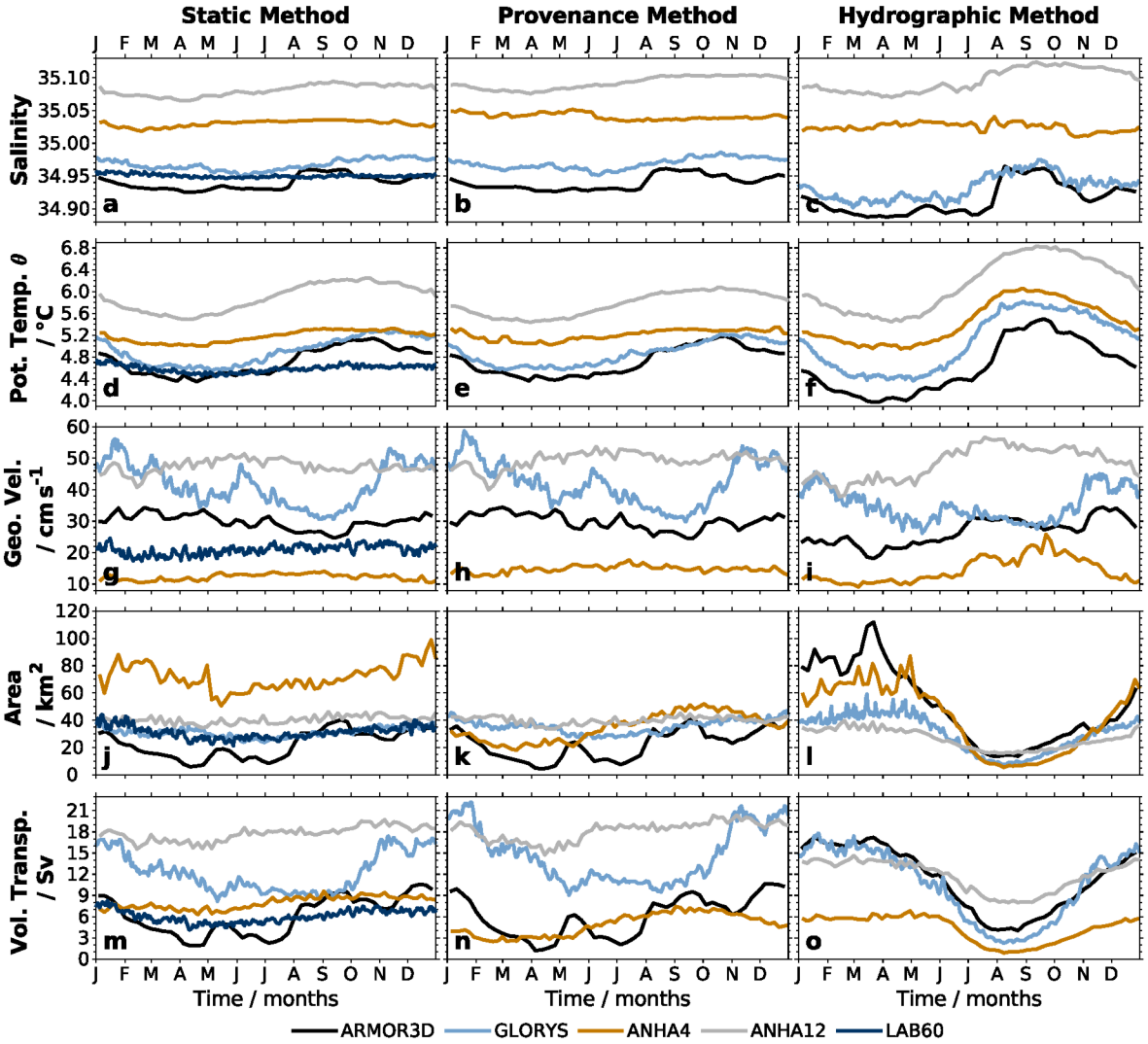

Figure 5.16: Climatological Irminger Water properties (top to bottom: salinity, potential temperature θ, geostrophic velocity, area, volume transport) at eastern AR7W averaged from 2002 - 2020. Colors indicate individual data sets: ARMOR3D (black), GLORYS (light blue), ANHA4 (orange), ANHA12 (gray), LAB60 (blue) from 2004 - 2018). Columns denote different methods (left to right: static, provenance, hydrographic method.

The seasonal variability for the IW_{stat} temperatures agrees well within the individual data sets.

Besides the hydrographic parameters, the downstream geostrophic velocity reveals seasonal variability (Figure 5.16 g). Generally, GLORYS and ANHA12 reveal higher IW_{stat} velocities compared to ARMOR3D. Especially the amplitude in GLORYS stands out, varying between 30 cm s^{-1} in September and 55 cm s^{-1} in January. For comparison, ARMOR3D varies by less than 10 cm s^{-1} between its seasonal minimum and maximum. The amplitudes are also small in ANHA12 and ANHA4. However, ANHA12

exhibits velocities of around 45 to 50 cm s^{-1}, while ANHA4 exhibits velocities of around 12 cm s^{-1}. Previously, it has been shown that the velocity in ARMOR3D is not responsible for shaping the variability of the IW_{stat} volume transport, but the area covered by the water mass (Chapter 3.3.2, Pacini et al., 2020). Comparing the IW_{stat} area (Figure 5.16 j) with the resulting IW_{stat} volume transport (Figure 5.16 m), this coherence becomes obvious. In GLORYS, the velocity dominates the volume transport. The large seasonal velocity differences outweigh the change in the area. As a result, the volume transport varies between 9 and 17 Sv for the static method. For ANHA4, the seasonality of the IW_{stat} volume transport is shaped by the velocity, for ANHA12 by the area. However, the magnitude is dominated by the higher salinities and temperatures compared to ARMOR3D. ANHA12 shows the highest IW_{stat} volume transport of up to almost 20 Sv, while ARMOR3D reveals the lowest, varying between 2 and 10 Sv.

LAB60 reveals minimal seasonal variability for all analyzed parameters. Its magnitudes are closest to ARMOR3D. However, the salinity distribution at eastern AR7W (Figure 5.3) and the IW_{stat} frequencies (Figure 5.15 k) have already suggested that IW is not correctly represented in LAB60. The salinity constantly increases with depth. Applying the static method divides the upper fresher depths from the deeper, more saline depths. Hence, the properties shown in Figure 5.16 approximately represent hydrography in a layer between $\sim$400 and 800 m. The agreement of the LAB60 magnitude with ARMOR3D is thus suggested not to be interpreted as similar representation of IW.

Provenance Method

Differences between the static and provenance methods for IW_{prov} salinities (Figure 5.16 b) are minimal. Similarly, ARMOR3D, GLORYS, and ANHA12 have their respective seasonal minimum in late spring and summer and their maximum in fall and winter. Changes for ANHA4 are more pronounced, revealing a maximum of IW_{prov} salinity in May and a minimum between June and November. Similar to the IW_{prov} salinity, the seasonal variability for the IW_{prov} temperature is like the variability for the static method.

This behavior changes for the provenance method (Figure 5.16 n). Here, the IW_{prov} volume transport in ANHA4 decreases to the approximate level of ARMOR3D due to the smaller IW_{prov} area. This result illustrates that the provenance method can incor-

porate systematic biases in the individual data sets into identifying the IW_{prov} area. As a result, it corrects the identified area against this bias. Differences in the identified area result from other differences like the vertical structure of the water column, horizontal structures of the WGC, or the representation of the IW_{prov} location in general (compare to Figure 5.15). The IW_{prov} volume transport in ANHA12 does not change compared to IW_{stat}.

Hydrographic Method

Also, for the hydrographic method, the variability of IW_{hydro} salinities (Figure 5.16 c) is similar to the two previously analyzed methods for ARMOR3D, GLORYS, and ANHA12. The increase in IW_{hydro} salinity in GLORYS is steeper compared to IW_{stat} and IW_{prov}. However, this increase is still not as steep as in ARMOR3D. IW_{hydro} salinity for ANHA4 indicates almost no seasonal variability. The seasonal variability for IW_{hydro} temperature agrees well within the individual data sets. However, the amplitude is highest for the hydrographic method, as seasonally more ambient waters are identified as IW_{hydro} and, thus, increase seasonal differences.

The seasonal variability of the IW_{hydro} volume transport differs strongly compared to the static and provenance methods. The seasonal time series is shifted by almost half a year and exhibits a minimum in August and a maximum from January to March across all data sets. This pattern approximately resembles the seasonal variability of a combination of IW_{stat} and uISIW (Figure 3.8), emphasizing once more that IW_{hydro} contains ambient waters with a similar vertical structure of the water column like uISIW.

5.4.4.2 Multi-year variability

The multi-year variability is presented in Figure 5.17. I further refer to the standardized time series (Figure 5.18) to highlight specific aspects of the multi-year variability.

Static Method

For the static method, the multi-year variability of the IW_{stat} salinity agrees well within the individual data sets (Figure 5.17 a). Like the seasonal variability, ANHA4 and ANHA12 stand out with the highest salinities and temperatures throughout the model

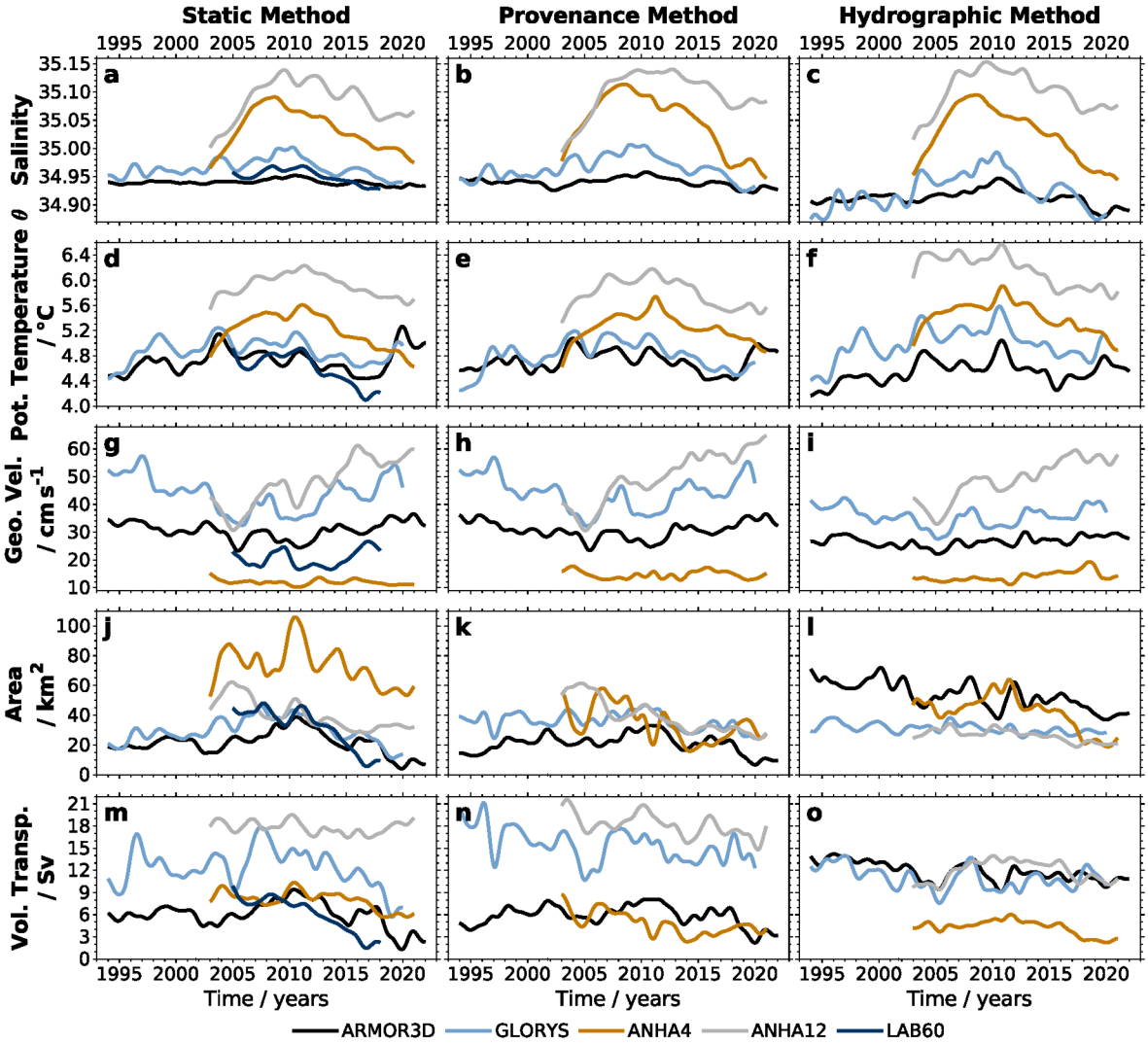

Figure 5.17: Irminger Water properties (top to bottom: salinity, potential temperature θ, geostrophic velocity, area, volume transport) at eastern AR7W. Colors indicate individual data sets: ARMOR3D (black), GLORYS (light blue), ANHA4 (orange), ANHA12 (gray), LAB60 (blue). Columns denote different methods (left to right: static, provenance, hydrographic method.

period. Notably, ANHA4 reveals the smallest IW_{stat} velocities accompanied by the largest area, resulting in volume transports that are close to the ARMOR3D. The multi-year variability of the IW_{stat} volume transport is smallest in ANHA12, revealing almost no changes within the 20 years. All other data sets show a clear decrease in IW_{stat} volume transports.

Provenance Method

Similar to previous results obtained with ARMOR3D (Chapter 4.9), applying the provenance method increases the salinity amplitude of the multi-year variability and reduces the volume transport amplitude. This behavior holds for GLORYS and ANHA4, although the differences between the static and provenance methods are smaller than in ARMOR3D. Applying the provenance method strengthens a negative volume transport trend for ANHA12 (static: -0.50 Sv per decade, provenance: -1.75 Sv per decade). This negative trend opposes a strong positive velocity trend that is already pronounced for the static method (static: 14.3 $\mathrm{cm\,s^{-1}}$ per decade, provenance: 16.4 $\mathrm{cm\,s^{-1}}$ per decade). Consequently, the IW area in ANHA12 is smaller in 2021 compared to the start in 2002 (static: -15.9 $\mathrm{km^2}$ per decade, provenance: -19.2 $\mathrm{km^2}$ per decade). In ANHA4, the mechanics of the provenance method become nicely visible. As the velocities in ANHA4 are generally low in the area of the IW core close to the continental slope (Figure E.3), the change in the IW area largely determines its final volume transport.

Hydrographic Method

The most notable feature in the hydrographic method is that the $\mathrm{IW_{hydro}}$ volume transport for ARMOR3D, GLORYS, and ANHA12 reveal similar values, while they were off by more than 10 Sv between ARMOR3D and ANHA12 for the static and provenance methods. Only ANHA4 indicates smaller $\mathrm{IW_{hydro}}$ volume transports, which is attributed to the smaller $\mathrm{IW_{hydro}}$ area compared to the other data sets.

Standardized time series

The differences within the individual data sets primarily result from their different magnitude. At the same time, the variability of all parameters agrees well. To highlight these characteristics, I assess standardized time series of the IW properties (Figure 5.18). For the $\mathrm{IW_{prov}}$ and $\mathrm{IW_{hydro}}$ area, the standardized time series show the variability agreement between ARMOR3D and GLORYS. This agreement is not as well identifiable in the non-standardized analysis. The only larger difference between the data sets is that ANHA4 and ANHA12 reveal differences in the $\mathrm{IW_{prov}}$ and $\mathrm{IW_{hydro}}$ area around 2005 and 2010 and, as a consequence thereof, also do not agree with ARMOR3D and GLORYS in the volume transport. In ANHA4, the $\mathrm{IW_{prov}}$ volume

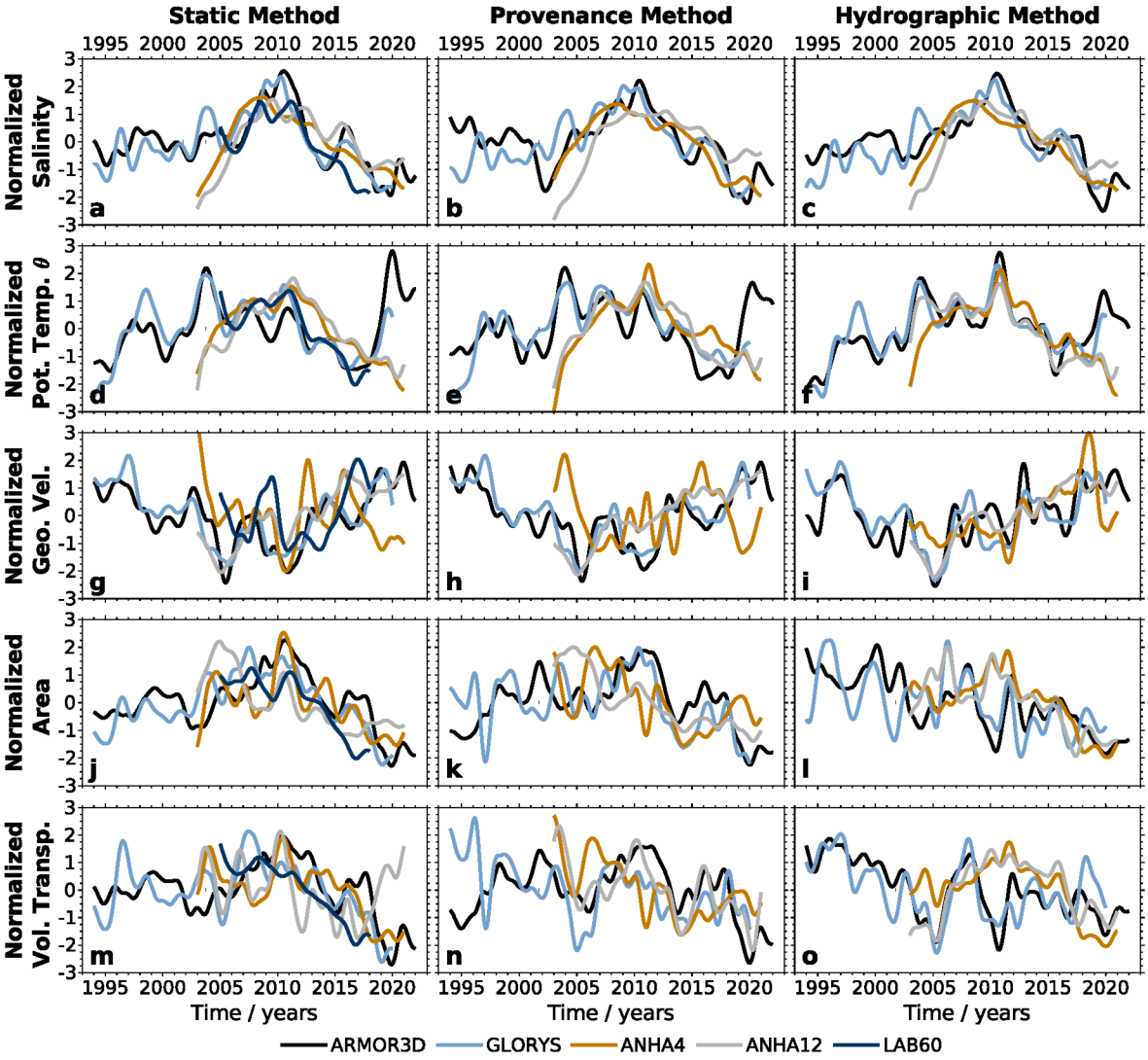

Figure 5.18: Similar to Figure 5.17 but for standardized time series.
Standardized Irminger Water properties (top to bottom: salinity, potential temperature θ, geostrophic velocity, area, volume transport). Colors indicate individual data sets: ARMOR3D (black), GLORYS (light blue), ANHA4 (orange), ANHA12 (gray), LAB60 (blue). Columns denote different methods (left to right: static, provenance, hydrographic method.

transport decreased until 2017 and increased afterward (Figure 5.18 n), while the IW_{stat} volume transport decreased almost continuously (Figure 5.18 m). The reason for this difference is the IW_{prov} salinity threshold for ANHA4, which is higher than the static threshold by a difference of $\sim$0.15 before 2017 and lower by a difference of $\sim$0.03 afterward (Figure 5.13). Throughout the entire period, the overall IW_{prov} volume transport was smaller compared to the IW_{stat} volume transport. This reduced volume transport resulted from the generally smaller IW_{prov} area compared to the IW_{stat} area (Figure 5.17 j, k and Figure 5.15 g, h).

Analyzing the multi-year variability of different IW properties for the individual methods and data sets reveals that the newly developed methods in Chapter 4.2 can also be applied to data sets other than ARMOR3D. For example, the difference in the ANHA4 volume transport between the static and the provenance method strengthens the results of Chapter 4.3, where ARMOR3D was used to show that using the static method, IW_{stat} volume transports were overestimated in times of a warm and saline BCS and underestimated in times of a cold and fresh BCS. For ANHA4, the provenance method corrects the general salinity bias. It thus adjusts the area of identified IW_{prov} to match the other data sets better. Applying the hydrographic method, the IW_{hydro} volume transports of ARMOR3D, GLORYS, and ANHA12 come closer together. For the static and provenance methods, differences between these data sets are large ($\sim 10\,Sv$), while the IW_{hydro} volume transports are almost identical. These results indicate that despite the differences in representing the subsurface temperature and salinity maximum in the water column, the hydrographic method identifies the same volume transports of the most saline and simultaneously warmest waters as IW_{hydro}.

5.5 Variability in the boundary current system

In this chapter, I analyze the BCS in ARMOR3D, GLORYS, ANHA4, and ANHA12, from the Irminger Sea into Baffin Bay and the western Labrador Sea. First, I present its mean hydrography in Chapter 5.5.1. In Chapter 5.5.2, I present the salinity distribution in four example sections, following Figure 4.11. Following that, I analyze the spatial variability of the IW properties within the BCS in Chapter 5.5.3 and discuss the IW thickness in the entire SPNA in Chapter 5.5.4.

5.5.1 Spatial hydrographic variability in the boundary current system

The following analysis investigates the spatial variability at the two along-slope sections that follow the 1,500 m isobath within the BCS in the different data sets (Sections 26 and 27, see Figure 5.2). These sections represent the main branches of IW within the BCS propagating into the Baffin Bay and the western Labrador Sea and allow the continuous tracking of the water over more than 3,000 km. The section is disrupted at Davis Strait for the Baffin Bay branch due to its shallow depth. Therefore, the position of the 1,500 m isobath was linearly interpolated between the Labrador Basin and Baffin

Bay. However, this does not ensure capturing the correct WGC pathway between Fylla Bank and Sisimiut (for the exact locations, refer to Figure 5.2 and Table 5.1). Thus, it is possible that at these locations, temperatures and salinities from outside the WGC affect the analysis.

In the following, I present mean states of the two 1,500 m isobath sections first for ARMOR3D (Figure 5.19). Subsequently, I compare the results for the other three data sets with ARMOR3D. The respective figures are presented in the Appendix (GLORYS: Figure F.1 and Figure F.2, ANHA4: Figure F.3 and Figure F.4, and ANHA12: Figure F.5 and Figure F.6). Although the two sections follow the 1,500 m isobath, the local bathymetry can still be shallower or deeper than 1,500 m. This results from choosing the grid point closest to the 1,500 m isobath in the individual data sets. For a better comparison between the data sets, I included the local bathymetry of ARMOR3D into the sections for GLORYS, ANHA4, and ANHA12 as well.

ARMOR3D

Along both the Baffin Bay and the Labrador Sea branches, the maximum subsurface salinities and temperatures indicating IW are subducted to greater depths with increasing distance from the Irminger Sea (Figure 5.19). This general behavior is in agreement with Spall and Pickart (2001), who stated that the sinking of water is restricted along the boundaries, accompanied by an along-boundary horizontal density gradient (Figure 5.19 e, f). Between Fylla Bank and Sisimiut (Sections 12 and 14), temperature and salinity indicate a rapid decrease and only minor remnants propagate further northward between $\sim$400 and 600 m depth (Figure 5.19, left column). However, this analysis only represents the mean state. Analyzing IW_{hydro} properties at these sections near Davis Strait suggests large seasonal variability (Appendix G, Figure G.1). This large seasonal variability agrees with local mooring observations (Curry et al., 2014). Curry et al. (2014) revealed seasonal variability at Davis Strait, with the highest volume transport of Atlantic-origin waters in winter and lowest in summer. These results agree with the seasonal variability of IW_{stat} salinity (Figure G.1), considering the significant correlation between the IW_{stat} salinity and volume transport (e.g., Chapter 3.3.1 and Chapter 5.4.4). Most of the warm and saline waters are blocked by the topography at Davis Strait. This analysis's shallowest point of Davis Strait is at a depth $<$400 m. However, the deepest sill of Davis Strait reaches 650 m (Tang et al., 2004).

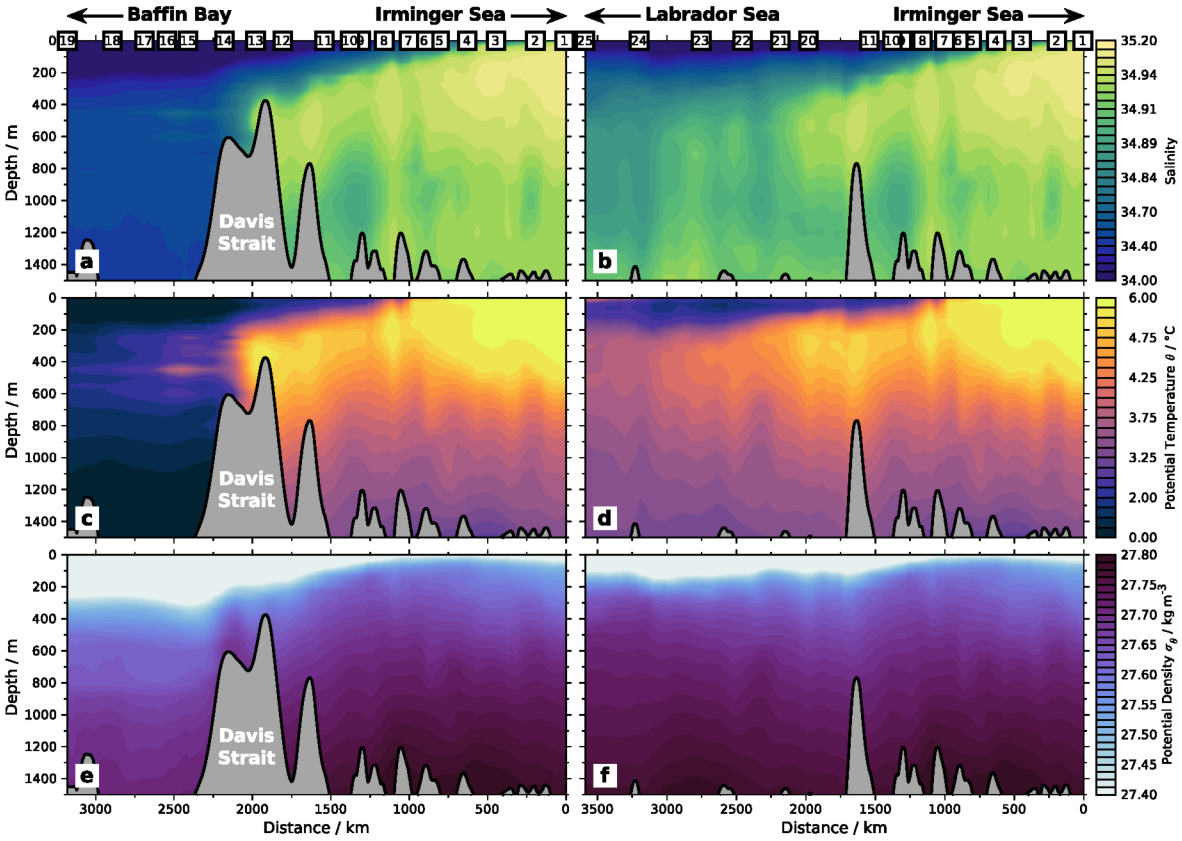

Figure 5.19: Hydrography in ARMOR3D along the two branches of the boundary current system along the 1,500 m isobath from 1993 - 2022 (left column: Irminger Sea into Baffin Bay - Section 26 in Figure 5.2; right column: Irminger Sea into the western Labrador Sea - Section 27 in Figure 5.2). Rows denote different properties (top to bottom: salinity, potential temperature θ, potential density σ_θ). Numbers in the upper column denote positions of individual cross-slope sections (see Table 5.1 and Figure 5.2).

Thus, the selected section does not capture the deepest parts of Davis Strait, which explains why warm and saline waters are also observed northward of Davis Strait at depths greater than the sill (Figure 5.19 a, c). Comparing the temperature and salinity with the density distribution downstream from the Irminger Sea indicates that entire density layers are subducted downstream of Cape Farewell (between Sections 5 and 7). Hence, the warm and saline waters do not experience much mixing but are rather subducted to greater depths, forming the characteristic subsurface temperature and salinity maximum within the WGC (Chapter 3).

Along the second branch that recirculates around the Labrador Sea after the bifurcation downstream of Paamiut (Figure 5.19, right column), the warm and saline waters continue to subduct off Labrador. At western AR7W (Section 24), the maximum

temperatures are at ∼400 m depth, while the maximum salinity is almost degraded. Generally, temperature and salinity seem more decoupled compared to regions further upstream. These results align with previous studies, which identified warm and saline IW at western AR7W (e.g., Yashayaev & Loder, 2016; Sanguineti, 2017) in the south-western Labrador Sea. Yashayaev and Loder (2016) compared measurements from two surveys, in 2008 and 2015. In the data from 2008, a distinct IW signal was visible at western AR7W. However, in 2015 neither an elevated temperature nor salinity signal was observed. Sanguineti (2017) still found a signal of IW at 53°N presenting ship-based measurements from a survey in summer 2009. While the years 2008 (western AR7W survey in Yashayaev & Loder, 2016) and 2009 (western AR7W survey Sanguineti, 2017) belonged to the years of maximum volume transport and highest salinities of IW, both properties were substantially lower in 2015 (western AR7W survey in Yashayaev & Loder, 2016). Consequently, I suggest that the observed distribution of hydrographic properties in ARMOR3D representing a 30-year average cannot exhibit distinct signals of IW so far downstream in the BCS at western AR7W. However, the elevated temperatures and salinities indicate the general presence of IW in these regions. Additionally, the isopycnals in ARMOR3D are almost horizontal at the Labrador shelf site downstream of Hudson Strait Outlet (Section 22), indicating less subduction. Nonetheless, the salinity maximum is still subducted to greater depths, as previously discussed in Kulan and Myers (2009). This phenomenon can be explained by diapycnal mixing, which refers to mixing across density layers (e.g., Brambilla et al., 2008b). Diapycnal mixing in the boundary current of the Labrador Sea was already described by Lumpkin et al. (2007) using an inverse model and by Fröhle et al. (2022) using an ocean-sea-ice model. Brambilla et al. (2008b) noted a vital diapycnal component during the formation of subpolar mode water. Also, for the production of LSW, the process of diapycnal mixing has been mentioned to play a role, albeit a relatively minor one (Yashayaev et al., 2007b; Yashayaev & Loder, 2016).

The analysis was repeated for along-slope sections that follow the 500 and 1,000 m isobath to test for differences regarding the horizontal position of the IW core (not shown). Similar to the analysis of the 1,500 m isobath, I chose the grid cells within the individual data sets closest to the respective isobath. For locations south of Davis Strait, the differences are negligible. The continental slope is so steep that the horizontal distance between the 500 and 1,500 m isobath is small. For the Northern LS section,

the 1,500 m isobath section performs best as it resembles the best position of the IW core (compare to Figure C.1). For Baffin Bay, the 500 m isobath section resembles the highest temperatures and salinities at depths between 200 and 600 m. The shelf is wider in these areas, and the shelf break is located at greater depths. Thus, I conclude that a combination of the 500 m isobath section within Baffin Bay and the 1,500 m for the rest of the BCS represents the IW core the best. Due to time constraints, such a combination could not be implemented.

GLORYS

The overall distribution of hydrographic properties along the two branches in GLORYS (Figure F.1) compares well with ARMOR3D. In agreement with Figure 5.9 and Figure 5.3, analyzing the 1,500 m isobath sections reveals slightly higher salinities and temperatures in GLORYS south of Davis Strait compared to ARMOR3D (Figure F.2). Only in Baffin Bay, GLORYS reveals salinities and temperatures lower than ARMOR3D, with Davis Strait as a sharp boundary. This difference between Baffin Bay and other regions further to the south can have different causes discussed in the following. As Baffin Bay is primarily covered by sea ice, this might influence the representation of the underlying ocean in ARMOR3D, as the satellite-derived fields include larger uncertainties. Another explanation could be that the advection of warmer and saline waters through Davis Strait is underrepresented in GLORYS, potentially due to coarse resolutions of the exact Davis Strait topography. However, GLORYS also reveals similarities with ARMOR3D. Similarly, GLORYS indicates diapycnal mixing along the continental slope in the northern and western Labrador Sea. While the isopycnals rise along the pathway downstream from Davis Strait, the isohalines deepen. This behavior indicates even more diapycnal mixing compared to ARMOR3D. Although the advection times did not provide physically meaningful results for GLORYS (Figure 5.10), the hydrographic structure along the 1,500 m isobath section compares well with ARMOR3D, and there are no unphysical features that would point to a substantial error in the data set. Possible explanations for the poor performance when calculating the advection times in GLORYS could be attributed to cross-slope processes. (Gou et al., 2023), for example, analyzed the WGC region and showed that local instabilities of the boundary current lead to the formation of Irminger Rings and boundary current eddies that transport water from the WGC into the interior Labrador Sea. Such processes

perpendicular to the boundary currents could affect local IW_{stat} properties that have been used for the calculation of the advection times but would have limited impact on the hydrographic performance along the 1,500 m isobath section.

ANHA4

In ANHA4 (Figure F.3), the salinity continuously increases with depth along both sections, which is different in ARMOR3D and GLORYS. Consequently, there is no characteristic subsurface salinity maximum in the typical depth range of IW. For temperature, such a subsurface maximum is located between 200 and 800 m depth in the WGC, propagating into Baffin Bay (Figure F.3 c), and the western Labrador Sea, where it is subducted to depths between 600 and 1,000 m (Figure F.3 d). ANHA4 is also warmer south of Davis Strait compared to ARMOR3D. The only exception is a negative anomaly at the surface of Uttorsiutit (Section 4) in the EGC. This anomaly is subducted to a depth of $\sim$200 m at Cape Desolation. From there, the anomaly is detected in Baffin Bay, and when recirculating around the Labrador Sea, it reaches Hudson Strait Inlet (Section 21). In Baffin Bay, a larger negative temperature anomaly is striking, with a temperature more than 1.5 °C colder compared to ARMOR3D, showing a strong horizontal gradient at Sisimiut (Section 14).

Another difference compared to ARMOR3D is that the hydrographic properties indicate higher salinities south of Davis Strait in ANHA4. However, there are also regions where the differences are reversed. Between 44° West (Section 7) and Paamiut (Section 11), ANHA4 indicates lower salinities compared to ARMOR3D in the upper 200 m (Figure F.4 a, b). The strongest anomaly, where ARMOR3D is more saline than ANHA4, occurs at Cape Desolation and eastern AR7W. This strong negative salinity anomaly also mirrors a negative density anomaly, with the lowest densities throughout the water column south of Davis Strait (Figure F.3 e, f). Assuming continuous advection in the model, this feature might indicate that salinity within ARMOR3D in the BCS is best represented at these two cross-slope sections due to the large amount of ship-based measurements conducted in these regions. This hypothesis was given in Chapter 3.3.1 (Figure B.2). Another reason that might explain parts of this large salinity, and, as a result, density differences between ANHA4 and ARMOR3D, is that the continental slope along both 1,500 m isobath sections is steepest in the area where the negative anomalies compared to ARMOR3D occur (compare the topography in Figure C.1).

ANHA12

As the analyses in Chapter 5.2 and Chapter 5.3.1 have already suggested, the 1,500 m isobath sections reveal that ANHA12 exhibits the highest salinities and temperatures in the BCS compared to the other data sets (Figure F.5). However, unlike ANHA4, ANHA12 reveals the characteristic IW subsurface salinity maximum. The differences between ANHA12 and ARMOR3D include a warmer and more saline water column south of Davis Strait at all depths (Figure F.6). Here, temperatures in ANHA12 are warmer by more than 1.5 °C almost everywhere, dominating the more saline waters in terms of their contribution to density, thus making the region south of Davis Strait less dense than ARMOR3D. The area of the strong negative salinity anomaly, highest at eastern AR7W and Cape Desolation in ANHA4, also reveals smaller salinities in ANHA12 compared to ARMOR3D. In these regions, fresh waters are located in the upper 200 m and are not seen further upstream. This salinity pattern agrees with GLORYS but does not agree with ARMOR3D (Figure 5.19 a, b) and ANHA4 (Figure F.3 a, b) where fresh waters are visible already in the EGC, agreeing with other studies such as Duyck and de Jong (2021) and Duyck et al. (2022). I suggest that these fresher waters are advected offshore from the shelf in GLORYS and ANHA12 at the locations of eastern AR7W and Cape Desolation, in line with Gou et al. (2023), who found that these regions exhibit a large exchange between shelf and open ocean in the LAB60 simulation. In Baffin Bay, the differences between ANHA12 and ARMOR3D exhibit a similar pattern to those between ANHA4 and ARMOR3D. Negative temperature and salinity anomalies occur in the upper 100 m and between 400 and 1,500 m. In between, positive anomalies indicate a stronger subsurface temperature and salinity maximum, suggesting a more distinct representation of IW (Figure F.6).

5.5.2 Salinity distribution in the boundary current system

To get a first impression on how the different methods distinguish between IW and ambient waters in the individual data sets, I present the distribution of salinity layers within the respective IW at different cross-slope sections. Following a similar analysis conducted for ARMOR3D in Chapter 4.4 (Figure 4.11), I present the salinity distribution at the four cross-slope sections: Sermiligaaq, eastern AR7W, western AR7W, and Sisimiut. I discuss the differences in performance across the four analyzed data sets for the three methods used to identify IW. The results for ARMOR3D are presented

in Figure 5.20, while the other data sets are presented in the Appendix H: GLORYS (Figure H.1), ANHA4 (Figure H.2), and ANHA12 (Figure H.3). Note that the results for ARMOR3D are identical to Figure 4.11. Here, I present them for a direct comparison with the results from the other data sets, using a similar y-axis spacing for each section and method.

Static Method

The variability of the salinity distribution obtained using the static method in ARMOR3D (Figure 5.20) and GLORYS (Figure H.1) is similar across the different sections. The only differences in the salinity distribution are attributed to the large-scale salinity bias between the two data sets, where GLORYS is more saline in the regions south of Davis Strait and fresher within Baffin Bay (Figure F.2). Due to this salinity bias, the amplitudes of the individual salinity levels are larger in GLORYS for the three more southern sections (Sermiligaaq, eastern AR7W, and western AR7W), accompanied by larger areas of the respective salinity levels. At Sisimiut, the amplitude in GLORYS is still larger compared to ARMOR3D. However, the areas of the individual salinity bins are small. Estimating multi-year variability is difficult due to the limited salinity distribution. In ANHA4 and ANHA12, the static method suggests a large salinity amplitude, especially for Sermiligaaq and eastern AR7W (Figure H.2 a, d and Figure H.3 a, d), where IW_{stat} is still identified down to the static salinity threshold.

Provenance Method

For all data sets, the provenance method performs as designed across all sections. The unrealistic cutoff at the IW_{stat} salinity threshold of $S = 34.92$ is replaced by a physically realistic pattern at the fresher limit of IW_{prov}, as discussed earlier in Chapter 4.4. This performance of the provenance method is also evident in ANHA4 and ANHA12. While the static method identifies waters as IW_{stat} that are fresher than the strongest IW_{stat} signal, but still more saline than the static threshold, the provenance method (Figure H.2 b, e and Figure H.3 b, e), with its higher IW_{prov} salinity thresholds, does not necessarily classify these fresher waters as IW_{prov}. Thus, the IW_{prov} salinity distribution follows the larger area of specific salinity bins and confines the IW_{prov} salinities to the most saline ones, as indicated in the T-S diagrams at eastern AR7W (Figure 5.12).

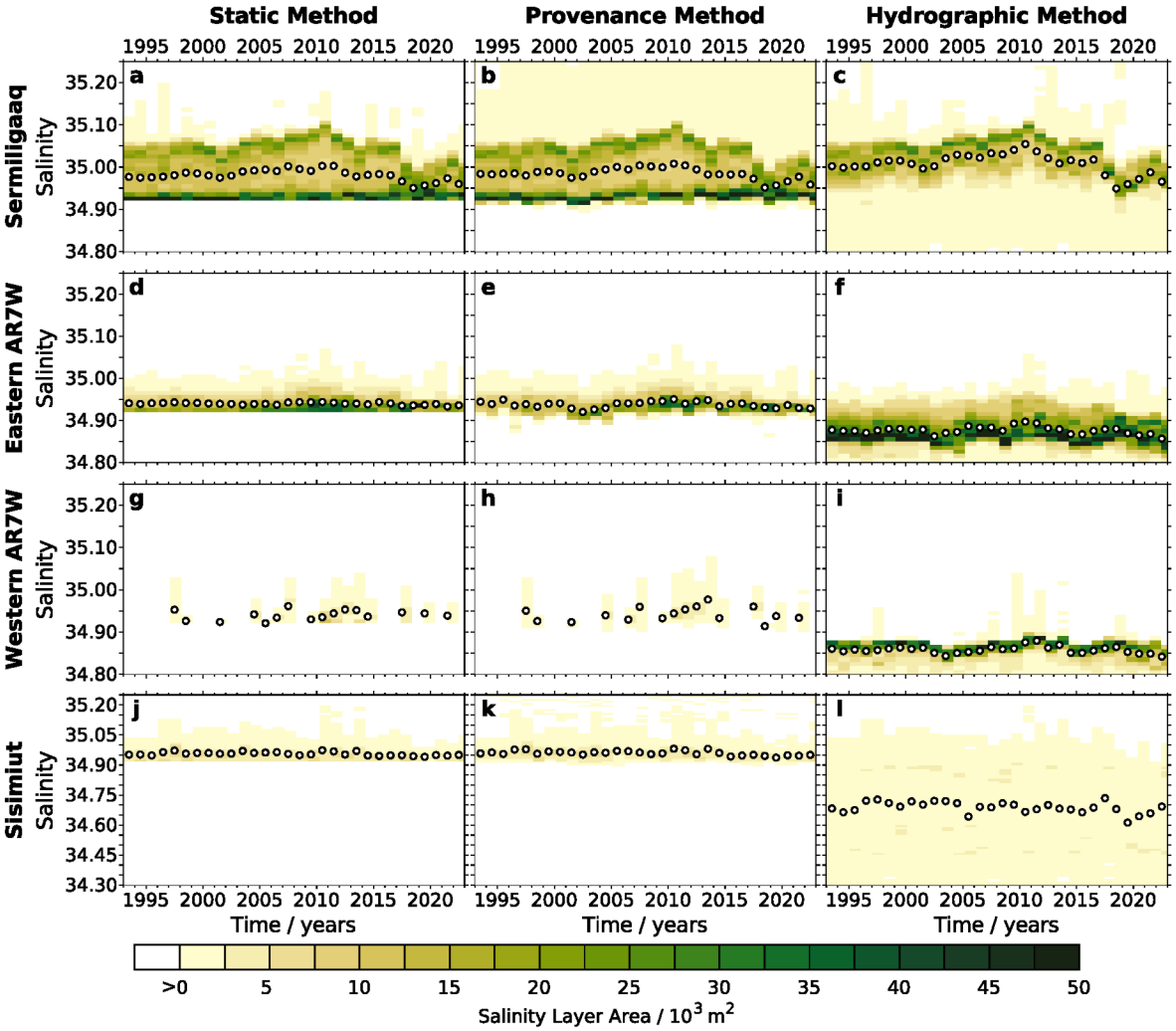

Figure 5.20: Yearly mean layer area for individual salinity bins obtained with different methods (left to right: static, provenance, hydrographic method) in ARMOR3D. Rows denote different sections (top to bottom: Sermiligaaq, eastern AR7W, western AR7W, Sisimiut. Circles denote yearly averaged salinities for the respective Irminger Water type.

Hydrographic Method

Similar to the analysis in Chapter 4.4 for ARMOR3D, the hydrographic method identifies IW_{hydro} in areas where the static and provenance methods identify remnants of the respective IW within all data sets. As a result, the hydrographic method can be applied to all data sets to gather information about the variability of IW_{hydro} in regions where IW is mixed with ambient waters below the IW_{stat} and IW_{prov} salinity thresholds.

5.5.3 From the Irminger Sea into Baffin Bay and the Labrador Sea

In the following, I analyze the mean IW properties along the BCS. Therefore, I analyze IW for the three methods at the two along-slope sections representing the branches of the BCS from the Irminger Sea into Baffin Bay and the western Labrador Sea. Additionally, the analysis includes IW properties within the IW core regions at the 25 individual cross-slope sections (Figure 5.2, Table 5.1). This IW core region has been selected manually for all cross-slope sections individually based on the mean salinity and geostrophic velocity within ARMOR3D. To ensure the best possible comparison across all data sets, the analyzed period for the this analysis is limited from 2002 to 2020. The results for ARMOR3D are presented in the main text (Figure 5.21). The results for GLORYS, ANHA4, and ANHA12 are presented in the Appendix (Figure I.1, Figure I.2, and Figure I.3).

ARMOR3D

In ARMOR3D, IW within the individual cross-slope sections exhibits a continuous cooling and freshening trend from Sermiligaaq in the northwestern Irminger Sea downstream toward Paamiut. This cooling and freshening hold, regardless of the method used to identify IW (Figure 5.21). Propagating into Baffin Bay, both IW_{stat} and IW_{prov} show an increase in temperature and salinity, while IW_{hydro} indicates a decrease. This increase leads me to conclude that, with the static and provenance methods, only a small core of the warmest and most saline waters remains. At the same time, the rest is mixed with ambient waters below the respective thresholds. The hydrographic method incorporates these ambient waters as long as the vertical structure of the water column is preserved. Consequently, it identifies colder and fresher IW_{hydro} downstream of Paamiut.

Analyzing the 1,500 m isobath sections yields results similar to those from the individual cross-slope sections. Downstream of Maniitsoq, both IW_{stat} and IW_{prov} are largely mixed below the respective thresholds, leaving only the confined warm and saline core. The hydrographic method reveals remnants of warm and saline waters mixed with colder and fresher ambient waters north of Maniitsoq (Figure 5.21 left column). In this case, the 1,500 m isobath section indicates higher salinities but similar temperatures compared to the individual sections. Additionally, the 1,500 m isobath section also

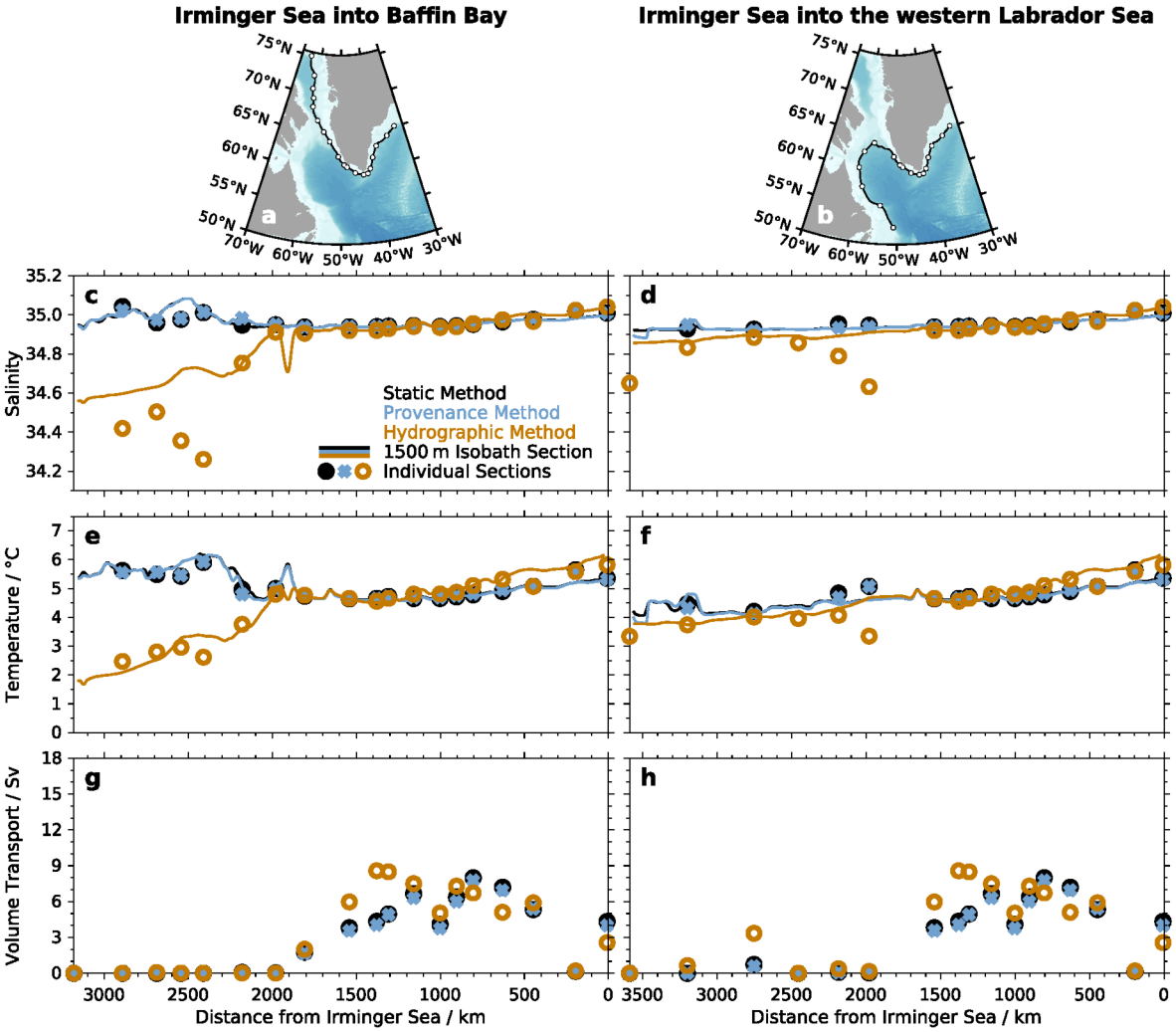

Figure 5.21: Irminger Water properties in the boundary current system in ARMOR3D averaged from 2002 - 2020 from the Irminger Sea into Baffin Bay (left) and into the western Labrador Sea (right). (a) and (b): Maps including the respective positions of individual cross-slope sections at the respective 1,500 m isobath section according to Figure 5.2. Other subfigures show Irminger Water properties (top to bottom: salinity, potential temperature θ, volume transport). Colors denote different methods: static (black), provenance (blue), hydrographic (orange). Solid lines represent the 1,500 m isobath sections. Black dots (static), blue crosses (provenance), orange circles (hydrographic) represent the individual cross-slope sections.

reveals a continuous freshening of IW_{hydro}, while the individual sections indicate a large salinity drop between Sisimiut and Aasiaat, followed by a salinification further northward. This behavior might suggest that the manually chosen width of the IW core region is too large at these sections, where only a smaller amount of IW_{hydro} remains. Further tests with varying widths of the IW core region have not been applied due to time constraints but could be worth investigating in the future.

As mentioned previously, Davis Strait represents the shallowest region of the 1,500 m isobath section. Directly at Davis Strait, between Fylla Bank and Maniitsoq, there is a confined salinity drop of 0.2. It appears that the linear interpolation of the WGC pathway between the Labrador Basin and Baffin Bay does not accurately capture the primary WGC pathway across Davis Strait, as discussed in Chapter 5.5.1. Consequently, only fresh waters are accounted for between Fylla Bank and Maniitsoq, resulting in the observed drop in salinity. IW_{stat} and IW_{prov} exhibit constant salinity but increased temperature in the same region. This behavior is attributed to the region's seasonality, predominantly influenced by the local sea ice cover. Seasonally, either no IW_{stat} or IW_{prov} is identified, or IW_{stat} and IW_{prov} exhibit higher temperatures. The total mean presented in this analysis (Figure 5.21) does not account for times with no IW_{stat} or IW_{prov}. Thus, it displays higher temperatures.

Overall, the analysis of IW properties obtained from the 1,500 m isobath section reveals that such an along-slope section yields physically realistic results. I suggest that a future adjustment of the chosen individual grid points along the main path of the WGC through Davis Strait, will correct for the otherwise unrealistic temperature and salinity changes between Fylla Bank and Maniitsoq. Therefore, such along-slope sections are a promising addition to analyzing the individual cross-slope sections within the BCS. Unfortunately, ARMOR3D does not include geostrophic velocities below sea ice. This absence of velocity information must be considered when analyzing the calculated IW volume transport in regions with more extensive temporary sea ice cover. Additionally, there is no along-slope velocity information within the 1,500 m isobath sections that consist of individual grid points. Consequently, only data about local IW thicknesses are available. However, information about the IW area across the entire boundary current is not. As a result, volume transports within the 1,500 m isobath sections cannot be computed. Noticeably, the volume transport calculated at the individual cross-slope sections is highest at Uttorsiutit and OSNAP East for the static and provenance methods rather than at Sermiligaaq, which is the most downstream cross-slope section (Figure 5.21 c). This result indicates that at OSNAP East, the last branches of the IC have aligned with the EGC, which agrees with the mean ARMOR3D velocity field in the Irminger Sea (not shown) and was already previously indicated (e.g., Daniault et al., 2011a, 2011b; Le Bras et al., 2020).

Regarding the second branch that recirculates across the northern Labrador Sea downstream of Paamiut, the 1,500 m isobath section again provides realistic results. It demonstrates a continuous cooling and freshening of IW along the entire pathway. When looking at the individual sections, the hydrographic method first indicates cooling and freshening at Northern LS, followed by subsequent salinification and warming, similar to the Baffin Bay sections. In this case, the chosen position of Northern LS might be too far north. As a result, it does not intersect the main IW branch during its westward recirculation in the Labrador Sea. Similar to the choice of a potentially too-wide IW core in the Baffin Bay sections, a further adjustment of the position of Northern LS could not be implemented due to time constraints.

GLORYS

The mean IW temperature and salinity at the cross-slope sections and the 1,500 m isobath sections compare well with ARMOR3D (Figure I.1). Both parameters decrease from the Irminger Sea downstream in the BCS. Like ARMOR3D, GLORYS also reveals a cooling and freshening at Northern LS and Hudson Strait Inlet and a subsequent increase in temperature and salinity in the hydrographic method. This characteristic is likely due to the recirculation in the Labrador Sea being located farther to the south. However, there are differences between GLORYS and ARMOR3D. For instance, GLORYS does not exhibit IW_{stat} and IW_{prov} north of Sisimiut, where ARMOR3D still shows small amounts of IW in the individual sections. Moreover, the IW volume transports in ARMOR3D steadily decrease downstream of Uttorsiutit in the EGC. In contrast, in GLORYS, the volume transport increases almost continuously from Sermiligaaq until they peak at eastern AR7W. This increase is followed by a rapid increase in the two downstream sections, Cape Desolation and Paamiut. At Paamiut, the volume transport drops below 1 Sv and remains below this value farther downstream.

ANHA4

Overall, the analysis of IW properties in the 1,500 isobath sections in ANHA4 (Figure I.2) reveals similar results compared to ARMOR3D. A notable signal is the drop in temperature and salinity between Fylla Bank and Maniitsoq. This signal has previously been identified in ARMOR3D and is attributed to the local topography in Davis

Strait and the functioning of the hydrographic method. IW salinities and temperatures decrease from the Irminger Sea downstream in the BCS. However, they are higher compared to ARMOR3D, consistent with earlier analyses (for example, Figure 5.6 and Figure F.4). However, several cross-slope sections indicate outliers toward lower salinities along the EGC, especially within the hydrographic method. One potential explanation for these differences compared to ARMOR3D could be the salinity differences themselves. In the EGC, ANHA4 exhibits lower salinities on the shelf and higher salinities further offshore in contrast to ARMOR3D (Figure 5.6 a, b). The lower salinities on the shelf extend further offshore in the upper 200 m. These differences eventually lead to lower quantities of identified IW_{hydro}, as depicted in Figure 5.11. The percentiles used to determine the depth of the warm and saline waters are optimized for the vertical temperature and salinity structure of ARMOR3D. Adjusting these percentiles for ANHA4 and the other data sets individually could resolve the differences in IW_{hydro} salinity at individual sections. Another potential factor is the definition of the IW core region, which has also been optimized for the representation of IW in ARMOR3D. Further differences between ANHA4 and ARMOR3D pertain to the evolution of the IW volume transport. In ARMOR3D, the volume transport steadily decreases from Uttorsiutit. In ANHA4, the volume transports remain low along the entire EGC and reach the highest values at the southwestern Greenland shelf, at OSNAP West and eastern AR7W. As previously shown, at eastern AR7W, ANHA4 exhibits the lowest IW velocities compared to all other data sets, likely contributing to the generally low volume transports.

ANHA12

In ANHA12 (Figure I.3), the evolution of IW properties within the 1,500 m isobath sections in the BCS is similar to ARMOR3D. ANHA12 not only indicates the continuous cooling and freshening along its downstream pathway in the BCS. It also reveals a similar pattern in the northern recirculation of the Labrador Sea, with colder and fresher IW_{hydro} at Northern LS and Hudson Strait Inlet. Similarly, the magnitude of the salinity drop between Fylla Bank and Maniitsoq in the 1,500 m isobath section (Figure I.3 c) agrees with ARMOR3D (Figure 5.21 c). The volume transport in ANHA12 at the individual cross-slope sections is similar to those in GLORYS and ANHA4, with the highest values occurring at eastern AR7W. However, all IW properties - salinity,

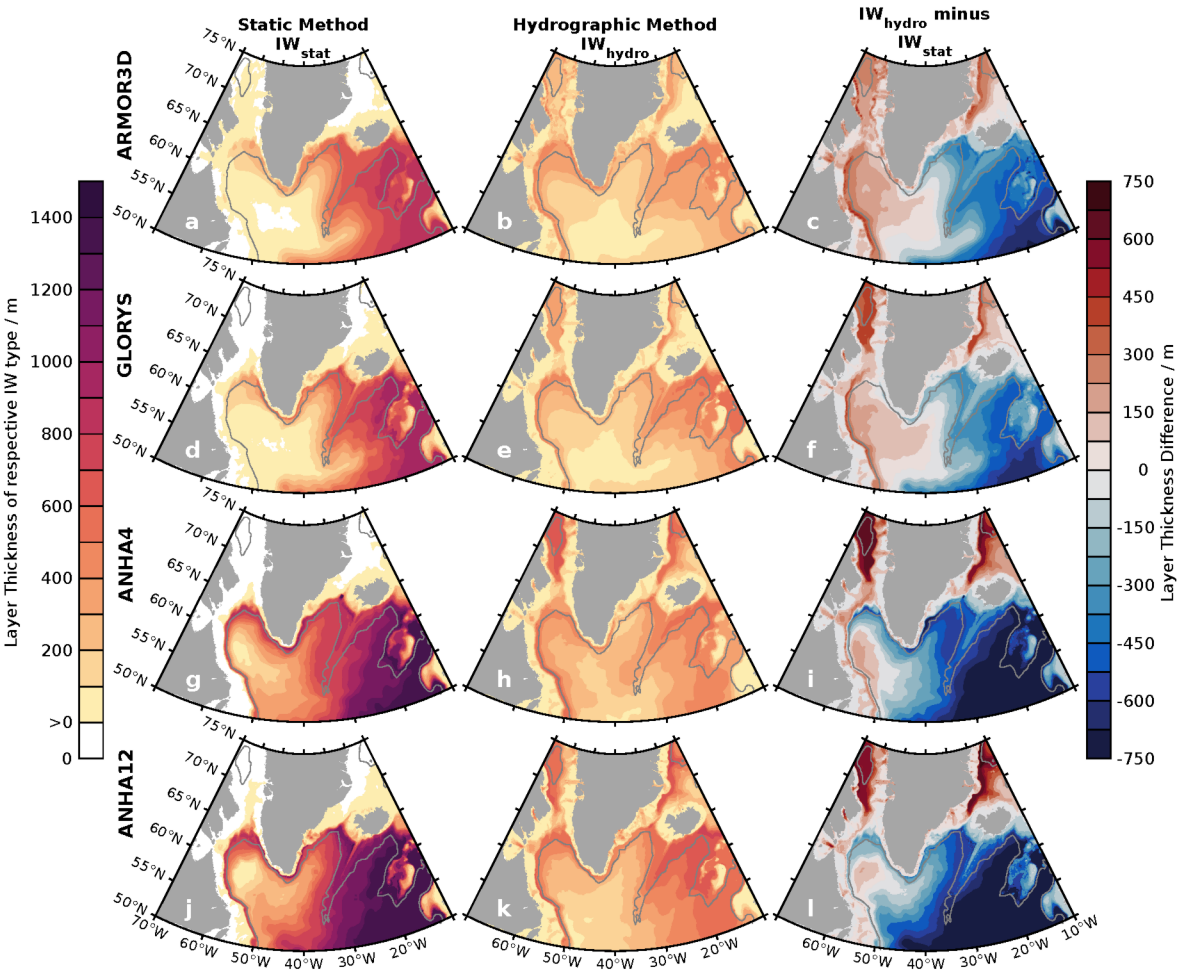

Figure 5.22: Irminger Water layer thickness for the static (left column) and hydrographic method (middle column). Right column: difference between static and hydrographic methods. Rows denote individual data sets (top to bottom: ARMOR3D, GLORYS, ANHA4, ANHA12). The gray line indicates the smoothed 2,000 m isobath.

temperature, and volume transport - reveal the highest values across all data sets, corresponding to the generally warmer and more saline water column (Figure F.6).

5.5.4 Irminger Water thickness in the different data sets

In the following, I discuss the spatial evolution of IW by analyzing the IW thicknesses in the SPNA, similar to what was already done in Figure 4.12 for the static and hydrographic methods in ARMOR3D. In this analysis, my focus is on comparing the results within the individual data sets (Figure 5.22). I do not consider regions in the NAC upstream from the Irminger Sea. Therefore, I solely concentrate on the calculated layer thickness downstream within the BCS.

Static Method

The overall pattern of IW layer thicknesses calculated with the static method is similar within the four analyzed data sets (Figure 5.22 left column). The previously mentioned bias toward higher salinities in GLORYS, ANHA4, and ANHA12 compared to ARMOR3D (Chapter 5.3.1, Figure 5.8) is reflected in generally larger layer thicknesses. ARMOR3D exhibits coarser horizontal resolution than the other data sets, which also affects the resolution of the IW layer thicknesses. In this context, ANHA12, with the highest horizontal resolution, reveals the sharpest contours for smaller features. Note that the horizontal resolution of LAB60 is higher than ANHA12 but is limited to the Labrador Sea and was only analyzed at eastern AR7W.

The extent of IW_{stat} in ARMOR3D and GLORYS downstream in the BCS is similar, reaching approximately to Hudson Strait Outlet, where the warm and saline waters are almost entirely mixed below the thresholds. Differences become evident in the Irminger Sea, where the most substantial IW_{stat} layer thicknesses in ARMOR3D and GLORYS are more constrained by the topography. In contrast, greater thicknesses spread further into the interior Irminger Basin in ANHA4 and ANHA12. Notably, ANHA4 and ANHA12 identify larger IW_{stat} thicknesses along the entire pathway from the Irminger Sea into the western Labrador Sea until 50°N. Additionally, the interior Labrador Sea reveals small amounts of IW_{stat} in ANHA4 and ANHA12, where none is identified in ARMOR3D and GLORYS. However, this difference could also be attributed to the overall salinity bias.

All data sets imply a pathway of IW_{stat} into Baffin Bay. In ARMOR3D, IW reaches furthest north, agreeing with the hydrographic structure north of Davis Strait in the individual data sets (Figure 5.21, Figure I.1, Figure I.2, and Figure I.3). A small branch also indicates that IW_{stat} is advected into Disko Bay. In ANHA12, a narrow tongue of IW_{stat} spreads into Baffin Bay but does not reach Disko Bay. Especially in the vicinity of Davis Strait, the horizontal resolution of the data sets plays an essential role in accurately representing the narrow troughs, which become more visible in the hydrographic method.

Hydrographic Method

Applying the hydrographic method, the patterns of IW_{hydro} thicknesses for the individual data sets are consistent (Figure 5.22 middle column). The impact of higher horizontal resolution in ANHA12 is still evident as it shows larger IW_{hydro} thicknesses concentrated along the topography. However, the magnitude of the thicknesses and the overall pattern are similar across all data sets. In all data sets, a distinct pathway of substantial IW_{hydro} thicknesses can be traced, recirculating in the Labrador Sea and propagating as far as 50°N. Additionally, pathways of IW_{hydro} through Davis Strait are visible. The clearest indication of the deep and narrow troughs is visible in ARMOR3D and ANHA12, despite ARMOR3D having the coarsest horizontal resolution. I conclude that the high horizontal resolution of ANHA12 is necessary to represent these narrow troughs in the simulations. Therefore, in GLORYS and ANHA4, the distribution of IW_{hydro} into Baffin Bay spans large portions of the entire width of Davis Strait. ARMOR3D only comprises observations and thus includes individual measurements within the narrow troughs. All data sets suggest that IW_{hydro} reaches the vicinity of marine-terminating glaciers in western Greenland, such as in Disko Bay, agreeing with e.g., Holland et al. (2008) who found warm subsurface waters within the fjords of Disko Bay. While ANHA4 exhibits the least amounts of IW_{hydro} in Disko Bay, the other data sets suggest approximately equal amounts.

Analyzing the IW_{hydro} thicknesses across the entire SPNA indicates that the hydrographic method identifies comparable amounts of IW_{hydro} within the different data sets. The method corrects for large-scale biases in the water column throughout the entire SPNA. It provides insight into structures and pathways of warm and saline waters in regions where IW_{stat} and IW_{prov} are already fully mixed with ambient waters, such as in Baffin Bay and the southwest Labrador Sea. Consequently, these two regions are the only locations where IW_{hydro} exhibits greater thicknesses compared to IW_{stat} (Figure 5.22 right column). This method is valuable for understanding the temporal variability of IW_{hydro}. Thus, I would advise against qualitative analyses of the results obtained with the hydrographic method outside of these areas: Baffin Bay and the western Labrador Sea.

5.6 Summary and Conclusion

In this chapter, I present the IW variability within the BCS, from the Irminger Sea into Baffin Bay as one branch and into the western Labrador Sea as another, as well as on 25 individual cross-slope sections. In addition, I present results for different data sets, comparing the multi-source observation-based ARMOR3D data sets with the ocean reanalysis GLORYS, and the two model simulations ANHA4 and ANHA12.

Comparing the different data sets reveals that ARMOR3D is the coldest and freshest data set (Figure 5.19), consecutively followed by GLORYS (Figure F.1), ANHA4 (Figure F.3), and ANHA12 (Figure F.5). Therefore, I had to adjust the criteria to isolate the Irminger Sea provenance region when applying the provenance method to identify IW_{prov} for ANHA4 and ANHA12. Continuing, the provenance method builds on calculating the advection times between the Irminger Sea provenance region and the individual cross-slope sections in the BCS. Therefore, I calculate lag correlations in the IW_{stat} salinity time series. In contrast to ARMOR3D, the calculated lag correlations did not show a continuous pattern in GLORYS, ANHA4, and ANHA12. Hence, I decided to utilize the advection times from ARMOR3D for the other data sets. However, the analysis showed that GLORYS, ANHA4, and ANHA12 have problems resembling the advection of the IW signal from the Irminger Sea provenance region within the BCS into Baffin Bay and the western Labrador Sea. One possible explanation why the advection times reveal unrealistic results could be attributed to cross-slope processes. If such processes dominate the individual regions at the cross-slope sections as indicated by Gou et al. (2023) for the WGC, they may affect the calculation for downward propagating properties in the BCS.

The multi-year variability of IW_{stat} within the different data sets in the Irminger Sea provenance region (Figure 5.9) and of IW_{stat}, IW_{prov}, and IW_{hydro} at eastern AR7W (Figure 5.17) agrees within the different data sets. In addition to the general temperature and salinity bias, the distribution of heat and salt in the water column differs between the individual data sets. As exemplified at eastern AR7W (Figure 5.3), in ARMOR3D, the most saline waters are located in the upper 500 m. In GLORYS, these are attached to the continental slope down to the analyzed maximum depth of 1,500 m. The same holds for ANHA12, while in ANHA4, the waters of maximum salinity are at depths greater than 1,000 m and thus do not agree with previously analyzed

ship-based data (Figure 3.4), DOORS data (Figure A.1) and mooring observations at OSNAP West (Pacini et al., 2020, their Figure 4). These mooring observations agree most with ARMOR3D when comparing all data sets at eastern AR7W (Figure 5.3) with Pacini et al. (2020, their Figure 4). This impression is further reinforced when comparing the OSNAP West mooring observations directly to OSNAP West in the different data sets (not shown).

In addition, I extracted sections that follow the 1,500 m isobath downstream from the Irminger Sea on a northern branch into Baffin Bay and on a southern branch recirculating into the western Labrador Sea for the different data sets individually. I compared the IW properties along these sections with 25 individual cross-slope sections for the different IW identification methods. As this analysis focuses on the spatial variability of IW properties analyzing a temporally mean state, the static and provenance methods deliver similar results. Downstream the bifurcation of the two branches at Paamiut, the hydrographic method results in similar IW properties that are only minimally fresher. Further downstream, the static and provenance methods indicate an increase in temperature and salinity at the individual cross-slope sections throughout all data sets. This increase is because only a minimal area of IW that experienced almost no mixing along its pathway is identified. Along the 1,500 m isobath section, no IW is identified in GLORYS, ANHA4, and ANHA12. Only in ARMOR3D, the 1,500 m isobath section identifies IW_{stat} and IW_{prov} north of Davis Strait due to the higher salinities and temperatures of ARMOR3D Figure 5.19) compared to the other data sets in the entire Baffin Bay (GLORYS: Figure F.1, ANHA4: Figure F.3, and ANHA12: Figure F.5). The hydrographic method reveals a pronounced cooling and freshening when entering Baffin Bay and a continuous cooling and freshening when recirculating in the Labrador Sea. The individual cross-slope sections mainly support the results of the 1,500 m isobath sections. I conclude that extracting such along-isobath sections in the BCS can deliver a solid impression of the spatial IW variability in the boundary current. In contrast to the cross-slope sections, they show a spatially higher resolved boundary current but come with the disadvantage of no along-slope velocities and, thus, volume transports, as the current direction would need to be adjusted at each selected grid point.

From the analysis of comparing IW properties using multiple data sets within the BCS, I answer the previously stated research questions and draw the following conclusions:

1. **How do the hydrography in GLORYS and different model simulations compare with ARMOR3D in the BCS?**

   The additional analyzed data sets indicate larger differences compared to ARMOR3D. The entire SPNA and BCS (except Baffin Bay) is warmer and more saline in GLORYS, ANHA4, and ANHA12. In addition, larger differences occur in the vertical distribution of heat and salt in the water column of eastern AR7W, concluding that ANHA4, ANHA12, and LAB60 do not fully represent IW (Figure 5.3) as seen in ARMOR3D and in-situ measurements. In general, an increase in the horizontal resolution in the model simulations does not come with an increase in the performance of IW and the vertical structure of the water column.

2. **How are Irminger Water properties changing along their pathway from the Irminger Sea in the boundary current system?**

   Analyzing cross-slope and along-slope sections within the BCS indicates a subsequent cooling and freshening of IW for all methods (Figure 5.21, Figure I.1, Figure I.2, and Figure I.3). The subduction of entire density layers downstream of Cape Farewell (Figure 5.19) indicates sinking of water along the BCS (Spall & Pickart, 2001). Estimates of IW volume transports indicate a continuous decrease while propagating downstream in ARMOR3D (Figure 5.21) but are less continuous in GLORYS, ANHA4, and ANHA12. Also, its maximum occurs further downstream compared to ARMOR3D, indicating that parts of IW are entrained into the BCS further south in the Irminger Sea (Figure I.1, Figure I.2, and Figure I.3).

3. **Can different methods to identify Irminger Water be used to overcome differences in individual data sets?**

   The provenance method corrects for general hydrographic biases (Garcia-Quintana et al., 2019; Gillard, 2020), reflected in the identified IW area (shown for eastern AR7W in Figure 5.17). However, it cannot adjust for differences in the vertical distributions of heat and salt in the water column and different velocity patterns

that finally shape the IW volume transport (Figure 5.3 and Figure E.3). The hydrographic method behaves similarly for other data sets than ARMOR3D. It adjusts IW_{hydro} according to the general hydrographic biases in the individual data sets. Thus, IW_{hydro} thicknesses are much more alike within the different data sets than IW_{stat} thicknesses (Figure 5.22). The provenance and hydrographic methods can overcome the large-scale hydrographical differences in the individual data sets. However, it cannot adjust for the different vertical structures of the water column.

The results show that the along-slope section from the Irminger Sea into Baffin Bay and the western Labrador Sea might require a minor adjustment of the individually chosen grid points. However, such an adjustment would only affect the Davis Strait region between Fylla Bank and Maniitsoq. In this region, the large drop in IW_{hydro} salinity accompanied by the increase in IW_{stat} and IW_{prov} temperatures indicate that the chosen grid points do not precisely follow the pathway of the IW core through the troughs connecting the Labrador Sea and Baffin Bay. Future analyses could investigate the local temporal variability at individual cross-slope sections or specific distances along the 1,500 m isobath sections to qualitatively determine multi-year or seasonal melting estimates of marine-terminating glaciers, for example, within Disko Bay (e.g., Huhn et al., pers. comm.). Additionally, my results could help the modeling community improve their models of representing IW within the BCS regarding its vertical position and horizontal advection. These steps would be necessary to analyze further the role of IW in the melting process of marine-terminating glaciers. Results from the hydrographic method in ARMOR3D and ANHA12 show that IW_{hydro} propagates, for example, into Disko Bay (Figure 5.22), agreeing with e.g., Holland et al. (2008). However, IW_{stat} and IW_{prov} do not reach so far north (Figure 5.22). Results from existing studies (e.g., Hansen et al., 2012; Gladish et al., 2014) that analyzed the role of Atlantic-origin waters in the melting of Greenland's marine-terminating glaciers could be reevaluated by applying the hydrographic method instead of using static thresholds to identify the warm waters to better represent the variability in the water column. I showed that using the provenance method corrects for the basin-wide hydrographic biases of elevated salinities and temperatures in the model simulations. An extension of the analysis further upstream in the NAC could be used to better estimate the advection time between specific locations along the NAC and different locations within the BCS.

"It isn't that life ashore is distasteful to me.
But life at sea is better."

Sir Francis Drake - English sea captain and explorer;
second captain to circumnavigate the globe;
namesake of the Drake Passage

Chapter 6

Summary & Conclusion

IW originates in the subtropics and is transported via the Gulf Stream, its extension, and the NAC into the Irminger Sea and via the IC into the BCS. In this region, IW is the warmest and most saline water mass in the upper 1,000 m. It is further advected into Baffin Bay and the western Labrador Sea (Figure 3.3 and Figure 4.12). Reaching Greenland's marine-terminating glaciers through deep troughs, IW significantly contributes to their melting (Holland et al., 2008; Rignot et al., 2012; Straneo & Cenedese, 2015). When advected further offshore into the central Irminger and Labrador Seas (e.g., Pennelly & Myers, 2020; Gou et al., 2023), it influences the local stratification in the water column and, thus, plays a vital role in forming dense water masses (e.g., Cuny et al., 2002; Myers et al., 2007).

Chapter 3, Chapter 4, and Chapter 5 within this thesis comprise the main analyses and results. Each chapter is structured to address the overarching research questions outlined in the Introduction (Chapter 1).

In the following, I summarize the main conclusions from the individual chapters and address the main research questions:

1. What processes shape the variability of Irminger Water at eastern AR7W on seasonal and multi-year time scales?

In Chapter 3, IW's temporal and spatial variability is demonstrated. For analyzing IW, previous studies relied on ship-based measurements to study multi-year variability (e.g., Myers et al., 2007, 2009; Ribergaard, 2014; Rykova et al., 2015). These expeditions primarily surveyed the Labrador Sea in late spring and summer and, thus, lacked seasonal observations. For example, in the region southwest of Greenland, the AR7W line exhibits exceptionally high temporal data coverage for oceanographic observational time series on multi-year time scales (e.g., Lazier et al., 2002; Yashayaev, 2007a; Kieke & Yashayaev, 2015; Yashayaev et al., 2015b). Studies analyzing seasonal variability of IW relied on mooring observations, such as the Davis Strait moorings (Curry et al., 2014) and the OSNAP moorings (e.g., Lozier et al., 2017; Pacini et al., 2020; Le Bras et al., 2020). The OSNAP moorings are limited in their temporal coverage as they were deployed in 2014 and lack spatial resolution, especially in the vertical.

To analyze seasonal and multi-year variability within a single data set, I utilize the multi-source observation-based ARMOR3D data set, comprising the years 1993 to 2022,

at a weekly resolution. ARMOR3D combines remote sensing data and in-situ measurements, bridging the temporal and spatial gaps often associated with pure in-situ observations. Initially, I validate ARMOR3D using the existing ship-based measurements at eastern AR7W and mooring observations from OSNAP West (Pacini et al., 2020). The results demonstrate that ARMOR3D realistically represents hydrography, including IW (e.g., Figure 3.4, Figure 3.5, Figure 3.6, and Figure 3.7). As a result, ARMOR3D enables the analysis of 30 years of IW variability in an observation-based data set for the first time.

In ARMOR3D, IW at eastern AR7W is dominated by winter convective mixing in the Irminger and Labrador Seas on seasonal time scales (e.g., Figure 3.8 and Figure 3.11 and Pacini et al., 2020; Le Bras et al., 2020). The timing of the seasonal variability between IW and uISIW agrees with the observations of OSNAP East moorings by Le Bras et al. (2020), who described the formation of uISIW during winter convection in the Irminger Sea. My results show that uISIW takes approximately 4.5 months to reach eastern AR7W after its formation: three months to propagate from the interior Irminger Sea into the EGC (Le Bras et al., 2020) and an additional 1.5 months to be advected within the BCS from OSNAP East toward eastern AR7W (Chapter 3 and Chapter 4).

On multi-year time scales, large-scale changes of the NAO and changes in size and strength of the SPG have an impact on the positioning of the NAC (Holliday et al., 2020), which determines the amount of Atlantic-origin waters transported into the Irminger Sea (Buch et al., 2004; Holliday et al., 2020). I find that with a delay of up to three years, this signal reaches eastern AR7W, shaping the local variability of IW (Figure 3.16). The multi-year variability of IW is dominated by an overall increase in IW salinity and volume transport until 2010, followed by a subsequent decrease with the lowest salinities and volume transports in 2019 and 2022. This decrease is a direct consequence of the freshening of the entire SPNA that reached the Irminger Sea in 2018 (Holliday et al., 2020; Biló et al., 2022). An open question remains regarding how such large-scale changes in the SPNA affect IW's core water mass properties and whether these changes can be implemented to identify IW based on non-static thresholds.

2. How can large-scale changes in the subpolar North Atlantic be incorporated into the process of identifying IW, and what are the resulting consequences for Irminger Water variability?

In Chapter 4, I present the development of two new methods to identify IW, which incorporate large-scale changes in the water column into the identification process. Similar approaches exist for identifying LSW (Pickart et al., 2003b; Yashayaev & Loder, 2017) and have been proposed for ISIW (Le Bras et al., 2022). Previous studies on IW have distinguished between pure and modified IW (Buch, 2000; Buch et al., 2004; Myers et al., 2009; Ribergaard, 2014), classifying spatial and temporal changes in IW as either warm and saline (pure) or colder and fresher (modified) compared to its pure state. Building on the idea of e.g., Buch (2000), Buch et al. (2004), Myers et al. (2009), and Ribergaard (2014), I develop two new methods to represent different states of IW. However, I do not define a specific number of IW states. Instead, I devise methods that automatically adjust for large-scale changes in the water column for each time step individually.

The first method developed in this thesis is the provenance method. It results in a more physically realistic representation of IW_{prov} compared to the static method used in the representation of IW_{stat} (Figure 4.11). Therefore, estimates of its volume transport at different locations within the BCS are also more realistic, as they incorporate large-scale changes in the water column (Figure 5.16 and Figure 5.17). I find that the IW_{stat} volume transport is overestimated by 1.3 Sv compared to IW_{prov} in anomalously warm and saline years. However, the IW_{stat} volume transport is underestimated by 0.9 Sv compared to IW_{prov} in anomalously cold and fresh years.

The second method developed in this thesis is the hydrographic method. Implementation of the hydrographic method enables the analysis of IW_{hydro} in regions further downstream in the BCS, where IW is mixed with colder and fresher ambient waters. These regions include, for example, Baffin Bay in the vicinity of the marine-terminating glaciers in western Greenland (Figure 5.22), as previously demonstrated by e.g., Holland et al. (2008), Hansen et al. (2012), and Gladish et al. (2014). Thus, the hydrographic method facilitates future analyses to directly quantify the local influence of IW_{hydro} on melting marine-terminating glaciers. The analyzed variability of IW_{hydro} on seasonal and multi-year time scales implies that it includes effects from processes that shape IW properties over these periods. These processes include modification due

to vertical mixing and convection on seasonal time scales (e.g., Le Bras et al., 2020; Gutjahr et al., 2022), as well as changes in size and strength of the SPG on multi-year time scales (Buch et al., 2004; Holliday et al., 2020, Chapter 3). The results concerning the multi-year variability of IW also reveal that the volume transport is predominantly aligned with salinity when applying the static and provenance methods. In ARMOR3D, both IW_{stat} and IW_{prov} were warmest from 2019 to 2022, coinciding with the lowest volume transport. Calculating heat transport would be necessary to analyze the direct impact of IW on the melting of marine-terminating glaciers on multi-year time scales. Additional analyses that build upon the previous results address the variability of IW in different model simulations. Given that the provenance and hydrographic methods are designed to account for large-scale differences in the water column, both methods are anticipated to correct potential biases in the model simulations.

3. How do different model simulations represent Irminger Water, and how does its observed variability compare to these simulations?

In Chapter 5, the results from the earlier Chapter 3 and Chapter 4 are compared with the ocean reanalysis GLORYS and the model simulations ANHA4, ANHA12, and LAB60 to provide insights into the representation of IW in these additional data sets. Previous studies showed that ANHA4 and ANHA12 exhibit higher salinity than observations in other regions (Garcia-Quintana et al., 2019; Gillard, 2020). In addition to these biases, the vertical structure of the entire water column differs between the model simulations and ARMOR3D (Figure 5.3). Furthermore, the vertical structure varies among the individual simulations. These differences are evident in the occurrence of warm and saline waters at greater depths in ANHA4 compared to ARMOR3D ($\sim$1,000 m in ANHA4 and $\sim$500 m in ARMOR3D). In ANHA12, the warmest and most saline waters occur at similar depths as in ARMOR3D, but they extend to depths of 1,500 m near the continental slope. Consequently, the horizontal hydrographic structure in ANHA12 suggests that parts of waters that are denser and more saline than IW, such as NEADW, are inaccurately identified as IW. LAB60 does not exhibit any characteristic of IW in the water column. Thus, IW variability in LAB60 should be handled carefully. Generally, increasing the horizontal resolution in the model simulations does not necessarily lead to an improved representation of IW or the vertical structure of the water column.

The provenance and hydrographic methods account for the overall salinity bias in ANHA4 and ANHA12. As a result, the representation of IW_{prov} and IW_{hydro} is closer to that in ARMOR3D, as compared to IW_{stat} (Figure 5.15, Figure 5.16, and Figure 5.17). Thus, I conclude that the provenance and hydrographic methods compensate for the general bias in the model simulations when calculating the respective thresholds. However, differences in the vertical structure of the water column cannot be compensated. When analyzing along-slope sections spanning from the Irminger Sea into Baffin Bay and the western Labrador Sea, the subsequent modification toward lower temperatures and salinities (e.g., Buch, 2000; Buch et al., 2004) is observable in all data sets. Especially in ARMOR3D, the subduction of entire density layers is evident, aligning with the findings of Spall and Pickart (2001), who previously described such sinking along the boundaries.

My thesis contributes to a better understanding of IW variability in the BCS. By validating ARMOR3D in the region of interest, it provides a tool for conducting further analyses with a high temporal resolution (weekly) over long time scales (since 1993). My results are relevant to various fields. They hold particular significance for the oceanographic community, which can use ARMOR3D and the newly developed methods to analyze and interpret IW variability. The findings also hold relevance for the modeling community, as they enhance the understanding of how IW is portrayed in individual model simulations, highlighting differences from observations, particularly in the vertical structure of the water column. Moreover, the glaciological community may find interest in the newly estimated variability of IW, especially IW_{hydro}, and its potential implications for the heat supplied by IW_{hydro} to the vicinity of the marine-terminating glaciers.

I have demonstrated that the volume transport of IW_{hydro}, representing the warm and saline waters in the BCS, decreased by 1.22 Sv per decade from 1993 to 2022. Simultaneously, the corresponding velocity increased by $0.96\,\mathrm{m\,s^{-1}}$ per decade over the same period. The decline in volume transport is attributed to changes in the temperature (increase of 0.10 °C per decade) and salinity (slight decrease of 0.004 per decade). Whether these trends stem from global warming or are part of long-term climate variability cannot be conclusively determined with the available data sets.

However, projected changes attributed to global warming are expected to influence IW

substantially. Due to Arctic Amplification, higher latitudes - especially in the Northern Hemisphere - experience more pronounced warming than lower latitudes. This trend will contribute to increased freshwater within the BCS, driven by increased melting of sea ice in the Arctic and increased runoff from Greenland (IPCC, 2021). As a result, the stratification in the SPNA will intensify, and the AMOC is projected to weaken (IPCC, 2021). Consequently, the weakening of the AMOC will decrease the transport of warm and saline waters from subtropical regions to higher latitudes, thereby reducing the volume transport of IW.

"I never think of the future. It comes soon enough."

Albert Einstein - Theoretical physicist,
Nobel laureate in Physics, 1921

Chapter 7

Outlook

Given the potential relevance of the results in this thesis for various disciplines, numerous opportunities for future work arise that can expand upon these findings. In the following outlook, I will address potential analyses that can build upon the outcomes achieved during this thesis, presenting these analyses by posing new research questions. Each of these research questions is briefly outlined in Figure 7.1.

1. What is the variability of warm and saline waters upstream from the Irminger Sea, and on what time scales do these variabilities correspond with the one found for Irminger Water?

In this thesis, I focused on analyzing the seasonal and multi-year variability within the Irminger Sea and further downstream within the BCS. Exploring the variability of warm and saline waters on different time scales further upstream from the Irminger Sea would be interesting, particularly within the NAC region (see Figure 1.4). This approach could potentially unveil additional mechanisms contributing to the long-term variability of IW and address local influences of the NAO and SPG changes on the warm and saline waters in the SPNA (Figure 7.1, black).

Advection times have been calculated between the Irminger Sea provenance region and the individual cross-slope sections for the provenance method. Similarly, advection times could be calculated between the Irminger Sea provenance region and sections crossing the NAC, such as along the Mid-Atlantic Ridge (e.g., Roessler et al., 2015; Breckenfelder et al., 2017), the Observatoire de la variabilité interannuelle et décennale en Atlantique Nord (OVIDE) line (e.g., Daniault et al., 2015), and at the entire OSNAP East line (Lozier et al., 2017). These sections provide in-situ data that could be utilized to further validate ARMOR3D, GLORYS, ANHA4, and ANHA12 within these regions.

2. Can numerical particle tracking tools be used to investigate pathways of Irminger Water?

Another possible analysis concerning the pathways of IW could involve using particle tracking tools (Figure 7.1, orange). Numerical particles could be seeded into the different model simulations using the Lagrangian trajectory tool Ariane (Blanke & Raynaud, 1997; Blanke et al., 1999). By doing so, the IW pathway from the Irminger Sea downstream within the BCS could be examined through forward tracking. Similarly,

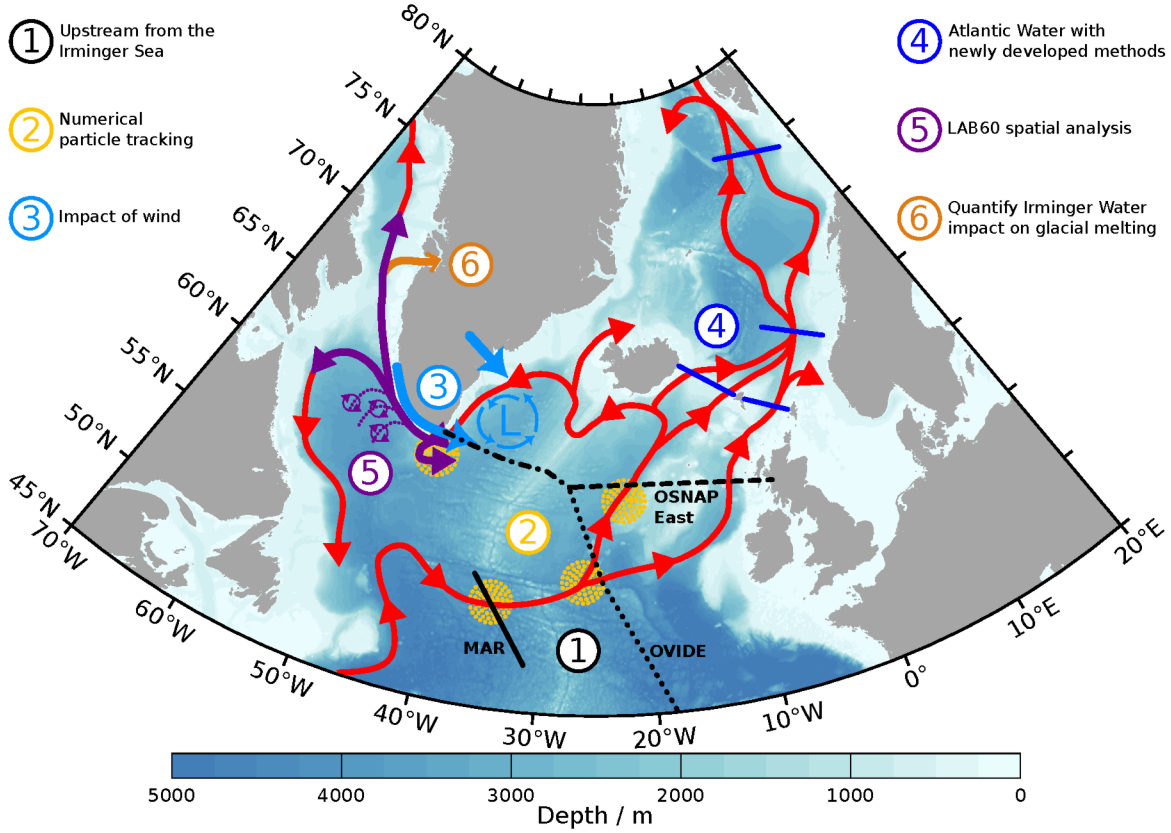

Figure 7.1: Map of the subpolar North Atlantic and Nordic Seas. Colors denote bathymetry. Red lines demonstrate idealized schematic warm and saline water pathways representing parts of major ocean currents based on Figure 1.4. The pathways in the Nordic Seas are based on Beszczynska-Möller et al. (2012) and Yashayaev et al. (2015b). Each potential future research question is addressed according to their respective number. A short explanation is given in the figure's upper left and right corner. Abbreviations: MAR - Mid-Atlantic Ridge, OVIDE - Observatoire de la variabilité interannuelle et décennale en Atlantique Nord, OSNAP - Overturning in the Subpolar North Atlantic Program.

the pathway from the Irminger Sea upstream into the NAC could be investigated via backward tracking. These analyses would facilitate the quantification of the amounts of IW that leave the BCS and spread offshore into the Irminger and Labrador Seas. Furthermore, this approach would enhance the comprehension of specific waters that ultimately reach Baffin Bay, reinforcing the outcomes obtained from the hydrographic method. The time lag analysis between changes in the SPG and changes in the IW volume transport at the individual cross-slope sections could be further assessed using the backward tracking method. Another particle experiment could be conducted further south in the North Atlantic, such as along the Mid-Atlantic Ridge, the OVIDE line, or OSNAP East. The precise location would depend on the findings from the backward

tracking analysis upstream from the Irminger Sea. This analysis would allow for quantifying the volume of Atlantic-origin waters entering the Irminger Sea, depending upon the state of the SPG. To examine the pathways of the NAC in the ANHA12 experiment, using Ariane, Nowitzki (2021) released particles at various positions along the 47/48 °N latitude at different times. These results could serve as a robust starting point for analyzing the pathways of the Atlantic-origin waters from the NAC into the Irminger Sea.

3. What are the direct and indirect influences of wind on Irminger Water, and can different influences be distinguished when analyzing IW variability in the boundary current system?

Winds significantly influence the hydrographic properties in the SPNA. The Greenland tip jets (see Chapter 3.3.3) cause substantial ocean heat loss in the Irminger Sea and, consequently, induce vertical convective mixing in the ocean (Paquin et al., 2016; Garcia-Quintana et al., 2019; Pacini & Pickart, 2023). Duyck et al. (2022) and Pacini and Pickart (2023) found that during the development phase of these Greenland tip jet events, local Ekman transport at the eastern boundary of the Labrador Sea moved surface waters offshore. This offshore transport, in turn, leads to the upwelling of warm and saline subsurface waters (IW) on the Greenland shelf. Pacini and Pickart (2023) concluded that the Greenland tip jets intensify convection in the Irminger Sea, consequently increasing the amount of LSW formed in the Irminger Sea (compare to ISIW in Chapter 1.3). Furthermore, the Greenland tip jets reduce convection in the Labrador Sea, reducing the amount of LSW formed in the Labrador Sea (Pacini & Pickart, 2023). A more detailed analysis of the impacts of the Greenland tip jets on hydrography along the Greenland shelf could be achieved using the individual gridded data sets presented in this thesis (Figure 7.1, blue). The increased Ekman transport and resulting upwelling on Greenland's western side in the eastern Labrador Sea occurred before the Irminger Sea's increased convection. Consequently, both signals - the local upwelling of IW in the eastern Labrador Sea and the arrival of convectively formed waters in the Irminger Sea - should be distinguishable within the individual cross-slope sections in the BCS. (Le Bras et al., 2022) addressed other effects of wind in the vicinity of Greenland. They found that northerly winds blowing along the pathway of the EGC in the Irminger Sea induce an onshore Ekman transport that forces slantwise convection as denser waters are transported over lighter waters. Slantwise convection

was already hypothesized along the western boundary of the Labrador Sea (Straneo, Kawase, & Riser, 2002; Straneo, Kawase, & Pickart, 2002). Similarly, katabatic winds impact the formation of dense waters in the boundary current of the western Irminger Sea (Gutjahr et al., 2022).

4. Can the newly developed methods of identifying Irminger Water within the boundary current system be implemented to identify Atlantic Water in the Nordic Seas and Arctic Ocean?

The hydrographic method provides IW_{hydro} thicknesses in the eastern SPNA (Figure 5.22). One potential future task could involve using the hydrographic method to analyze warm and saline Atlantic Water along its pathway into the Nordic Seas and Arctic Ocean (Figure 7.1, dark green). Similar to previous studies that analyzed IW using static thresholds, studies in higher latitudes examined Atlantic Water using static thresholds (e.g., Beszczynska-Möller et al., 2012; Fu et al., 2023). Implementing the provenance method to investigate Atlantic Water variability along different sections or using the hydrographic method to study Atlantic Water in a broader context could account for large-scale changes in the water column, similar to the results demonstrated within the BCS. Particularly considering that the Atlantic Water entering the Arctic Ocean is undergoing warming (Beszczynska-Möller et al., 2012; Polyakov et al., 2017), I suggest that the hydrographic method automatically accounts for this warming trend, assuming the general structure of the water column for temperature and salinity remains consistent. Additionally, since the term Atlantification (Polyakov et al., 2017; Smedsrud et al., 2021; Wendisch et al., 2023) denotes a simultaneous increase in Atlantic Water temperature and salinity in the Arctic Ocean, I propose that the hydrographic method is suitable for identifying temporally and spatially varying Atlantic Water throughout the Arctic Ocean.

5. Does LAB60 reveal a distinct subsurface temperature and salinity maximum further upstream from eastern AR7W, and if so, where does the vertical structure of the water column change?

Future work could involve a more detailed analysis of LAB60 (Figure 7.1, purple). Due to time limitations, this thesis was restricted to analyzing LAB60 only at east-

ern AR7W. Here, the IW properties coincide well with ARMOR3D using the static method to identify IW_{stat}. However, the vertical structure of the water column does not resemble ARMOR3D (Figure 5.3) and in-situ observations.

Thus, an initial analysis using LAB60 could focus on a cross-slope section closest to the boundary of the nested 1/60° domain. Such a section could be 44° West (Section 7), considering the sections analyzed in this thesis. If a characteristic subsurface temperature and salinity maximum resembling IW could be identified close to the boundary of the 1/60° domain, further analyses would follow the BCS downstream to observe how such a characteristic subsurface temperature and salinity maximum changes. In such a case, extracting an along-slope section following Chapter 5.5 could also be helpful to identify where within the BCS such a subsurface signal is diluted. Pennelly and Myers (2020) already analyzed the pathway of IW in LAB60 by utilizing similar static thresholds as Myers et al. (2007, see Table 4.1). By tracking IW as a passive tracer, Pennelly and Myers (2020) found IW within the entire BCS and also in the interior Labrador Sea. Their results compare well with the calculated IW_{stat} thickness in ANHA12 (Figure 5.22).

Pennelly and Myers (2020) also compared LAB60 at AR7W with a scientific cruise in May 2008 (included in ARMOR3D, see Table 2.1, Harrison, 2008) and found that LAB60 was too warm and saline, with the highest salinities reaching greater depth of $\sim$1,500 to 2,000 m, aligning with the averaged results at eastern AR7W found in this thesis (Figure 5.3 i). Due to this model bias and the chosen IW thresholds, their identified IW may contain larger amounts of ambient waters, such as NEADW. As the provenance method has adjusted persistent biases in GLORYS, ANHA4, and ANHA12, applying this method to LAB60 would be interesting. However, that would require a larger LAB60 domain spanning the Irminger Sea. However, as the overall bias between LAB60 and ARMOR3D is smaller than the biases between ANHA4 or ANHA12 and ARMOR3D, the largest issue in LAB60 remains the missing subsurface temperature and salinity maximum in the typical IW depth of 500 m when referring to eastern AR7W.

6. Can the obtained time series of hydrographic Irminger Water variability be used to quantify a direct influence on the melting estimates of marine-terminating glaciers?

The hydrographic method allows the analysis of IW_{hydro} variability, which can be considered as remnants of former pure IW. Consequently, this new method could be utilized to compare the subsurface melting of Greenland's glaciers with the variability of IW_{hydro} (e.g., Huhn et al., pers. comm., Figure 7.1, light green) as the primary contributor of heat in the subsurface layers of the fjords (Holland et al., 2008; Rignot et al., 2012; Myers & Ribergaard, 2013; Straneo & Cenedese, 2015). Previous studies that used static thresholds to estimate the contribution of Atlantic-origin waters to the melting of marine-terminating glaciers in Greenland could reassess their findings using the new temporally varying thresholds (e.g., Hansen et al., 2012; Gladish et al., 2014). Such a reevaluation and resulting new estimates could substantially enhance the understanding of IW's role in melting Greenland's marine-terminating glaciers and, consequently, its contribution to global sea level rise.

"We've always defined ourselves by the ability to overcome the impossible. And I count these moments. These moments when I dare to aim higher, to break barriers, to reach for the stars, to make the unknown known. I count these moments as our proudest achievements."

Joseph A. Cooper - Character in the movie Interstellar, 2014,
NASA pilot and engineer

Appendix

In the following Appendix, I present figures that underline specific statements in the main text. When comparing results obtained from ARMOR3D, GLORYS, ANHA4, and ANHA12, I often present the results from ARMOR3D in the main text and include the results for the other three data sets here for completeness. All figures shown in the Appendix have been used and described in the main text. Thus, I only provide brief additional information within the individual subchapters without going into a detailed discussion of the figures.

A Irminger Water frequencies in ARMOR3D and in-situ data

As an additional comparison between ARMOR3D and purely in-situ observations, I have included an analysis of IW frequencies using the DOORS data in Figure A.1. The results for DOORS and the comparison with ship-based data and ARMOR3D have been previously discussed in Chapter 3.2.

B Seasonal Irminger Water variability

In order to demonstrate that the rapid increase in IW salinity and volume transport observed in ARMOR3D does not occur upstream of AR7W, I present the annual climatology at OSNAP West between 1993 and 2022 (Figure B.1 a - d). For a more meaningful comparison between the climatologies of ARMOR3D and the OSNAP West mooring data, I provide the annual climatology calculated between 2014 and 2018 for both data sets (Figure B.1 e - h).

I have calculated IW salinity, temperature, velocity, and volume transport for each available in-situ realization of AR7W (Table 2.1). Additionally, I have analyzed ARMOR3D at the specific time of the in-situ measurements, which has been the week closest to the date of the measurements. This detailed analysis has allowed me to compare in-situ data with ARMOR3D in terms of the annual climatology (Chapter 3.3.1, Figure B.2). My findings have indicated that ship-based in-situ data and ARMOR3D essentially reveal akin IW properties. There is no clear indication that the difference between both data sets depends on the time of the year when the measurements were taken or whether the measurements were taken early or later in the period of available in-situ data between 1993 and 2018. Also, I have identified similar high salinities and volume transports for three in-situ realizations compared to ARMOR3D at the end of July. Hence, I cannot exclude that the 'jump' in ARMOR3D is, in fact, a valid signal.

C Hydrography at the cross-slope sections

I present salinity from ARMOR3D at the 25 cross-slope sections, following Figure 5.2 and Table 5.1 (Figure C.1). Tracing the path within the BCS downstream from the northernmost section in the Irminger Sea (Section 1 - Sermiligaaq) to the northernmost section in Baffin Bay (Section 19 - Qimusseriarsuaq) or the southernmost section in the western Labrador Sea (Section 25 - Northern Peninsula) illustrates the freshening of the water column. Furthermore, this representation highlights the different shapes of the local continental slopes and shelves while providing insight into the location of the most saline waters within the water column.

D Sea ice concentration

The regions around southern Greenland, including eastern AR7W, rarely experience sea ice. However, when analyzing other sections in the BCS, sea ice plays a crucial role by releasing freshwater during melting and releasing brine during freezing. Sections within Baffin Bay, in particular, experience extensive sea ice coverage in winter, which influences local temperature and salinity patterns. When calculating the thresholds for the hydrographic method, I found an apparent coherence between the salinity thresholds and the local sea ice concentration (Figure 4.7 and Figure 4.8). The sea ice concentration also provides initial insight into the regions where IW volume transports calculated in ARMOR3D require cautious interpretation, as ARMOR3D does not account for geostrophic velocities below sea ice. Hence, there might be an identified area of IW, but the calculated volume transport could be zero.

E Hydrography at eastern AR7W in multiple data sets

In Chapter 5.2.1, I have presented the averaged salinity at eastern AR7W across five data sets (ARMOR3D, GLORYS, ANHA4, ANHA12, and LAB60) between 2002 and 2020, along with their differences from ARMOR3D. Here, I present the averaged potential temperature θ (Figure E.1), potential density σ_θ (Figure E.2), and geostrophic velocity (Figure E.3) at eastern AR7W within these data sets. This analysis provides insights into areas further offshore compared to areas closer to the continental slope, where the temperature difference from ARMOR3D peaks across all other data sets. The large temperature imprint results in negative density anomalies compared to ARMOR3D and stronger horizontal density gradients, inferring differences in geostrophic

velocities. The other data sets reveal slightly higher velocities from ∼2 to 3 cm s^{-1} at a distance of 120 km offshore compared to ARMOR3D. Further to the shore, velocity differences reverse. At the continental slope, GLORYS and ANHA12 again reveal higher velocities compared to ARMOR3D, up to ∼15 cm s^{-1}. At the same time, ANHA4 only does so at the shelf break. Given the interaction between the IW area and its velocity is crucial for calculating volume transports, understanding the differences in hydrographic properties and velocities among the individual data sets holds key importance.

F Mean hydrography in the boundary current system

In Chapter 5.5.1, I have presented the 1,500 m isobath sections, enabling a detailed tracing of hydrographic properties from the Irminger Sea into Baffin Bay and the western Labrador Sea. I have presented the results for ARMOR3D in the main body (Chapter 5.5.1). Here, I present the results for the other three data sets, along with their differences compared to ARMOR3D: GLORYS (Figure F.1 and Figure F.2), ANHA4 (Figure F.3 and Figure F.4), and ANHA12 (Figure F.5 and Figure F.6).

G Salinity variability at the cross-slope sections

To gain insight into the IW_{stat} salinity (static method), I present results for all 25 cross-slope sections, following Figure 5.2 and Table 5.1. Figure G.1 displays the averaged climatological seasonal variability between 1993 and 2022. Figure G.2 shows multi-year variability for the same period. This perspective highlights the general freshening within the BCS. Furthermore, the results indicate a general salinity increase at the Baffin Bay sections, indicating times of the year when IW has not been identified. The rise in salinity may result from various mechanisms. IW is subsequently mixed with colder and fresher ambient waters. Thus, reaching the northernmost section analyzed in this thesis, only a smaller area with high salinities might be left. At the same time, the rest of the former IW is mixed below the static threshold. Another explanation might be the entrainment of brine into the water column. This hypothesis is underlined as high salinities form when the local sea ice concentration increases. Another explanation might lead back to the creation of the ARMOR3D fields. The data set strongly depends on satellite sea surface information, especially in regions with low data coverage. The entire procedure of creating the ARMOR3D fields might be error-prone to the existence of sea ice and thus locally and temporally resulting in defective data.

H Irminger Water salinity distribution

I have presented the area covered by specific salinity bins within IW for ARMOR3D in the main body (Chapter 5.5.2, Figure 5.20). Here, I provide the corresponding results for the other three data sets: GLORYS (Figure H.1), ANHA4 (Figure H.2), and ANHA12 (Figure H.3).

I Irminger Water properties in the boundary current system

I have presented the IW properties at the cross-slope sections and the 1,500 m isobath sections for ARMOR3D in the main body (Chapter 5.5.3, Figure 5.21). Here, I present the corresponding results for the other three data sets: GLORYS (Figure I.1), ANHA4 (Figure I.2), and ANHA12 (Figure I.3).

J Contribution to other studies

I contributed as a co-author to the study led by Gou et al. (2023), titled "Variability of eddy formation off the west Greenland coast from a 1/60° model". The study analyzed the barotropic and baroclinic instability west of Greenland using LAB60. We found that the variability of uISIW in the WGC on different time scales shapes the baroclinic instability. Thus, more uISIW in the water column leads to enhanced baroclinic instability as it increases the horizontal density gradient. These instabilities contribute to forming Irminger Rings and boundary current eddies that transport waters from the BCS into the interior Labrador Sea. Irminger Rings are buoyant eddies shed from the WGC near Cape Desolation (Fratantoni, 2001; Cuny et al., 2002). Boundary current eddies are formed in the boundary current (also in the Labrador Current) mainly via baroclinic instability (Pacini & Pickart, 2022). At OSNAP West, the formation of boundary current eddies is correlated with the LSW volume transport (Pacini & Pickart, 2022). While Irminger Rings have a lifespan of $\sim$100 days (Lilly et al., 2003; Luo et al., 2011; Rieck et al., 2019; Pennelly & Myers, 2022), the lifespan of the boundary current eddies is shorter (e.g., Chanut et al., 2008).

In the study, I calculated the volume transport time series of IW and uISIW at eastern AR7W and OSNAP West using ARMOR3D. Additionally, I contributed to the study by writing paragraph 2.a.2 about ARMOR3D and proofreading the manuscript multiple times during the submission and revision processes.

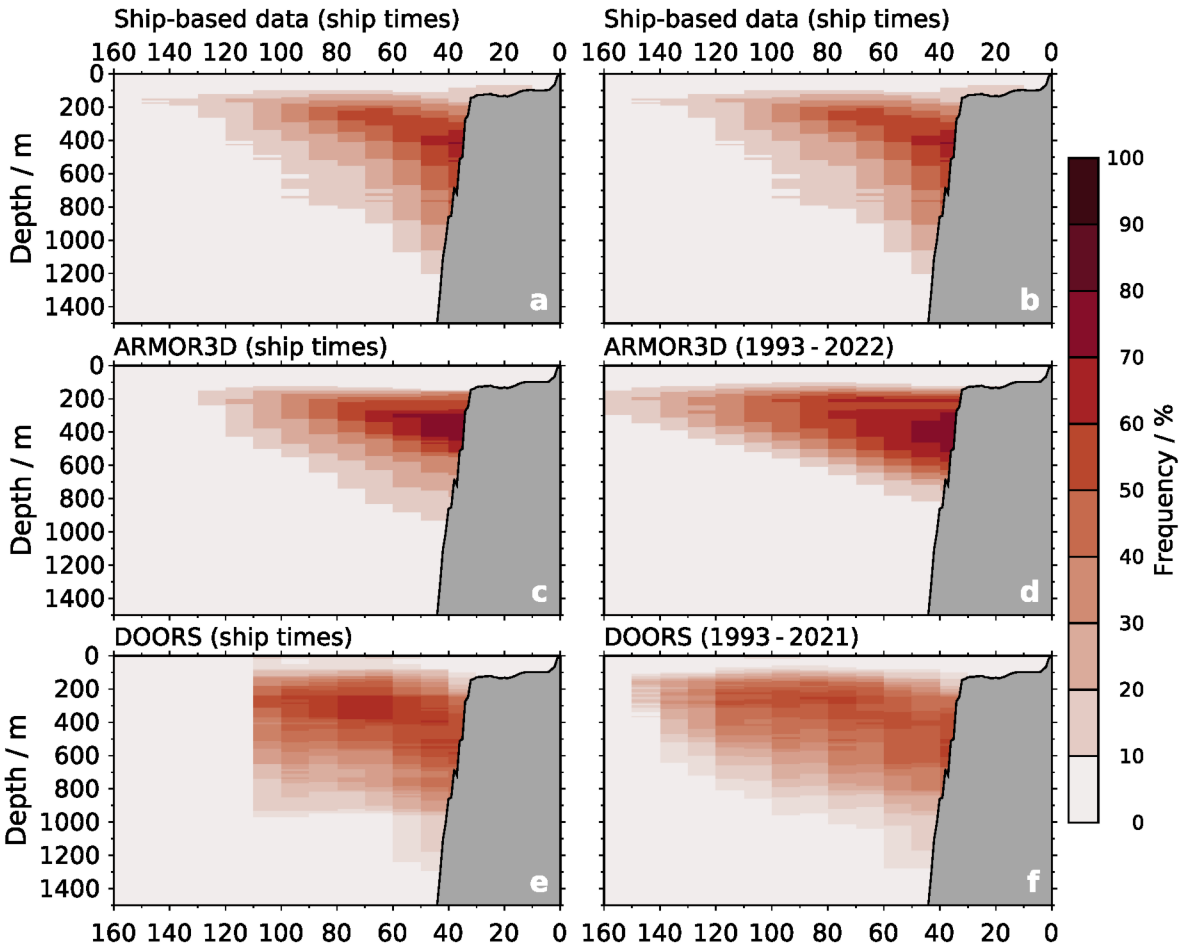

Figure A.1: Similar to Figure 3.4 but including the analysis for DOORS.
Total Irminger Water frequency (%) at eastern AR7W for different data sets (top to bottom: ship-based data (Chapter 2.5.1, Table 2.1), ARMOR3D, DOORS). The left column denotes frequencies only at available ship times (Table 2.1), the right column fully available times for the individual data sets (1993 - 2022 for ARMOR3D, 1993 - 2021 for DOORS).

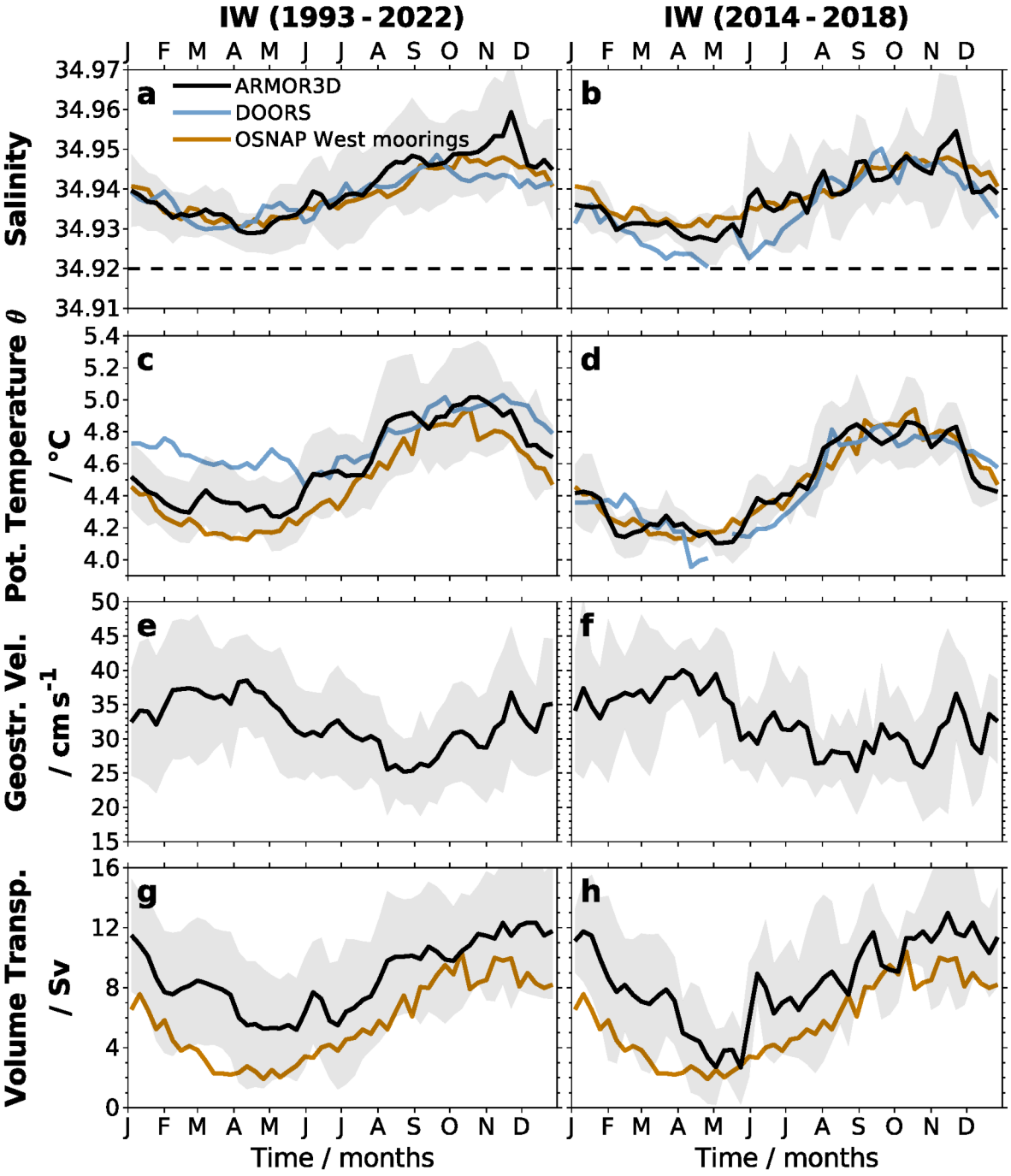

Figure B.1: Similar to Figure 3.8 but for two different periods, only for Irminger Water. Annual climatology of mean Irminger Water properties from 1993 - 2022 (left column) and 2014 - 2018 (right column) at OSNAP West. Properties are salinity (a, b), potential temperature θ (c, d), geostrophic velocity (e, f), volume transport (g, h). Bold, black lines indicate ARMOR3D with shaded standard deviation. Blue lines represent DOORS; orange lines represent OSNAP West mooring observations from 2014 - 2018, OSNAP West data from Pacini et al. (2020).

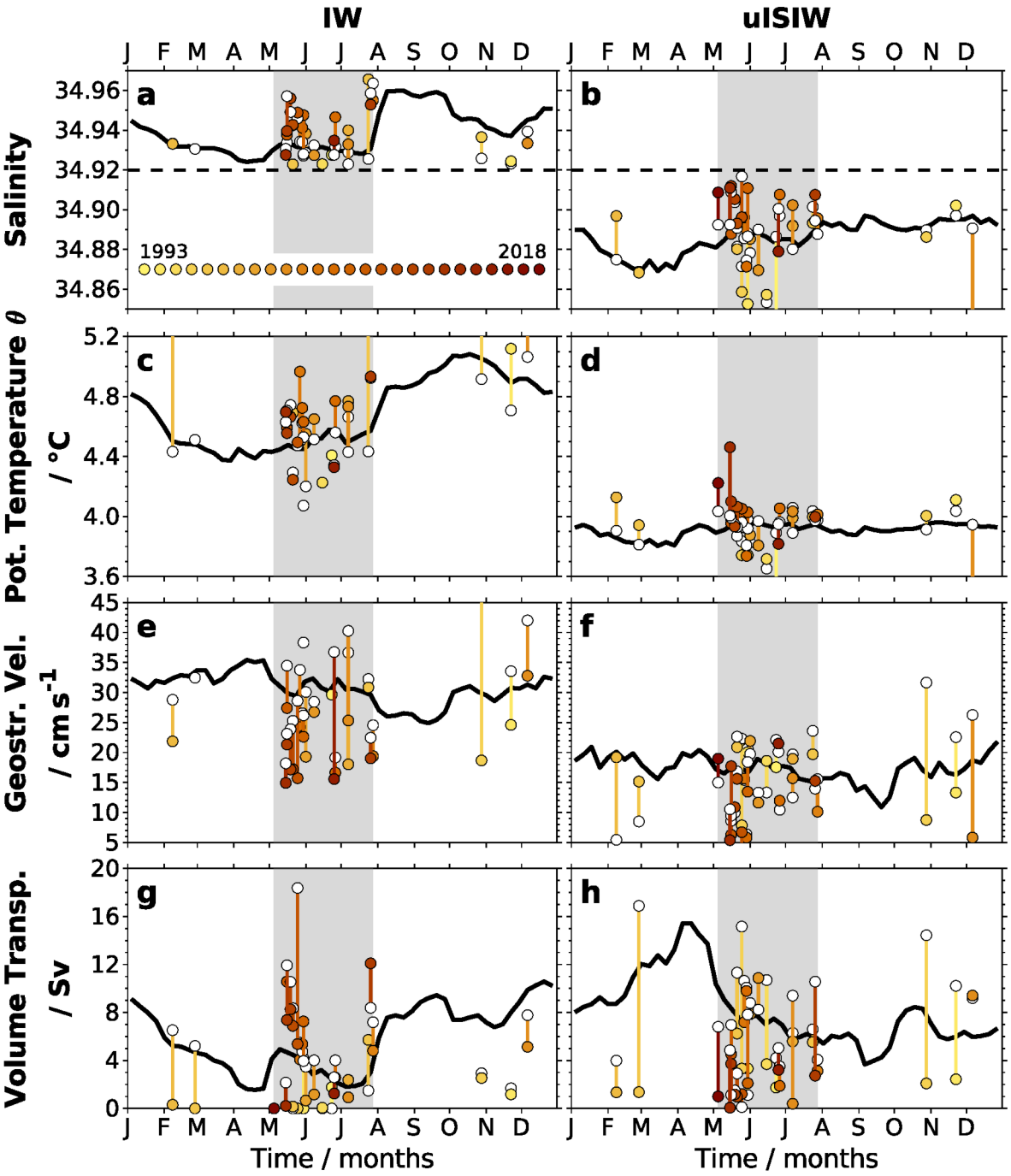

Figure B.2: Similar to Figure 3.8 but including ship-based measurements.
Annual climatology of mean Irminger Water (left column, IW) and upper Irminger Sea Intermediate Water (right column, uISIW) properties at eastern AR7W from 1993-2022. Properties are salinity (a, b), potential temperature θ (c, d), geostrophic velocity (e, f), volume transport (g, h). Bold, black lines indicate ARMOR3D. Gray shaded area shows the period with most ship-based observations from Figure 2.3. Colored circles represent single values from individual scientific cruises (yellow indicates earlier measurements, red later measurements). White circles represent single values from ARMOR3D at the time of the corresponding ship-based measurement. Colored vertical lines connect the pairs of ship-based data and ARMOR3D.

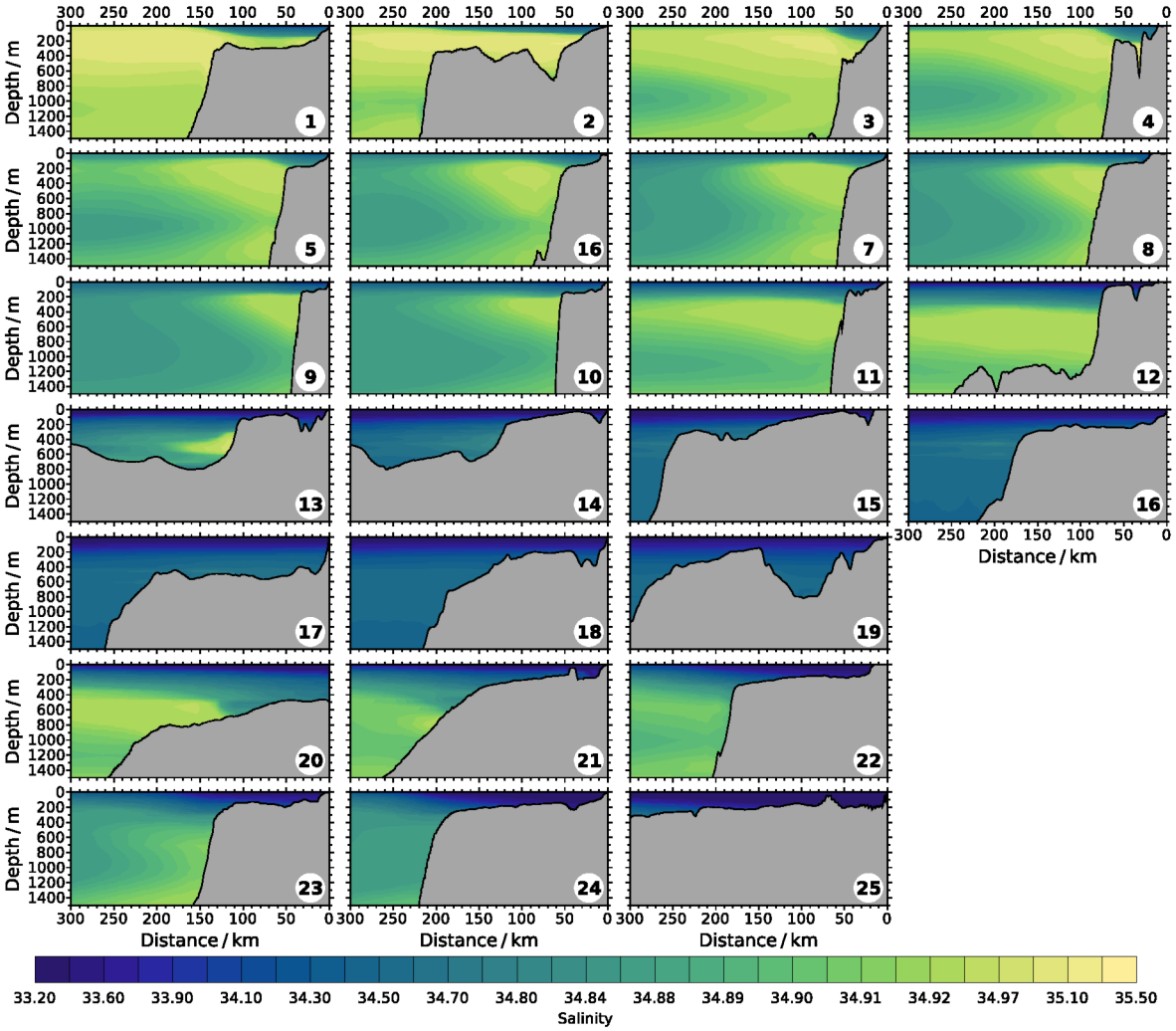

Figure C.1: ARMOR3D salinity averaged from 1993 - 2022 in the upper 1,500 m from the coast to a distance 300 km offshore at all investigated cross-slope sections (Figure 5.2). Numbers correspond to the individual sections assigned in Table 5.1.

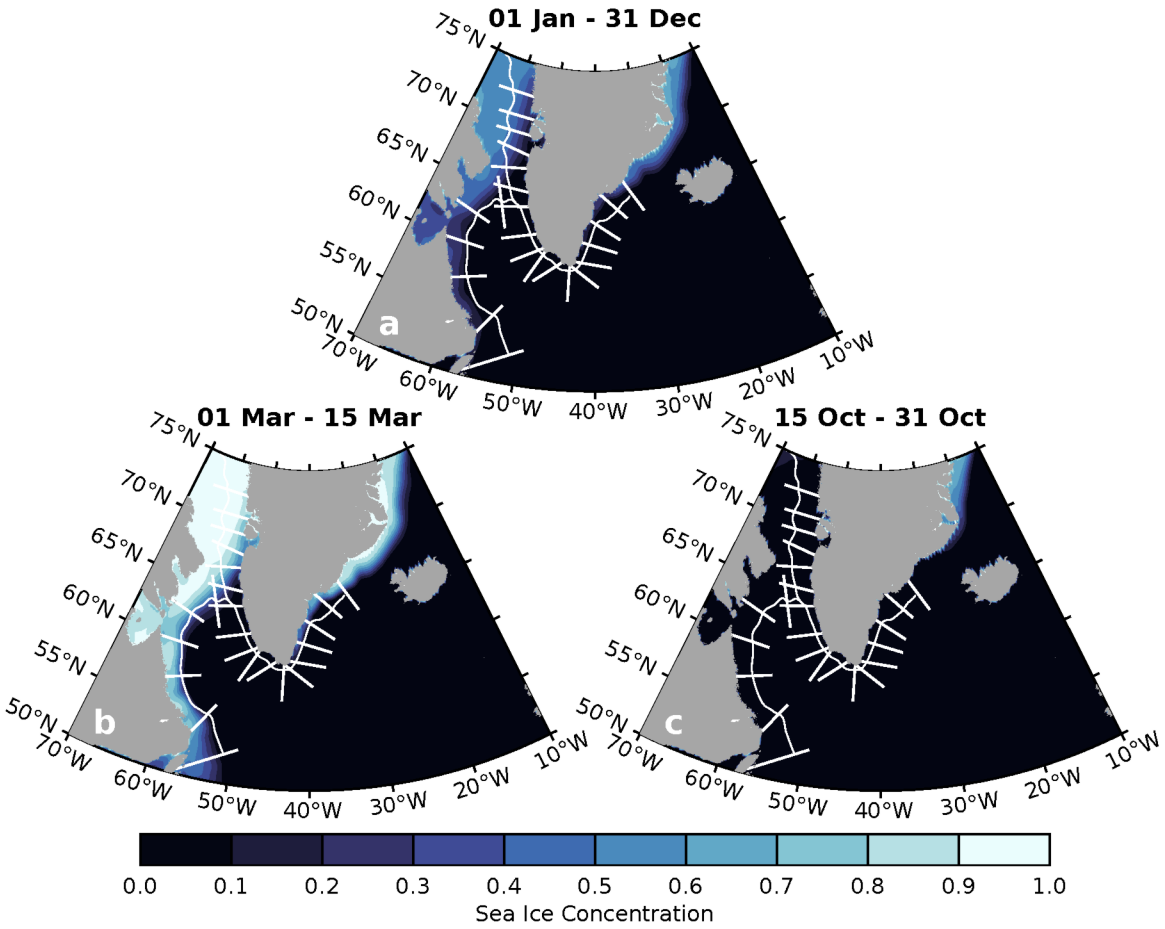

Figure D.1: Sea ice conentration from the National Snow and Ice Data Center averaged from 1993 - 2021 (DiGirolamo et al., 2022) for diffent times of the year: 01 Jan - 31 Dec (a), 01 Mar - 15 Mar (b), 15 Oct - 31 Oct (c). (b) represents maximum sea ice concentration at Sisimiut, (c) represents minimum sea ice concentration at Sisimiut.

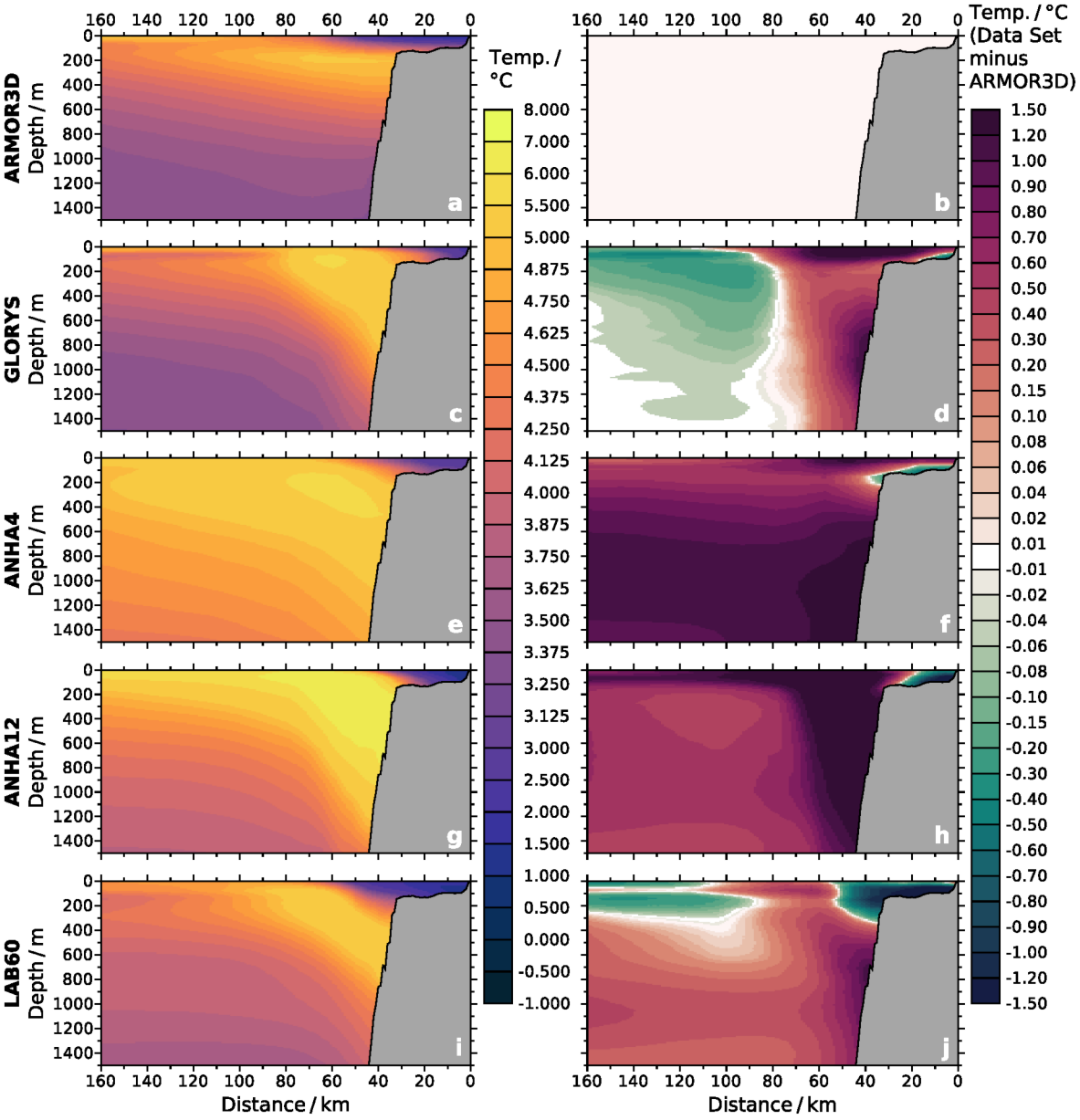

Figure E.1: Similar to Figure 5.3 but for the potential temperature.
Potential temperature θ at eastern AR7W in the upper 1,500 m from the coast to a distance 160 km offshore averaged from 2002 - 2020. The left column indicates data from the individual data sets (top to bottom: ARMOR3D, GLORYS, ANHA4, ANHA12, LAB60 from 2004 - 2018). The right column indicates the difference to ARMOR3D (data set minus ARMOR3D).

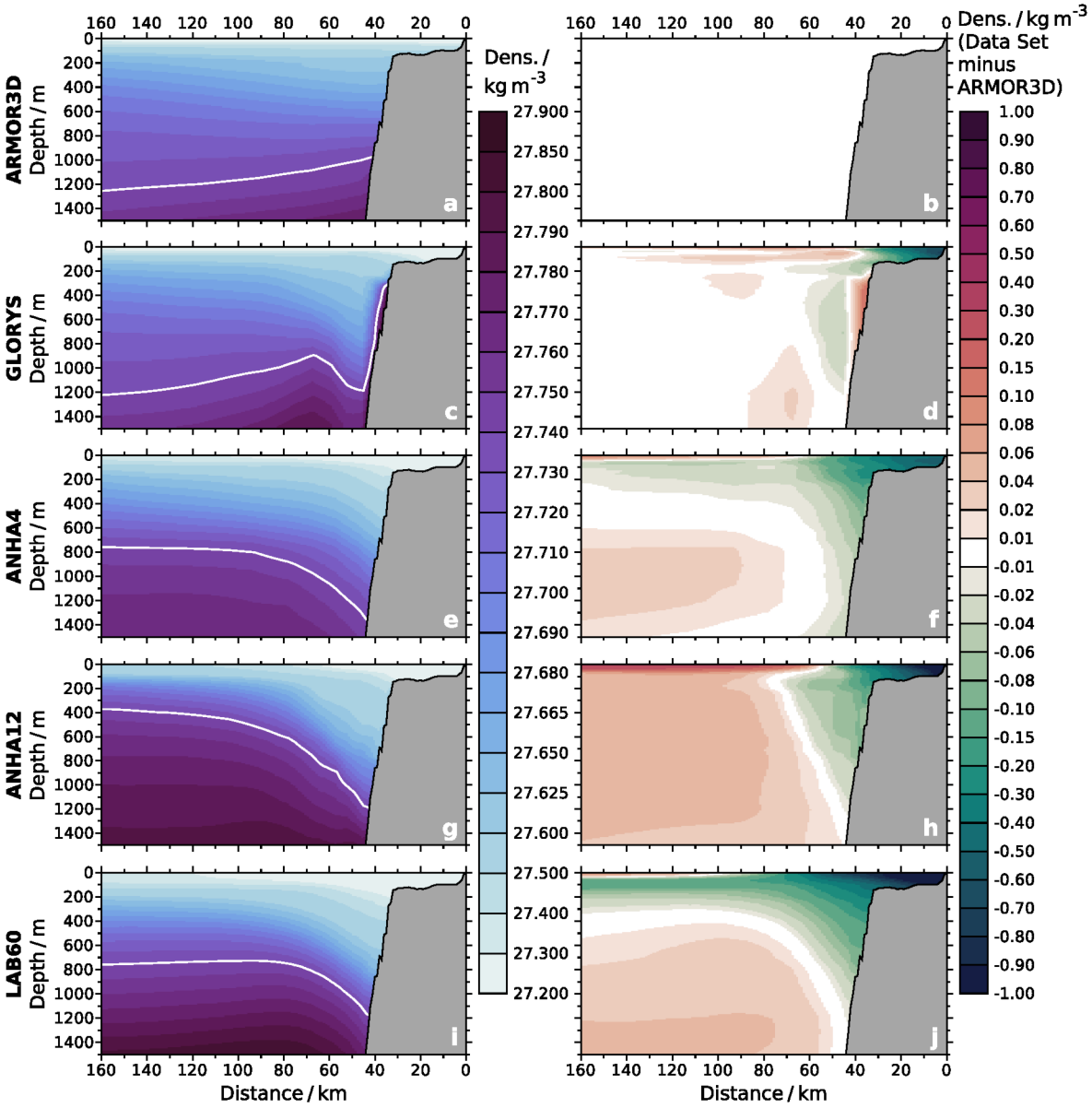

Figure E.2: Similar to Figure 5.3 but for the potential density.
Potential density σ_θ at eastern AR7W in the upper 1,500 m from the coast to a distance 160 km offshore averaged from 2002 - 2020. The left column indicates data from the individual data sets (top to bottom: ARMOR3D, GLORYS, ANHA4, ANHA12, LAB60 from 2004 - 2018). The white contour describes the 27.74 isopycnal that defines the IW_{stat} density threshold (Chapter 3.2, Table 3.1). The right column indicates the difference to ARMOR3D (data set minus ARMOR3D).

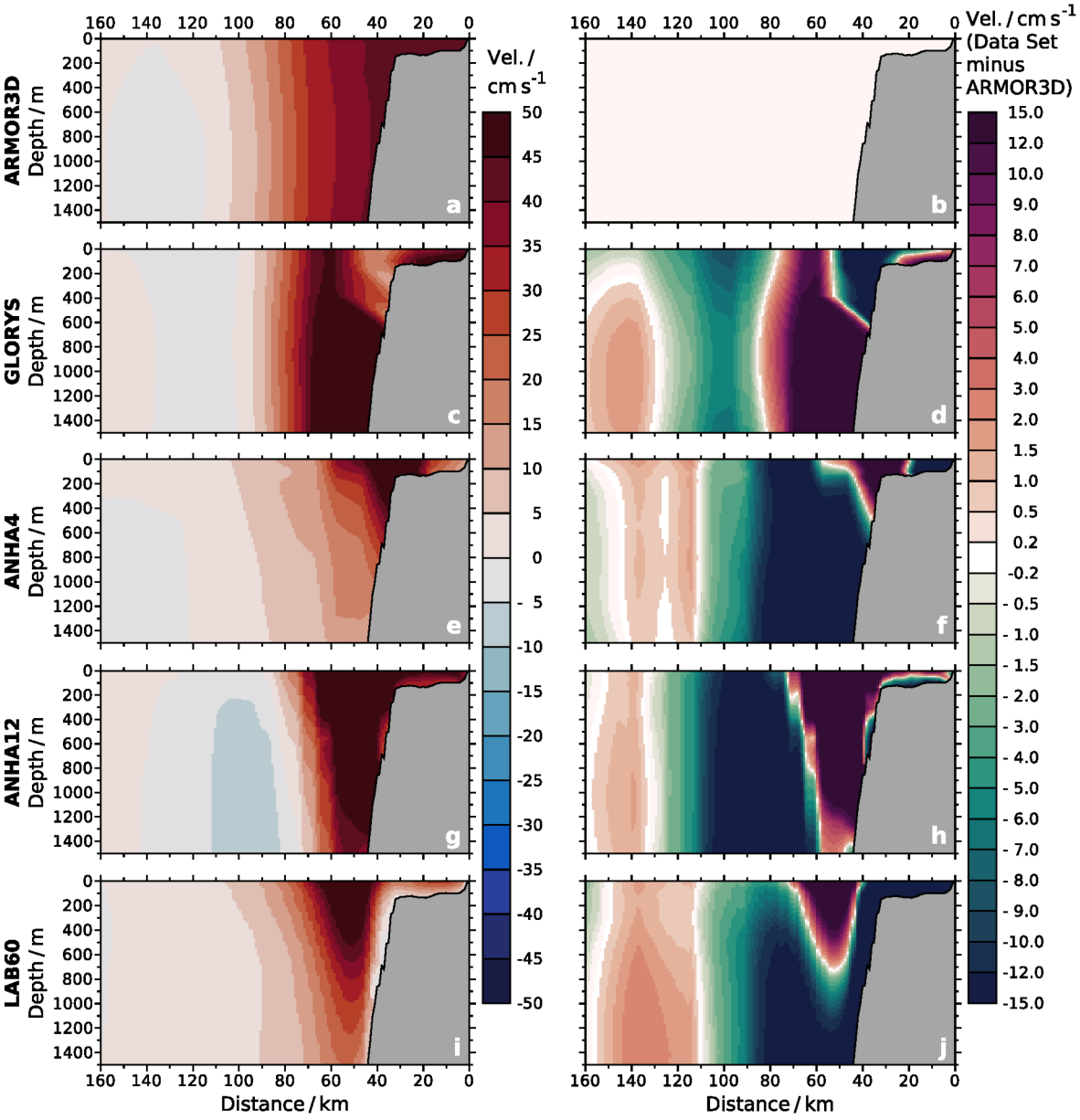

Figure E.3: Similar to Figure 5.3 but for the geostrophic cross-section velocities. Geostrophic cross-section velocities at eastern AR7W in the upper 1,500 m from the coast to a distance 160 km offshore averaged from 2002 - 2020. The left column indicates data from the individual data sets (top to bottom: ARMOR3D, GLORYS, ANHA4, ANHA12, LAB60 from 2004 - 2018). The right column indicates the difference to ARMOR3D (data set minus ARMOR3D).

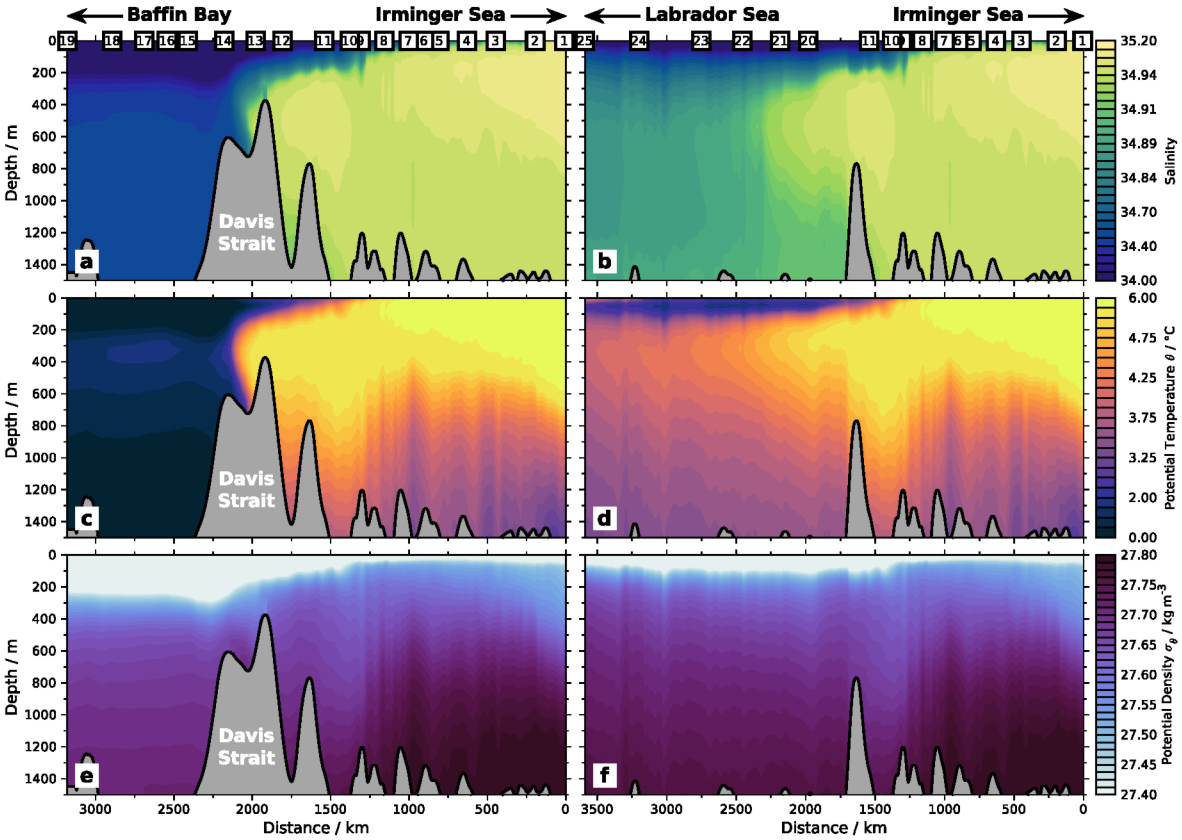

Figure F.1: Similar to Figure 5.19 but for GLORYS.
Hydrography in GLORYS along the two branches of the boundary current system along the 1,500 m isobath from 1993 - 2020 (left column: Irminger Sea into Baffin Bay - Section 26 in Figure 5.2; right column: Irminger Sea into the western Labrador Sea - Section 27 in Figure 5.2). Rows denote different properties (top to bottom: salinity, potential temperature θ, potential density σ_θ). Numbers in the upper column denote positions of individual cross-slope sections (see Table 5.1 and Figure 5.2). The local bathymetry is from ARMOR3D (see Figure 5.19).

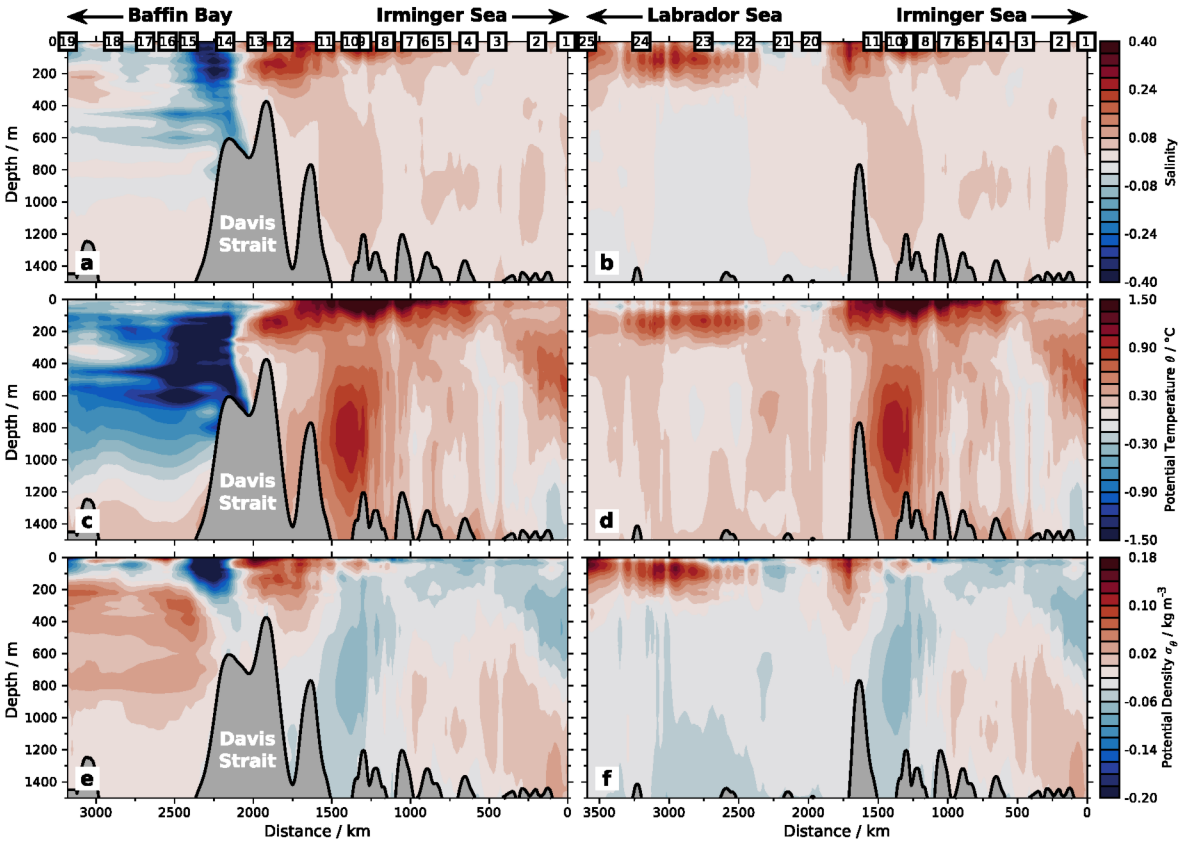

Figure F.2: Hydrography difference between GLORYS and ARMOR3D along the two branches of the boundary current system along the 1,500 m isobath from 2002 - 2020 (left column: Irminger Sea into Baffin Bay - Section 26 in Figure 5.2; right column: Irminger Sea into the western Labrador Sea - Section 27 in Figure 5.2). Rows denote different properties (top to bottom: salinity, potential temperature θ, potential density σ_θ). Numbers in the upper column denote positions of individual cross-slope sections (see Table 5.1 and Figure 5.2). The local bathymetry is from ARMOR3D (see Figure 5.19).

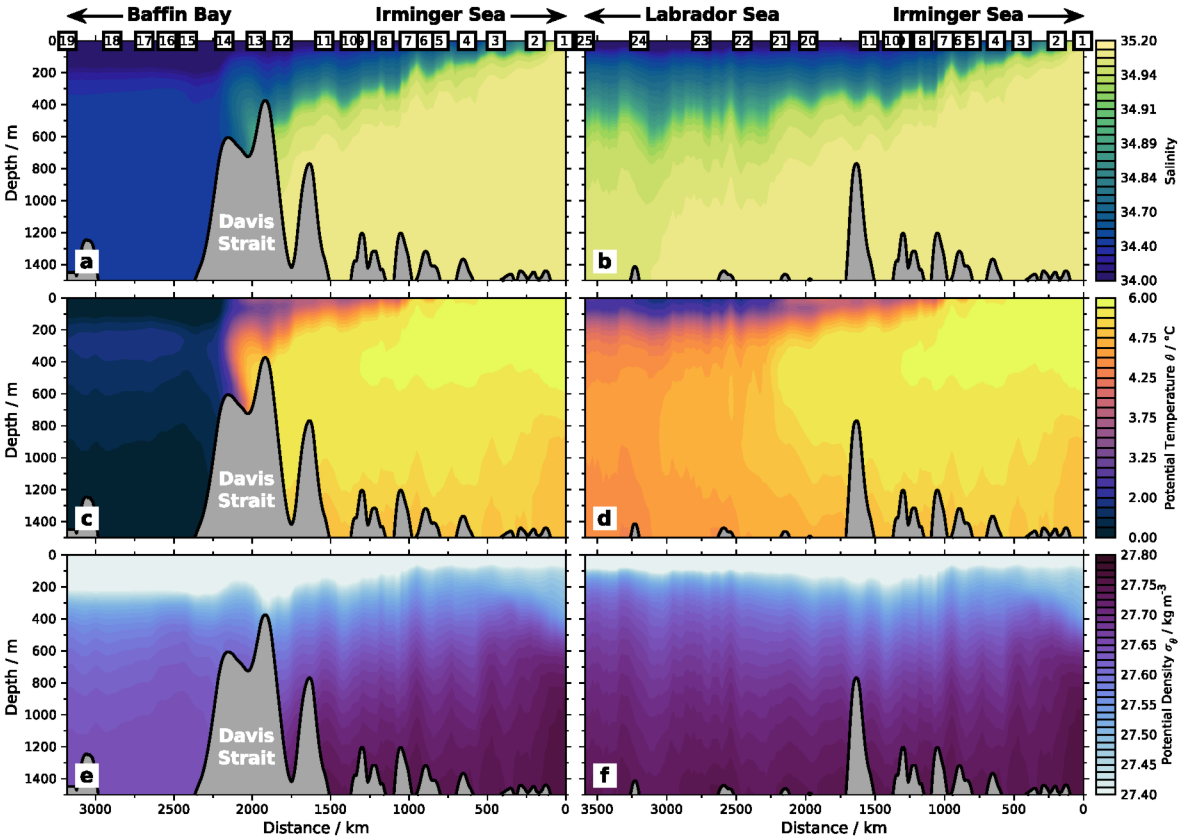

Figure F.3: Similar to Figure 5.19 but for ANHA4.
Hydrography in ANHA4 along the two branches of the boundary current system along the 1,500 m isobath from 2002 - 2021 (left column: Irminger Sea into Baffin Bay - Section 26 in Figure 5.2; right column: Irminger Sea into the western Labrador Sea - Section 27 in Figure 5.2). Rows denote different properties (top to bottom: salinity, potential temperature θ, potential density σ_θ). Numbers in the upper column denote positions of individual cross-slope sections (see Table 5.1 and Figure 5.2). The local bathymetry is from ARMOR3D (see Figure 5.19).

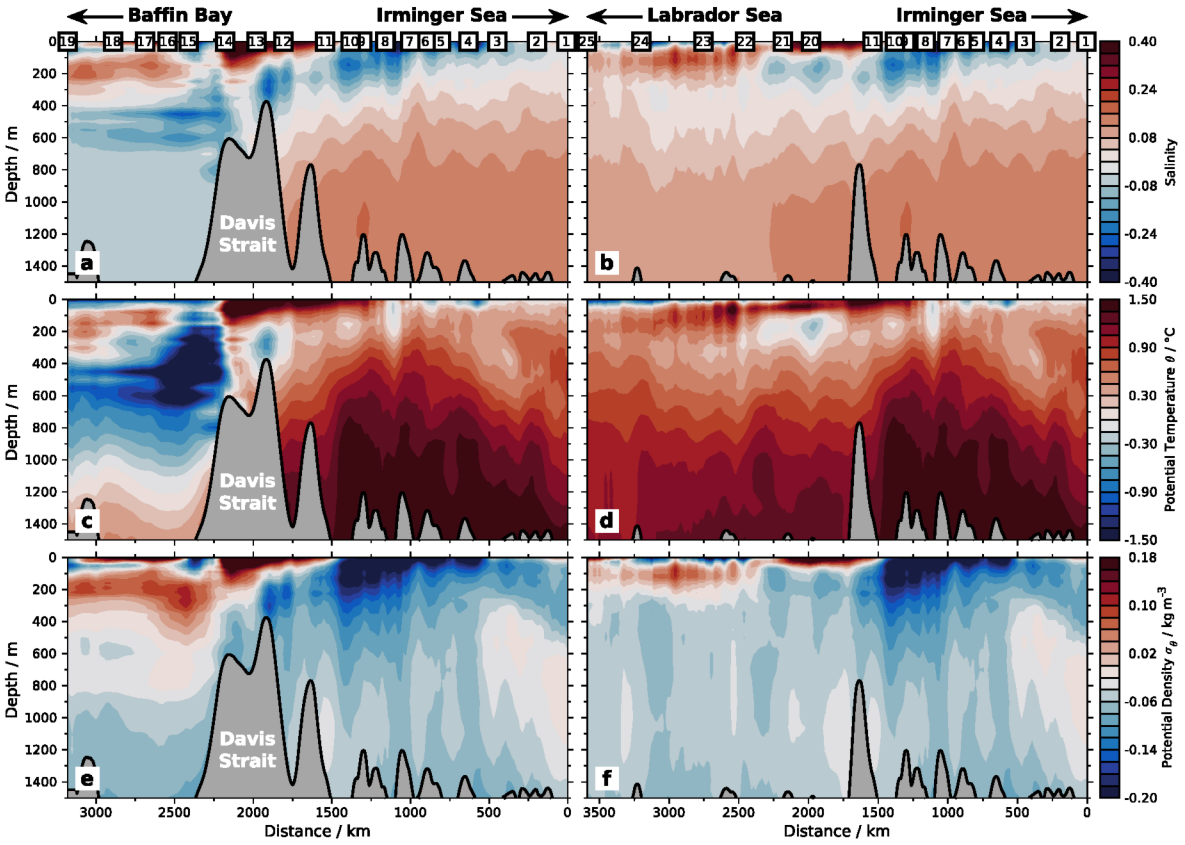

Figure F.4: Similar to Figure F.2 but for ANHA4.
Hydrography difference between ANHA4 and ARMOR3D along the two branches of the boundary current system along the 1,500 m isobath from 2002 - 2020 (left column: Irminger Sea into Baffin Bay - Section 26 in Figure 5.2; right column: Irminger Sea into the western Labrador Sea - Section 27 in Figure 5.2). Rows denote different properties (top to bottom: salinity, potential temperature θ, potential density σ_θ). Numbers in the upper column denote positions of individual cross-slope sections (see Table 5.1 and Figure 5.2). The local bathymetry is from ARMOR3D (see Figure 5.19).

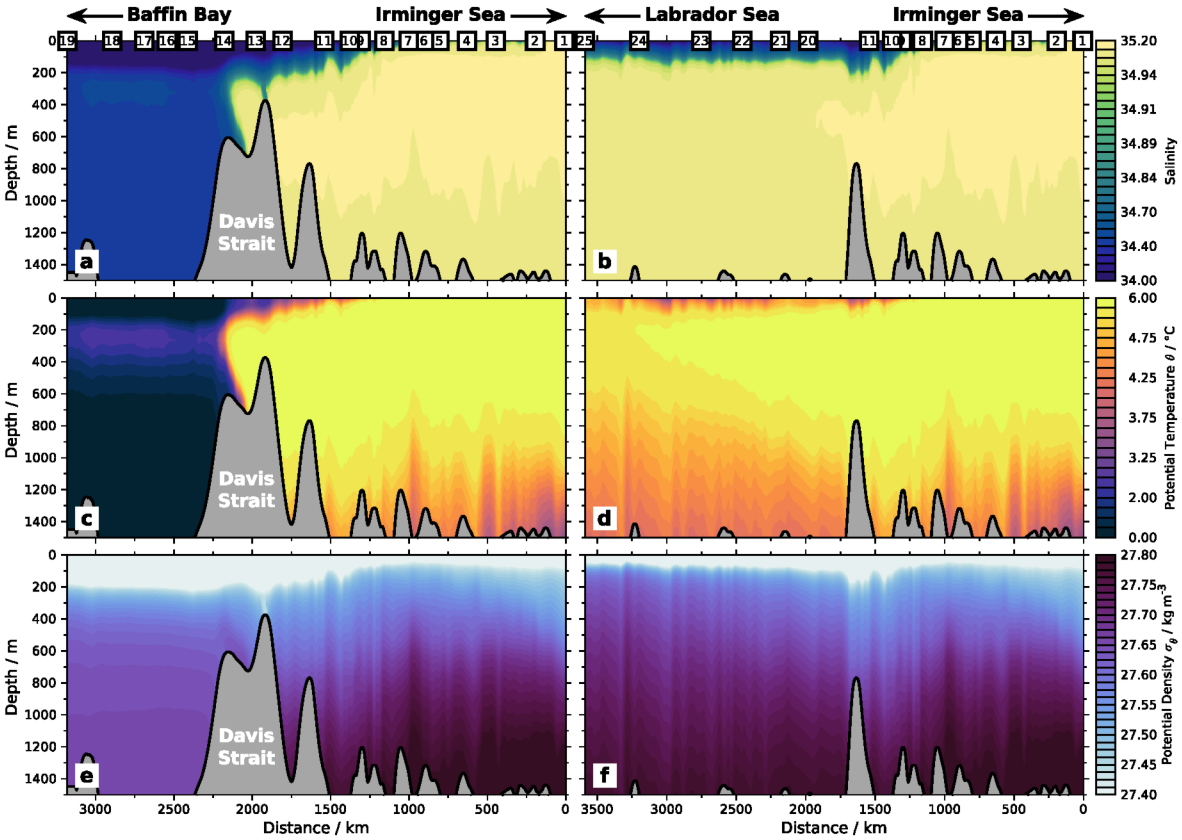

Figure F.5: Similar to Figure 5.19 but for ANHA12.
Hydrography in ANHA12 along the two branches of the boundary current system along the 1,500 m isobath from 2002 - 2021 (left column: Irminger Sea into Baffin Bay - Section 26 in Figure 5.2; right column: Irminger Sea into the western Labrador Sea - Section 27 in Figure 5.2). Rows denote different properties (top to bottom: salinity, potential temperature θ, potential density σ_θ). Numbers in the upper column denote positions of individual cross-slope sections (see Table 5.1 and Figure 5.2). The local bathymetry is from ARMOR3D (see Figure 5.19).

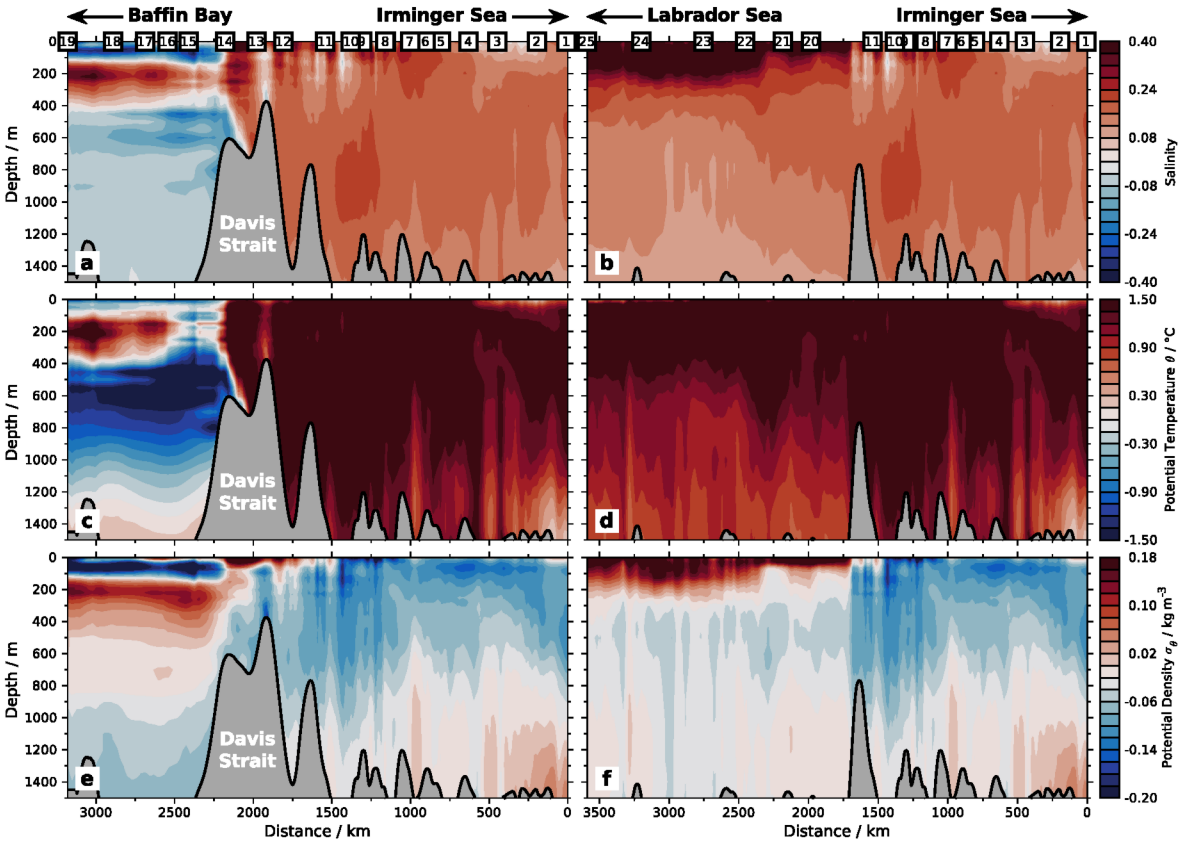

Figure F.6: Similar to Figure F.2 but for ANHA12.
Hydrography difference between ANHA12 and ARMOR3D along the two branches of the boundary current system along the 1,500 m isobath from 2002 - 2020 (left column: Irminger Sea into Baffin Bay - Section 26 in Figure 5.2; right column: Irminger Sea into the western Labrador Sea - Section 27 in Figure 5.2). Rows denote different properties (top to bottom: salinity, potential temperature θ, potential density σ_θ). Numbers in the upper column denote positions of individual cross-slope sections (see Table 5.1 and Figure 5.2). The local bathymetry is from ARMOR3D (see Figure 5.19).

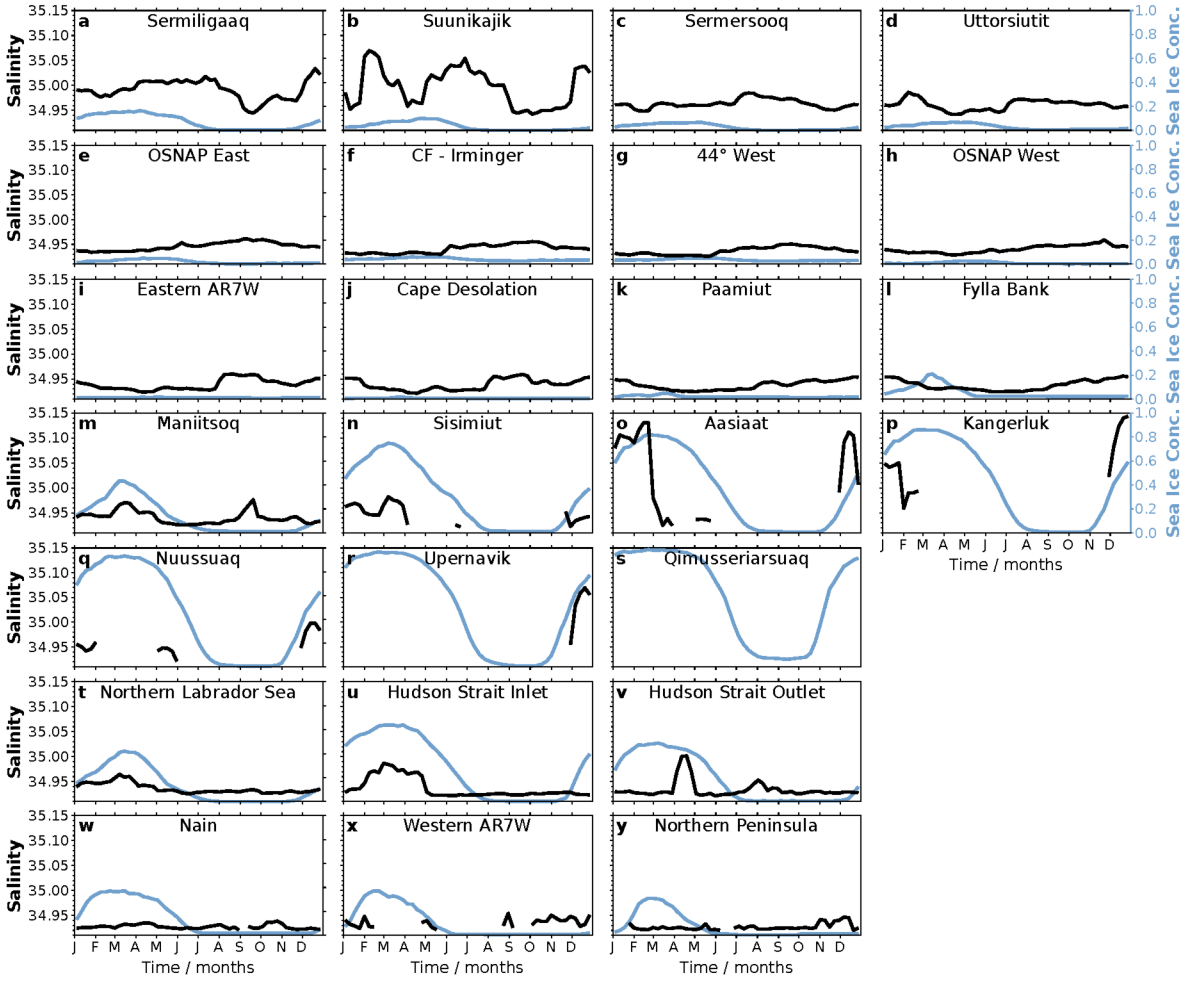

Figure G.1: Seasonal variability of Irminger Water salinity (black) in ARMOR3D obtained with the static method (1993 - 2022) and sea ice concentration (blue) from the National Snow and Ice Data Center (1993 - 2021) as climatologies (DiGirolamo et al., 2022). Subfigures denote the time series at individual cross-slope sections following Table 5.1 and Figure 5.2.

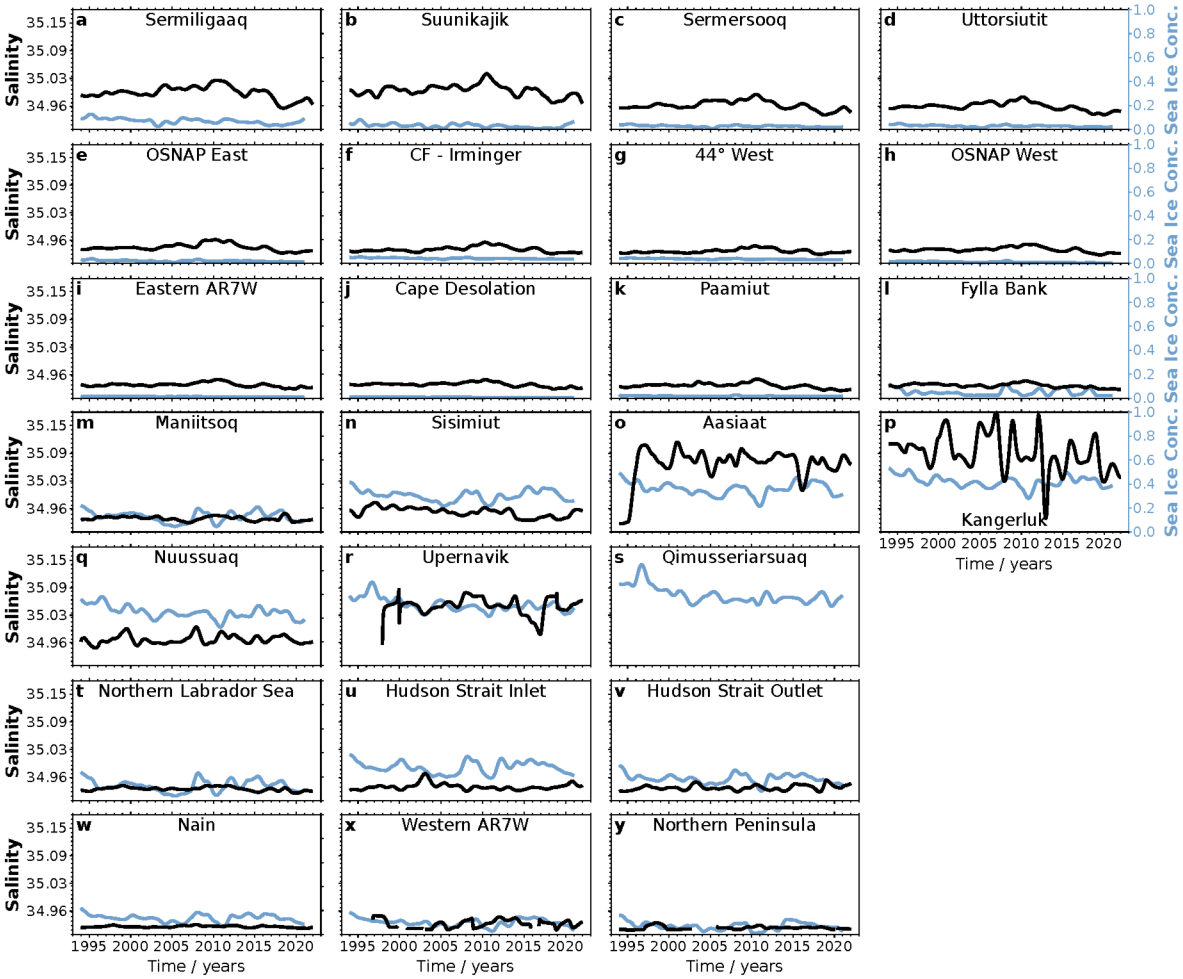

Figure G.2: Multi-year variability of Irminger Water salinity (black) in ARMOR3D obtained with the static method and sea ice concentration (blue) from the National Snow and Ice Data Center (DiGirolamo et al., 2022). A 2-year running average including a Hanning window was applied. Subfigures denote the time series at individual cross-slope sections following Table 5.1 and Figure 5.2.

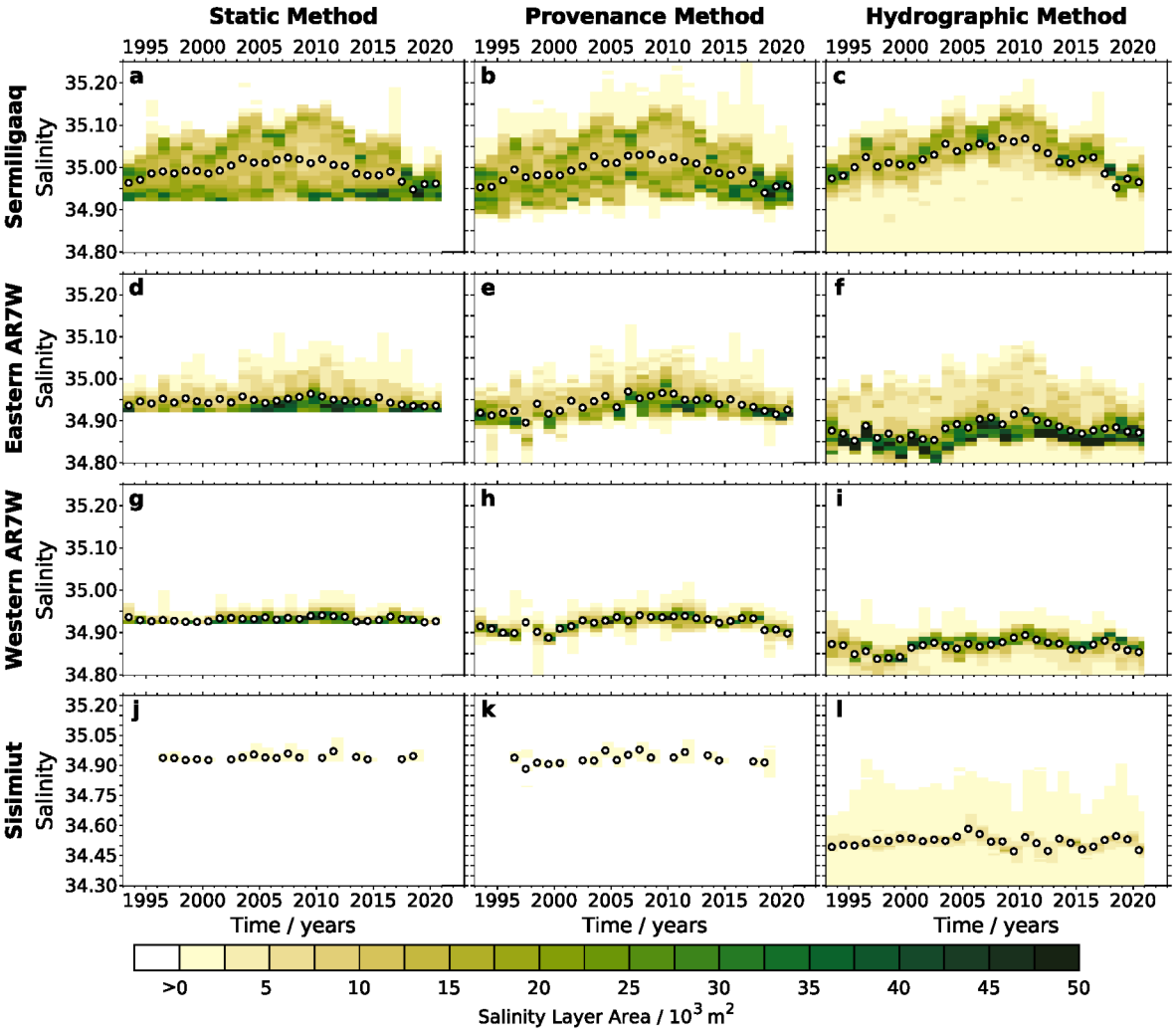

Figure H.1: Similar to Figure 5.20 but for GLORYS.
Yearly mean layer area for individual salinity bins obtained with different methods (left to right: static, provenance, hydrographic method) in GLORYS. Rows denote different sections (top to bottom: Sermiligaaq, eastern AR7W, western AR7W, Sisimiut. Circles denote yearly averaged salinities for the respective Irminger Water type.

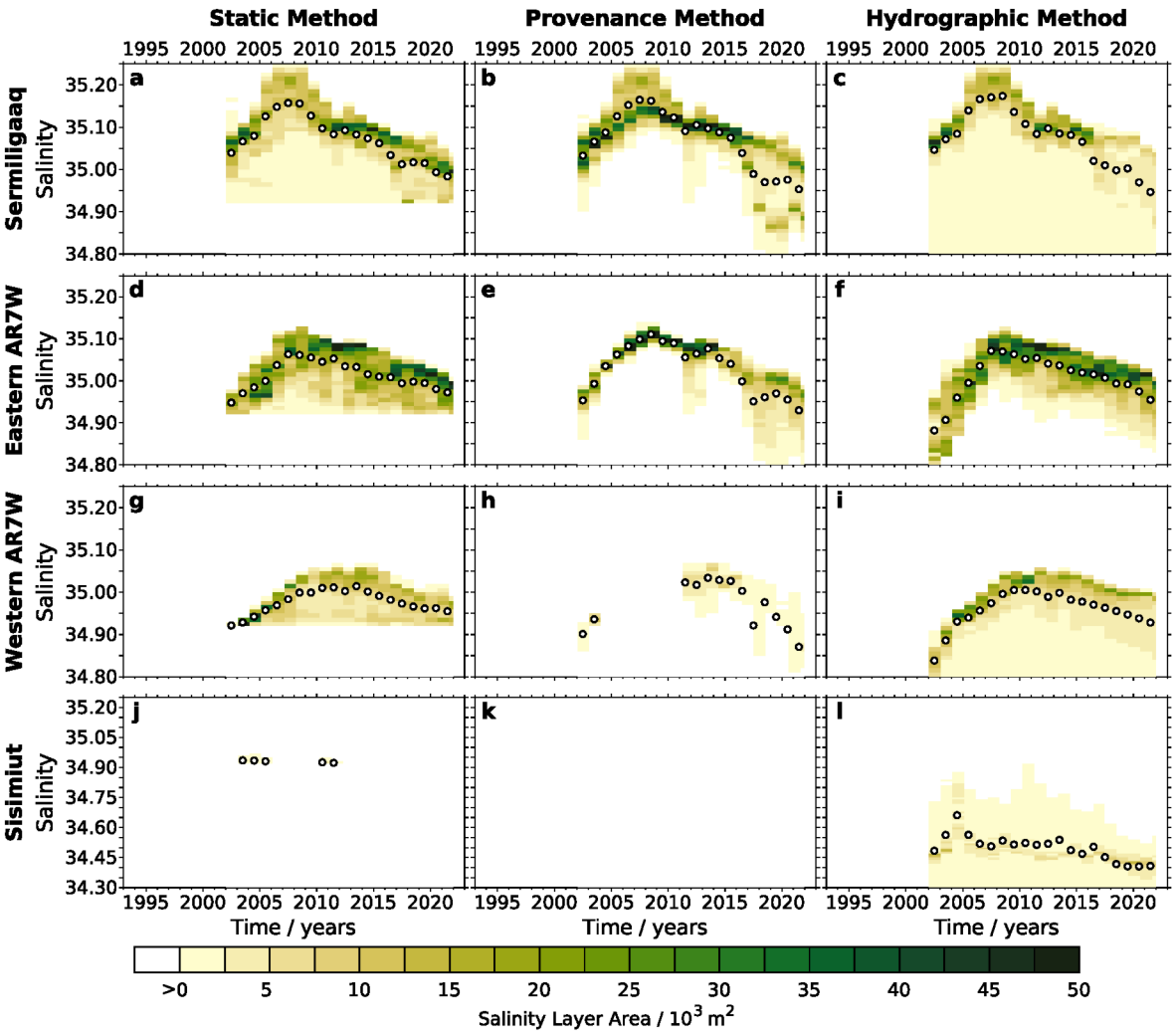

Figure H.2: Similar to Figure 5.20 but for ANHA4.
Yearly mean layer area for individual salinity bins obtained with different methods (left to right: static, provenance, hydrographic method) in ANHA4. Rows denote different sections (top to bottom: Sermiligaaq, eastern AR7W, western AR7W, Sisimiut. Circles denote yearly averaged salinities for the respective Irminger Water type.

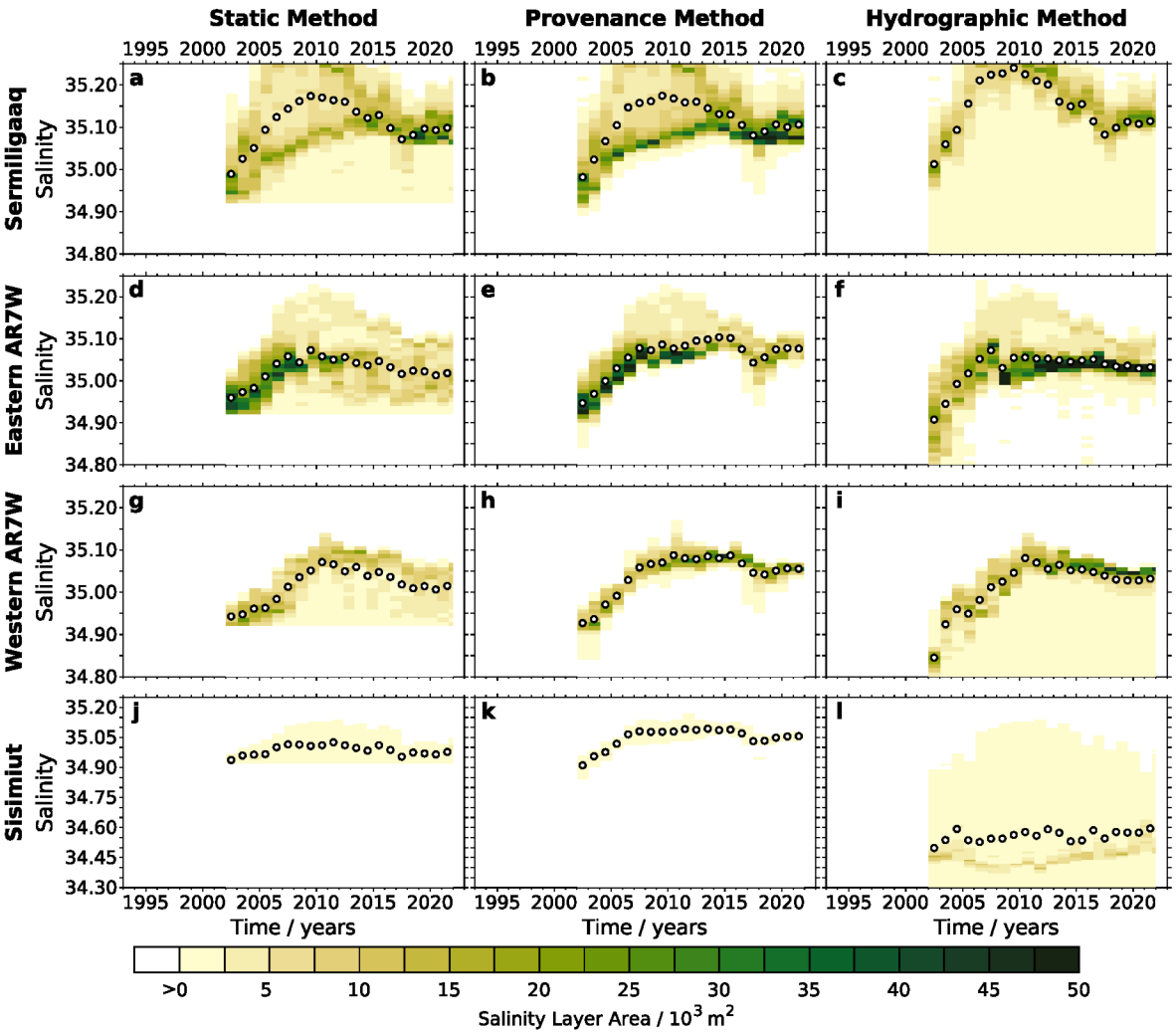

Figure H.3: Similar to Figure 5.20 but for ANHA12.
Yearly mean layer area for individual salinity bins obtained with different methods (left to right: static, provenance, hydrographic method) in ANHA12. Rows denote different sections (top to bottom: Sermiligaaq, eastern AR7W, western AR7W, Sisimiut. Circles denote yearly averaged salinities for the respective Irminger Water type.

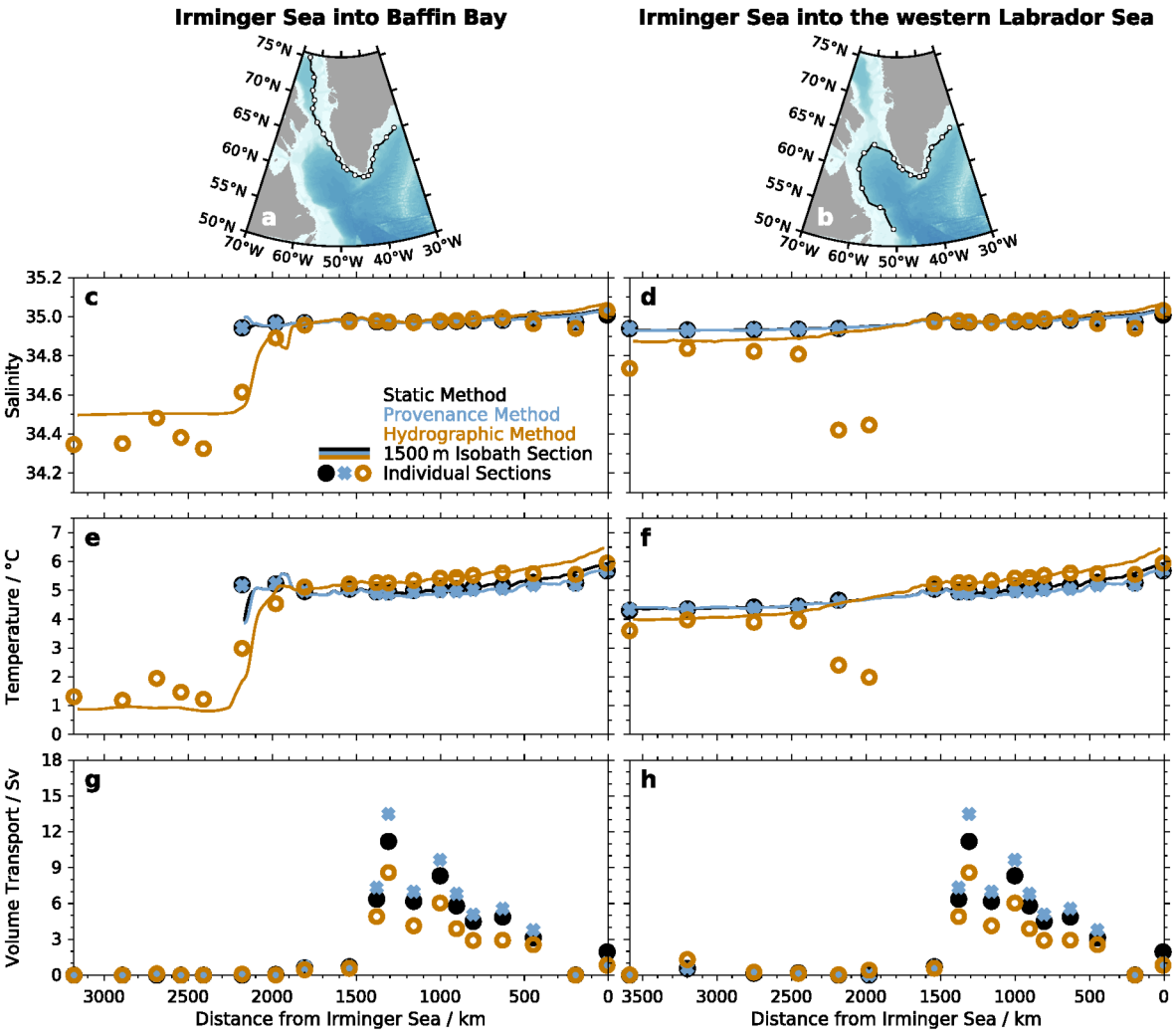

Figure I.1: Similar to Figure 5.21 but for GLORYS.
Irminger Water properties in the boundary current system in GLORYS averaged from 2002 - 2020 from the Irminger Sea into Baffin Bay (left) and into the western Labrador Sea (right). (a) and (b): Maps including the respective positions of individual cross-slope sections at the respective 1,500 m isobath section according to Figure 5.2. Other subfigures show Irminger Water properties (top to bottom: salinity, potential temperature θ, volume transport). Colors denote different methods: static (black), provenance (blue), hydrographic (orange). Solid lines represent the 1,500 m isobath sections. Black dots (static), blue crosses (provenance), orange circles (hydrographic) represent the individual cross-slope sections.

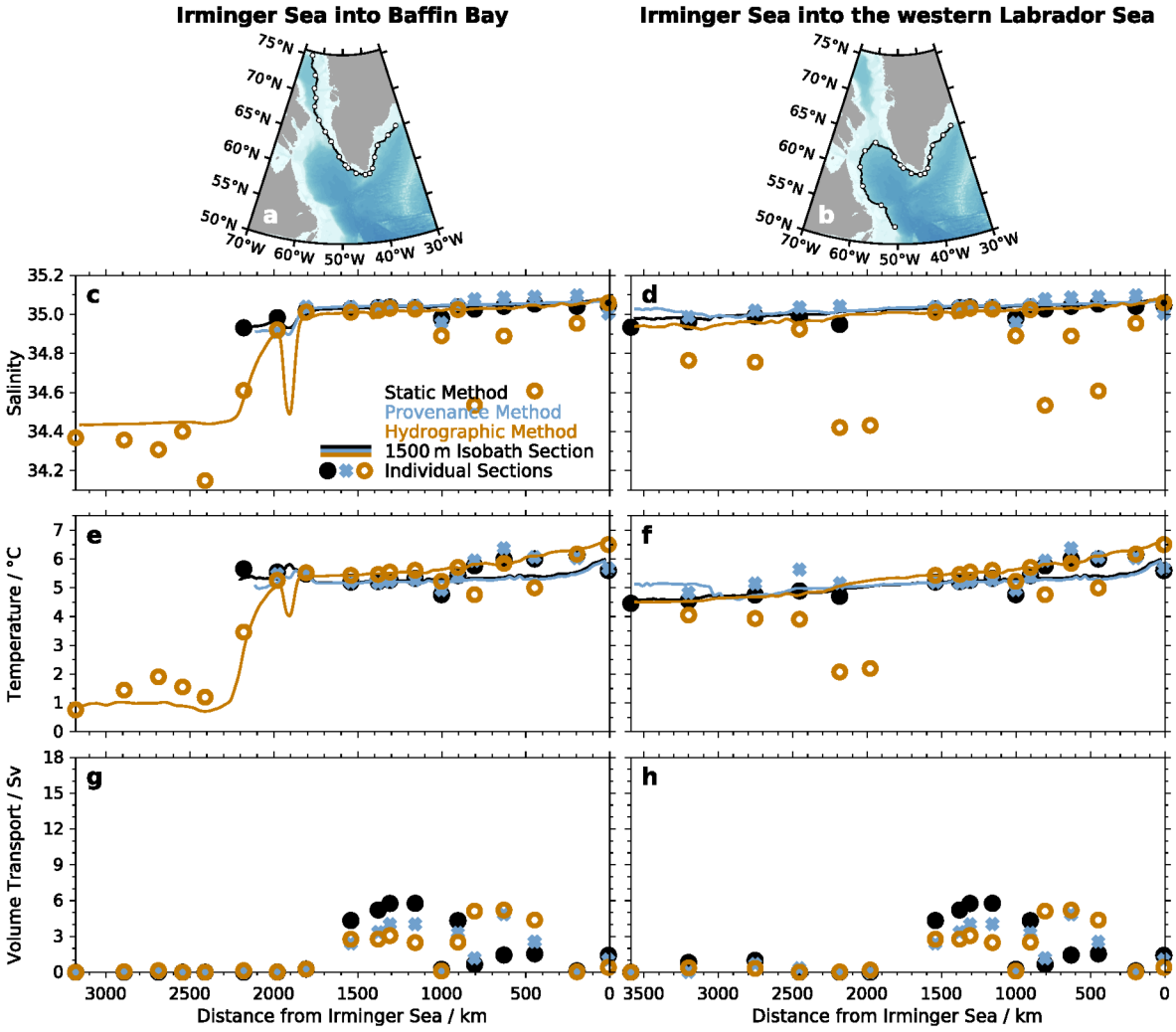

Figure I.2: Similar to Figure 5.21 but for ANHA4.
Irminger Water properties in the boundary current system in ANHA4 averaged from 2002 - 2020 from the Irminger Sea into Baffin Bay (left) and into the western Labrador Sea (right). (a) and (b): Maps including the respective positions of individual cross-slope sections at the respective 1,500 m isobath section according to Figure 5.2. Other subfigures show Irminger Water properties (top to bottom: salinity, potential temperature θ, volume transport). Colors denote different methods: static (black), provenance (blue), hydrographic (orange). Solid lines represent the 1,500 m isobath sections. Black dots (static), blue crosses (provenance), orange circles (hydrographic) represent the individual cross-slope sections.

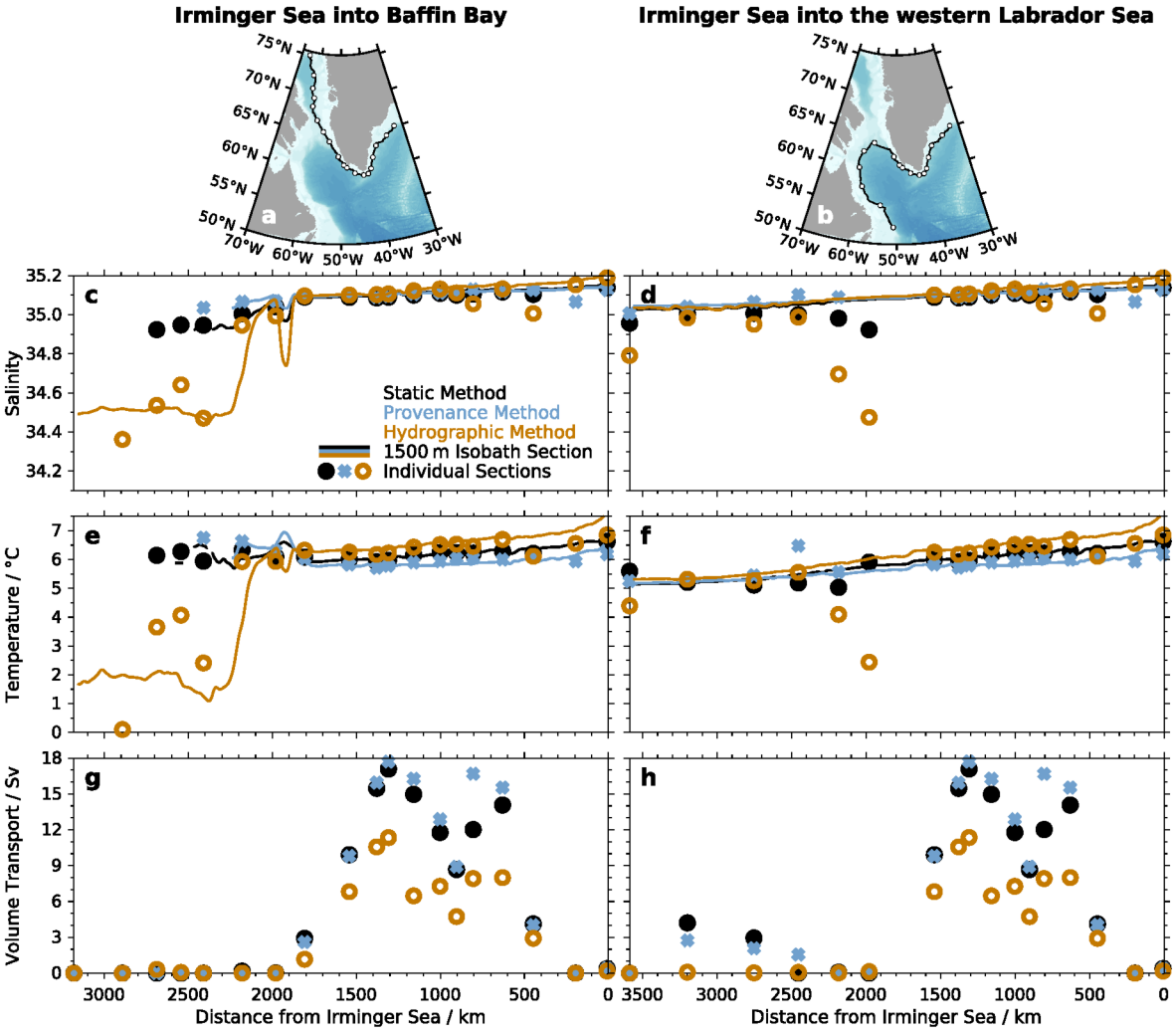

Figure I.3: Similar to Figure 5.21 but for ANHA12.
Irminger Water properties in the boundary current system in ANHA12 averaged from 2002 - 2020 from the Irminger Sea into Baffin Bay (left) and into the western Labrador Sea (right). (a) and (b): Maps including the respective positions of individual cross-slope sections at the respective 1,500 m isobath section according to Figure 5.2. Other subfigures show Irminger Water properties (top to bottom: salinity, potential temperature θ, volume transport). Colors denote different methods: static (black), provenance (blue), hydrographic (orange). Solid lines represent the 1,500 m isobath sections. Black dots (static), blue crosses (provenance), orange circles (hydrographic) represent the individual cross-slope sections.

Acronyms

AMOC	Atlantic Meridional Overturning Circulation
ANHA	Arctic Northern Hemisphere Atlantic
ANHA4	ANHA experiment with 1/4° horizontal resolution
ANHA12	ANHA experiment with 1/12° horizontal resolution
AR7W	Atlantic Repeat Hydrography 7 West
BCS	Boundary Current System
CTD	conductivity-temperature-depth
DOORS	Deep-Ocean Observation and Research Synthesis
EGC	East Greenland Current
GLORYS	Global Ocean Physics Reanalysis
IC	Irminger Current
IW	Irminger Water
$\mathbf{IW_{stat}}$	Irminger Water identified using the static method
$\mathbf{IW_{prov}}$	Irminger Water identified using the provenance method
$\mathbf{IW_{hydro}}$	Irminger Water identified using the hydrographic method
IPCC	Intergovernmental Panel on Climate Change
ISIW	Irminger Sea Intermediate Water
LAB60	ANHA4-SPG12-LAB60 - ANHA simulation with 1/60° in Labrador Sea
LSW	Labrador Sea Water
MLD	Mixed Layer Depth
NAC	North Atlantic Current
NAO	North Atlantic Oscillation
NEADW	North East Atlantic Deep Water
NEMO	Nucleus for European Modelling of the Ocean
NOAA	National Oceanic and Atmospheric Administration
OSNAP	Overturning in the Subpolar North Atlantic Program
OVIDE	Observatoire de la variabilité interannuelle et décennale en Atlantique Nord
SPG	subpolar gyre
SPNA	Subpolar North Atlantic
SSH	Sea Surface Height
uISIW	upper Irminger Sea Intermediate Water
WGC	West Greenland Current
WOCE	World Ocean Circulation Experiment

List of Figures

List of Tables

References

Amante, C., & Eakins, B. W. (2009). *ETOPO1 1 Arc-Minute Global Relief Model: Procedures, Data Sources and Analysis. NOAA Technical Memorandum NESDIS NGDC-24.* National Geophysical Data Center, NOAA. doi: 10.7289/V5C8276M

Argo. (2000). Argo float data and metadata from Global Data Assembly Centre (Argo GDAC). *SEANOE*. doi: 10.17882/42182

Aumont, O., Éthé, C., Lovato, T., Mouchet, A., Nurser, G., Palmiéri, J., & Yool, A. (2019). Tracers in Ocean Paradigm (TOP) – The NEMO passive tracers engine. *Zenodo*, Version 4.0.1. doi: 10.5281/zenodo.1471700

Bamber, J. L., Tedstone, A. J., King, M. D., van den Broeke, M. R., & Noel, B. (2018). Land Ice Freshwater Budget of the Arctic and North Atlantic Oceans: 1. Data, Methods, and Results. *J. Geophys. Res.: Oceans*, 123, 18271837. doi: 10.1002/2017JC013605

Barnston, A. G., & Livezey, R. E. (1987). Classification, Seasonality and Persistence of Low-Frequency Atmospheric Circulation Patterns. *Mon. Wea. Rev.*, 115, 1083-1126. doi: 10.1175/1520-0493(1987)115⟨1083:CSAPOL⟩2.0.CO;2

Beaird, N., Straneo, F., & Jenkins, W. (2015). Spreading of Greenland meltwaters in the ocean revealed by noble gases. *Geophys. Res. Lett.*, 42, 7705-7713. doi: 10.1002/2015GL065003

Beaird, N., Straneo, F., & Jenkins, W. (2018). Export of Strongly Diluted Greenland Meltwater From a Major Glacial Fjord. *Geophys. Res. Lett.*, 45, 4163-4170. doi: 10.1029/2018GL077000

Bernard, B., Madec, G., Penduff, T., Molines, J.-M., Treguier, A.-M., Sommer, J. L., ... Cuevas, B. D. (2006). Impact of partial steps and momentum advection schemes in a global ocean circulation model at eddy-permitting resolution. *Ocean Dyn.*, 56(5), 543-567. doi: 10.1007/s10236-006-0082-1

Bersch, M. (2002). North Atlantic Oscillation-induced changes of the upper layer circulation in the northern North Atlantic Ocean. *J. Geophys. Res.: Oceans*, 107, 3156. doi: 10.1029/2001JC000901

Beszczynska-Möller, A., Fahrbach, E., Schauer, U., & Hansen, E. (2012). Variability in Atlantic water temperature and transport at the entrance to the Arctic Ocean, 1997 – 2010. *ICES J. of Mar. Sc.*, 69, 852-863. doi: 10.1093/icesjms/fss056

Biló, T. C., Straneo, F., Holte, J., & Bras, I. A.-A. L. (2022). Arrival of New Great Salinity Anomaly Weakens Convection in the Irminger Sea. *Geophys. Res. Lett.*, 49, e2022GL098857. doi: 10.1029/2022GL098857

Blanke, B., & Raynaud, S. (1997). Kinematics of the Pacific Equatorial Undercurrent: An Eulerian and Lagrangian Approach from GCM Results. *Nature Geosciences*, 27, 1038-1053. doi: 10.1175/1520-0485(1997)027⟨1038:KOTPEU⟩2.0.CO;2

Blanke, B., Arhan, M., Madec, G., & Roche, S. (1999). Warm water paths in the equatorial Atlantic as diagnosed with a general circulation model. *J. Phys. Oceanogr.*, 29, 2753-2768. doi: 10.1175/1520-0485(1999)029⟨2753:WWPITE⟩2.0.CO;2

Bouillon, S., Maqueda, M. A. M., Legat, V., & Fichefet, T. (2009). An elastic-viscous-plastic sea ice model formulated on Arakawa B and C grids. *Ocean Modelling*,

26(3-4), 174-184. doi: 10.1016/j.ocemod.2009.01.004

Boyer, T. P., Garcia, H. E., Locarnini, R. A., Zweng, M. M., Reagan, A. V. M. J. R., Weathers, K. A., ... Smolyar, I. V. (2018). World Ocean Atlas 2018. *NOAA National Centers for Environmental Information*. Retrieved from https://accession.nodc.noaa.gov/NCEI-WOA18

Brachet, S., & Traon, P. Y. L. (2004). Mesoscale variability from a high-resolution model and from altimeter data in the North Atlantic Ocean. *J. Geophys. Res.: Oceans*, 109, C12025. doi: 10.1029/2004JC002360

Brambilla, E., & Talley, L. D. (2008). Subpolar Mode Water in the northeastern Atlantic: 1. Averaged properties and mean circulation. *J. Geophys. Res.*, 113, C04025. doi: 10.1029/2006JC004062

Brambilla, E., Talley, L. D., & Robbins, P. E. (2008b). Subpolar Mode Water in the northeastern Atlantic: 2. Origin and transformation. *J. Geophys. Res.*, 113, C04026. doi: 10.1029/2006JC004063

Breckenfelder, T., Rhein, M., Roessler, A., Böning, C. W., Biastoch, A., Behrens, E., & Mertens, C. (2017). Flow paths and variability of the North Atlantic Current: A comparison of observations and a high-resolution model. *J. Geophys. Res.: Oceans*, 122, 2686-2708. doi: 10.1002/2016JC012444

Bretherton, F. P., Davies, R. E., & Fandry, C. B. (1976). A technique for objective analysis and design of oceanographic experiments applied to MODE-73. *Deep-Sea Res.*, 23, 559-582. doi: 10.1016/0011-7471(76)90001-2

Broecker, W. S. (1987). The biggest chill. *Nat. Hist. Mag.*, 97, 74-82.

Buch, E. (2000). Air-Sea-Ice Conditions off Southwest Greenland, 1981–97. *J. Northw. Atl. Fish. Sci.*, 26, 123-136. doi: 10.2960/J.v26.a6

Buch, E. (2002). Present oceanographic conditions in Greenland Waters. *Danish Meteorological Institute Copenhagen*.

Buch, E., Pedersen, S. A., & Ribergaard, M. H. (2004). Ecosystem Variability in West Greenland Waters. *J. Northw. Atl. Fish. Sci.*, 34, 13-28. doi: 10.2960/J.v34.m479

Böning, C. W., Wagner, P., Handmann, P., Schwarzkopf, F. U., Getzlaff, K., & Biastoch, A. (2023). Decadal changes in Atlantic overturning due to the excessive 1990s Labrador Sea convection. *Nature Communications*, 14, 4635. doi: 10.1038/s41467-023-40323-9

Carmack, E. C., Yamamoto-Kawai, M., Haine, T. W. N., Bacon, S., Bluhm, B. A., Lique, C., ... Williams, W. J. (2016). Freshwater and its role in the Arctic Marine System: Sources, disposition, storage, export, and physical and biogeochemical consequences in the Arctic and global oceans. *J. Geophys. Res.: Biogeosciences*, 121, 678-717. doi: :10.1002/2015JG003140

Castro de la Guardia, L., Garcia-Quintana, Y., Claret, M., Hu, X., Galbraith, E. D., & Myers, P. G. (2019). Assessing the Role of High-Frequency Winds and Sea Ice Loss on Arctic Phytoplankton Blooms in an Ice-Ocean-Biogeochemical Model. *J. Geophys. Res.: Biogeosciences*, 124(9), 2728-2750. doi: 10.1029/2018JG004869

Chafik, L. (2019). *North Atlantic subpolar gyre index.* Dataset version 3.0. Bolin Centre Database. Retrieved 28.06.2021, from https://doi.org/10.17043/chafik-2019-3 doi: 10.17043/chafik-2019-3

Chafik, L., Holliday, N. P., Bacon, S., & Rossby, T. (2022). Irminger Sea Is the Center of Action for Subpolar AMOC Variability. *Geophys. Res. Lett.*, 49, e2022GL099133.

doi: 10.1029/2022GL099133

Chanut, J., Barnier, B., Large, W., Debreu, L., Penduff, T., Molines, J. M., & Mathiot, P. (2008). Mesoscale Eddies in the Labrador Sea and Their Contribution to Convection and Restratification. *J. Phys. Oceanogr.*, 38, 1617-1643. doi: 10.1175/2008JPO3485.1

Chelton, D. B., deSzoeke, R. A., Schlax, M. G., Naggar, K. E., & Siwertz, N. (1998). Geographical Variability of the First Baroclinic Rossby Radius of Deformation. *J. Phys. Oceanogr.*, 28, 433-460. doi: 10.1175/1520-0485(1998)028⟨0433:GVOTFB⟩2.0.CO;2

Choi, Y., Morlighem, M., Rignot, E., & Wood, M. (2021). Ice dynamics will remain a primary driver of Greenland ice sheet mass loss over the next century. *Commun. Earth Environ.*, 2, 26. doi: 10.1038/s43247-021-00092-z

Clarke, R. A. (1984). Transport through the Cape Farewell-Flemish Cap section. *Rapp. P. V. Reun. Cons. Int. Explor. Mer.*, 185, 120-130.

Clarke, R. A. (1996). *CTD data from Cruise 18HU96026_1.* CCHDO. Retrieved 03.04.2010, from https://cchdo.ucsd.edu/cruise/18HU96026_1

Clarke, R. A. (1997). *CTD data from Cruise 18HU97009_1.* CCHDO. Retrieved 03.04.2010, from https://cchdo.ucsd.edu/cruise/18HU97009_1

Clarke, R. A. (1999). *CTD data from Cruise 18HU19990627.* CCHDO. Retrieved 16.07.2013, from https://cchdo.ucsd.edu/cruise/18HU19990627

Clarke, R. A. (2001). *CTD data from Cruise 18HU2001022_1.* CCHDO. Retrieved 12.06.2009, from https://cchdo.ucsd.edu/cruise/18HU2001022_1

Clarke, R. A. (2002). *CTD data from Cruise 18HU20020623.* CCHDO. Retrieved 16.07.2013, from https://cchdo.ucsd.edu/cruise/18HU20020623

Clarke, R. A. (2003). *CTD data from Cruise 18HU200307_1.* CCHDO. Retrieved 17.07.2013, from https://cchdo.ucsd.edu/cruise/18HU200307_1

Cohen, J., Screen, J. A., Furtado, J. C., Barlow, M., Whittleston, D., Coumou, D., ... Jones, J. (2014). Recent Arctic amplification and extreme mid-latitude weather. *Nature Geosciences*, 7, 627-637. doi: 10.1038/NGEO2234

Cromwell, T. (1953). Circulation in a meridional plane in the Central Equatorial Pacific. *J. of Mar. Res.*, 12(2). Retrieved from https://elischolar.library.yale.edu/journal_of_marine_research/793

Cuny, J., Rhines, P. B., Niiler, P. P., & Bacon, S. (2002). Labrador Sea Boundary Currents and the Fate of the Irminger Sea Water. *J. Phys. Oceanogr.*, 32, 627-647. doi: 10.1175/1520-0485(2002)032⟨0627:LSBCAT⟩2.0.CO;2

Curry, B., Lee, C. M., Petrie, B., Moritz, R. E., & Kwok, R. (2014). Multiyear Volume, Liquid Freshwater, and Sea Ice Transports through Davis Strait, 2004–10. *J. Phys. Oceanogr.*, 44, 1244-1266. doi: 10.1175/JPO-D-13-0177.1

Daniault, N., Lherminier, P., & Mercier, H. (2011a). Circulation and Transport at the Southeast Tip of Greenland. *J. Phys. Oceanogr.*, 41, 437-457. doi: 10.1175/2010JPO4428.1

Daniault, N., Mercier, H., & Lherminier, P. (2011b). The 1992–2009 transport variability of the East Greenland-Irminger Current at 60°N. *Geophys. Res. Lett.*, 38, L07601. doi: 10.1029/2011GL046863

Daniault, N., Mercier, H., Lherminier, P., Sarafanov, A., Falina, A., Zunino, P., ...

Gladyshev, S. (2015). The northern North Atlantic Ocean mean circulation in the early 21st century. *Prog. in Ocean.*, 146, 142-158. doi: 10.1016/j.pocean.2016.06.007

d'Asaro, E. (1998). *CTD data from Cruise KN156.* LDEO. Retrieved 09.04.2010, from http://xtide.ldeo.columbia.edu/labseacd/data/dataset14.html

de Jong, M. F., van Aken, H. M., Våge, K., & Pickart, R. S. (2012). Convective mixing in the central Irminger Sea: 2002-2010. *Deep-Sea Res. I*, 63, 36-51. doi: 10.1016/j.dsr.2012.01.003

de Jong, M. F., Bower, A. S., & Furey, H. H. (2014). Two Years of Observations of Warm-Core Anticyclones in the Labrador Sea and Their Seasonal Cycle in Heat and Salt Stratification. *J. Phys. Oceanogr.*, 44, 427-444. doi: 10.1175/JPO-D-13-070.1

de Jong, M. F., & de Steur, L. (2016). Strong winter cooling over the Irminger Sea in winter 2014–2015, exceptional deep convection, and the emergence of anomalously low SST. *Geophys. Res. Lett.*, 43, 7106-7113. doi: 10.1002/2016GL069596

Desbruyères, D. G., Mercier, H., Maze, G., & Daniault, N. (2019). Surface predictor of overturning circulation and heat content change in the subpolar North Atlantic. *Ocean Sci.*, 15, 817. doi: 10.5194/os-15-809-2019

Dickson, R. R., Meincke, J., Malmberg, S.-A., & Lee, A. J. (1988). The "Great Salinity Anomaly" in the Northern North Atlantic 1968-1982. *Prog. in Ocean.*, 20, 103-151. doi: 10.1016/0079-6611(88)90049-3

DiGirolamo, N., Parkinson, C. L., Cavalieri, D. J., Gloersen, P., & Zwally, H. J. (2022). *Sea Ice Concentrations from Nimbus-7 SMMR and DMSP SSM/I-SSMIS Passive Microwave Data, Version 2.* Boulder, Colorado USA. NASA National Snow and Ice Data Center Distributed Active Archive Center. Retrieved 03.2023, from https://nsidc.org/data/nsidc-0051/versions/2 doi: 10.5067/MPYG15WAA4WX

Droghei, R., Nardelli, B. B., & Santoleri, R. (2018). A New Global Sea Surface Salinity and Density Dataset From Multivariate Observations (1993-2016). *Frontiers in Marine Science*, 5/84, 1-13. doi: 10.3389/fmars.2018.00084

Drévillon, M., Fernandez, E., & Lellouche, J. M. (2022a). Global Ocean Physical Multi Year Product GLOBAL_MULTIYEAR_ PHY_001_030 - CMEMS-GLO-PUM-001-030. *CMEMS*, 1.4. https://catalogue.marine.copernicus.eu/documents/PUM/CMEMS-GLO-PUM-001-030.pdf.

Drévillon, M., Lellouche, J.-M., Régnier, C., Garric, G., Bricaud, C., Hernandez, O., & Bourdallé-Badie, R. (2022b). Global Ocean Physical Multi Year Product GLOBAL_MULTIYEAR_ PHY_001_030 - CMEMS-GLO-QUID-001-030. *CMEMS*, 1.6. https://catalogue.marine.copernicus.eu/documents/QUID/CMEMS-GLO-QUID-001-030.pdf.

Dukhovskoy, D. S., Yashayaev, I., Proshutinsky, A., Bamber, J. L., Bashmachnikov, I. L., Chassignet, E. P., ... Tedstone, A. J. (2019). Role of Greenland Freshwater Anomaly in the Recent Freshening of the Subpolar North Atlantic. *J. Geophys. Res.: Oceans*, 124, 3333-3360. doi: 10.1029/2018JC014686

Duyck, E., & de Jong, M. F. (2021). Circulation Over the South-East Greenland Shelf and Potential for Liquid Freshwater Export: A Drifter Study. *Geophys. Res. Lett.*, 48, e2020JB020886. doi: 10.1029/2020GL091948

Duyck, E., Gelderloss, R., & de Jong, M. F. (2022). Wind-Driven Freshwater Export at Cape Farewell. *J. Geophys. Res.: Oceans*, 127, e2021JC018309. doi: 10.1029/

2021JC018309

Duyck, E., & de Jong, M. F. (2023). Cross-Shelf Exchanges Between the East Greenland Shelf and Interior Seas. *J. Geophys. Res.: Oceans*, 128, e2023JC019905. doi: 10.1029/2023JC019905

Enderlin, E. M., Howat, I. M., Jeong, S., Noh, M.-J., van Angelen, J. H., & van den Broeke, M. R. (2014). An improved mass budget for the Greenland ice sheet. *Geophys. Res. Lett.*, 41, 866-872. doi: 10.1002/2013GL059010

Falina, A., Sarafanov, A., & Sokov, A. (2007). Variability and renewal of Labrador Sea Water in the Irminger Basin in 1991-2004. *J. Geophys. Res.: Oceans*, 112, C01006. doi: 10.1029/2005JC003348

Fichefet, T., & Maqueda, M. A. M. (1997). Sensitivity of a global sea ice model to the treatment of ice thermodynamics and dynamics. *J. Geophys. Res.*, 102(C6), 12609-12646. doi: 10.1029/97JC00480

Fofonoff, N. P., & Millard, R. C. (1983). Algorithms for Computation of Fundamental Properties of Seawater. *UNESCO Tech. Papers in Mar. Sc.*, 44, 53pp. doi: 10.25607/OBP-1450

Frajka-Williams, E., Ansorge, I. J., Baehr, J., Bryden, H. L., Chidichimo, M. P., Cunningham, S. A., ... Wilson, C. (2019). Atlantic Meridional Overturning Circulation: Observed Transport and Variability. *Frontiers in Marine Science*, 6. doi: 10.3389/fmars.2019.00260

Fratantoni, D. M. (2001). North Atlantic surface circulation during the 1990s observed with satellite-tracked drifters. *J. Geophys. Res.: Oceans*, 106, 22067-22093. doi: 10.1029/2000JC000730

Fried, N., & de Jong, M. F. (2022). The role of the Irminger Current in the Irminger Sea northward transport variability. *J. Geophys. Res.: Oceans*, 127, e2021JC018188. doi: 10.1029/2021JC018188

Fröhle, J., Handmann, P. V. K., & Biastoch, A. (2022). Major sources of North Atlantic Deep Water in the subpolar North Atlantic from Lagrangian analyses in an eddy-rich ocean model. *Ocean Sci.*, 18, 1431-1450. doi: 10.5194/os-18-1431-2022

Fu, C., Pennelly, C., Garcia-Quintana, Y., & Myers, P. G. (2023). Pulses of Cold Atlantic Water in the Arctic Ocean From an Ocean Model Simulation. *J. Geophys. Res.: Oceans*, 128, e2023JC019663. doi: 10.1029/2023JC019663

Galbraith, E. D., Gnanadesikan, A., Dunne, J. P., & Hiscock, M. R. (2009). Regional impacts of iron-light colimitation in a global biogeochemical model. *Biogeos. Discuss.*, 6(4), 7517-7564. doi: 10.5194/bgd-6-7517-2009

Garcia-Quintana, Y., Courtois, P., Hu, X., Pennelly, C., Kieke, D., & Myers, P. G. (2019). Sensitivity of Labrador Sea Water Formation to Changes in Model Resolution, Atmospheric Forcing, and Freshwater Input. *J. Geophys. Res.: Oceans*, 124, 2126-2152. doi: 10.1029/2018JC014459

García-Ibáñez, M. I., Pardo, P. C., Carracedo, L. I., Mercier, H., Lherminier, P., Ríos, A. F., & Pérez, F. F. (2015). Structure, transports and transformations of the water masses in the Atlantic Subpolar Gyre. *Prog. in Ocean.*, 135, 18-36. doi: 10.1016/j.pocean.2015.03.009

Gelderloos, R., Katsman, C. A., & Drijfhout, S. S. (2011). Assessing the Roles of Three Eddy Types in Restratifying the Labrador Sea after Deep Convection. *J. Phys. Oceanogr.*, 41, 2102-2119. doi: 10.1175/JPO-D-11-054.1

Gillard, L. C. (2020). Modelling the interconnection of the ocean and the Greenland Ice Sheet. *Dissertation*, University of Alberta.

Gladish, C. V., Holland, D. M., & Lee, C. M. (2014). Oceanic Boundary Conditions for Jakobshavn Glacier. Part II: Provenance and Sources of Variability of Disko Bay and Ilulissat Icefjord Waters, 1990–2011. *J. Phys. Oceanogr.*, 45, 33-63. doi: 10.1175/JPO-D-14-0045.1

Goelzer, H., Nowicki, S., Payne, A., Larour, E., Seroussi, H., Lipscomb, W. H., ... van den Broeke, M. (2020). The future sea-level contribution of the Greenland ice sheet: a multi-model ensemble study of ISMIP6. *The Cryosphere*, 14, 3071-3096. doi: 10.5194/tc-14-3071-2020

Good, S. A., Martin, M. J., & Rayner, N. A. (2013). EN4: Quality controlled ocean temperature and salinity profiles and monthly objective analyses with uncertainty estimates. *J. Geophys. Res.: Oceans*, 118, 6704-6716. doi: 10.1002/2013JC009067

Gordon, L. I., Jennings, J. C., Ross, A. A., & Krest, J. M. (1994). World ocean circulation experiment. WOCE operations manual. Volume 3. The observational programme. Section 3.1. WOCE hydrographic programme. Part 3.1.3. WHP operations and methods. (revision 1). *WOCE*. Retrieved from https://www.osti.gov/biblio/149787

Gou, R., Feucher, C., Pennelly, C., & Myers, P. G. (2021). Seasonal Cycle of the Coastal West Greenland Current System Between Cape Farewell and Cape Desolation From a Very High-Resolution Numerical Model. *J. Geophys. Res.: Oceans*, 126, e2020JC017017. doi: 10.1029/2020JC017017

Gou, R., Pennelly, C., & Myers, P. G. (2022). The Changing Behavior of the West Greenland Current System in a Very High-Resolution Model. *J. Geophys. Res.: Oceans*, 127, e2022JC018404. doi: 10.1029/2022JC018404

Gou, R., Li, P., Wiegand, K. N., Pennelly, C., Kieke, D., & Myers, P. G. (2023). Variability of eddy formation off the west Greenland coast from a 1/60° model. *J. Phys. Oceanogr.*, in press.. doi: 10.1175/JPO-D-23-0004.1

Greiner, E., Verbrugge, N., Mulet, S., & Guinehut, S. (2020). Multi Observation Global Ocean 3D Temperature Salinity Heights Geostrophic Currents and MLD Product MULTIOBS_GLO_PHY_TSUV_3D_MYNRT_015_012 - CMEMS-MOB-QUID-015-012. *CMEMS*, 1.0. https://catalogue.marine.copernicus.eu/documents/QUID/CMEMS-MOB-QUID-015-012.pdf.

Grist, J. P., Josey, S. A., Boehme, L., Meredith, M. P., Laidre, K. L., Heide-Jørgensen, M. P., ... Coward, A. C. (2014). Seasonal variability of the warm Atlantic water layer in the vicinity of the Greenland shelf break. *Geophys. Res. Lett.*, 41, 8530-8537. doi: 10.1002/2014GL062051

Gülk, B., Roquet, F., Naveira Garabato, A. C., Rousset, C., & Madec, G. (2023). Variability and Remote Controls of the Warm-Water Halo and Taylor Cap at Maud Rise. *J. Geophys. Res.: Oceans*, 128, e2022JC019517. doi: 10.1029/2022JC019517

Guinehut, S. (2020). Multi Observation Global Ocean 3D Temperature Salinity Heights Geostrophic Currents and MLD Product MULTIOBS_GLO_PHY_TSUV_3D_MYNRT_015_012 - CMEMS-MOB-PUM-015-012. *CMEMS*, 1.0. https://catalogue.marine.copernicus.eu/documents/PUM/CMEMS-MOB-PUM-015-012.pdf.

Guinehut, S., Dhomps, A.-L., Larnicol, G., & Traon, P.-Y. L. (2012). High resolution 3D temperature and salinity fields derived from in situ and satellite observations.

Ocean Sci., 8(5), 845-857. doi: 10.5194/os-8-845-2012

Guo, X., Zhu, X.-H., Wu, Q.-S., & Huang, D. (2012). The Kuroshio nutrient stream and its temporal variation in the East China Sea. *J. Geophys. Res.*, 117, C01026. doi: 10.1029/2011JC007292

Gutjahr, O., Jungclaus, J. H., Brüggemann, N., Haak, H., & Marotzke, J. (2022). Air-Sea Interactions and Water Mass Transformation During a Katabatic Storm in the Irminger Sea. *J. Geophys. Res.: Oceans*, 127, e2021JC018075. doi: 10.1029/2021JC018075

Hannachi, A., Jolliffe, I. T., & Stephenson, D. B. (2007). Empirical orthogonal functions and related techniques in atmospheric science: A review. *Int. J. Climatol.*, 27, 1119-1152. doi: 10.1002/joc.1499

Hansen, M. O., Nielsen, T. G., Stedmon, C. A., & Munk, P. (2012). Oceanographic regime shift during 1997 in Disko Bay, Western Greenland. *Limnol. Oceanagr.*, 57, 634-644. doi: 10.4319/lo.2012.57.2.0634

Harrison, G. (2000). *CTD data from Cruise 18HU2000009_1.* CCHDO. Retrieved 16.07.2013, from https://cchdo.ucsd.edu/cruise/18HU2000009_1

Harrison, G. (2004). *CTD data from Cruise 18HU20040515.* CCHDO. Retrieved 17.07.2013, from https://cchdo.ucsd.edu/cruise/18HU20040515

Harrison, G. (2005). *CTD data from Cruise 18HU20050526.* CCHDO. Retrieved 17.07.2013, from https://cchdo.ucsd.edu/cruise/18HU20050526

Harrison, G. (2008). *CTD data from Cruise 18HU20080520.* CCHDO. Retrieved 17.07.2013, from https://cchdo.ucsd.edu/cruise/18HU20080520

Harrison, G. (2010). *CTD data from Cruise 18HU20100513.* CCHDO. Retrieved 18.07.2013, from https://cchdo.ucsd.edu/cruise/18HU20100513

Hátún, H., Sandø, A. B., Drange, H., Hansen, B., & Valdimarsson, H. (2005). Influence of the Atlantic Subpolar Gyre on the Thermohaline Circulation. *Science*, 309, 1841-1844. doi: 10.1126/science.1114777

Hátún, H., & Chafik, L. (2018). On the Recent Ambiguity of the North Atlantic Subpolar Gyre Index. *J. Geophys. Res.: Oceans*, 123, 5072-5076. doi: 10.1029/2018JC014101

Head, E. (2002). *CTD data from Cruise 18HU20021129.* CCHDO. Retrieved 19.07.2010, from https://cchdo.ucsd.edu/cruise/18HU20021129

Hendry, R. M. (2006). *CTD data from Cruise 18HU20060524.* CCHDO. Retrieved 17.07.2013, from https://cchdo.ucsd.edu/cruise/18HU20060524

Hendry, R. M. (2007). *CTD data from Cruise 18HU20070510.* CCHDO. Retrieved 17.07.2013, from https://cchdo.ucsd.edu/cruise/18HU20070510

Hendry, R. M. (2009). *CTD data from Cruise 18HU20090517.* CCHDO. Retrieved 17.07.2013, from https://cchdo.ucsd.edu/cruise/18HU20090517

Hersbach, H., Bell, B., Berrisford, P., Biavati, G., Horányi, A., Sabater, J. M., ... Thépaut, J.-N. (2019). ERA5 monthly averaged data on single levels from 1959 to present. *Copernicus Climate Change Service (C3S) Climate Data Store (CDS)*, Retrieved 15.02.2023. Retrieved from https://doi.org/10.24381/cds.f17050d7 doi: 10.24381/cds.f17050d7

Holland, D. M., Thomas, R. H., de Young, B., Ribergaard, M. H., & Lyberth, B. (2008). Acceleration of Jakobshavn Isbræ triggered by warm subsurface ocean

waters. *Nature Geosciences*, 1, 659-664. doi: 10.1038/ngeo316

Holliday, N. P., Meyer, A., Bacon, S., Alderson, S. G., & de Cuevas, B. (2007). Retroflection of part of the east Greenland current at Cape Farewell. *Geophys. Res. Lett.*, 34, L07609. doi: 10.1029/2006GL029085

Holliday, N. P., Hughes, S. L., Bacon, S., Beszczynska-Möller, A., Hansen, B., Lavín, A., ... Walczowski, W. (2008). Reversal of the 1960s to 1990s freshening trend in the northeast North Atlantic and Nordic Seas. *Geophys. Res. Lett.*, 35, L03614. doi: 10.1029/2007GL032675

Holliday, N. P., Bacon, S., Allen, J., & McDonagh, E. L. (2009). Circulation and Transport in the Western Boundary Currents at Cape Farewell, Greenland. *J. Phys. Oceanogr.*, 39, 1854 - 1870. doi: 10.1175/2009JPO4160.1

Holliday, N. P., Bersch, M., Berx, B., Chafik, L., Cunningham, S., Florindo-López, C., ... Yashayaev, I. (2020). Ocean circulation causes the largest freshening event for 120 years in eastern subpolar North Atlantic. *Nature Communications*, 11, 585. doi: 10.1038/s41467-020-14474-y

Hu, D., Wu, L., Cai, W., Gupta, A. S., Ganachaud, A., Qiu, B., ... Kessler, W. S. (2015). Pacific western boundary currents and their roles in climate. *Nature*, 522, 299-308. doi: 10.1038/nature14504

Hu, X., Sun, J., Chan, T. O., & Myers, P. G. (2018). Thermodynamic and dynamic ice thickness contributions in the Canadian Arctic Archipelago in NEMO-LIM2 numerical simulations. *The Cryosphere*, 12, 1233-1247. doi: 10.5194/tc-12-1233-2018

Huhn, O., Rhein, M., Steinfeldt, R., Sültenfuß, J., & Kieke, D. (pers. comm.). Submarine Meltwater along the Greenland Coast, from 79 North Glacier towards the Labrador Sea.

Hurrell, J. W., Kushnir, Y., Ottersen, G., & Visbeck, M. (2003). An overview of the North Atlantic Oscillation. *The North Atlantic Oscillation: Climatic Significance and Environmental Impact (eds. J. W. Hurrell, Y. Kushnir, G. Ottersen, and M. Visbeck)*. doi: 10.1029/134GM01

Huyer, A. (1983). Coastal Upwelling in the California Current System. *Prog. in Ocean.*, 12, 259-284. doi: 10.1016/0079-6611(83)90010-1

Iakovleva, D. A., & Bashmachnikov, I. L. (2021). On the seesaw in interannual variability of upper ocean heat advection between the North Atlantic Subpolar Gyre and the Nordic Seas. *Dyn. Atmos. Oceans*, 96, 101263. doi: 10.1016/j.dynatmoce.2021.101263

Imawaki, S., Bower, A. S., Beal, L., & Qiu, B. (2013). Western boundary currents. Ocean Circulation and Climate: A 21st Century Perspective, G. Siedler et al., Eds., Academic Press. *International Geophysics*, 103, 305-338. doi: 10.1016/B978-0-12-391851-2.00013-1

IPCC. (2021). Authors: Masson-Delmotte, V., Zhai, P., Pirani, A., Connors, S. L., Péan, C., Berger, S., Caud, N., Chen, Y., Goldfarb, L., Gomis, M. I., Huang, M., Leitzell, K., Lonnoy, E., Matthews, J. B. R., Maycock, T. K., Waterfield, T., Yelekçi, O., Yu, R. & Zhou, B. (eds.). IPCC, 2021: Climate Change 2021: The Physical Science Basis. Contribution of Working Group I to the Sixth Assessment Report of the Intergovernmental Panel on Climate Change. *Cambridge University Press, Cambridge, United Kingdom and New York, NY, USA, In press*. doi: 10.1017/9781009157896

Jackson, L. C., Kahana, R., Graham, T., Ringer, M. A., Woollings, T., Mecking, J. V.,

& Wood, R. A. (2015). Global and European climate impacts of a slowdown of the AMOC in a high resolution GCM. *Clim. Dyn*, 45, 3299-3316. doi: 10.1007/s00382-015-2540-2

Johannessen, O. M., Korablev, A., Miles, V., Miles, M. W., & Solberg, K. E. (2011). Interaction Between the Warm Subsurface Atlantic Water in the Sermilik Fjord and Helheim Glacier in Southeast Greenland. *Surv. in Geophysics*, 32(4-5), 387-396. doi: 10.1007/s10712-011-9130-6

Josey, S. A., de Jong, M. F., Oltmanns, M., Moore, G. K., & Weller, R. A. (2019). Extreme Variability in Irminger Sea Winter Heat Loss Revealed by Ocean Observatories Initiative Mooring and the ERA5 Reanalysis. *Geophys. Res. Lett.*, 46, 293-302. doi: 10.1029/2018GL080956

Kawasaki, T., & Hasumi, H. (2014). Effect of freshwater from the West Greenland Current on the winter deep convection in the Labrador Sea. *Ocean Modelling*, 75, 51-64. doi: 10.1016/j.ocemod.2014.01.003

Kenchington, E., Yashayaev, I., Tendal, O. S., & Jørgensbye, H. (2017). Water mass characteristics and associated fauna of a recently discovered Lophelia pertusa (Scleractinia: Anthozoa) reef in Greenlandic waters. *Polar Biol.*, 40, 321-337. doi: 10.1007/s00300-016-1957-3

Khatiwala, S. P., & Fairbanks, R. G. (1999). Freshwater sources to the coastal ocean off northeastern North America: Evidence from $H_2{}^{18}O/H_2{}^{16}O$. *J. Geophys. Res.*, 104(C8), 18241-18255. doi: 10.1029/1999JC900155

Khazendar, A., Fenty, I. G., Carroll, D., Gardner, A., Lee, C. M., Fukumori, I., ... Willis, J. (2019). Interruption of two decades of Jakobshavn Isbrae acceleration and thinning as regional ocean cools. *Nature Geosciences*, 12, 277-283. doi: 10.1038/s41561-019-0329-3

Kieke, D. (2005). Water Mass Circulation and Variability in the Subpolar North Atlantic. *Dissertation*, University of Bremen.

Kieke, D., & Yashayaev, I. (2015). Studies of Labrador Sea Water formation and variability in the subpolar North Atlantic in the light of international partnership and collaboration. *Prog. in Ocean.*, 132, 220-232. doi: 10.1016/j.pocean.2014.12.010

Kiilerich, A. (1943). The Hydrography of the West Greenland Fishing Banks. *Medd. Komm. for Danmarks Fiskeri- og Havundersogelser*, Bind II.

Killworth, P. D. (1983). Deep convection in the World Ocean. *Rev. Geophys.*, 21, 1-26. doi: 10.1029/RG021i001p00001

Koul, V., Tesdal, J.-E., Bersch, M., Hátún, H., Brune, S., Borchert, L., ... Baehr, J. (2020). Unraveling the choice of the north Atlantic subpolar gyre index. *Sci. Reports*, 10, 1005. doi: 10.1038/s41598-020-57790-5

Krauss, W. (1986). The North Atlantic Current. *J. Geophys. Res.*, 91(C4), 5061-5074. doi: 10.1029/JC091iC04p05061

Kuhlbrodt, T., Griesel, A., Montoya, M., Levermann, A., Hofmann, M., & Rahmstorf, S. (2007). On the driving processes of the Atlantic Meridional Overturning Circulation. *Rev. Geophys.*, 45, RG2001. doi: 10.1029/2004RG000166

Kulan, N., & Myers, P. G. (2009). Comparing two climatologies of the labrador sea: Geopotential and isopycnal. *Atmos.–Ocean*, 47:1, 19-39. doi: 10.3137/OC281.2009

Käse, R. H., Biastoch, A., & Stammer, D. B. (2001). On the Mid-Depth Circulation in the Labrador and Irminger Seas. *Geophys. Res. Lett.*, 28, 3433-3436. doi: 10.1029/2001GL013192

Latif, M., Roeckner, E., Mikolajewicz, U., & Voss, R. (2000). Tropical Stabilization of the Thermohaline Circulation in a Greenhouse Warming Simulation. *J. Climate*, 13, 1809-1813. doi: 10.1175/1520-0442(2000)013⟨1809:L⟩2.0.CO;2

Lavender, K. L., Davis, R. E., & Owens, W. B. (2000). Mid-depth recirculation observed in the interior Labrador and Irminger seas by direct velocity measurements. *Nature*, 407, 66-69. doi: 10.1038/35024048

Lazier, J. (1973). The renewal of Labrador Sea Water. *DSR*, 20, 341-353. doi: 10.1016/0011-7471(73)90058-2

Lazier, J. (1993). *CTD data from Cruise 18HU93019_1.* CCHDO. Retrieved 22.10.2010, from https://cchdo.ucsd.edu/cruise/18HU93019_1

Lazier, J. (1994). *CTD data from Cruise 18HU94008_1.* CCHDO. Retrieved 09.03.2010, from https://cchdo.ucsd.edu/cruise/18HU94008_1

Lazier, J. (1995). *CTD data from Cruise 18HU95011_1.* CCHDO. Retrieved 03.04.2010, from https://cchdo.ucsd.edu/cruise/18HU95011_1

Lazier, J. (1996). *CTD data from Cruise 18HU96006_1.* CCHDO. Retrieved 03.04.2010, from https://cchdo.ucsd.edu/cruise/18HU96006_1

Lazier, J., Hendry, R., Clarke, A., Yashayaev, I., & Rhines, P. (2002). Convection and restratification in the Labrador Sea, 1990–2000. *DSR-1*, 49, 1819-1835. doi: 10.1016/S0967-0637(02)00064-X

Le Bras, I. A.-A., Straneo, F., Holte, J., de Jong, M. F., & Holliday, N. P. (2020). Rapid Export of Waters Formed by Convection Near the Irminger Sea's Western Boundary. *Geophys. Res. Lett.*, 47, e2019GL085989. doi: 10.1029/2019GL085989

Le Bras, I. A.-A., Callies, J., Straneo, F., Biló, T. C., Holte, J., & Johnson, H. L. (2022). Slantwise Convection in the Irminger Sea. *J. Geophys. Res.: Oceans*, 127, e2022JC019071. doi: 10.1029/2022JC019071

Lee, A. J. (1968). NORWESTLANT Surveys: Physical Oceanography. *ICNAF Special Publ.*, 7, Part I: 31 - 54, Part II: 38 - 159.

Lilly, J. M., Rhines, P. B., Schott, F., Lavander, K., Lazier, J., Send, U., & D'Asaro, E. (2003). Observations of the Labrador Sea eddy field. *Prog. in Ocean.*, 59, 75-176. doi: 10.1016/j.pocean.2003.08.013

Loder, J., Petrie, B., & Gawarkiewicz, G. (1998). The Coastal Ocean off Northeastern North America: A Large-Scale View, eds. A. R. Robinson and K. H. Brink. *The Sea*, 11, 105-133.

Lozier, M. S. (2023). Overturning in the Subpolar North Atlantic: a review. *Phil. Trans. A.*

Lozier, M. S., Bacon, S., Bower, A. S., Cunningham, S. A., de Jong, M. F., de Steur, L., ... Zika, J. D. (2017). Overturning in the Subpolar North Atlantic Program: A New International Ocean Observing System. *Bull. Amer. Meteor. Soc.*, 98(4), 737-752. doi: 10.1175/BAMS-D-16-0057.1

Lumpkin, R., Speer, K. G., & Koltermann, K. P. (2007). Transport across 48°N in the Atlantic Ocean. *J. Phys. Oceanogr.*, 38, 733-752. doi: 10.1175/2007JPO3636.1

Luo, H., Bracco, A., & Lorenzo, E. D. (2011). The interannual variability of the surface eddy kinetic energy in the Labrador Sea. *Prog. in Ocean.*, 91, 295-311. doi: 10.1016/j.pocean.2011.01.006

Madec, G., Delecluse, P., Imbard, M., & Lévy, C. (1998). OPA 8 Ocean General Circulation Model - Reference Manual. *Note du Pôle de modélisation, LODYC and Institut Pierre-Simon Laplace (IPSL) Note 11*, (Tech. Rep.).

Madec, G., Bell, M., Blaker, A., Bricaud, C., Bruciaferri, D., Castrillo, M., ... Wilson, C. (2023). NEMO Ocean Engine Reference Manual. *Zenodo*, Version 4.2.1. doi: 10.5281/zenodo.8167700

Malmberg, S.-A., & Jónsson, S. (1997). Timing of deep convection in the Greenland and Iceland Seas. *ICES J. of Mar. Sc.*, 54, 300-309. doi: 10.1006/jmsc.1997.0221

Maury, M. F., & Leighly, J. (1855). The Physical Geography of the Sea, and its Meteorology, Cambridge, MA and London, England. *Harvard University Press, 1963*. doi: 10.4159/harvard.9780674865280

Megann, A., Blaker, A., Josey, S., New, A., & Sinha, B. (2021). Mechanisms for Late 20th and Early 21st Century Decadal AMOC Variability). *J. Geophys. Res.: Oceans*, 126, e2021JC017865. doi: 10.1029/2021JC017865

Mesinger, F., & Arakawa, A. (1976). Numerical methods used in atmospheric models: volume 1). *GARP Publications Series*, 17, International Council of Scientific Unions (ICSU) - WMO.

Mortensen, J., Bendtsen, J., Lennert, K., & Rysgaard, S. (2014). Seasonal variability of the circulation system in a west Greenland tidewater outlet glacier fjord, Godthåbsfjord (64 °N). *J. Geophys. Res.: Earth Surf.*, 119, 2591-2603. doi: 10.1002/2014JF003267

Mortensen, J., Rysgaard, S., Arendt, K. E., Juul-Pedersen, T., Søgaard, D. H., Bendtsen, J., & Meire, L. (2018). Local Coastal Water Masses Control Heat Levels in a West Greenland Tidewater Outlet Glacier Fjord. *J. Geophys. Res.: Oceans*, 123, 8068-8083. doi: 10.1029/2018JC014549

Muilwijk, M., Smedsrud, L. H., Ilicak, M., & Drange, H. (2018). Atlantic Water Heat Transport Variability in the 20th Century Arctic Ocean From a Global Ocean Model and Observations. *J. Geophys. Res.: Oceans*, 123, 8159-8179. doi: 10.1029/2018JC014327

Mulet, S., Rio, M.-H., Mignot, A., Guinehut, S., & Morrow, R. (2012). A new estimate of the global 3D geostrophic ocean circulation based on satellite data and in-situ measurements. *Research Part II : Topical Studies in Oceanography*, 77-80(0), 70-81. doi: 10.1016/j.dsr2.2012.04.012

Mulet, S., Rio, M.-H., Etienne, H., Artana, C., Cancet, M., Dibarboure, G., ... Strub, P. T. (2021). The new CNES-CLS18 global mean dynamic topography. *Ocean Sci.*, 17, 789-808. doi: 10.5194/os-17-789-2021

Myers, P. G., Kulan, N., & Ribergaard, M. H. (2007). Irminger Water variability in the West Greenland Current. *Geophys. Res. Lett.*, 34, L17601. doi: 10.1029/2007GL030419

Myers, P. G., Donnelly, C., & Ribergaard, M. H. (2009). Structure and variability of the West Greenland Current in Summer derived from 6 repeat standard sections. *Prog. in Ocean.*, 80, 93-112. doi: 10.1016/j.pocean.2008.12.003

Myers, P. G., & Ribergaard, M. H. (2013). Warming of the Polar Water Layer in

Disko Bay and Potential Impact on Jakobshavn Isbrae. *J. Phys. Oceanogr.*, 43, 2629-2640. doi: 10.1175/JPO-D-12-051.1

Myers, P. G., de la Guardia, L. C., Fu, C., Gillard, L. C., Grivault, N., Hu, X., ... Romanski, J. (2021). Extreme High Greenland Blocking Index Leads to the Reversal of Davis and Nares Strait Net Transport Toward the Arctic Ocean. *Geophys. Res. Lett.*, 48, e2021GL094178. doi: 10.1029/2021GL094178

Nitani, H. (1972). Beginning of the Kuroshio. Kuroshio - Its Physical Aspects, H. Stommel and K. Yoshida, Eds. *University of Tokyo Press*, 129-163.

NOAA. (2009). *ETOPO1 1 Arc-Minute Global Relief Model.* National Oceanic and Atmospheric Administration, National Geophysical Data Center, NOAA National Centers for Environmental Information. Retrieved 20.03.2020, from https://www.ncei.noaa.gov/access/metadata/landing-page/bin/iso?id=gov.noaa.ngdc.mgg.dem:316

NOAA. (2023a). *Global Surface Temperature.* National Oceanic and Atmospheric Administration. Retrieved 14.02.2023, from https://www.ncei.noaa.gov/products/land-based-station/noaa-global-temp

NOAA. (2023b). *Daily NAO Index time series.* National Oceanic and Atmospheric Administration. Retrieved 15.03.2023, from https://www.cpc.ncep.noaa.gov/products/precip/CWlink/pna/nao.shtml#publication

Nowitzki, H. (2021). Pathways and variability of the circulation in the subpolar eastern North Atlantic studied with inverted echo sounders and model data. *Dissertation*, University of Bremen.

Olbers, D., Willebrand, J., & Eden, C. (2012). *Ocean Dynamics.* doi: 10.1007/978-3-642-23450-7

Orsi, A. H. (2010). Recycling bottom waters. *Nature Geosciences*, 3, 307-309. doi: 10.1038/ngeo854

Pacini, A., Pickart, R. S., Bahr, F., Torres, D. J., Ramsey, A. L., Holte, J., ... de Jong, M. F. (2020). Mean Conditions and Seasonality of the West Greenland Boundary Current System near Cape Farewell. *J. Phys. Oceanogr.*, 50, 2849-2871. doi: 10.1175/JPO-D-20-0086.1

Pacini, A., & Pickart, R. S. (2022). Meanders of the West Greenland Current near Cape Farewell. *Deep-Sea Res.*, 179, 103664. doi: 10.1016/j.dsr.2021.103664

Pacini, A., & Pickart, R. S. (2023). Wind-forced upwelling along the West Greenland shelfbreak: Implications for Labrador Sea Water formation. *J. Geophys. Res.: Oceans*, 128, e2022JC018952. doi: 10.1029/2022JC018952

Paillet, J., Arhan, M., & McCartney, M. S. (1998). Spreading of Labrador Sea Water in the eastern North Atlantic. *J. Geophys. Res.: Oceans*, 103, 10223-10239. doi: 10.1029/98JC00262

Palter, J. B. (2015). The role of the Gulf Stream in European climate. *Annu. Rev. Mar. Sci.*, 7, 113-137. doi: 10.1146/annurev-marine-010814-015656

Palter, J. B., Caron, C.-A., Lavender, K., Wills, J. K., Trossman, D. S., Yashayaev, I., & Gilbert, D. (2016). Variability of the directly observed, middepth subpolar North Atlantic circulation. *Geophys. Res. Lett.*, 43, 2700-2708. doi: 10.1002/2015GL067235

Paquin, J.-P., Lu, Y., Higginson, S., Dupont, F., & Garric, G. (2016). Modelled Variations of Deep Convection in the Irminger Sea during 2003–10. *J. Phys. Oceanogr.*, 46, 179-196. doi: 10.1175/JPO-D-15-0078.1

Pennelly, C., Hu, X., & Myers, P. G. (2019). Cross-Isobath Freshwater Exchange Within the North Atlantic Subpolar Gyre. *J. Geophys. Res.: Oceans*, 124, 6831-6853. doi: 10.1029/2019JC015144

Pennelly, C., & Myers, P. G. (2020). Introducing LAB60: A 1/60 ∘ NEMO 3.6 numerical simulation of the Labrador Sea. *Geosci. Model Dev.*, 13, 4959-4975. doi: 10.5194/gmd-13-4959-2020

Pennelly, C. (2021). Modelling Sources of Stratification within the Labrador Sea. *Dissertation*, University of Alberta.

Pennelly, C., & Myers, P. G. (2022). Tracking Irminger Rings' properties using a sub-mesoscale ocean model. *Prog. in Ocean.*, 201, 102735. doi: 10.1016/j.pocean .2021.102735

Pickart, R. S. (1992). Water mass components of the North Atlantic deep western boundary current. *Deep-Sea Res.*, 39(9), 1553-1572. doi: 10.1016/0198-0149(92) 90047-W

Pickart, R. S. (1997). *CTD data from Cruise KN147*. LDEO. Retrieved 11.03.2010, from http://xtide.ldeo.columbia.edu/labseacd/data/dataset13.html

Pickart, R. S., Spall, M. A., Ribergaard, M. H., Moore, G. W. K., & Milliff, R. F. (2003a). Deep convection in the Irminger Sea forced by the Greenland tip jet. *Nature*, 424, 152-156. doi: 10.1038/nature01729

Pickart, R. S., Straneo, F., & Moore, G. W. K. (2003b). Is Labrador Sea Water formed in the Irminger basin? *Deep-Sea Res. I*, 50, 23-52. doi: 10.1016/S0967-0637(02) 00134-6

Polyakov, I. V., Pnyushkov, A. V., Alkire, M. B., Ashik, I. M., Baumann, T. M., Carmack, E. C., ... Yulin, A. (2017). Greater role for Atlantic inflows on sea-ice loss in the Eurasian Basin of the Arctic Ocean. *Science*, 356, 285-291. doi: 10.1126/science.aai820

Porter, D. F., Tinto, K. J., Boghosian, A. L., Csatho, B. M., Bell, R. E., & Cochran, J. R. (2018). Identifying Spatial Variability in Greenland's Outlet Glacier Response to Ocean Heat. *Front. Earth Sc.*, 6, 90. doi: 10.3389/feart.2018.00090

Portis, D. H., Walsh, J. E., el Hamly, M., & Lamb, P. J. (2001). Seasonality of the North Atlantic Oscillation. *J. Climate*, 14, 2069-2078. doi: 10.1175/1520 -0442(2001)014⟨2069:SOTNAO⟩2.0.CO;2

Qiu, B., & Lukas, R. (1996). Seasonal and interannual variability of the North Equatorial Current, the Mindanao Current, and the Kuroshio along the Pacific western boundary. *J. Geophys. Res.*, 101, 12315-12330. doi: 10.1029/95JC03204

Rahmstorf, S. (2002). Ocean circulation and climate during the past 120,000 years. *Nature*, 419, 207-214. doi: 10.1038/nature01090

Rattan, S., Myers, P. G., Treguier, A.-M., Theetten, S., Biastoch, A., & Böning, C. (2010). Towards an understanding of Labrador Sea salinity drift in eddy-permitting simulations. *Ocean Modelling*, 35, 77-88. doi: 10.1016/j.ocemod.2010 .06.007

Reigstad, M., Wassmann, P., Riser, C. W., Øygarden, S., & Rey, F. (2002). Variations in hydrography, nutrients and chlorophyll α in the marginal ice-zone and the central Barents Sea. *J. Mar. Sys.*, 38, 9-29. doi: 10.1016/S0924-7963(02)00167-7

Reynaud, T. H., Weaver, A. J., & Greatbatch, R. J. (1995). Summer mean circulation of the northwestern Atlantic Ocean. *J. Geophys. Res.*, 100, 779-816. doi: 10.1029/

94JC02561

Rhein, M., Kieke, D., & Steinfeldt, R. (2015). *Physical oceanography during cruise SUBPOLAR with RV THALASSA in the subpolar North Atlantic in June-July 2005.* PANGAEA. Retrieved from https://doi.org/10.1594/PANGAEA.844874 doi: 10.1029/2006GL028540

Ribergaard, M. H. (2014). Oceanographic investigations off West Greenland 2013. *AFO Scientific Council Documents Tech*, Report 14/001, 1-50.

Rieck, J. K., Böning, C. W., & Getzlaff, K. (2019). The Nature of Eddy Kinetic Energy in the Labrador Sea: Different Types of Mesoscale Eddies, Their Temporal Variability, and Impact on Deep Convection. *J. Phys. Oceanogr.*, 49, 2075-2094. doi: 10.1175/JPO-D-18-0243.1.

Rignot, E., Fenty, I., Menemenlis, D., & Xu, Y. (2012). Spreading of warm ocean waters around Greenland as a possible cause for glacier acceleration. *Ann. Glac.*, 53, 257-266. doi: 10.3189/2012AoG60A136

Roessler, A., Rhein, M., Kieke, D., & Mertens, C. (2015). Long-term observations of North Atlantic Current transport at the gateway between western and eastern Atlantic. *J. Geophys. Res.: Oceans*, 120, 4003-4027. doi: 10.1002/2014JC010662

Rossby, T. (1996). The North Atlantic Current and Surrounding Waters: At the Crossroads. *Rev. Geophys.*, 34.4, 463-481. doi: 10.1029/96RG02214

Rykova, T., Straneo, F., Lilly, J. M., & Yashayaev, I. (2009). Irminger Current Anticyclones in the Labrador Sea observed in the hydrographic record, 1990 –2004. *J. Mar. Res.*, 67, 361 - 384. doi: 10.1357/002224009789954739

Rykova, T., Straneo, F., & Bower, A. S. (2015). Seasonal and interannual variability of the West Greenland Current System in the Labrador Sea in 1993–2008. *J. Geophys. Res.: Oceans*, 120, 1318 - 1332. doi: 10.1002/2014JC010386

Rysgaard, S., Boone, W., Carlson, D., Sejr, M. K., Bendtsen, J., Juul-Pedersen, T., ... Mortensen, J. (2020). An Updated View on Water Masses on the pan-West Greenland Continental Shelf and Their Link to Proglacial Fjords. *J. Geophys. Res.: Oceans*, 125, e2019JC015564. doi: 10.1029/2019JC015564

Rühs, S., Oliver, E. C. J., Biastoch, A., Böning, C. W., Dowd, M., Getzlaff, K., ... Myers, P. G. (2021). Changing Spatial Patterns of Deep Convection in the Subpolar North Atlantic. *J. Geophys. Res.: Oceans.*, 126, e2021JC017245. doi: 10.1029/2021JC017245

Sanchez-Franks, A., Holliday, N. P., Evans, D. G., Fried, N., Tooth, O., Chafik, L., ... Johnson, H. L. (2023). The Irminger Gyre as a key driver of the subpolar North Atlantic overturning on monthly timescales. *Authorea*, preprint. doi: 10.22541/essoar.168182248.82025084/v1

Sanguineti, L. (2017). Labrador Sea Water exported through Flemish Pass: Hydrographic trends and transport variability inducing processes. *Dissertation*, University of Bremen.

Sarafanov, A. (2009). On the effect of the North Atlantic Oscillation on temperature and salinity of the subpolar North Atlantic intermediate and deep waters. *ICES J. of Mar. Sc.*, 66, 1148-1454. doi: 10.1093/icesjms/fsp094

Schmitz, W. J. (1996). On the World Ocean Circulation: Volume 1. Technical Report WHOI-96-03. *Woods Hole Oceanographic Institution*, 1. doi: 10.1575/1912/355

Schneider, L., Kieke, D., Jochumsen, K., Colbourne, E., Yashayaev, I. M., Steinfeldt,

R., ... Rhein, M. (2015). *Physical oceanography during Maria S. Merian cruise MSM28.* PANGAEA. Retrieved from https://doi.org/10.1594/PANGAEA.864250 doi: 10.1594/PANGAEA.864250

Schott, F. (1997). *CTD data from Cruise M39/4.* LDEO. Retrieved 14.03.2010, from http://xtide.ldeo.columbia.edu/labsea/data/dataset22.html

Seale, A., Christoffersen, P., Mugford, R. I., & O'Leary, M. (2011). Ocean forcing of the Greenland Ice Sheet: Calving fronts and patterns of retreat identified by automatic satellite monitoring of eastern outlet glaciers. *J. Geophys. Res.: Earth Surface*, 116, F03013. doi: 10.1029/2010JF001847

Siedler, G., Griffies, S. M., Gould, J., & Church, J. A. (2013). Ocean Circulation and Climate - A 21st Century Perspective. *International Geophysics*, 103.

Smedsrud, L. H., Muilwijk, M., Brakstad, A., Madonna, E., Lauvset, S. K., Spensberger, C., ... Årthun, M. (2021). Nordic Seas Heat Loss, Atlantic Inflow, and Arctic Sea Ice Cover Over the Last Century. *Rev. Geophys.*, 60, e2020RG000725. doi: 10.1029/2020RG000725

Spall, M. A., & Pickart, R. S. (2001). Where Does Dense Water Sink? A Subpolar Gyre Example. *J. Phys. Oceanogr.*, 31, 810–826. doi: 10.1175/1520-0485(2001)031⟨0810:WDDWSA⟩2.0.CO;2

Stark, J. D., Donlon, C. J., Martin, M. J., & McCulloch, M. E. (2007). OSTIA : An operational, high resolution, real time, global sea surface temperature analysis system. *OCEANS 2007 - Europe*, 1-4. doi: doi:10.1109/OCEANSE.2007.4302251

Stein, M. (2004). Climatic Overview of NAFO Subarea 1, 1991–2000. *J. Northw. Atl. Fish. Sci.*, 34, 29-41. doi: doi:10.2960/J.v34.m474

Steinfeldt, R., Mertens, C., Kieke, D., & Rhein, M. (2019a). *Physical oceanography during Maria S. Merian cruise MSM43.* PANGAEA. Retrieved from https://doi.org/10.1594/PANGAEA.897988 doi: 10.1594/PANGAEA.897988

Steinfeldt, R., Kieke, D., & Rhein, M. (2019b). *Physical oceanography during Maria S. Merian cruise MSM73.* PANGAEA. Retrieved from https://doi.org/10.1594/PANGAEA.923565 doi: 10.1594/PANGAEA.923565

Stendardo, I., Kieke, D., Rhein, M., Gruber, N., & Steinfeldt, R. (2015). *Physical oceanography during cruise M85/1 with METEOR in the subpolar North Atlantic in June-August 2011.* PANGAEA. Retrieved from https://doi.org/10.1594/PANGAEA.844877 doi: 10.1594/PANGAEA.844877

Stendardo, I., Rhein, M., & Steinfeldt, R. (2020). The North Atlantic Current and its Volume and Freshwater Transports in the Subpolar North Atlantic, Time Period 1993–2016. *J. Geophys. Res.: Oceans*, 125, e2020JC016065. doi: 10.1029/2020JC016065

Stendardo, I., Nardelli, B. B., Durante, S., Iudicone, D., & Kieke, D. (in revision). Variability of Subpolar Mode Water in the Subpolar North Atlantic. *J. Geophys. Res.: Oceans*.

Stewart, R. H. (2008). Introduction To Physical Oceanography. *Department of Oceanography, Texas A&M University*. Retrieved from https://hdl.handle.net/1969.1/160216

Stommel, H. (1948). The westward intensification of wind-driven ocean currents. *Eos Trans. AGU*, 29(2), 202-206. doi: 10.1029/TR029i002p00202

Straneo, F., Kawase, M., & Pickart, R. S. (2002). Effects of Wind on Convection in Strongly and Weakly Baroclinic Flows with Application to the Labrador Sea. *J. Phys. Oceanogr.*, 32, 2603-2618. doi: 10.1175/1520-0485(2002)032⟨2603:EOWOCI⟩2.0.CO;2

Straneo, F., Kawase, M., & Riser, S. C. (2002). Idealized Models of Slantwise Convection in a Baroclinic Flow. *J. Phys. Oceanogr.*, 32, 558-572. doi: 10.1175/1520-0485(2002)032⟨0558:IMOSCI⟩2.0.CO;2

Straneo, F., Pickart, R. S., & Lavender, K. (2003). Spreading of Labrador sea water: an advective-diffusive study based on Lagrangian data. *Deep-Sea Res. I*, 50, 701-719. doi: 10.1016/S0967-0637(03)00057-8

Straneo, F. (2006). On the Connection between Dense Water Formation, Overturning, and Poleward Heat Transport in a Convective Basin. *J. Phys. Oceanogr.*, 36, 1822-1840. doi: 10.1175/JPO2932.1

Straneo, F., & Heimbach, P. (2013). North Atlantic warming and the retreat of Greenland's outlet glaciers. *Nature*, 504, 36-43. doi: doi:10.1038/nature12854

Straneo, F., & Cenedese, C. (2015). The Dynamics of Greenland's Glacial Fjords and Their Role in Climate. *Annu. Rev. Mar. Sci.*, 7, 89-112. doi: 10.1146/annurev-marine-010213-135133

Tagklis, F., Bracco, A., Ito, T., & Castelao, R. M. (2020). Submesoscale modulation of deep water formation in the Labrador Sea. *Sci. Reports*, 10, 17489. doi: 10.1038/s41598-020-74345-w

Tang, C. C. L., Ross, C. K., Yao, T., Petrie, B., DeTracey, B. M., & Dunlap, E. (2004). The circulation, water masses and sea-ice of Baffin Bay. *Prog. in Ocean.*, 63, 183-228. doi: 10.1016/j.pocean.2004.09.005

The IMBIE Team. (2020). Mass balance of the Greenland Ice Sheet from 1992 to 2018. *Nature*, 579, 233-239. doi: 10.1038/s41586-019-1855-2

Thomas, M. D., & Zhang, R. (2022). Two Sources of Deep Decadal Variability in the Central Labrador Sea Open-Ocean Convection Region. *Geophys. Res. Lett.*, 49, e2022GL098825. doi: 10.1029/2022GL098825

Treguier, A. M., Theetten, S., Chassignet, E. P., Penduff, T., Smith, R., Talley, L., ... Böning, C. (2005). The North Atlantic Subpolar Gyre in Four High-Resolution Models. *J. Phys. Oceanogr.*, 35, 757-774. doi: 10.1175/JPO2720.1

Våge, K., Pickart, R. S., Moore, G. W. K., & Ribergaard, M. H. (2008a). Winter Mixed Layer Development in the Central Irminger Sea: The Effect of Strong, Intermittent Wind Events. *J. Phys. Oceanogr.*, 38, 541-565. doi: 10.1175/2007JPO3678.1

Våge, K., Spengler, T., Davies, H. C., & Pickart, R. S. (2009). Multi-event analysis of the westerly Greenland tip jet based upon 45 winters in ERA-40. *Q. J. R. Meteorol. Soc.*, 135, 1999-2011. doi: 10.1002/qj.488

Våge, K., Pickart, R. S., Sarafanov, A., Knutsen, Ø., Mercier, H., Lherminier, P., ... Bacon, S. (2011). The Irminger Gyre: Circulation, convection, and interannual variability. *Deep-Sea Res. I*, 58, 590-614. doi: 10.1016/j.dsr.2011.03.001

van Aken, H. M., de Jong, M. F., & Yashayaev, I. (2011). Decadal and multi-decadal variability of Labrador Sea Water in the north-western North Atlantic Ocean derived from tracer distributions: Heat budget, ventilation, and advection. *Deep-Sea Res. I*, 58, 505-523. doi: 10.1016/j.dsr.2011.02.008

van den Broeke, M. R., Smeets, C. J. P. P., & van de Wal, R. S. W. (2011). The seasonal cycle and interannual variability of surface energy balance and melt in the ablation zone of the west Greenland ice sheet. *The Cryosphere*, 5, 377-390. doi: 10.5194/tc-5-377-2011

Vihma, T., Graversen, R., Chen, L., Handorf, D., Skific, N., Francis, J. A., ... Overland, J. E. (2019). Effects of the tropospheric large-scale circulation on European winter temperatures during the period of amplified Arctic warming. *Int. J. Climatol.*, 40(1), 509-529. doi: 10.1002/joc.6225

Wassmann, P., Bauerfeind, E., Fortier, M., Fukuchi, M., Hargrave, B., Moran, B., ... Shevchenko, V. (2004). Particulate Organic Carbon Flux to the Arctic Ocean Sea Floor. The Organic Carbon Cycle in the Arctic Ocean, Stein, R., MacDonald, R. W. (eds). *Springer, Berlin, Heidelberg*, 101-138. doi: 10.1007/978-3-642-18912-8_5

Weiss-Gibbons, T. (2022). Impacts of River Runoff in the Arctic Ocean: Modelling Changes in Flow and Temperature. *Master's Thesis*, University of Alberta.

Wendisch, M., Brückner, M., Crewell, S., Ehrlich, A., Notholt, J., Lüpkes, C., ... Zeppenfeld, S. (2023). Atmospheric and Surface Processes, and Feedback Mechanisms Determining Arctic Amplification: A Review of First Results and Prospects of the $(AC)^3$ Project. *Bull. Amer. Meteor. Soc.*, 104, E208–E242. doi: 10.1175/BAMS-D-21-0218.1

Wett, S., Rhein, M., Kieke, D., Mertens, C., & Moritz, M. (2023). Meridional connectivity of a 25-year observational AMOC record at 47°N. *Geophys. Res. Lett.*, 50, e2023GL103284. doi: 10.1029/2023GL103284

Wiegand, K., Kieke, D., Myers, P. G., & Yashayaev, I. (under review). Variability of Irminger Water off western Greenland between 1993 and 2021 in the ARMOR3D data set. *J. Geophys. Res.: Oceans*.

Wilks, D. (2011). Statistical methods in the atmospheric sciences. *International Geophysics Series*.

Williams, W. J., & Carmack, E. C. (2015). The 'interior' shelves of the Arctic Ocean: Physical oceanographic setting, climatology and effects of sea-ice retreat on cross-shelf exchange. *Prog. in Ocean.*, 139, 24-41. doi: 10.1016/j.pocean.2015.07.008

WOCE. (2002). *Physical oceanography during METEOR cruise M30/3 on section A01W.* PANGAEA. Retrieved from https://doi.org/10.1594/PANGAEA.293964 doi: 10.1594/PANGAEA.293964

Wood, M., Rignot, E., Fenty, I., An, L., Bjørk, A., van den Broeke, M., ... Zhang, H. (2021). Ocean forcing drives glacier retreat in Greenland. *Sci. Adv.*, 7, 1-10. doi: 10.1126/sciadv.aba7282

Wunsch, C. (2005). The Total Meridional Heat Flux and Its Oceanic and Atmospheric Partition. *J. Climate*, 18, 4374-4380. doi: https://doi.org/10.1175/JCLI3539.1

Yashayaev, I. (2007a). Hydrographic changes in the Labrador Sea, 1960–2005. *Prog. in Ocean.*, 73, 242-276. doi: 10.1016/j.pocean.2007.04.015

Yashayaev, I., van Aken, H. M., Holliday, N. P., & Bersch, M. (2007b). Transformation of the Labrador Sea Water in the subpolar North Atlantic. *Geophys. Res. Lett.*, 34, L22605. doi: 10.1029/2007GL031812

Yashayaev, I., Bersch, M., & van Aken, H. M. (2007c). Spreading of the Labrador Sea Water to the Irminger and Iceland basins. *Geophys. Res. Lett.*, 34, L10602. doi: 10.1029/2006GL028999

Yashayaev, I. (2011). *CTD data from Cruise 18HU20110506.* CCHDO. Retrieved 03.04.2014, from https://cchdo.ucsd.edu/cruise/18HU20110506

Yashayaev, I., & Seidov, D. (2015a). The role of the Atlantic Water in multidecadal ocean variability in the Nordic and Barents Seas. *Prog. in Ocean.*, 132, 68-127. doi: 10.1016/j.pocean.2014.11.009

Yashayaev, I., Seidov, D., & Demirov, E. (2015b). A new collective view of oceanography of the Arctic and North Atlantic basins. *Prog. in Ocean.*, 132, 1-21. doi: 10.1016/j.pocean.2014.12.012

Yashayaev, I., & Loder, J. W. (2016). Recurrent replenishment of Labrador Sea Water and associated decadal-scale variability. *J. Geophys. Res.: Oceans*, 121, 8095-8114. doi: 10.1002/2016JC012046

Yashayaev, I., & Loder, J. W. (2017). Further intensification of deep convection in the Labrador Sea in 2016. *Geophys. Res. Lett.*, 44, 1429-1438. doi: 10.1002/2016GL071668

Yashayaev, I., Peterson, I., & Wang, Z. (2022). Meteorological, Sea Ice, and Oceanographic Conditions in the Labrador Sea during 2020. *DFO Can. Sci. Advis. Sec. Res. Doc.*, 39, 1-62. Retrieved 06.10.2022, from https://publications.gc.ca/collections/collection_2022/mpo-dfo/fs70-5/Fs70-5-2022-039-eng.pdf

Yeager, S., Castruccio, F., Chang, P., Danabasoglu, G., Maroon, E., Small, J., ... Zhang, S. (2021). An outsized role for the Labrador Sea in the multidecadal variability of the Atlantic overturning circulation. *Sci. Adv.*, 7, eabh3592. doi: 10.1126/sciadv.abh3592

Zhu, J., & Demirov, E. (2011). On the mechanism of interannual variability of the Irminger Water in the Labrador Sea. *J. Geophys. Res.: Oceans*, 116, C03014. doi: 10.1029/2009JC005677

Acknowledgments

First of all, I want to thank my supervisor Dagmar Kieke. Dagmar, your regular and steady feedback and support, especially during the initial stages of my Ph.D., have been so valuable in guiding me into the project. You have given me the freedom to develop my ideas and have channeled them with your expertise onto the right path. During the pandemic, our virtual meetings were an anchor that kept the progress of my project in place. Moreover, you always have an open ear for other topics besides Irminger Water and science.

I extend my gratitude to the oceanography working group at the University of Bremen for engaging discussions during the North Atlantic meetings, providing feedback on scientific presentations and questions, and sharing numerous lunch breaks that helped clear the head. I also want to highlight my gratitude to Monika Rhein for her support in providing additional funding. Further, I want to thank my fellow office friends Wiebke and Simon. Despite the constrained office hours in 2020 and 2021, I enjoyed your daily company and distracting scientific and non-scientific discussions.

I also like to express my gratitude to my co-supervisor, Paul G. Myers, from the University of Alberta. I might have spent more time in your lab without the pandemic repeatedly deferring my research stay. Nevertheless, my time in Edmonton was nothing short of inspiring and immensely valuable. Additionally, the period was productive, as I almost fully developed the provenance and hydrographic methods during my 10-week stay in your lab. Therefore, Paul, I extend my thanks to you for your daily feedback throughout my stay in Canada, as well as during the remote group meetings over the course of my Ph.D. I also extend my appreciation to the entire Numerical Modeling group at the UofA for their warm welcome into the small lab family.

Being a part of the ArcTrain family, I want to thank all my fellow colleagues and friends. The workshops, seminars, workshops, social events, and lunch breaks wouldn't have been such positive experiences without you! ArcTrain's support has been invaluable, aiding in conferences, retreats, international annual meetings, and my research stay in Edmonton. These events have played a crucial role in helping me expand my network and prepare for upcoming challenges. I want to offer a major thank you to Jenny and Jan for putting up with me in our Edmonton apartment!

I extend my gratitude to my complete thesis committee: Dagmar Kieke, Paul G. Myers, Monika Rhein, and Gunnar Spreen. Your consistent guidance has steered me through my project, helping me by asking the right questions at the right times.

I am also very grateful to all participants, scientists, and crew members of the RV METEOR cruise M164 and the WSRV ATAIR cruise 006-1. Embracing the ocean has become a profound passion for me, even though my parents could never have foreseen this due to my childhood fear of boarding ships. Much like those preceding, these cruises have strengthened my goal to continue my career in sea-going oceanography. Witnessing the ocean's immense forces and the boundless horizon is always a breath-takingly beautiful experience. However, I digress...

I also want to highlight and thank Igor Yashayaev for his regular support, questions, and comments during the last 1.5 years, adding significant value to the studies of Chapter 3 and Chapter 4, and for providing me with the DOORS data set. Additionally, I want to thank Astrid Pacini (University of Washington) and Robert S. Pickart (Woods Hole Oceanographic Institution) for sending me the time series of Irminger Water properties from the OSNAP West moorings.

Naturally, I am also grateful to all my friends who, knowingly or unknowingly, provided me with mental support. Particularly during the pandemic, our virtual and in-situ meetings have given me the support I needed. A special thank you goes to Miri and Simon for having been my sole social contacts amidst the most stringent constraints of the pandemic and for designating their guest towel with my name. I would also like to emphasize those who provided me with feedback on this thesis. A big thank you to Andrea, Birte, Marek, Ria, Reiner, Tim, Simon, and Vasco!

My deepest gratitude is directed to my family. Your unwavering support has been with me not just during the past four years but for over 31 years. This thesis, along with numerous preceding achievements, would have remained unreachable without your steadfast support. A significant portion of the credit for this thesis belongs to you!

Funding and Data Acknowledgments

This thesis was funded by the German Research Foundation (Deutsche Forschungsgemeinschaft) through the International Research Training Group ArcTrain 'Processes and impacts of climate change in the North Atlantic Ocean and the Canadian Arctic' (IRTG 1904 ArcTrain, grant 221211316, sub-project HB-07/3 of D. Kieke). I extend my gratitude to everyone who contributed to the generation of the data sets used in this thesis.

ARMOR3D

This thesis has been conducted using E.U. Copernicus Marine Service Information (Guinehut et al., 2012; Mulet et al., 2012). For further information on ARMOR3D, please follow (Greiner et al., 2020; Guinehut, 2020).
Product Identifier: MULTIOBS_GLO_PHY_TSUV_3D_MYNRT_015_012
doi: https://doi.org/10.48670/moi-00052

GLORYS

For information on GLORYS, please follow (Drévillon et al., 2022a, 2022b).
Product Identifier: GLOBAL_MULTIYEAR_PHY_001_030
doi: https://doi.org/10.48670/moi-00021

NEMO

The analyzed model data have been provided by Paul G. Myers from the University of Alberta. For information on NEMO, please follow (Madec et al., 1998, 2023). The individual model simulations follow Weiss-Gibbons (2022) for ANHA4, X. Hu et al. (2018) for ANHA12, and Pennelly and Myers (2020) for LAB60.

Ship-based data

I would like to acknowledge the efforts of scientists and crew members from numerous research cruises aboard various vessels (CSS Hudson, METEOR, Knorr, RV THALASSA, and MARIA S. MERIAN) whose data I have utilized in this thesis (see Table 2.1).

DOORS

I thank I. Yashayaev (Bedford Institute of Oceanography) for providing the DOORS data used in this thesis.

OSNAP

OSNAP data were collected and made freely available by the OSNAP project and all the national programs that contribute to it (www.o-snap.org). Data can be downloaded following https://doi.org/10.35090/gatech/70342. I thank A. Pacini (University of Washington) and R. S. Pickart (Woods Hole Oceanographic Institution) who provided me with time series of IW properties calculated from OSNAP West mooring observations.

Argo

The DOORS data include data from the International Argo Program (Argo, 2000). These data were collected and made freely available by the International Argo Program and the national programs that contribute to it (https://argo.ucsd.edu, https://www.ocean-ops.org). The Argo Program is part of the Global Ocean Observing System.

Global radiation

European Centre for Medium-Range Weather Forecasts Re-Analysis 5 radiation data used in Figure 1.1 have been obtained following Hersbach et al. (2019).

Global surface temperature

Global surface temperatures used in Figure 1.3 have been obtained from NOAA (2023a).

Etopo1

Etopo1 data have been obtained from NOAA (2009), see also Amante and Eakins (2009).

Sea ice concentration

Sea ice concentration data have been used from the National Snow and Ice Data Center (DiGirolamo et al., 2022).

NAO

The NAO index analyzed in Chapter 3.3.5 was obtained from NOAA (2023b).

SPG

I also want to thank L. Chafik (Stockholm University) for providing SPG index data (Chafik, 2019). I used his SPG index for comparison with the SPG index calculated from ARMOR3D in Chapter 3.3.5. For more information on the analysis of the SPG index from Chafik (2019), please refer to (Hátún & Chafik, 2018).

Declaration of Originality

I, Kevin Niklas Wiegand, certify that the work presented here is, to the best of my knowledge and belief, original and the result of my own investigations, except as acknowledged, and has not been submitted, either in part or whole, for a degree at this or any other University. Parts of Chapter 1, Chapter 2, and most parts of Chapter 3 are part of a study that is currently under review (as of August 24, 2023) for publication in the peer-reviewed Journal of Geophysical Research: Ocean, Wiegand et al. (under review). Parts of Chapter 1 and most parts of Chapter 4 are part of a study currently preparing for publication in the peer-reviewed Journal of Geophysical Research: Ocean. The text of both mentioned manuscripts has been partially adapted to fit the context of this thesis.

Place, Date

Kevin Niklas Wiegand